

# High Frequency Electromagnetic Links for Wireless Power Transfer

**James Lawson**  
January 2017

Thesis submitted in partial fulfilment of the  
requirements for the degree of  
Doctor of Philosophy of Imperial College London  
and the Diploma of Imperial College

Wireless Power Lab  
Control and Power Group  
Department of Electrical and Electronic Engineering  
Imperial College London  
London, SW7 2AZ  
United Kingdom

## Abstract

This thesis investigates inductive links used in wireless power transfer systems. Inductive power transfer can be used as a power delivery method for a variety of portable devices, from medical implants to electric vehicles and is gaining increased interest. The focus is on high quality factor coils and MHz operation, where accurate measurements are difficult to achieve.

Fast models of all pertinent aspects of inductive power transfer systems for constant cross section coils are developed. These models are used to optimise a new coil winding pattern that aims to increase efficiency in volume constrained scenarios. Measurement systems are developed to measure coil  $Q$  factors in excess of 1,000. The prototype measurement systems are verified against models of that system, as well as finite element simulations of the coil under test.

Shielding of inductive power transfer systems is then investigated. A structure typically used at GHz frequencies, the artificial magnetic conductor, is miniaturised as an alternative to conventional ferrite backed ground plane shielding. Finite element simulation shows this structure significantly improves link efficiency. The artificial magnetic conductor prototype does not result in a gain in efficiency expected, however it does display the properties expected of an artificial magnetic conductor, including increased coupling factor.

Finally, an unconventional inductive power transfer system is presented where transmitter and receiver are up to 6 m away from each other and of radically different size. This system provides mW level power to remote devices in a room, for example thermostats or e-ink displays. Conventional approaches to design do not consider the distortion of the magnetic field caused by metallic objects in the room. It was found that treating the system as a decoupled receiver and transmitter provides a better prediction of received power in real world environments.

## **Declaration and Copyright**

### **Declaration:**

I hereby certify that the material and artefacts presented in this thesis, which I now submit for the award of Doctor of Philosophy of Imperial College London, is entirely my own work unless cited, acknowledged or declared otherwise within the text of this thesis.

**James Lawson**

### **Copyright:**

The copyright of this thesis rests with the author and is made available under a Creative Commons Attribution Non-Commercial No Derivatives license. Researchers are free to copy, distribute or transmit the thesis on the condition that they attribute it, that they do not use it for commercial purposes and that they do not alter, transform or build upon it. For any reuse or redistribution, researchers must make clear to others the license terms of this work.

# Contents

|  |           |
|--|-----------|
| <b>List of Figures</b>                                   | <b>3</b>  |
| <b>1 Introduction</b>                                    | <b>1</b>  |
| 1.1 Motivation for inductive power transfer (IPT)        | 1         |
| 1.2 Condensed history of inductive power transfer        | 1         |
| 1.3 Structure of this chapter                            | 2         |
| 1.4 IPT link theory                                      | 3         |
| 1.4.1 Parallel resonant receiver load                    | 4         |
| 1.4.2 Series resonant receiver load                      | 5         |
| 1.4.3 Resistive receiver load                            | 6         |
| 1.4.4 Choice of tuning                                   | 7         |
| 1.5 Examples   | 7         |
| 1.5.1 Example 1 - $Q$ factor requirement                 | 7         |
| 1.5.2 Example 2 - Optimal load                           | 8         |
| 1.5.3 Example 3 - Frequency requirement                  | 9         |
| 1.6 Thesis organisation                                  | 11        |
| <b>2 Modelling and simulation of inductive links</b>     | <b>13</b> |
| 2.1 Introduction   | 13        |
| 2.1.1 Inductive link model                               | 15        |
| 2.2 Introduction to coil types                           | 15        |
| 2.2.1 Discretisation of filamentary models of coils      | 15        |
| 2.2.2 Volumetrically efficient coil (VEC)                | 16        |
| 2.2.3 Parametric coil equations                          | 16        |
| 2.3 Method   | 19        |
| 2.3.1 Calculation methodology                            | 19        |
| 2.3.2 Calculation of inductances                         | 19        |
| 2.3.3 Calculation of magnetic fields                     | 20        |
| 2.3.4 Calculation of resistances                         | 22        |
| 2.3.5 Simulation tool for skin effect modelling of tubes | 25        |
| 2.4 Results  | 27        |
| 2.4.1 Inductance   | 27        |
| 2.4.2 Resistance   | 33        |
| 2.4.3 Optimal tube geometry                              | 41        |
| 2.4.4 Magnetic field modelling                           | 41        |
| 2.4.5 Full IPT system example                            | 42        |
| 2.5 Conclusion and further work                          | 47        |



|          |  |            |
|----------|--|------------|
| <b>3</b> | <b>Measurement of wireless power transfer coils</b>                          | <b>48</b>  |
| 3.1      | Introduction . . . . .   | 48         |
| 3.1.1    | Literature review . . . . .  | 49         |
| 3.2      | Definitions of Q . . . . .   | 50         |
| 3.2.1    | Energy definition . . . . .  | 50         |
| 3.2.2    | Bandwidth definition . . . . .   | 51         |
| 3.3      | Coil model for inductive power transfer . . . . .                            | 52         |
| 3.4      | Capacitance extraction method . . . . .                                      | 53         |
| 3.5      | Resonator loss relocation . . . . .  | 54         |
| 3.6      | Series resonance with additional capacitor . . . . .                         | 55         |
| 3.7      | Measurement methods . . . . .  | 55         |
| 3.7.1    | Vector network analyser (VNA) . . . . .                                      | 55         |
| 3.7.2    | Single port direct measurement . . . . .                                     | 63         |
| 3.7.3    | Single port direct with resonance measurement . . . . .                      | 63         |
| 3.7.4    | Two port direct measurement . . . . .  | 63         |
| 3.7.5    | Two port direct measurement with resonance . . . . .                         | 65         |
| 3.7.6    | Transmission type measurement . . . . .                                      | 65         |
| 3.7.7    | Impedance analyser . . . . .   | 72         |
| 3.8      | Reference coil measurements . . . . .  | 74         |
| 3.8.1    | Introduction . . . . .   | 74         |
| 3.8.2    | Coil EM simulation models . . . . .  | 74         |
| 3.8.3    | Results comparison - transmission type measurement . . . . .                 | 76         |
| 3.8.4    | Varying distance between coupling loops . . . . .                            | 83         |
| 3.9      | Automatic measurement system . . . . .                                       | 86         |
| 3.9.1    | Connector repeatability . . . . .  | 86         |
| 3.9.2    | Shielding . . . . .  | 87         |
| 3.9.3    | Calibration . . . . .  | 88         |
| 3.9.4    | Measurement procedure . . . . .  | 88         |
| 3.9.5    | Initial measurements . . . . .   | 88         |
| 3.9.6    | Two channel prototype . . . . .  | 89         |
| 3.9.7    | Calibration theory . . . . .   | 93         |
| 3.10     | Conclusion . . . . .   | 104        |
| <b>4</b> | <b>Artificial magnetic conductors applied to wireless power transfer</b>     | <b>105</b> |
| 4.1      | Introduction . . . . .   | 105        |
| 4.2      | High impedance ground plane as artificial magnetic conductor (AMC) . . . . . | 106        |
| 4.3      | Survey of existing applicable metamaterials research . . . . .               | 108        |
| 4.4      | Initial simulation case study . . . . .                                      | 109        |
| 4.5      | Comparison charging pad system . . . . .                                     | 114        |
| 4.5.1    | Introduction . . . . .   | 114        |
| 4.5.2    | Results . . . . .  | 115        |
| 4.5.3    | field simulations . . . . .  | 138        |
| 4.5.4    | Conclusions and further work . . . . .                                       | 141        |

|          |  |            |
|----------|--|------------|
| <b>5</b> | <b>Long range inductive power transfer system</b>                              | <b>142</b> |
| 5.1      | Introduction . . . . .   | 142        |
| 5.2      | Design . . . . .   | 144        |
| 5.2.1    | Transmit coil . . . . .  | 144        |
| 5.2.2    | Amplifier . . . . .  | 144        |
| 5.2.3    | Miniaturised receiver coils . . . . .  | 144        |
| 5.2.4    | 170 mm receiver coil . . . . .   | 146        |
| 5.3      | Long range IPT approximations . . . . .  | 149        |
| 5.4      | Results . . . . .  | 149        |
| 5.5      | Conclusion . . . . .   | 150        |
| <b>6</b> | <b>Conclusions and further work</b>  | <b>152</b> |
| 6.1      | Overview and main findings . . . . .   | 152        |
| 6.2      | Author's contribution . . . . .  | 155        |
| 6.2.1    | Measurement of wireless power transfer coils . . . . .                         | 155        |
| 6.2.2    | Modelling and simulation of inductive links . . . . .                          | 156        |
| 6.2.3    | Artificial magnetic conductors applied to wireless power<br>transfer . . . . . | 156        |
| 6.2.4    | Long range inductive power transfer system . . . . .                           | 156        |
| 6.3      | Collaboration . . . . .  | 156        |
| 6.4      | Suggestions for further work . . . . .   | 157        |
| 6.4.1    | Inconclusive areas of this thesis . . . . .                                    | 157        |
| 6.4.2    | Speculative areas of inductive power transfer development . . . . .            | 158        |
| <b>7</b> | <b>Publications</b>  | <b>159</b> |
| 7.1      | Conference papers . . . . .  | 159        |
| 7.2      | Patents . . . . .  | 159        |
|          | <b>Appendices</b>  | <b>168</b> |
| <b>A</b> | <b>Grover <math>f(\tau^2)</math> table</b>                                     | <b>168</b> |
| <b>B</b> | <b>Verification resistor measurement</b>                                       | <b>169</b> |
| <b>C</b> | <b>MATLAB code for inductance calculation</b>                                  | <b>170</b> |
| <b>D</b> | <b>MATLAB code for tube resistance calculation</b>                             | <b>172</b> |
| <b>E</b> | <b>MATLAB code for magnetic field calculation</b>                              | <b>176</b> |
| <b>F</b> | <b>MATLAB code for processing of impedance measurements</b>                    | <b>178</b> |

# List of Figures

|      |  |    |
|------|--|----|
| 1.1  | Transformer model of inductive power transfer system. . . . .  | 3  |
| 1.2  | Transformer model of inductive power transfer system with receiver referred to transmitter coil (left) and further transformation into reflected impedance upon transmitter coil caused by the receiver coil and load (right). . . . .   | 3  |
| 1.3  | Receiver load configurations, from left to right: parallel resonant, series resonant, resistive. . .   | 4  |
| 1.4  | Case study of effect on coil $Q$ on inductive link efficiency. . . . .   | 8  |
| 1.5  | Optimal loads at 10 MHz for loops. . . . .   | 9  |
| 1.6  | Relative efficiencies of loop IPT systems as the real load deviates from its optimal value. . .  | 9  |
| 1.7  | Simplified model showing the $Q$ with respect to frequency. Of particular note is that the coil $Q$ has a maxima at 17.9 MHz due to the balance of radiation and skin effect losses. . . . .   | 10 |
| 2.1  | Transformer model of inductive link including coils self capacitance. . . . .  | 14 |
| 2.2  | Dimensional constraints of an inductive Link. . . . .  | 14 |
| 2.3  | Table of existing coils windings in MHz IPT . . . . .  | 16 |
| 2.4  | Four turn volumetrically efficient coil (VEC) cross section, showing return conductors on the right hand side. . . . .   | 17 |
| 2.5  | Meshing of a single, isolated tube using a simple meshing algorithm. . . . .   | 26 |
| 2.6  | Zoomed view of meshing of a single, isolated tube (Fig. 2.5). . . . .  | 27 |
| 2.7  | A comparison of the self inductances of helical coils. . . . .   | 27 |
| 2.8  | A comparison of the self inductances of planar spiral coils. . . . .   | 27 |
| 2.9  | A comparison of the self inductances of volumetrically efficient coils. . . . .  | 28 |
| 2.10 | Analytically solved lengths of coils compared with summing the total length of filaments that make up the filamentary models. . . . .  | 28 |
| 2.11 | Diagram showing coil 4 at centre to centre distance of 84 mm with 90° of rotation about the x axis. . . . .  | 29 |
| 2.12 | Helical coil (Table 2.7) to helical coil mutual inductance with respect to air gap between the coils. . . . .  | 30 |
| 2.13 | PSC (Table 2.8) to PSC mutual inductance with respect to air gap between the coils. . . .  | 30 |
| 2.14 | VEC (Table 2.9) to VEC mutual inductance with respect to air gap between the coils. . . .  | 31 |
| 2.15 | Mutual inductance between two coil 4 (Table 2.7) with respect to x axis displacement a fixed 48 mm air gap. . . . .  | 31 |
| 2.16 | Mutual inductance between two coil 4 (Table 2.7) with respect to rotation about the x axis of one of the coils at a fixed 84 mm centre to centre distance. This distance is the same as the 48 mm air gap at 0° and multiples of 180° rotation in figure 2.15. As only one coil is rotated about its centre and the coils are three dimensional the air gap between the coils is less for other angles, an example of this is shown in figure 2.11. Where the inductance is recorded as negative this is because the polarity of the induced voltage on the rotated coil has reversed. . | 32 |

|      |  |    |
|------|--|----|
| 2.17 | Model of skin effect resistance of tubes compared with finite element simulations (FE) conducted in Fast Henry and data from Dwight. . . . .           | 33 |
| 2.18 | Model of internal inductance of tubes compared with finite element simulations (FE) conducted in Fast Henry. . . . .                                   | 33 |
| 2.19 | Loop radius to conductor radius ratio model and simulation comparison for AC resistance. . .   | 34 |
| 2.20 | Dimensionless proximity factor modelling comparison with finite element simulation. . . . .  | 35 |
| 2.21 | CST simulation of coil 1 (Table 2.7) of coils resistance when fit to LCR coil model compared with tube resistance model. . . . .                       | 36 |
| 2.22 | CST simulation of coil 2 (Table 2.7) of coils resistance when fit to LCR coil model compared with tube resistance model. . . . .                       | 37 |
| 2.23 | CST simulation of coil 3 (Table 2.7) of coils resistance when fit to LCR coil model compared with tube resistance model. . . . .                       | 37 |
| 2.24 | CST simulation of coil 4 (Table 2.7) of coils resistance when fit to LCR coil model compared with tube resistance model. . . . .                       | 37 |
| 2.25 | CST simulation of coil 5 (Table 2.8) of coils resistance when fit to LCR coil model compared with tube resistance model. . . . .                       | 38 |
| 2.26 | CST simulation of coil 6 (Table 2.8) of coils resistance when fit to LCR coil model compared with tube resistance model. . . . .                       | 38 |
| 2.27 | CST simulation of coil 7 (Table 2.8) of coils resistance when fit to LCR coil model compared with tube resistance model. . . . .                       | 38 |
| 2.28 | CST simulation of coil 8 (Table 2.8) of coils resistance when fit to LCR coil model compared with tube resistance model. . . . .                       | 39 |
| 2.29 | CST simulation of coil 9 (Table 2.9) of coils resistance when fit to LCR coil model compared with tube resistance model. . . . .                       | 39 |
| 2.30 | CST simulation of coil 10 (Table 2.9) of coils resistance when fit to LCR coil model compared with tube resistance model. . . . .                      | 39 |
| 2.31 | CST simulation of coil 11 (Table 2.9) of coils resistance when fit to LCR coil model compared with tube resistance model. . . . .                      | 40 |
| 2.32 | CST simulation of coil 12 (Table 2.9) of coils resistance when fit to LCR coil model compared with tube resistance model. . . . .                      | 40 |
| 2.33 | CST simulations of coils 1- 4 (Table 2.7) showing that losses beyond 10 MHz begin to be affected by other factors than the skin effect . . . . .       | 40 |
| 2.34 | FE simulations showing the spacing of tubes for optimal $Q$ . . . . .  | 41 |
| 2.35 | Coil 4 (blue) with path the $\mathbf{B}$ field is plotted along (red) when the coil is excited with 1 A. . .   | 42 |
| 2.36 | Magnetic field along the path shown in figure 2.35. . . . .  | 42 |
| 2.37 | Optimisation sweep of two turn VEC showing for this particular parameter sweep that minimal turn spacing and maximum turn radius is desirable. . . . . | 43 |
| 2.38 | Equivalent circuit of optimal VEC magnetic link used to determine secondary current. . . . .   | 44 |
| 2.39 | Complex Tx and Rx coil current for optimal VEC magnetic link with optimal load. . . . .  | 44 |
| 2.40 | $x = 0$ cut plane from which the field plots are generated, the air gap between the two coils is 150 mm, this is three times the coils radii. . . . .  | 45 |
| 2.41 | Magnetic field strength extracted from CST simulation $x = 0$ cut plane for optimal VEC system operating into optimal load. . . . .                    | 46 |
| 2.42 | Magnetic field strength generated by model $x = 0$ cut plane for optimal VEC system operating into optimal load. . . . .                               | 46 |
| 3.1  | Parallel LCR resonator. . . . .  | 51 |

|      |   |    |
|------|---|----|
| 3.2  | Comparison between energy and bandwidth $Q$ definitions for different proportionalities of $R$ .  | 52 |
| 3.3  | Coil model for IPT.   | 53 |
| 3.4  | Coil capacitance fit plot over a wide frequency range.  | 54 |
| 3.5  | Internal inductance variation for straight conductive tube.   | 54 |
| 3.6  | Series resonant coil measurement configuration.   | 55 |
| 3.7  | Single and two port impedance measurement method comparison for real load.  | 56 |
| 3.8  | Single port direct measurement performance in the presence of reactance.  | 57 |
| 3.9  | Two port direct measurement performance in the presence of reactance.   | 57 |
| 3.10 | Coaxial cable with loop antenna.  | 58 |
| 3.11 | Configuration for ADT1-6T+ differential S-parameters.   | 59 |
| 3.12 | ADT1-6T+, $S_{cc11}$ .  | 60 |
| 3.13 | ADT1-6T+, $S_{cc21}$ .  | 60 |
| 3.14 | ADT1-6T+, $S_{cc22}$ .  | 60 |
| 3.15 | ADT1-6T+, $S_{cd22}$ .  | 60 |
| 3.16 | ADT1-6T+, $S_{dc21}$ .  | 61 |
| 3.17 | ADT1-6T+, $S_{dd22}$ .  | 61 |
| 3.18 | ADT1-6T+, CMRR  | 61 |
| 3.19 | Direct single port measurement of a 3 turn VEC with and without balun - note that impedances far from $50\Omega$ will have a large uncertainty. | 62 |
| 3.20 | Single port measurement without resonance (Balun not shown).  | 63 |
| 3.21 | Two port measurement without resonance and series impedance, $p$ , in measurement path.   | 63 |
| 3.22 | Transmission type measurement system showing coupling loops, coil under test and VNA.   | 65 |
| 3.23 | Coupling loop used in transmission type measurement.  | 65 |
| 3.24 | Mutual inductances of measurement system  | 66 |
| 3.25 | Passive frequency domain simulation model of transmission type measurement system.  | 66 |
| 3.26 | 0.09 m distance between coupling loops.   | 68 |
| 3.27 | 0.13 m distance between coupling loops.   | 68 |
| 3.28 | 0.17 m distance between coupling loops.   | 68 |
| 3.29 | 0.21 m distance between coupling loops.   | 68 |
| 3.30 | 0.25 m distance between coupling loops.   | 69 |
| 3.31 | 0.29 m distance between coupling loops.   | 69 |
| 3.32 | 0.33 m distance between coupling loops.   | 69 |
| 3.33 | 0.37 m distance between coupling loops.   | 69 |
| 3.34 | 0.41 m distance between coupling loops.   | 70 |
| 3.35 | 0.45 m distance between coupling loops.   | 70 |
| 3.36 | 0.49 m distance between coupling loops.   | 70 |
| 3.37 | 0.53 m distance between coupling loops.   | 70 |
| 3.38 | 0.57 m distance between coupling loops.   | 71 |
| 3.39 | 0.61 m distance between coupling loops.   | 71 |
| 3.40 | E4990A impedance analyser performance measuring real loads in the presence of reactance for the frequency range 1 kHz to 1 MHz.                 | 72 |
| 3.41 | E4990A impedance analyser performance measuring real loads in the presence of reactance for the frequency range 5 MHz to 10 MHz.                | 73 |
| 3.42 | E4990A impedance analyser performance measuring real loads in the presence of reactance for the frequency range 10 MHz to 120 MHz.              | 73 |
| 3.43 | Reference coils.  | 75 |
| 3.44 | Reference coil with capacitor attachment board.   | 75 |

|      |   |    |
|------|---|----|
| 3.45 | Relative permittivity of coil former. . . . .   | 76 |
| 3.46 | Measured loss of coil former dielectric, note the results show lower loss than is discernible with the test equipment. The gap in the data at 14 MHz is an artefact of the resonance associated with cable lengths used to connect the fixture. . . . . | 76 |
| 3.47 | ESR of reference coil 1 attachment board. . . . .   | 78 |
| 3.48 | ESR of reference coil 2 attachment board. . . . .   | 78 |
| 3.49 | ESR of reference coil 3 attachment board. . . . .   | 78 |
| 3.50 | ESR of reference coil 4 attachment board. . . . .   | 79 |
| 3.51 | Self inductances and capacitances of measurement system elements, *model value. . . . .   | 80 |
| 3.52 | Transmission modelling and measurement comparison for reference coil 1. . . . .   | 81 |
| 3.53 | Transmission modelling and measurement comparison for reference coil 2. . . . .   | 81 |
| 3.54 | Transmission modelling and measurement comparison for reference coil 3. . . . .   | 81 |
| 3.55 | Transmission modelling and measurement comparison for reference coil 4. . . . .   | 82 |
| 3.56 | Transmission modelling and measurement comparison for long coil. . . . .  | 83 |
| 3.57 | Comparison of modelled measurement system with and without test loop to test loop coupling  | 84 |
| 3.58 | Variation in $Q$ for modelled measurement system with test loop spacing, for 470 pF tuning capacitor. Actual $Q$ is 574, 585, 607, 623 for coils 1 to 4, respectively. . . . .  | 85 |
| 3.59 | Variation in $Q$ for modelled measurement system with test loop spacing, for 120 pF tuning capacitor. Actual $Q$ is 698, 739, 808, 821 for coils 1 to 4, respectively. . . . .  | 85 |
| 3.60 | Automatic measurement system with two measurement channels. . . . .   | 86 |
| 3.61 | Real portion measurement standard deviation for shorting bar in series test fixture. . . . .  | 87 |
| 3.62 | Shielding efficacy results showing the majority of the magnetic coupling is between the coil and the PCB tracks. . . . .  | 87 |
| 3.63 | Initial series coil measurements of coil 3 using single channel prototype. . . . .  | 89 |
| 3.64 | Two channel measurement system prototype, controlled by microprocessor development board. Insert shows reference standards. . . . .   | 89 |
| 3.65 | Measurement of Short standard using calibrated impedance analyser. . . . .  | 90 |
| 3.66 | Measurement of Open standard using calibrated impedance analyser. . . . .   | 90 |
| 3.67 | Measurement of Load standard using impedance analyser. . . . .  | 91 |
| 3.68 | Measurement of Short standard using two channel prototype with no error correction. . . . .   | 91 |
| 3.69 | Measurement of Open standard two channel using using prototype with no error correction. . . . .  | 91 |
| 3.70 | Measurement of Load standard using two channel prototype with no error correction. . . . .  | 91 |
| 3.71 | Measurements of Verification standard. This shows that the two terminal measurement system can resolve resistances similar to that of a coil at resonance while switching its measurement channel. . . . .  | 92 |
| 3.72 | Fixture and device under test . . . . .   | 93 |
| 3.73 | Example of a simple fixture that the model of figure 3.72 can be applied to . . . . .   | 94 |
| 3.74 | Simulated example showing correctable parasitic elements, for what each element corresponds to physically see figure 3.72 and 3.73 . . . . .  | 97 |
| 3.75 | Uncorrected measurement of $\mathbf{X_S}$ with Short circuit termination . . . . .  | 97 |
| 3.76 | Uncorrected measurement of $\mathbf{X_S}$ with Open circuit termination . . . . .   | 98 |
| 3.77 | Uncorrected measurement of $\mathbf{X_S}$ with Load circuit termination . . . . .   | 98 |
| 3.78 | Uncorrected measurement of $\mathbf{X_C}$ with Short circuit termination . . . . .  | 98 |
| 3.79 | Uncorrected measurement of $\mathbf{X_C}$ with Open circuit termination . . . . .   | 98 |
| 3.80 | Uncorrected measurement of $\mathbf{X_C}$ with Load circuit termination . . . . .   | 99 |
| 3.81 | $S_{11}$ parameter of $\mathbf{X_S}$ recovered from SOL standard measurements compared with $S_{11}$ of original $\mathbf{X_S}$ . . . . .   | 99 |

|      |   |     |
|------|---|-----|
| 3.82 | $S_{21}$ parameter of $\mathbf{X}_S$ recovered from SOL standard measurements compared with $S_{21}$ of original $\mathbf{X}_S$ . . . . .   | 99  |
| 3.83 | $S_{22}$ parameter of $\mathbf{X}_S$ recovered from SOL standard measurements compared with $S_{22}$ of original $\mathbf{X}_S$ . . . . .   | 100 |
| 3.84 | $S_{11}$ parameter of $\mathbf{X}_C$ recovered from SOL standard measurements compared with $S_{11}$ of original $\mathbf{X}_C$ . . . . .   | 100 |
| 3.85 | $S_{21}$ parameter of $\mathbf{X}_C$ recovered from SOL standard measurements compared with $S_{21}$ of original $\mathbf{X}_C$ . . . . .   | 100 |
| 3.86 | $S_{22}$ parameter of $\mathbf{X}_C$ recovered from SOL standard measurements compared with $S_{22}$ of original $\mathbf{X}_C$ . . . . .   | 101 |
| 3.87 | $S_{11}$ parameter of network $\mathbf{A}$ (Fig. 3.72) recovered from SOL standard measurements of $\mathbf{X}_C$ and $\mathbf{X}_S$ . . . . .  | 101 |
| 3.88 | $S_{21}$ parameter of network $\mathbf{A}$ (Fig. 3.72) recovered from SOL standard measurements of $\mathbf{X}_C$ and $\mathbf{X}_S$ . . . . .  | 101 |
| 3.89 | $S_{22}$ parameter of network $\mathbf{A}$ (Fig. 3.72) recovered from SOL standard measurements of $\mathbf{X}_C$ and $\mathbf{X}_S$ . . . . .  | 102 |
| 3.90 | $S_{11}$ parameter of network $\mathbf{C}$ (Fig. 3.72) recovered from SOL standard measurements of $\mathbf{X}_C$ and $\mathbf{X}_S$ . . . . .  | 102 |
| 3.91 | $S_{21}$ parameter of network $\mathbf{C}$ (Fig. 3.72) recovered from SOL standard measurements of $\mathbf{X}_C$ and $\mathbf{X}_S$ . . . . .  | 102 |
| 3.92 | $S_{22}$ parameter of network $\mathbf{C}$ (Fig. 3.72) recovered from SOL standard measurements of $\mathbf{X}_C$ and $\mathbf{X}_S$ . . . . .  | 103 |
| 3.93 | Final recovered impedance connected to the output network $\mathbf{X}_C$ reconstructed by de-embedding the network $\mathbf{X}_C$ . The impedance is the same as simulated $0.2653\Omega$ in series with $2.533\mu\text{H}$ . The real portion of this result is most accurately determined at the first zero crossing of Fig. 3.80. . . . .  | 103 |
| 4.1  | IPT coils over backing plates. . . . .  | 106 |
| 4.2  | Unit cell of developed AMC. . . . .   | 106 |
| 4.3  | Transmission line model of AMC. . . . .   | 107 |
| 4.4  | Unit cell simulation for TE excitation. . . . .   | 110 |
| 4.5  | Unit cell simulation for TM excitation. . . . .   | 110 |
| 4.6  | 1 MHz (upper) and 12.3 MHz (lower), RMS surface tangential H field strength for 1 W excitation. . . . .   | 111 |
| 4.7  | Maximum power transfer efficiency of shielding solutions at a coaxial distance between identical wire loops of 495 mm. The wire loops have a conductive sheet positioned 10 mm behind each of them (apart from in the freespace case where this sheet is not present). The depth of ferrite covering this conductive plane is varied for the ferrite cases. In the AMC case this ferrite depth is 5 mm but due to the engineered structure peak efficiency exceeds that of the same depth of ferrite slab. The low efficiency at 4 MHz in the AMC case is not a simulation artefact and instead shows the surface resonance frequency where the AMC is presenting a conductive sheet close to the coils. All simulations were conducted with open boundary conditions spaced 100 mm from the structure. . . . . | 112 |
| 4.8  | Maximum power transfer efficiency of shielding solutions using lossless ferrite model. . . . .  | 112 |
| 4.9  | Z-parameters of AMC scenario. . . . .   | 113 |
| 4.10 | Cross section showing charging pad structure (AMC type shown), not to scale. . . . .  | 115 |
| 4.11 | AMC (L) and Ferrite (R) charging pads. . . . .  | 115 |



|      |   |     |
|------|---|-----|
| 4.12 | Real portion of permeability fit. Note extrapolated data is inaccurate due to polynomial fit, this has been taken into account in results discussion. . . . .   | 116 |
| 4.13 | Imaginary portion of permeability fit. Note extrapolated data is inaccurate due to polynomial fit, this has been taken into account in results discussion. . . . .  | 116 |
| 4.14 | Effective self inductance of simulated (CST) and measured charging pads, truncated vertical scale for readability. . . . .  | 117 |
| 4.15 | Effective self inductance of simulated (CST) and measured charging pads. The ADJ plot has the resonant frequency relocated to the same frequency as simulation for comparison of amplitude. . . . .   | 118 |
| 4.16 | Effective resistance of simulated (CST) and measured charging pads. . . . .   | 118 |
| 4.17 | Effective self inductance of simulated (CST) AMC charging pads with identical tuning capacitors and 5% tolerance tuning capacitors. . . . .   | 118 |
| 4.18 | Charging pad resonant $Q$ measurement. . . . .  | 119 |
| 4.19 | Measured pads resonant $Q$ . . . . .  | 119 |
| 4.20 | Simulated pads resonant $Q$ . . . . .   | 120 |
| 4.21 | Measured and simulated pads effective coupling factor, $k$ , with 0.05 m air gap between coils. .   | 121 |
| 4.22 | Measured and simulated pads effective coupling factor, $k$ , with 0.10 m air gap between coils. .   | 121 |
| 4.23 | Measured and simulated pads effective coupling factor, $k$ , with 0.15 m air gap between coils. .   | 121 |
| 4.24 | Measured and simulated pads effective coupling factor, $k$ , with 0.20 m air gap between coils .  | 122 |
| 4.25 | Measured effective coupling factor, $k$ , with 0.25 m air gap between coils . . . . .   | 122 |
| 4.26 | Measured effective coupling factor, $k$ , with 0.30 m air gap between coils . . . . .   | 122 |
| 4.27 | Measured effective coupling factor, $k$ , with 0.35 m air gap between coils . . . . .   | 123 |
| 4.28 | Measured effective coupling factor, $k$ , with 0.40 m air gap between coils . . . . .   | 123 |
| 4.29 | Measured effective coupling factor, $k$ , with 0.45 m air gap between coils . . . . .   | 123 |
| 4.30 | Measured transmission coefficient, with 0.05 m air gap between coils . . . . .  | 124 |
| 4.31 | Measured transmission coefficient, with 0.10 m air gap between coils. . . . .   | 125 |
| 4.32 | Measured transmission coefficient, with 0.15 m air gap between coils. . . . .   | 125 |
| 4.33 | Measured transmission coefficient, with 0.20 m air gap between coils. . . . .   | 125 |
| 4.34 | Measured transmission coefficient, with 0.25 m air gap between coils. . . . .   | 126 |
| 4.35 | Measured transmission coefficient, with 0.30 m air gap between coils. . . . .   | 126 |
| 4.36 | Measured transmission coefficient, with 0.35 m air gap between coils. . . . .   | 126 |
| 4.37 | Measured transmission coefficient, with 0.40 m air gap between coils. . . . .   | 127 |
| 4.38 | Measured transmission coefficient, with 0.45 m air gap between coils. . . . .   | 127 |
| 4.39 | $\mu'$ comparison between measurement of ferrite sheet stacks, simulation and data sheet values. Note CST results are inaccurate below 10 MHz due to the polynomial fit. . . . .  | 128 |
| 4.40 | $\mu''$ comparison between measurement of ferrite sheet stacks, simulation and data sheet values. Note CST results are inaccurate below 10 MHz due to the polynomial fit. . . . .   | 128 |
| 4.41 | Loss tangent comparison between measurement of 10 stacked ferrite sheets, simulation and data sheet values. We have omitted the loss tangent data for the stacks less than 10 sheets deep for clarity as it practically overlaps the 10 stack data. . . . . | 129 |
| 4.42 | Predicted fractional power transfer efficiency for 12.9 MHz, from link efficiency equation. Using resonant measurements of pad $Q$ and measured, $k$ . . . . .  | 130 |
| 4.43 | Measured fractional power transfer efficiency comparison between ferrite and AMC wireless power links at 70 mm air gap and approximately 12.9 MHz operation. Measurement made by load sweeps, on real link, with voltage and current monitoring. . . . .    | 130 |
| 4.44 | Predicted fractional power transfer efficiency for 16.941 MHz, from link efficiency equation. Using resonant measurements of pad $Q$ and measured, $k$ . . . . .  | 132 |



|      |   |     |
|------|---|-----|
| 4.45 | Measured fractional power transfer efficiency comparison between ferrite and AMC wireless power links at 100 mm air gap and approximately 16.941 MHz operation. Measurement made by load sweeps, on real link, with voltage and current monitoring. . . . .                           | 132 |
| 4.46 | AMC optimal frequency tuning. . . . .   | 133 |
| 4.47 | Ferrite optimal frequency tuning. . . . .   | 133 |
| 4.48 | AMC fixed 12.9 MHz tuning. . . . .  | 133 |
| 4.49 | Ferrite fixed 12.9 MHz tuning . . . . .   | 134 |
| 4.50 | Simulated fractional maximum power transfer efficiency with 0.05 m air gap between coaxially aligned coils. . . . .   | 134 |
| 4.51 | Simulated fractional maximum power transfer efficiency with 0.10 m air gap between coaxially aligned coils. . . . .   | 134 |
| 4.52 | Simulated fractional maximum power transfer efficiency with 0.15 m air gap between coaxially aligned coils. . . . .   | 135 |
| 4.53 | Simulated fractional maximum power transfer efficiency with 0.20 m air gap between coaxially aligned coils. . . . .   | 135 |
| 4.54 | Simulated optimal series secondary load real portion for ferrite pad . . . . .  | 135 |
| 4.55 | Simulated optimal series secondary load imaginary portion for ferrite pad . . . . .   | 136 |
| 4.56 | Simulated optimal series secondary load real portion for AMC . . . . .  | 136 |
| 4.57 | Simulated optimal series secondary load imaginary portion for AMC . . . . .   | 136 |
| 4.58 | Simulated optimal series secondary load real portion for ferrite pad with 50 pF of parallel loading on both pads . . . . .  | 137 |
| 4.59 | Simulated optimal series secondary load imaginary portion for ferrite pad with 50 pF of parallel loading on both pads . . . . .   | 137 |
| 4.60 | AMC cut plane E-field vector magnitude. This is comparable to the ferrite case. . . . .   | 138 |
| 4.61 | Ferrite cut plane E-field vector magnitude. This is comparable to the AMC case. . . . .   | 139 |
| 4.62 | AMC cut plane H-field vector magnitude. Showing much greater magnitude than the ferrite case of figure 4.63. . . . .  | 139 |
| 4.63 | Ferrite cut plane H-field vector magnitude. Considerably less than the AMC case (Fig. 4.62. . . . .   | 140 |
| 5.1  | Transmission type coil measurement method used for long range IPT system development. . . . .   | 145 |
| 5.2  | $Q$ factor measurements and simulation results for 20 mm coils. Simulation of solid wire coil —, Litz wire coil $\nabla$ (measurement), Solid wire $\bullet$ (measurement), PCB coil $\blacksquare$ (measurement). . . . .  | 147 |
| 5.3  | Class-E amplifier and connection to $T_x$ coil. . . . .   | 147 |
| 5.4  | 170 mm and 20 mm $R_x$ coils. . . . .   | 148 |
| 5.5  | 1 m $T_x$ coil and Class-E amplifier. . . . .   | 148 |
| 5.6  | Load power transferred to 170 mm by 170 mm $R_x$ coil from 1 m by 1 m $T_x$ coil with 98 W DC power input to $T_x$ amplifier. Simulation using round loops approximation —, Prediction using local magnetic field strength $\square$ , Measured power at $R_x$ coil $\circ$ . . . . . | 150 |
| 6.1  | Transformer model of inductive link including coils self capacitance. . . . .   | 152 |
| 6.2  | Magnetic field strength generated by model $x = 0$ cut plane for optimal VEC system operating into optimal load. . . . .  | 154 |
| 6.3  | Unit cell of developed AMC. . . . .   | 155 |
| B.1  | Measurement of a $10.967\Omega$ resistor through a balun to show that methodology is valid. . . . .   | 169 |

# List of Tables

|     |  |     |
|-----|--|-----|
| 3.1 | Modelled mutual inductances and coupling factors of coils to coupling loops. Distance is coil to coupling loop; the coils are placed centrally between the two coupling loops. . . . .                     | 84  |
| 4.1 | Table of existing high impedance surfaces. . . . .   | 108 |
| 5.1 | Miniaturised 20 mm diameter receiver coils . . . . .   | 146 |
| 5.2 | Long range IPT system coils. <sup>1</sup> Simulation result. . . . .   | 147 |
| 5.3 | long-range IPT system results . . . . .  | 150 |
| A.1 | This table is found on Pg. 79 and 80. of [1] and used in the calculation of mutual inductance between loops. Further tables for close loops and very distant loops are available in the same book. . . . . | 168 |

# Nomenclature

|                            |  |
|----------------------------|--|
| $\alpha$                   | Parametric path equation   |
| $\alpha_x$                 | Parametric path equation $x$ component   |
| $\alpha_y$                 | Parametric path equation $y$ component   |
| $\alpha_{n \rightarrow i}$ | Radial angle   |
| $\delta$                   | Skin depth [m].  |
| $\eta$                     | Fractional link efficiency, this varies between 0 and 1, where 1 is a totally efficient magnetic link and 0 totally inefficient. This does not include the losses in power electronics required for a complete system. The assumption the system is operating with series or parallel receiver tuning is also made. Also wave impedance. |
| $\eta_0$                   | Impedance of free space.   |
| $\eta_{Res}$               | Fractional link efficiency with restive receiver load.   |
| $\eta_{RxPar}$             | Fractional receiver efficiency, parallel tuned.  |
| $\eta_{RxRes}$             | Fractional receiver efficiency, resistive receiver load.   |
| $\eta_{RxSer}$             | Fractional receiver efficiency, series tuned.  |
| $\eta_{TxPar}$             | Fractional transmitter efficiency, parallel tuned.   |
| $\eta_{TxSer}$             | Fractional transmitter efficiency, series tuned.   |
| $\Gamma$                   | Reflection coefficient.  |
| $\gamma$                   | Procession variable for PSC  |
| $\gamma_\theta$            | Angular procession of PSC central path   |
| $\Im$                      | Imaginary.   |
| $\lambda$                  | Wavelength [m]. Or arbitrary scaler.   |
| $\hat{\mathbf{Q}}$         | Normalised direction vector.   |
| $\mathbf{B}$               | Vector magnetic field [T]  |
| $\mathbf{P}$               | Point in 3D space where a field is sampled.  |
| $\mu$                      | Permeability [H].  |
| $\mu_0$                    | Vacuum permeability $4\pi \times 10^{-7}$ [H].   |

|            |   |
|------------|---|
| $\omega$   | Angular frequency [rad].  |
| $\omega_p$ | Angular frequency where reflected parallel tuned coil impedance is real [rad].                        |
| $\omega_s$ | Angular frequency where reflected series tuned coil impedance is real [rad].                          |
| $o$        | Variable in proximity calculation   |
| $\phi$     | Distance from the tube centres to the central axis of the VEC [m]                                     |
| $\Re$      | Real.   |
| $\rho$     | Resistivity [ $\Omega \text{ m}$ ].   |
| $\sigma$   | Conductivity [ $\text{S m}^{-1}$ ].   |
| $\tau^2$   | See Appendix A. name of variable changed from original $k^2$ to avoid confusion with coupling factor. |
| $\zeta$    | Central path radius of VEC [m].   |
| $a$        | The outer radius of a coil turns conductor [m].   |
| $C_T$      | Tuning capacitor [F].   |
| $D$        | The air gap between coils in an inductive link [m].   |
| $G_p$      | Proximity factor.   |
| $H_{Rx}$   | The height of the receiver coil [m].  |
| $H_{Tx}$   | The height of the transmitter coil [m].   |
| $I$        | General current [A].  |
| $I_{b1}$   | Branch 1 current [A].   |
| $I_{b2}$   | Branch 2 current [A].   |
| $I_{in}$   | Input current [A].  |
| $k$        | Coupling factor. Or wave number.  |
| $L$        | General inductance [H].   |
| $l$        | General length [m].   |
| $L_1$      | Path of filaments used for self inductance calculation.   |
| $L_2$      | Path of filaments used for self inductance calculation.   |
| $L_3$      | Path of filaments used for mutual inductance calculation.   |
| $l_n$      | Length of turn $n$ [m]  |
| $L_{ext}$  | External inductance [H]   |
| $L_{int}$  | Internal inductance [H]   |
| $L_{loop}$ | Inductance of a loop [H].   |
| $L_{Rx}$   | Self inductance of receiver coil [H].   |

|                |  |
|----------------|--|
| $L_{TxRx}$     | Mutual inductance between transmitter and receiver coil [H].   |
| $L_{Tx}$       | Self inductance of transmitter coil [H].   |
| $m$            | Variable in skin effect calculation.   |
| $M_{12}$       | Mutual inductance between two filamentary paths [H]  |
| $M_{looploop}$ | Mutual inductance between two loops [H].   |
| $N$            | Number of turns.   |
| $n$            | Transformer ratio.   |
| $N_{Rx}$       | Number of turns receiver coil.   |
| $N_{Tx}$       | Number of turns transmitter coil.  |
| $p$            | Fourier variable   |
| $Q$            | Quality factor: A dimensionless quantity defined as the ratio of peak energy stored in a resonator to the energy lost per resonant cycle. Extensive discussion in the measurement chapter. |
| $q$            | Dimension.   |
| $q$            | Variable in skin effect calculation.   |
| $Q_{Rx}$       | Quality factor of receiver coil.   |
| $Q_{Tx}$       | Quality factor of transmitter coil.  |
| $R$            | Vector distance [m].   |
| $r$            | General radial distance [m]  |
| $r_{i,corr_x}$ | Filament correction vector in $x$ direction [m]  |
| $r_{i,corr_y}$ | Filament correction vector in $y$ direction [m]  |
| $R_{LParOpt}$  | Optimal resistive load for parallel resonant IPT system. Required to achieve $\eta$ [%].   |
| $R_{LSerOpt}$  | Optimal resistive load for series resonant IPT system. Required to achieve $\eta$ [%].   |
| $R_L$          | A resistive load [%].  |
| $r_{Max}$      | The maximum outer radius of a coil [m].  |
| $r_{Min}$      | The minimum inner radius of a coil [m].  |
| $R_{rad}$      | Resistor representing radiation loss [%].  |
| $r_{RxMax}$    | The maximum outer radius of receiver coil [m].   |
| $r_{RxMin}$    | The minimum inner radius of receiver coil [m].   |
| $R_{Rx}$       | Resistor in series with receiver coil representing its losses [%].   |
| $R_{skin}$     | Resistor representing skin effect loss [%].  |
| $r_{TxMax}$    | The maximum outer radius of transmitter coil [m].  |

|             |   |
|-------------|---|
| $r_{TxMin}$ | The minimum inner radius of transmitter coil [m].   |
| $R_{Tx}$    | Resistor in series with transmitter coil representing its losses [ $\Omega$ ].            |
| $t$         | Wall thickness [m] or dimensionless stepping variable for filament models.                |
| $t_{step}$  | Quantisation of filament structure.   |
| $v$         | Tube centre to centre distance [m]  |
| $x$         | Dimension, sometimes general variable.  |
| $y$         | Dimension.  |
| $Y_g$       | Effective admittance of a grid of patches.  |
| $Y_s$       | Effective admittance of a substrate.  |
| $z$         | Dimension.  |
| $Z_L$       | Complex load [ $\Omega$ ].  |
| $Z_{eqPar}$ | Complex parallel resonant load receiver impedance reflected to transmitter [ $\Omega$ ].  |
| $Z_{eqSer}$ | Complex series resonant load receiver impedance reflected to transmitter [ $\Omega$ ].    |
| $Z_{eq}$    | Complex equivalent impedance [ $\Omega$ ].  |
| $Z_{RxPar}$ | Complex parallel resonant load receiver impedance [ $\Omega$ ].                           |
| $Z_{RxSer}$ | Complex series resonant load receiver impedance [ $\Omega$ ].                             |
| $Z_{Rx}$    | Complex receiver impedance, found by voltage source in series with $L_{Rx}$ [ $\Omega$ ]. |

## Acknowledgements

Sometimes it's good to reflect upon what we once were and what we hope to become. I view the sum of the past four years as a positive thing. During the course of this PhD I have had the opportunity to implement ideas and create systems that at the start I would have dismissed as impossible. Partly that is due to the support I have received from others and I would like to acknowledge that in this section.

I have had the good fortune of receiving supervision from Paul Mitcheson for this project. Paul's enthusiasm for engineering knows little restraint, as a result projects have been attempted, often with success, that did not seem possible at their inception. I must also make apology for the considerable drain I have incurred on his staff account, we should have definitely got plates instead. I'm sure the future is bright for high power, high frequency, power electronics.

I would like to thank David Yates for technical guidance.

I would like to thank Professor Alessandro Astolfi the control and power groups assistance with test equipment and engineering experience.

I would like to thank Lingxin Lan for his help with the automatic measurement system.

I would like to thank Alwyn Elliott for organising IPT/Energy Harvesting meetings and bringing the biscuits.

I would like to thank Shahrokh Mohammadi for facilitating the lobster related discussions.

I would like to thank the following people for help with proof reading, while not inflicting up on them any responsibility for my poor English: Sarah Fox, Paul Mitcheson, Alwyn Elliott, David Mack and Jonathan Hazell.

I was funded by EPSRC and EDF under CASE award voucher number 11220474 in addition, funding is gratefully acknowledged from Her Majestys Government.

# Chapter 1

## Introduction

### 1.1 Motivation for inductive power transfer (IPT)

Traditionally electronic devices have been directly powered from electrochemical batteries or remote generation via wired connections. However there are many scenarios where the transfer of power via wires is impossible, unsafe or inconvenient. Inductive power transfer (IPT) is a technology that can efficiently provide power without wires, through dielectric media, with gaps up to 5m between the transmitter and receiver [2][3]. To demonstrate the utility of IPT three examples have been selected. When electrical devices are implanted inside the human body their power consumption often exceeds that which can be supplied by implanted batteries for the duration of the devices operation. A particular medical device that has been identified as conducive to IPT is the left ventricular assist device [4][5]. In the conventional wired implementation a drive line punctures the skin (air or electric) with a battery or compressor external to the body. In older versions a chest vent was also required, however in more recent designs this has been eliminated. If the drive line were eliminated by usage of an inductive power transfer system the quality of life and outcomes of the patients fitted with these devices could be greatly improved as they would no longer be subject to infection to the wound caused by the drive line. As the body is a partially conductive medium [6] other methods of wireless power transfer such as far field and capacitive power transfer are not suitable as they would cause unacceptable heating [7].

The second example is that of electric vehicle charging, the cables most commonly used to deliver power present a trip hazard and are vulnerable to damage, they also cannot charge a car while it is in motion. Proposed inductive power transfer systems would allow a car to be charged while in motion (dynamic charging) from charging pads buried in roads [8]. If widely implemented could reduce the weight and cost of electric vehicles by reducing the required battery capacity.

The third selected example is that of a magnetically levitating train. They require electrical power to levitate using their super conducting electro magnets, however they can travel at speeds above which electrical pantographs are reliable. Inductive power transfer presents a solution where the available power to the train is independent of forward velocity and there is no pantograph wear [9].

### 1.2 Condensed history of inductive power transfer

The first resonant inductive power transfer systems were created by Nikola Tesla in the 19th century [10], however his systems were limited by the switching technology employed at the time. The fastest switch he developed was a mechanically complex mercury jet interrupter capable of 200 kHz. Nevertheless he identified many important aspects of inductive power transfer such as receiver resonance, the importance of high  $Q$



factor and the mechanism and need to avoid radiative emissions. A significant weakness of his work was its poor documentation, as he did not publish scientific papers, only patent filings in largely non technical language, court statements or material for the popular press. As such his influence on the modern era of inductive power transfer is limited as in the majority of literature he is simply stating the results of his experiments without detail or methods.

The modern era of inductive power transfer largely started in the 1989/1990 at the University of Auckland with the work of John Boys, Andrew Green and Grant Covic [11], developing inductive track systems for materials handling. Their work was facilitated by the, at that time, recent invention of the modern power silicon MOSFET. This allowed the power electronics involved to operate reliably and efficiently at 10 kHz. However to operate efficiently with large air gaps the switching frequency of their systems was too low. Later systems produced by the same group with larger air gaps use higher frequencies [12]. The majority of their systems have continued to operate at frequencies below 100 kHz and utilise soft magnetic materials to ensure high coupling factors. The coupling factor enhancement approach results in pads that perform efficiently with large air gaps, in real world environments but are heavy and costly due to the large quantity of magnetic material used.

In the early 2000's Vandevorde and Puers conducted research into inductive powering of medical devices [13]. Their systems focused upon the lower power regime with a maximum power transfer of a few tens of Watts for biomedical applications. The systems typically use air cored coils and sometimes efficient class-e drivers, with efficiencies from DC to load of up to 80% achieved. However they never operated efficiently with large air gaps due to the relatively low  $Q$  of their coils at the selected frequencies of operation.

The publication of André Kurs et al. in 2007 of a paper [14] describing an inductive power transfer system capable of 2 m air gap of 60 W demonstrated the possibility of high link efficiencies while using simple air cored coils and MHz operating frequencies, generating mass interest in the field of inductive power transfer. However the Tx coil driver used in the work was a commercial RF power amplifier and therefore DC to load efficiency of the system was very poor, around 10%. The 2011 paper of Lee and Lorenz [15] represents an early attempt to optimise the inductive link of air core systems, recognising that the IPT link can be modelled as a weakly coupled transformer and demonstrating many concepts such as the optimal receiver load that have become fundamental to MHz inductive power transfer. However the amplifier technology employed was still a commercial RF power amplifier that severely limited the overall DC to load efficiency of the system.

The first system demonstrated by the Imperial Wireless Power Lab [16] in 2013 exhibited high end to end efficiencies by addressing the losses in power electronics. In this system a Class-E inverter operating at 6 MHz is able to deliver power to a load through a 0.23 m air gap with 77% efficiency. Further advances have now raised the potential efficient operating range of the power electronics used for IPT systems to 27 MHz [17], facilitated through use of modern wide band-gap MOSFETs. Increasingly such electronics are gaining the ability to operate over a wide load range [18], resulting in IPT links been capable of operating over a wider range of coil displacements.

### 1.3 Structure of this chapter

Basic IPT theory will first be described along with a discussion of the effect of operating frequency on system performance. Where it will be shown to be, for the systems of interest to this thesis, that operation at MHz frequencies is beneficial. The common use of resonant receiver loads is described, followed by an example illustrating how high  $Q$  factor is important for efficient operation. The final section of the introduction explains the structure of the rest of the thesis and the research questions that have been addressed.

## 1.4 IPT link theory

Inductive power transfer (IPT) is the transfer of electrical power via loosely, inductively, coupled coils (Fig. 1.1). Power is transmitted by exciting the transmitter coil (Tx) with an alternating current and received by the current this induces through a load,  $Z_L$ , connected to the receiver coil (Rx). The transmitter and receiver coils have self inductances  $L_{Tx}$ ,  $L_{Rx}$  and series losses represented by  $R_{Tx}$ ,  $R_{Rx}$ . The coils have mutual inductive coupling,  $L_{TxRx}$ , allowing a coupling factor,  $k$ , defined as:

$$k = \frac{L_{TxRx}}{\sqrt{L_{Tx}L_{Rx}}}, \quad (1.1)$$

and the transformer ratio,  $n$ :

$$n = \sqrt{\frac{L_{Rx}}{L_{Tx}}}. \quad (1.2)$$

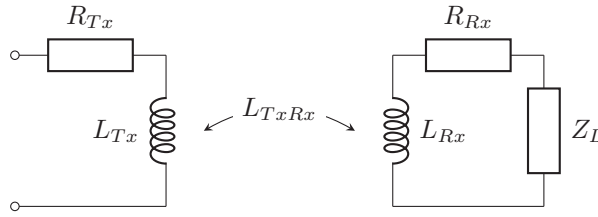


Figure 1.1: Transformer model of inductive power transfer system.

For an IPT system,  $k$ , is always far below its maximum unity value; as the majority of the magnetic flux produced by a coil is not linked with the other coil. In a conventional transformer,  $k$ , is however close to unity; the primary and secondary (analogous to transmitter and receiver) are wound around a high permeability core ensuring that most of the magnetic flux produced by a winding is linked to the other winding. In an IPT system this core is not present or split with an air gap between transmitter and receiver coils; this results in most of the magnetic flux not linking transmitter and receiver coils. To aid analysis of this scenario the receiver coil can be referred to the primary coil as shown in figure 1.2.

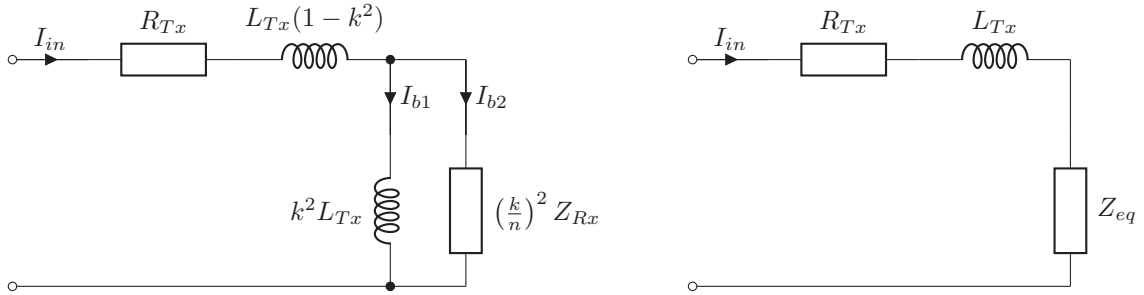


Figure 1.2: Transformer model of inductive power transfer system with receiver referred to transmitter coil (left) and further transformation into reflected impedance upon transmitter coil caused by the receiver coil and load (right).

The following analysis is partly based on the analysis of Schuylenbergh and Puers [19]. Three possible receiver loads are postulated (Fig. 1.3): parallel resonant load, series resonant load and resistive load as per a conventional transformer. The effect of the reflected receiver coil upon the primary coil can be expressed in the form of an equivalent impedance,  $Z_{eq}$ :

$$Z_{eq} = -j\omega L_{Tx}k^2 + \frac{1}{\frac{1}{k^2 L_{Tx}} + \left(\frac{k}{n}\right)^2 \frac{1}{Z_{Rx}}}, \quad (1.3)$$

where  $Z_{Rx}$  is the receiver impedance. The equivalent circuit from this transformation is shown on the right side of figure 1.2.

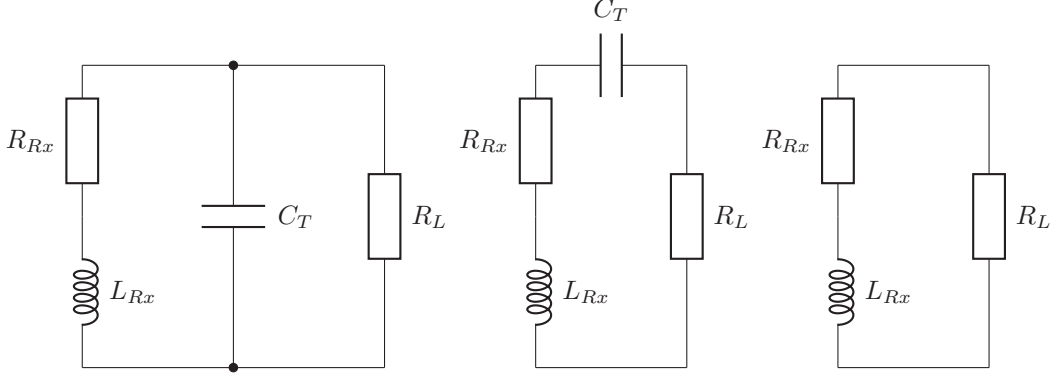


Figure 1.3: Receiver load configurations, from left to right: parallel resonant, series resonant, resistive.

#### 1.4.1 Parallel resonant receiver load

In the case of a parallel resonant load the receiver impedance,  $Z_{RxPar}$  is given by:

$$Z_{RxPar} = j\omega L_{Rx} + R_{Rx} + \frac{1}{j\omega C_T + \frac{1}{R_L}}. \quad (1.4)$$

Hence in the case of the parallel resonant receiver circuit by substitution in equation 1.3:

$$Z_{eqPar} = \omega^2 k^2 L_{Tx} L_{Rx} \left( \frac{R_L + R_{Rx} + \omega^2 C_T^2 R_L^2 - j\omega(L_{Rx} - C_T R_{Load}^2 + \omega^2 C_T^2 L_{Rx} R_{Load}^2)}{(R_{Load} + R_{Rx})^2 + \omega^2(L_{Rx}^2 + R_{Load}^2 C_T(R_{Rx}^2 C_T - 2L_{Rx})) + \omega^4 L_{Rx}^2 C_T^2 R_{Load}^2} \right) \quad (1.5)$$

This reflected impedance is real at:

$$\omega(\Im Z_{eqPar} = 0) = \sqrt{\frac{1}{L_{Rx} C_T} - \frac{1}{R_L^2 C_T^2}} = \omega_p. \quad (1.6)$$

Operating with purely real reflected impedance results in a system where the reactance at the input to the transmitting coil does not vary with coupling, this greatly simplifies matching to tuned amplifiers and is the normal operating mode. At this frequency:

$$Z_{eqPar}(\omega = \omega_p) = \frac{k^2 L_{Tx} (C_T R_L^2 - L_{Rx})}{R_L C_T (R_L C_T R_{Rx} + L_{Rx})}. \quad (1.7)$$

The transmitter fractional link efficiency,  $\eta_{Tx}$ , is defined as the ratio of the power that reaches the receiver circuit to the total power put into the inductive link:

$$\eta_{TxPar}(\omega = \omega_p) = \frac{Z_{eqPar}(\omega = \omega_p)}{Z_{eqPar}(\omega = \omega_p) + R_{Rx}}, \quad (1.8)$$

$$\eta_{TxPar}(\omega = \omega_p) = \frac{L_{Tx}^2 (C_T R_L^2 - L_{Rx})}{R_{Tx} R_L C_T L_{Rx} (R_{Rx} R_L C_T + L_{Rx}) + L_{Tx}^2 (C_T R_L^2 - L_{Rx})}. \quad (1.9)$$

The receiver fractional link efficiency,  $\eta_{Rx}$ , is defined as ratio of real power dissipated in the load to the total power that reaches the receiver:

$$\eta_{RxPar} = \frac{L_{Rx}}{R_L C_T R_{Rx} + L_{Rx}}. \quad (1.10)$$

Therefore the fractional link efficiency with respect to load,  $\eta_{Par}$ , can be found by the product of the transmitter and receiver efficiencies:

$$\eta_{Par} = \eta_{TxPar}\eta_{RxPar} = \frac{k^2 Q_{Tx} Q_{Rx}}{\left(1 + \frac{Q_{Rx}}{\omega_p C_T R_L} + k^2 Q_{Tx} Q_{Rx}\right) (\omega_p C_T R_L + Q_{Rx})} \quad (1.11)$$

The optimal load,  $R_{LParOpt}$ , is found by finding the value of  $R_L$  at the maxima of  $\eta_{Par}$ :

$$\begin{aligned} \frac{d\eta_{Par}}{dR_L} = & \frac{Q_{Rx}^3 Q_{Tx} k^2}{C_T R_L^2 \omega_p (Q_{Rx} + C_T R_L \omega_p) (Q_{Rx} Q_{Tx} k^2 + \frac{Q_{Rx}}{C_T R_L \omega_p} + 1)^2} \\ & - \frac{C_T Q_{Rx}^2 Q_{Tx} k^2 \omega_p}{(Q_{Rx} + C_T R_L \omega_p)^2 (Q_{Rx} Q_{Tx} k^2 + \frac{Q_{Rx}}{C_T R_L \omega_p} + 1)}, \end{aligned} \quad (1.12)$$

$$R_{LParOpt} = \frac{Q_{Rx} \sqrt{Q_{Rx} Q_{Tx} k^2 + 1}}{C_T Q_{Rx} Q_{Tx} \omega_p k^2 + C_T \omega_p}. \quad (1.13)$$

By substitution into of the optimal load into equation 1.11 the upper bound on the link efficiency is found:

$$\eta = \frac{k^2 Q_{Tx} Q_{Rx}}{(1 + \sqrt{1 + k^2 Q_{Tx} Q_{Rx}})^2}. \quad (1.14)$$

#### 1.4.2 Series resonant receiver load

In the case of a series resonant load the receiver impedance,  $Z_{RxSer}$ , is given by:

$$Z_{RxSer} = j\omega L_{Rx} + R_{Rx} + \frac{1}{j\omega C_{TS}} + R_L. \quad (1.15)$$

Hence in the case of the series resonant receiver circuit by substitution in equation 1.3:

$$Z_{eqSer} = \frac{\omega^3 k^2 L_{Tx} L_{Rx} C_T (\omega C_T (R_L + R_{Rx}) + j(1 - \omega^2 L_{Rx} C_T))}{\omega^2 C_T^2 (R_L + R_{Rx})^2 + (1 - \omega^2 L_{Rx} C_T)^2}. \quad (1.16)$$

This reflected impedance is real at:

$$\omega(\Im Z_{eqSer} = 0) = \sqrt{\frac{1}{L_{Rx} C_T}} = \omega_s. \quad (1.17)$$

Operating with purely real reflected impedance results in a system where the the reactance at the input to the transmitting coil does not vary with coupling, this greatly simplifies matching to tuned amplifiers and is the normal operating mode. At this frequency:

$$Z_{eqSer}(\omega = \omega_s) = \frac{k^2 L_{Tx}}{C_T (R_L + R_{Rx})} \quad (1.18)$$

the transmitter fractional link efficiency,  $\eta_{Tx}$ , is defined as the ratio of the power that reaches the receiver circuit to the total power put into the inductive link:

$$\eta_{TxSer}(\omega = \omega_s) = \frac{k^2 L_{Tx}}{K^2 L_{Tx} + R_{Tx} C_T (R_{Rx} + R_L)}. \quad (1.19)$$

The receiver fractional link efficiency,  $\eta_{Rx}$  is defined as the ratio of real power dissipated in the load to the total power that reaches the receiver:

$$\eta_{RxSer} = \frac{\omega_s C_T R_L}{\omega_s C_T R_L + \frac{1}{Q_{Rx}}}. \quad (1.20)$$

Therefore the fractional link efficiency with respect to load,  $\eta_{Ser}$ , can be found by the product of the transmitter and receiver efficiencies:

$$\eta_{Ser} = \eta_{TxSer} \eta_{RxSer} = \frac{k^2 Q_{Tx} \omega_s C_T R_L}{\left(\omega_s C_T R_L + k^2 Q_{Tx} + \frac{1}{Q_{Rx}}\right) \left(\omega_s C_T R_L + \frac{1}{Q_{Rx}}\right)} \quad (1.21)$$

The optimal load,  $R_{LSerOpt}$ , is found by finding the value of  $R_L$  at the maxima of  $\eta_{Ser}$ :

$$\begin{aligned} \frac{d\eta_{Ser}}{dR_L} &= \frac{C_T Q_{Tx} k^2 \omega_s}{\left(\frac{1}{Q_{Rx}} + C_T R_L \omega_s\right) (Q_{Tx} k^2 + \frac{1}{Q_{Rx}} + C_T R_L \omega_s)} \\ &\quad - \frac{C_T^2 Q_{Tx} R_L k^2 \omega_s^2}{\left(\frac{1}{Q_{Tx}} + C_T R_L \omega_s\right) (Q_{Tx} k^2 + \frac{1}{Q_{Rx}} + C_T R_L \omega_s)^2} \\ &\quad - \frac{C_T^2 Q_{Tx} R_L k^2 \omega_s^2}{\left(\frac{1}{Q_{Rx}} + C_T R_L \omega_s\right)^2 (Q_{Tx} k^2 + \frac{1}{Q_{Rx}} + C_T R_L \omega_s)}, \end{aligned} \quad (1.22)$$

$$R_{LSerOpt} = \frac{\sqrt{Q_{Rx} Q_{Tx} k^2 + 1}}{C_T Q_{Rx} \omega_s}. \quad (1.23)$$

By substitution into of the optimal load into equation 1.21 the upper bound on the link efficiency is found:

$$\eta = \frac{k^2 Q_{Tx} Q_{Rx}}{(1 + \sqrt{1 + k^2 Q_{Tx} Q_{Rx}})^2} \quad (1.24)$$

This is the same as for the parallel resonant coil, however the parallel resonant coil has a greater optimal  $R_L$  value and absorbs the receiver coils parallel effective capacitance into the tuning capacitor.

### 1.4.3 Resistive receiver load

In the case of a resistive load the receiver impedance,  $Z_{RxRes}$ , is given by:

$$Z_{RxRes} = j\omega L_{Rx} + R_{Rx} + R_L. \quad (1.25)$$

In the receiver coil there is only one current branch therefore the receiver efficiency,  $\eta_{RxRes}$ , can be stated as:

$$\eta_{RxRes} = \frac{P_{out}}{P_{total}} = \frac{R_L}{R_{Rx} + R_L}, \quad (1.26)$$

the same as the series resonant load case. The link efficiency,  $\eta_{Res}$ , is somewhat more difficult to find due to the multi branch network. The current magnitudes are used to find the dissipation in the various branches of the equivalent circuit shown in the left side of figure 1.2. Firstly the input current,  $I_{in}$  to the link is found in terms of the receiver coil referred branch current,  $I_{b2}$ :

$$I_{in} = I_{b2} \left( \frac{j\omega k^2 L_{tx} + j\omega \left(\frac{k}{n}\right)^2 L_{Rx} + (R_{Rx} + R_L) \left(\frac{k}{n}\right)^2}{j\omega k^2 L_{Tx}} \right). \quad (1.27)$$

The fractional link efficiency can be stated in terms of the current magnitudes:

$$\eta_{Res} = \frac{|I_{b2}|^2 \left(\frac{k}{n}\right)^2 R_L}{|I_{in}|^2 R_{Tx} + |I_{b2}|^2 \left(\frac{k}{n}\right)^2 (R_{Rx} + R_L)}, \quad (1.28)$$

by substitution using equation 1.27:

$$\eta_{Res} = \frac{L_{Tx}^2 R_L k^2 n^2 \omega^2}{L_{Tx}^2 k^2 n^2 \omega^2 (R_L + R_{Rx}) + R_{Rx} (L_{Rx}^2 \omega^2 + 2L_{Rx} L_{Tx} n^2 \omega^2 + L_{Tx}^2 n^4 \omega^2 + R_L^2 + 2R_L R_{Rx} + R_{Rx}^2)}. \quad (1.29)$$

The fractional link efficiency equation is unfortunately frequency dependent, precluding simple definite statements about the relative efficiency of the restive load case to the tuned load cases. However it is possible to observe that for an inductive power transfer system with resistive load, the fractional link efficiency will be far below 1, simply because the numerator is proportional to  $k^2$  while there are terms in the denominator that are independent of  $k$ . As air core IPT systems usually operate with  $k < 0.1$  the efficiency will be low.

The cause of the increased losses of the resistive load in comparison to the resonant cases is apparent by examination of the equivalent circuit of the transmitter with referred receiver (Fig. 1.2). The receiver efficiency in the non resonant case is not lower than the resonant cases. The additional losses are caused by the inductance  $k^2 L_{Tx}$ . In the resonant cases  $k^2 L_{Tx}$  is part of a resonant circuit and therefore is not causing power loss through  $R_{Tx}$  while in the resistive case it's causing a reactive power flow through  $R_{Tx}$  increasing transmitter losses. This is an interesting result as in some applications minimising receiver size and reliability is more important than efficiency and as such non-resonant receivers may have some niche applications.

#### 1.4.4 Choice of tuning

It is clear by comparison between the link efficiency equation (Eq. 1.24) and the link efficiency equation for the resistive load case (Eq. 1.29) that a resonant receiver coil is required for efficient operation with low coupling factors. The choice between of parallel and series resonant operation however, as they have the same upper bound on efficiency is more nuanced and is dependent upon the application. For a series resonant receiver the optimal load is smaller than the parallel tuned case. In the parallel tuned case the coils capacitance is absorbed into the tuning capacitor, simplifying design. At the same power output level the parallel tuned case will have a greater output voltage than the series tuned case.

### 1.5 Examples

#### 1.5.1 Example 1 - $Q$ factor requirement

The self,  $L_{loop}$ , and mutual inductance,  $M_{LoopLoop}$ , of two loops of 150 mm outer radius,  $r_{Max}$ , composed of 5 mm radius,  $a$ , wire has been calculated for coaxial centre to centre distances,  $D$ , from 0.05 m to 0.6 m. The inductances are used to calculate the coupling factor between the two loops. The formula [20];

$$L_{loop} \cong \mu_0 r_{Max} \left( \ln \left( \frac{8r_{Max}}{a} \right) - 2 \right), r_{Max} \gg a, \quad (1.30)$$

is used to calculate the self inductance of the loops. The formula [1]:

$$M_{LoopLoop} = f(\tau^2) r_{Max} (1 \times 10^{-6}), \quad (1.31)$$

$$\tau^2 = \frac{(D(1 \times 10^2))^2}{4(r_{Max}(1 \times 10^2))^2 + (D(1 \times 10^2))^2}, \quad (1.32)$$

where  $f(\tau^2)$  is calculated using linear interpolation of the table in Appendix A. For more complex shaped coils the inductance calculation methods presented in the modelling chapter could be used instead. The link efficiency with respect to distance is then compared for coils of varying  $Q$  using equation 1.24 (Fig. 1.4).

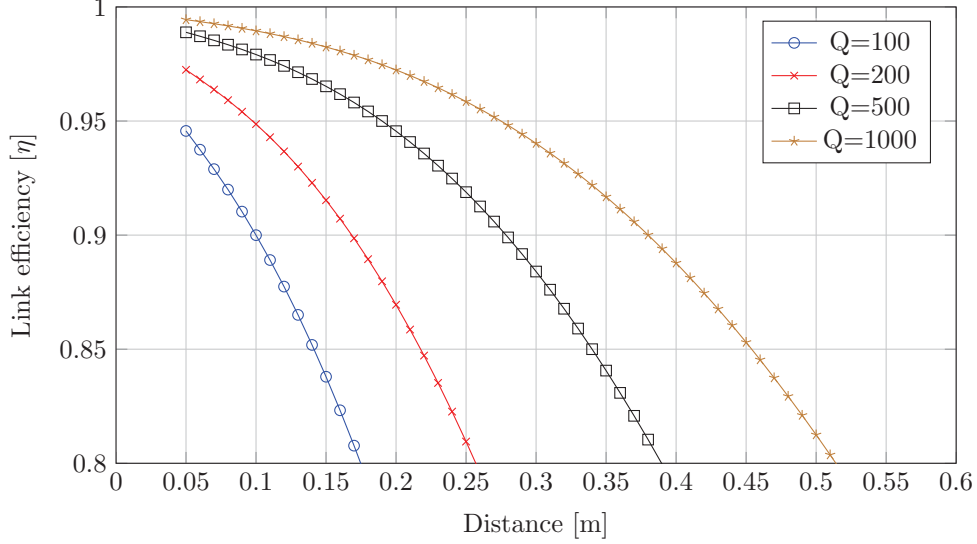


Figure 1.4: Case study of effect on coil  $Q$  on inductive link efficiency.

If an overall system efficiency of 85% is targeted it is reasonable to expect a  $\eta > 0.9$  to allow a minimal budget for power electronic losses. It is observed that the point of  $\eta = 0.9$  increases from 0.1 m to 0.38 m when the  $Q$  is increased from 100 to 1000, a significant increase in distance that enables applications such as wireless car charging. With these dimensions coils have been demonstrated with  $Q$  in excess of 1,000 at MHz ISM frequencies [16][15].

### 1.5.2 Example 2 - Optimal load

In the previous example it was shown that increasing the  $Q$  of the coils in an IPT system results in more efficient operation at a given distance and increases the range at which an IPT coil system can maintain efficient operation. However maximal efficiency is only achieved when the optimal load is presented to the IPT system. As previously shown this consists of a real and imaginary component, for a complete system the real component is supplied by a high frequency rectifier and the complex by a fixed value series or parallel tuning capacitor. If by operating at high  $Q$  the system becomes overly sensitive to the real portion of the load it may be difficult to control the high frequency rectifier adequately to achieve maximal efficiency.

In order to assess whether this concern is valid the previous loops example has been re-purposed. The loops are placed at a fixed coaxial separation of 0.25 m resulting in  $k = 0.0472$  with optimal loads recorded in table 1.5 and operated at 10 MHz. The real portion of the optimal load has been altered from its optimal value (which is very similar for all loops) by multiplication by a factor varied between 0.5 and 2 and the complete IPT system simulated using SPICE. The relative efficiency compared to the theoretical maximum,  $\eta$ , with respect to the load multiplication factor has then been plot (Fig. 1.6).

The results show contrary to expectations increasing the coil  $Q$  for a system of fixed geometry reduces sensitivity to variations in the real load. This is because because the efficiency of the system has improved by increasing the  $Q$ . The increase in efficiency results in less variation in performance with changes in model parameters.

| $Q$  | $\eta$ | Optimal Load                 |
|------|--------|------------------------------|
| 100  | 0.6566 | $(1.9885 - 41.2141i) \Omega$ |
| 200  | 0.8094 | $(1.9566 - 41.2223i) \Omega$ |
| 500  | 0.9188 | $(1.9475 - 41.2232i) \Omega$ |
| 1000 | 0.9585 | $(1.9461 - 41.2216i) \Omega$ |

Figure 1.5: Optimal loads at 10 MHz for loops.

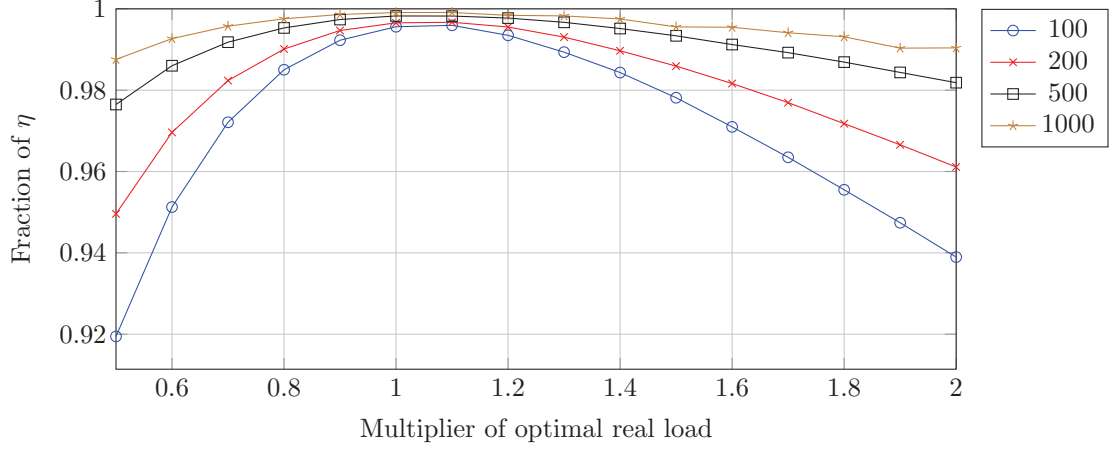


Figure 1.6: Relative efficiencies of loop IPT systems as the real load deviates from its optimal value.

### 1.5.3 Example 3 - Frequency requirement

Earlier sections of this introduction identified the need for resonant receiver loads and high  $Q$  coils to maximise the efficient range of IPT systems. However in justifying MHz IPT it remains to show that for air cored coils increasing the coupling factor,  $k$ , is not generally possible and that the maximum  $Q$  factor is achieved at MHz frequencies.

By assuming all the turns of the coils are coaxial filamentary current loops of average turn radii, located at the coils centres, an approximate mutual inductance formula can be stated [20]:

$$L_{TxRx} \approx N_{Tx}^2 N_{Rx}^2 \frac{\mu_0 \pi \left( \frac{r_{TxMax} + r_{TxMin}}{2} \right)^2 \left( \frac{r_{RxMax} + r_{RxMin}}{2} \right)^2}{2(D - \frac{1}{2}H_{Tx}H_{Rx})^3}, \quad (1.33)$$

$$D \gg r_{TxMax}, r_{RxMax}. \quad (1.34)$$

Where,  $r_{Max}$ , is the outer radius of the turns,  $r_{Min}$ , is the inner radius of the turns,  $D$ , the distance between the coils and  $H$ , the coils height. Gains in mutual inductance due to increasing turn count,  $N$ , have little effect on overall coupling factor (Eq. 1.1) as for short round loop type coils as [21]:

$$L_{Tx}, L_{Rx} \propto N^2. \quad (1.35)$$

When the outer radius and height of the coils are constrained it is not generally possible to increase the coupling factor. The remaining avenue to increase the range and efficiency of the inductive link is to improve the coils  $Q$ .

The mechanisms of the AC losses in a coil, represented by,  $R_{Tx}$  and  $R_{Rx}$ , are resistive losses due to the current distribution in the turns and radiation loss caused by far field radiated energy. The total loss resistance can be split into separate losses [21]:

$$R_{Tx,Rx} = R_{rad} + R_{skin} G_p, \quad (1.36)$$



where  $R_{rad}$  is the coils radiation resistance,  $R_{skin}$  an isolated conductors skin effect resistance and  $G_p$  the proximity factor. The proximity factor takes into account the increase in resistance due to current redistribution caused by other turns in the coils cross section. In an IPT coil, due to the skin effect, it is a reasonable assumption that the turns are electrically thick and that as such the coil current flows entirely on the outside of the conductor. With this assumption the proximity factor will be constant with respect to frequency. The modelling chapter of this thesis found the proximity factor to be between 1 and 1.5 depending on coil turn spacing; for this simplified analysis it is ignored. An approximation to the skin effect resistance of an electrically thick tube of outer radius,  $a$ , in terms of length,  $l$ , is [21]:

$$R_{skin} = \frac{l}{2\pi a} \sqrt{\frac{\omega\mu}{2\sigma}}. \quad (1.37)$$

The radiation resistance of simple structures such as wire loops (magnetic dipole) can be calculated analytically, however expressions do not generally exist for more complex structures. Therefore the solution for the magnetic dipole is used to approximate the radiation resistance of more complex coils by assuming each turn is an layered magnetic dipole [22]:

$$R_{rad} = \left(\frac{377}{6\pi}\right) \left(\frac{2\pi}{\lambda}\right)^4 (N\pi r^2)^2, \quad (1.38)$$

where,  $r$ , is the mean turn radius. As the coils are electrically small it can be assumed that the phase velocity in the coil is the speed of light. As  $R_{rad} \propto \omega^4$  and  $R_{skin} \propto \omega^{0.5}$  the point of maximum  $Q$  will lie at a point where  $R_{rad} < R_{skin}$  and therefore where the radiated energy from the magnetic link is small.

For this analysis to proceed a scenario must be utilised as the exact frequency of maximum  $Q$  varies with conductor outer radius and turn count. The selected scenario is a wireless car receiver coil, one of the examples given in the motivation section. The receiver coil is a helix with  $r_{Max}$  of 155 mm, a turn to turn gap,  $s$ , of 10 mm. Composed of 5 mm outer radius copper tubes with 0.7 mm thick walls, with a total of 3 turns,  $N$ . The total length of the coil is 2.83 m, the conductivity of the tube is  $3.89 \times 10^7 \text{ S m}^{-1}$  and the self inductance,  $L_{Rx}$ , is 4.22  $\mu\text{H}$ . The dimensional parameters of this coil have been selected to maximise the  $Q$  taking into account skin effect losses and the dimensional constraints of the scenario.

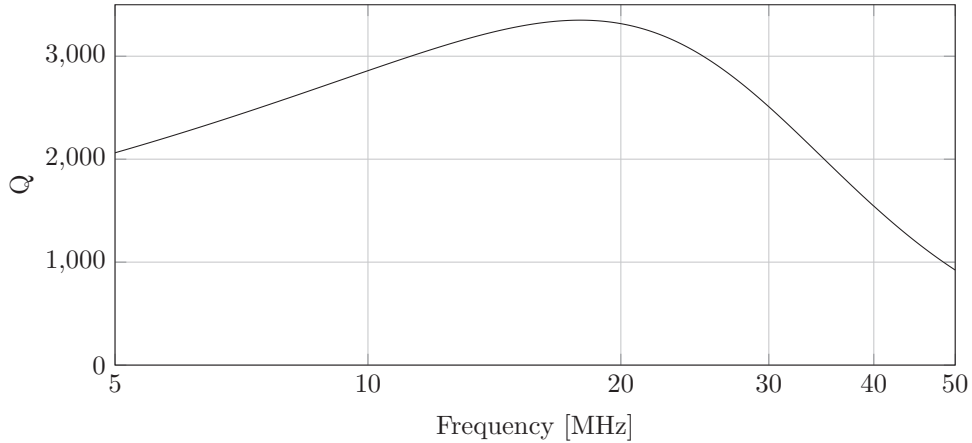


Figure 1.7: Simplified model showing the  $Q$  with respect to frequency. Of particular note is that the coil  $Q$  has a maxima at 17.9 MHz due to the balance of radiation and skin effect losses.

The point of maximum  $Q$  in this case using this simple model is predicted to be 17.9 MHz (Fig. 1.7). Electrically shorter coils (for example in a phone charging application) will have higher optimally efficient frequencies of operation, while electrically longer coils such as those used for the powering of magnetically

levitating trains will have lower optimal frequencies of operation. This analysis is consistent with analysis of loop antenna that found the maximum  $Q$  of loop antenna at a circumference to wavelength ratio of 0.1 [23]. ISM (industrial scientific and medical) band B frequencies are located at 13.56 MHz, 27.12 MHz and 40.68 MHz. Operation in these bands does not require licensing and a band A frequency at 6.78 MHz (does not require authorisation for specific applications). The majority of this thesis assumes operation in these ISM bands.

In this section it has been shown that for typical IPT systems the most efficient frequencies of operation are in the MHz range due to the point of maximum  $Q$  for typically dimensioned coils lying in this range. In most applications one of the ISM frequencies would be a good compromise between efficiency and legality of the system.

## 1.6 Thesis organisation

As switching technology has advanced [24] so has IPT technology, the efficient operating frequency of IPT systems now extends to 27 MHz. The available electronics technology is no longer the limiting factor in frequency selection for applications with a received power less than 50 W. However with the flexibility in frequency selection that modern switching devices afford; the weaknesses of current approaches to the inductive link become apparent. This thesis focuses on problems around the magnetic link at ISM frequencies (6.78 MHz and 13.56 MHz). Due to the dimensional constraints of most common applications, operating in this frequency range results in the greatest link efficiency.

The first technical chapter is on coil modelling. Aspects of the behaviours of air core coils have been examined by many researchers, however there is no complete model of an inductive link. In this chapter new and existing models are verified and combined to successfully model the behaviour of inductive links. This combined model is then used to optimise an inductive link that uses a coil with a new winding pattern. Optimisation is performed by exhaustively sweeping the practical parameter range of the coils geometry. The optimisation only takes a few minutes in contrast to the weeks this process would take using conventional finite element simulation. Furthermore the optimised coil uses a new coil winding pattern that attempts to improve link efficiency by balancing coupling factor and  $Q$ . The optimised coil has its behaviour simulated using finite element simulation and modelled with good correspondence observed between the approaches. The models calculate the self and mutual inductances of coils, the skin effect resistance, proximity factor and the vector magnetic field of the system in operation.

The second technical chapter address the measurement of coils. Frequently the  $Q$  factors of coils used in MHz inductive links are not known due to the lack of existing method to measure their  $Q$ . In this chapter such a method is developed. The chapter begins by defining the  $Q$  of an inductive coil and the correct processing that should be applied to results from FE simulation in order to obtain the coil  $Q$ . Different methods of measuring coils are explored before a method based on the transmission resonant  $Q$  is arrived at. A measurement apparatus using this method is constructed and modelled. This apparatus is used to measured a set of reference coils and the results compared to full wave simulations of those coils. However this method is laborious and slow, therefore a new measurement method is proposed that supports automatic switching of tuning frequency is proposed.

The third technical chapter describes an attempt to develop a new kind of magnetic shielding for inductive power transfer systems. In many real world applications magnetic flux must be confined to the gap between the transmitting and receiving coils. The conventional solution to this problem is to use ferrite backed ground planes behind the coils. However these structures are expensive and heavy due to the quantity of ferrite that must be used. If a method existed to reduce the quantity of ferrite required without reducing performance this would be useful. The developed shield is an artificial magnetic conductor (AMC) which

theoretical results in increased efficiency. The AMC uses a novel construction to operate at frequencies twenty times lower than any example located in the literature. The AMC prototype displays many of the characteristics of an AMC such as greatly increased self and mutual inductances of the link. However it also causes greater than expected loss, possibly due to the compromises that had to be made due to availability of materials. This increased loss means that the link efficiency using the prototype does not match that of a conventional ferrite backed ground plane. However finite element simulation shows that this structure holds great promise if the source of the loss could be found and corrected.

The fourth chapter describes the design and construction of an unconventional IPT system. This system is designed with an energy harvesting approach and operates by filling a room with a magnetic field generated by a large coil. This coil is then harvested by a much smaller coil that could be embedded in an item. The system is able to supply 10 mW with 6 m separation between transmitter and receiver. A new approach to the design of such systems is proposed based on an energy harvesting model and shown to be more effective at predicting the real world efficiency than conventional magnetic coupling theory. This is because the magnetic field in real rooms does not correspond to the decay rate expected due to metallic object interaction with the magnetic field.

## Chapter 2

# Modelling and simulation of inductive links

The previous chapter introduced basic inductive power transfer (IPT) theory, showing that for long range and high link efficiency, coil  $Q$  must be high. This chapter uses more complex models to show while coil  $Q$  should generally be high there is some trade off between coil  $Q$  and coupling factor,  $k$ .

Fast models are developed to simulate the inductive behaviour and losses of IPT coils as well as the magnetic fields that they produce while in operation. Some of these models originate from the literature and some are new techniques. There is a focus on flexibility rather than coil specific codes. The models are compared with finite element simulation. The models are used to successfully optimise a inductive link for link efficiency and then simulate the links magnetic behaviour. This magnetic link uses a new coil winding pattern termed the *volumetrically efficient coil* that attempts to, within a height constrained environment, improve the link efficiency.

### 2.1 Introduction

Improving the efficiency of wireless power transfer systems is important. Consider a home car charging scenario operating at 3 kW received power, if the system is 80% efficient 750 W of heat is generated during charging. This amount of generated heat requires expensive, noisy forced air cooling to avoid component failure. If instead the system was 95% efficient only 160 W needs to be dissipated, spread over all the components of the system this could be with silent convection cooling or small and cheap fan heat sinks.

The fractional magnetic link efficiency,  $\eta$ , is the upper bound upon an inductive links end to end efficiency. The Magnetic link efficiency of a resonant secondary inductive power transfer system is [13]:

$$\eta = \frac{k^2 Q_{Tx} Q_{Rx}}{(1 + \sqrt{1 + k^2 Q_{Tx} Q_{Rx}})^2}, \quad (2.1)$$

$$k = \frac{L_{TxRx}}{\sqrt{L_{Tx} L_{Rx}}}. \quad (2.2)$$

Assuming that the parasitic shunt capacity of the coils (Fig. 2.1) is negligible and they are electrically short the quality factor  $Q$  can be given by ( $Q$  is extensively discussed in the measurement chapter):

$$Q = \frac{|Z_{IM}|}{Z_{RE}} = \frac{\omega L}{R}. \quad (2.3)$$

For the best possible magnetic link efficiency  $k^2 Q_{Tx} Q_{Rx}$  should be maximised within the dimensional

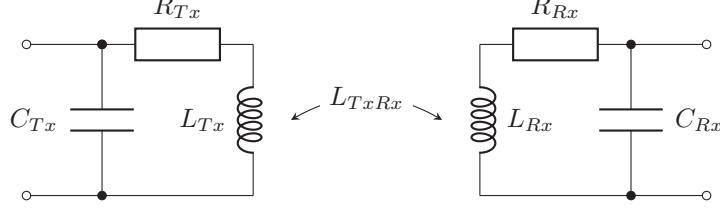


Figure 2.1: Transformer model of inductive link including coils self capacitance.

constraints of the system. This requires consideration of the coils mutual inductance,  $L_{TxRx}$ , as well as the individual coils losses,  $R_{Tx}$ ,  $R_{Rx}$  and self inductance,  $L_{Tx}$ ,  $L_{Rx}$ , at the operating frequency. Typical dimensional constraints for IPT systems restrict the heights  $H_{Tx}$ ,  $H_{Rx}$ , inner radii  $r_{TxMin}$ ,  $r_{RxMin}$  and outer radii,  $r_{TxMax}$ ,  $r_{RxMax}$ , of the coils while requiring an air gap,  $D$ , between the coils as shown in figure 2.2. This effectively constraints the IPT coils to two cylindrical volumes.

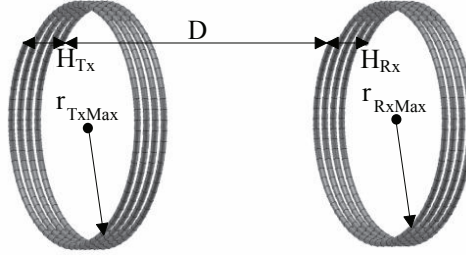


Figure 2.2: Dimensional constraints of an inductive Link.

Simple approximate equations can provide some insight into how a dimensionally constrained coil inductive link could be optimised. By assuming all the turns of the coils are coaxial filamentary current loops of average turn radii, located at the coils centres, a mutual inductance formula can be stated [20]:

$$L_{TxRx} \approx N_{Tx}^2 N_{Rx}^2 \frac{\mu_0 \pi \left( \frac{r_{TxMax} + r_{TxMin}}{2} \right)^2 \left( \frac{r_{RxMax} + r_{RxMin}}{2} \right)^2}{2(D - \frac{1}{2}H_{Tx}H_{Rx})^3}, \quad (2.4)$$

$$D \gg r_{TxMax}, r_{RxMax}. \quad (2.5)$$

From these equations it is observed that maximising turn radii of the coils is desirable to increase the mutual inductance between the coils. Furthermore the  $Q$  factor of the coils should be maximised through increasing the coil windings conductor radius,  $a$ , and through reducing the proximity effect by increasing the turn to turn spacing,  $s$ . However in a scenario with limited volume to contain the coil windings these requirements often contradict. Consider for example a planar spiral coil (PSC), as  $a$  and  $s$ , increase, the average turn radius decreases, therefore, to increase  $Q$  the mutual inductance must decrease. Gains in mutual inductance due to increasing turn count,  $N$ , have little effect on overall coupling factor for short round loop type coils since [21]:

$$L_{Tx}, L_{Rx} \propto N^2. \quad (2.6)$$

For  $N > 1$  the maximum link efficiency is insensitive to the number of turns for typical IPT coils;  $N$  is selected by consideration of the coils inductance and electrical length. Therefore the problem of the design of optimal link efficiency IPT coils for a given air gap and dimensional constraint is to choose optimal  $a$  and  $s$  for both coils. This may not be the  $a$  and  $s$  that gives the maximum coil  $Q$  at the operating frequency due to the consideration of the coupling factor [25].

The method most often used for extraction of the coil parameters is finite element simulation, with a typical simulation of an inductive link taking 4 h on an 6 core, 16 GB RAM workstation. Allocating more

computing resource reduces the time taken, but the point remains that a sweep of the full manufacturable parameter space takes a considerable length of time. In this chapter various numerical models are utilised and derived to model the inductive link's equivalent electrical parameters. These models generate results in a matter of seconds, while remaining general enough to be applied to the class of coils with uniform cross section. This allows for fast optimisation of the inductive link.

Although in finite element simulations, and in actual measurement values of the effective coil self capacity,  $C_{Tx}$ ,  $C_{Rx}$  are determined, there is no attempt to calculate their values in this chapter. Fundamentally the coils self capacity is a phenomenon of electrical length. If there were no phase retardation about the coil there would not be a potential difference to cause the coils self capacity or transmission line effects. Attempts to model this capacitance, excepting full field finite element simulations, have (to the authors knowledge) not resulted in accurate predications for all but special cases, such as helical coils [26] and are particularly difficult to make for the squat coils employed in IPT. Regardless this capacitance does not influence the fractional link efficiency,  $\eta$ , the primary parameter of interest for optimisation of the inductive link. The greatest effect it has on the design of the inductive link is to constrain the maximum operating frequency to the lowest self resonant frequency of the coils. However, if the coils have high  $Q$  and remain under  $\frac{1}{10}\lambda$  in length they will not have a self resonant frequency lower than the system operating frequency.

### 2.1.1 Inductive link model

To calculate the currents flowing in the inductive link and therefore the magnetic field, circuit simulations of the inductive link are performed (SPICE or similar). The parameters of the coils have been found through the modelling code ( $L_{Tx}$ ,  $L_{Rx}$ ,  $L_{TxRx}$ ,  $R_{skin}$ ,  $G_p$  and  $R_{rad}$ ), however a secondary load must also be selected to transfer power to. The optimal secondary load where,  $\eta$ , is achieved takes the form of a tuning capacitor selected to resonate the secondary coil at the operating frequency of the link and a series or parallel resistive load [13]. The optimal series resistive portion of the load is,  $R_{LSerOpt}$ :

$$R_{LSerOpt} = \omega L_{Rx} \left( \frac{\sqrt{1 + k^2 Q_{Tx} Q_{Rx}}}{Q_{Rx}} \right), \quad (2.7)$$

and the parallel optimal load,  $R_{LParOPT}$ :

$$R_{LParOPT} = \frac{Q_{Rx} \sqrt{Q_{Rx} Q_{Tx} k^2 + 1}}{C_T Q_{Rx} Q_{Tx} \omega k^2 + C_T \omega}, \quad (2.8)$$

where  $C_T$  is the receiver coil tuning capacitance, including the coils self capacity  $C_{Rx}$ . The phase relationship between the primary and secondary coils and their magnitudes for the desired power transfer is found from the optimal load using circuit simulation.

## 2.2 Introduction to coil types

### 2.2.1 Discretisation of filamentary models of coils

The inductance calculation method requires filamentary models of the coils, which can be generated from the coils' parametric equations. These models comprise of straight line segments. In addition the length of each turn is required for the calculation of coil loss resistance. The coil equations have been written in terms of;  $N$  (number of turns),  $s$  (turn edge to turn edge spacing),  $a$  (turn conductor radius) and  $r_{Max}$  (maximum outer radius of the coil) as these are the design parameters of the coil. It was found experimentally that to achieve 1% convergence in the inductance calculation method, the parametric variable,  $t$ , should be defined as:

$$t_{step} = \begin{cases} \frac{\pi}{180} & \text{if } \frac{100a}{r_{Max}} \geq 1 \\ \frac{100a\pi}{180r_{Max}} & \text{if } \frac{100a}{r_{Max}} < 1 \end{cases}$$

$$t = 0, t_{step}, 2t_{step} \dots 2\pi N \quad (2.9)$$

### 2.2.2 Volumetrically efficient coil (VEC)

| Coil Winding   | Frequency<br>[MHz] | $\eta$ | $Q_{Tx}$          | $Q_{Rx}$          | $D$<br>[mm] | $r_{TxMax}$<br>[mm] | $r_{RxMax}$<br>[mm] | $H_{Tx}$<br>[mm] | $H_{Rx}$<br>[mm] | Ref. |
|----------------|--------------------|--------|-------------------|-------------------|-------------|---------------------|---------------------|------------------|------------------|------|
| Surface Spiral | 3.7                | 0.9    | 2012              | 2012              | 300         | 170                 | 170                 | 27               | 27               | [15] |
| Helical        | 6                  | 0.95   | 1270              | 1100              | 230         | 155                 | 105                 | 50               | 90               | [16] |
| PSC            | 3.45               | >80    | 2608 <sup>1</sup> | 1983 <sup>1</sup> | 300         | 200                 | 200                 | 10 <sup>2</sup>  | 10               | [27] |

Figure 2.3: Table of existing coils windings in MHz IPT

The focus of this research is in inductive power transfer systems where the air gap is a significant fraction of the coil outer radius and magnetic materials are not used to increase  $k$ . Large radius hollow conductors are used to form the coils as they maximise the cross sectional area high frequency currents can flow in while removing unnecessary conductor material. Systems of this type have been demonstrated with a variety of different coil winding patterns (Table. 2.3). Of particular interest is the surface spiral coil [29], this coil has a number of advantages over helical and planar spiral coils (PSCs). Firstly the start and end coordinates of the coil are at the same point in space which minimises the additional series resistance and additional coil volume of the connection to the coils tuning capacitor. Secondly the turns are wound in three dimensions which has the effect of making the coil occupy less volume for a given turn radius and spacing in comparison to a helical coil, whilst not suffering as dramatic a reduction in turn radius as a PSC. However the design has a significant weakness in that the electric field between the first and last turn (which are in close physical proximity) is very strong causing the Q factor of coils to reduce significantly due to dielectric losses. In [29] Q factor was halved by using a support structure with a loss tangent of 0.003. For the surface spiral to outperform other coil types within the same volume constraint the support structure for the plated copper must be made of very low loss dielectric such as PTFE that is hard to form into the required shape. This coil type is also difficult to construct as the support dielectric cannot be fully plated due to the requirement to have insulating gaps between turns, yet is required to support the coil during the plating process.

A new coil is proposed henceforth referred to as the *volumetrically efficient coil* (VEC), this coil has the same winding pattern as the surface spiral coil however instead of a thin tape conductor hollow tubes are used (Fig. 2.4). As the turn advances it twists around a central axis such that the end of the final turn joins to the start of the first turn (a small gap in practise is put here to allow a potential to develop across the coil). As the coil turns are largely self supporting, dielectric losses in practical coils are much lower than in surface spiral type coils.

### 2.2.3 Parametric coil equations

#### (Volumetrically efficient coil (VEC))

The parametric equations of this coil's path, use centre to centre tube spacing,  $v$ , for convenience:

$$v = s + 2a. \quad (2.10)$$

<sup>1</sup>The Wayne Kerr 6500B used to obtain these results has a base Q accuracy of 0.05%( $Q + 1/Q$ ) [28]

<sup>2</sup>Not including feed structure

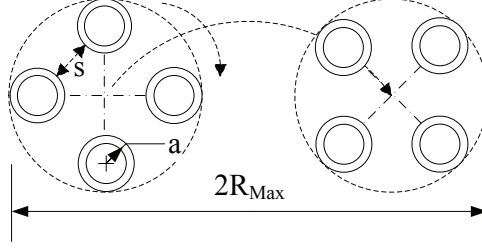


Figure 2.4: Four turn volumetrically efficient coil (VEC) cross section, showing return conductors on the right hand side.

Using the centre to centre tube spacing the distance from the tube centres to the central axis of the VEC,  $\phi$ , is therefore:

$$\phi = v \left( \frac{\sin(\frac{\pi}{2} - \frac{\pi}{N})}{\sin(\frac{2\pi}{N})} \right). \quad (2.11)$$

In the case of two turns, due to the limit condition, this equation will not evaluate correctly and must be replaced with:

$$\phi = \frac{v}{2}, \quad (2.12)$$

the solution to the limit of equation 2.11. The general case of any two dimensional central axis for the turns to be traced around can be found using:

$$x = \alpha_x + \phi \cos\left(\frac{t}{N}\right) \cos(t), \quad (2.13)$$

$$y = \alpha_y + \phi \cos\left(\frac{t}{N}\right) \sin(t), \quad (2.14)$$

$$z = \phi \sin\left(\frac{t}{N}\right), \quad (2.15)$$

where  $\alpha$  is the parametric path of the central axis to trace around, for example this could be elliptical. In the particular case of a circular coil path the central path radius,  $\zeta$ , is defined as:

$$\zeta = r_{Max} - a - \phi. \quad (2.16)$$

Therefore the path equations of the central axis path are:

$$\alpha_x = \zeta \cos(t), \quad (2.17)$$

$$\alpha_y = \zeta \sin(t). \quad (2.18)$$

To calculate the length of the VECs turns the path integral for the turn number,  $n$ , must be solved numerically:

$$\frac{dx}{dt} = -\zeta \sin(t) - \frac{\phi \sin(\frac{t}{N}) \cos(t)}{N} - \phi \cos(\frac{t}{N}) \sin(t), \quad (2.19)$$

$$\frac{dy}{dt} = \zeta \cos(t) - \frac{\phi \sin(\frac{t}{N}) \cos(t)}{N} - \phi \cos(\frac{t}{N}) \sin(t), \quad (2.20)$$

$$\frac{dz}{dt} = \frac{\phi \cos(\frac{t}{N})}{N}, \quad (2.21)$$

$$l_n = \int_{2\pi(n-1)}^{2\pi n} \sqrt{\left(\frac{dx}{dt}\right)^2 + \left(\frac{dy}{dt}\right)^2 + \left(\frac{dz}{dt}\right)^2} dt. \quad (2.22)$$



The height,  $H$ , of the coil is simply the outer diameter of the circular cross section of the turns:

$$H = 2\phi + 2a. \quad (2.23)$$

### Helix

For the helix (Fig. 2.11) the parametric equations are:

$$x = (r_{Max} - a) \cos(t), \quad (2.24)$$

$$y = (r_{Max} - a) \sin(t), \quad (2.25)$$

$$z = \frac{t(s + 2a)}{2\pi}. \quad (2.26)$$

Thus the length of one turn of the helix, can be written as:

$$l_n = 2\pi \sqrt{(r_{Max} - a)^2 + \left(\frac{2a + s}{2\pi}\right)^2}, \quad (2.27)$$

and the height of the coil,  $H$ , is:

$$H = N(2a + s) + 2a. \quad (2.28)$$

### PSC

For the PSC the parametric equations are:

$$\gamma = 2a + s, \quad (2.29)$$

$$x = \left((r_{Max} - a) - \frac{\gamma t}{2\pi}\right) \cos(t), \quad (2.30)$$

$$y = \left((r_{Max} - a) - \frac{\gamma t}{2\pi}\right) \sin(t), \quad (2.31)$$

$$z = 0. \quad (2.32)$$

The length of turns for the PSC can be solved exactly however the equations are too long to include in this chapter or even appendix. Instead the following equations can be numerically evaluated, or solved using a symbolic solver to obtain the exact length of each turn:

$$\gamma_\theta = (r_{Max} - a) - \frac{\gamma}{2\pi}\theta, \quad (2.33)$$

$$\frac{d\gamma_\theta}{d\theta} = -\frac{\gamma}{2\pi}, \quad (2.34)$$

$$l_n = \int_{2\pi(n-1)}^{2\pi n} \sqrt{\gamma_\theta^2 + \left(\frac{d\gamma_\theta}{d\theta}\right)^2} d\theta, \quad (2.35)$$

where  $\gamma_\theta$  is the angular procession of the coils central path. The height of the PSC is simply,  $2a$ , not including the feed structure, as all the turns lie on the same plane.

## 2.3 Method

### 2.3.1 Calculation methodology

The method for calculating the properties of the inductive link is to generally regard phenomena as separable where possible and then to find models for these phenomena or develop new models where existing models are lacking. The inductance and resistance phenomena are regarded as totally separate while the resistance phenomena are solved as the supposition of two current distributions. The phenomena are combined to simulate the overall behaviour of the inductive link via the circuit model (Fig. 2.1).

### 2.3.2 Calculation of inductances

To calculate inductances it is desirable to have a method that can be used with all three studied coil types (Helical, PSC and VEC) and able to calculate both self and mutual inductances. The proposed method is capable of all of these calculations. There exist methods for the calculation of PSC and helical coils, however these methods rely on parameter tables [1] or have limitations on coil aspect ratios and are specific to the coil type. Furthermore as the VEC is a new coil type there exists no formula for calculation of its self or mutual inductances. The existing calculation methods for inductive coils originate from an era before the digital computer and as such are constrained by need to make results hand calculable, digital computers are now easily accessible and therefore a method relying on a large number of calculations is not problematic, so long as the calculations can be completed quickly by a desktop computer.

The proposed method is to discretise the coils into many small filaments and to solve the inductance matrix of all filaments. This is a method of finite elements, however the number of elements numbering in the hundreds per coil and therefore quickly solvable.

The self inductance of the coils is solved via the the concept of geometric mean distance whereby two paths are plotted radially offset from the centre path of the coil by the half the geometric mean distance each in the normal direction to the coils path. This is such that the mean path of the two filaments is the coils path and the filaments are spaced from each other by the geometric mean distance. The paths shall be referred to as  $L_1$  and  $L_2$ . Thus far this just one of the standard ways of calculating an inductance formula, for example [30] uses this method to derive the self inductance formula for a loop of round wire, the crucial next step is that the path is discretised into short straight connected filaments. This allows the inductance between these two paths to be calculated by calculation of the inductances between each filament, by repeatedly solving the inductance between straight current paths at arbitrary position and orientation in 3D space.

The same mathematics is used for the calculation of self and mutual inductance; in both cases the mutual inductance between a path of filaments is found. For the mutual inductance case the filamentary paths trace the centre of the coil conductors. In the self inductance case the two coil paths are displaced radially from the centrer path of the coil by half the geometric mean distance in opposing directions. For an electrically thick tube or rod the geometric mean distance is  $0.7788a$  as given by Maxwell [31]. The total inductance between the paths  $L_1$  and  $L_2$  is given by the Neumann formula:

$$M_{12} = \frac{\mu_0}{4\pi} \oint_{L_1} \oint_{L_2} \frac{dl \cdot ds}{R}. \quad (2.36)$$

Where  $dl$  and  $ds$  are an infinitesimal element of the paths  $L_1$  and  $L_2$  respectively and,  $R$ , is the scalar distance from  $dl$  to  $ds$ . To evaluate this numerically the paths are approximated as straight line segments; let  $[x_m, y_m, z_m]$  be the Cartesian coordinates of the  $m^{th}$  point on the path  $L_1$  and  $[x_n, y_n, z_n]$  be the coordinates of the  $n^{th}$  point on the path  $L_2$ . By considering the paths to consist of straight line segments

it can be defined:

$$\overrightarrow{dl_m} = (x_{m+1} - x_m)\hat{x} + (y_{m+1} - y_m)\hat{y} + (z_{m+1} - z_m)\hat{z}, \quad (2.37)$$

$$\overrightarrow{ds_n} = (x_{n+1} - x_n)\hat{x} + (y_{n+1} - y_n)\hat{y} + (z_{n+1} - z_n)\hat{z}. \quad (2.38)$$

The distance between the midpoints of  $dl$  and  $ds$  is then found:

$$l_{m,mid} = \frac{(x_{m+1} + x_m)}{2}\hat{x} + \frac{(y_{m+1} + y_m)}{2}\hat{y} + \frac{(z_{m+1} + z_m)}{2}\hat{z}, \quad (2.39)$$

$$s_{n,mid} = \frac{(x_{n+1} + x_n)}{2}\hat{x} + \frac{(y_{n+1} + y_n)}{2}\hat{y} + \frac{(z_{n+1} + z_n)}{2}\hat{z}. \quad (2.40)$$

The scalar distance between  $l_{m,mid}$  and  $s_{n,mid}$  is given by:

$$R_{m,n} = \|l_{m,mid} - s_{n,mid}\|. \quad (2.41)$$

It follows that the inductance between the two discretised paths is:

$$M_{12} = \frac{\mu_0}{4\pi} \sum_{m=1}^{m=M} \sum_{n=1}^{n=N} \frac{\overrightarrow{dl_m} \cdot \overrightarrow{ds_n}}{R_{m,n}}. \quad (2.42)$$

Where,  $M$ , and  $N$ , are the total number of segments in their respective paths. MATLAB code for the calculation of inductances is included in Appendix C. For all tested coils the self inductance is calculated in less than one second on a desktop computer. The MATLAB code for generation of the paths  $L_1$  and  $L_2$  as well as the coils centre path  $L_3$  (used to calculate mutual inductance) is included in Appendix D. To calculate mutual inductance the same calculation is performed, substituting,  $L_3$ , of the transmitter coil for,  $L_1$ , and  $L_3$ , of the receiver coil for  $L_2$ .

### 2.3.3 Calculation of magnetic fields

To calculate the magnetic field from a coil or collection of coils again a filamentary approach is utilised. The coils central paths,  $L_3$ , are plot as a chain of filaments as per calculation of mutual inductances. The current in each chain of filaments is assumed to be constant, the vector contribution of each filament to the magnetic field at the point in 3D space to be solved is calculated. By summation of the individual contributions the overall field is calculated. To calculate the total  $\mathbf{B}$  field of an IPT system the phase relationship and RMS magnitude relationship between the currents in the primary and secondary coils must be known (found via equivalent circuit modelling).

The total field is constructed from the supposition of all magnetic fields produced by the filaments therefore the solution for the magnetic field at an arbitrary point,  $\mathbf{P}$ , from a straight filament, must be found. This is solved by transformation of the solution to the in plane magnetic field magnitude of a finite wire. There is always a plane where the magnetic flux direction vector is perpendicular to the plane at point  $\mathbf{P}$  and also the filament lies on the plane. By transforming the solution in this plane the vector field at point  $\mathbf{P}$  can be found.

Firstly the scalar distance of the point  $\mathbf{P}$  from the filament assuming the filament has infinite extent is found. To calculate this the normalised direction vector  $\hat{\mathbf{Q}}$  for start point,  $\mathbf{S}$ , and end point,  $\mathbf{E}$ , of the filament is found:

$$\hat{\mathbf{Q}} = \frac{\mathbf{S} - \mathbf{E}}{\|\mathbf{S} - \mathbf{E}\|}. \quad (2.43)$$

The direction vector,  $\overrightarrow{P\hat{1}}$ , from the closest point on line  $\mathbf{S} + \lambda\hat{\mathbf{Q}}$ , where  $\lambda$  is an arbitrary scaler, to  $\mathbf{P}$ ,

assuming the start of the line is from  $\mathbf{S}$  and proceeds in the direction of  $\mathbf{E}$  is found:

$$\vec{P1} = ((\mathbf{S}_x - \mathbf{P}_x)\hat{\mathbf{Q}}_x + (\mathbf{S}_y - \mathbf{P}_y)\hat{\mathbf{Q}}_y + (\mathbf{S}_z - \mathbf{P}_z)\hat{\mathbf{Q}}_z)\hat{\mathbf{Q}}, \quad (2.44)$$

and the direction vector  $\vec{P2}$  from  $\mathbf{E}$  proceeding in the direction of  $\mathbf{S}$ :

$$\vec{P2} = ((\mathbf{E}_x - \mathbf{P}_x)\hat{\mathbf{Q}}_x + (\mathbf{E}_y - \mathbf{P}_y)\hat{\mathbf{Q}}_y + (\mathbf{E}_z - \mathbf{P}_z)\hat{\mathbf{Q}}_z)\hat{\mathbf{Q}}. \quad (2.45)$$

The vector norms;  $\|\vec{P1}\|$  and  $\|\vec{P2}\|$  give the lengths of  $\vec{P1}$  and  $\vec{P2}$  and are use to select the minimum length direction vector solution of  $\mathbf{P}$  to the line  $\mathbf{S} + \lambda\hat{\mathbf{Q}}$ . This minimum length direction vector is referred to as  $\vec{P3}$ . The next stage in the calculation is to find the scaler offsets along the line  $\mathbf{S} + \lambda\hat{\mathbf{Q}}$  and  $\mathbf{E} + \lambda\hat{\mathbf{Q}}$  to the point  $P + \vec{P3}$ . The offset from  $\mathbf{E}$ :

$$\mathbf{E_o} = \mathbf{E} - \mathbf{P3}, \quad (2.46)$$

and from  $\mathbf{S}$ ;

$$\mathbf{S_o} = \mathbf{S} - \mathbf{P3}. \quad (2.47)$$

Therefore the magnitude of the distance from the end points are found:

$$d_e = \|\mathbf{E_o} - \mathbf{P}\|, \quad (2.48)$$

and for the second equation:

$$d_s = \|\mathbf{S_o} - \mathbf{P}\|. \quad (2.49)$$

These scaler offsets do not necessarily have the correct signs. To correct the signs firstly the length of the filament,  $l_w$ , is calculated:

$$l_w = \|\mathbf{S} - \mathbf{E}\|. \quad (2.50)$$

There are three zones along the line where  $P + \vec{P3}$ ; the first zone is before  $\mathbf{S}$  at this point both  $d_s$  and  $d_e$  should have their signs flipped, at this point  $d_s - l_w \geq 0$  and  $d_s > d_e$ . The next zone along the line is beyond point  $\mathbf{S}$  but before  $\mathbf{E}$  whereupon the sign of  $d_s$  should be flipped, this is the default condition. The final zone is beyond  $\mathbf{E}$  whereupon  $d_e - l_w \geq 0$  and  $d_e > d_s$  and all signs should remain the same. Using  $d_s$  and  $d_e$  the in plane angles from the start and end points of the filament can be found:

$$\phi_1 = \arctan \frac{d_e}{\|\mathbf{P3}\|}, \quad (2.51)$$

$$\phi_2 = \arctan \frac{d_s}{\|\mathbf{P3}\|}. \quad (2.52)$$

The Biot-Savart law states:

$$d\mathbf{B} = \frac{\mu_0 I}{4\pi} \frac{d\mathbf{l} \times \mathbf{r}}{r^3}, \quad (2.53)$$

where  $d\mathbf{l}$  is a small length of filament,  $r$  the in plane distance from point  $\mathbf{P}$ . Therefore using the previously found angles the magnetic field magnitude at  $\mathbf{P}$  can be calculated:

$$|\mathbf{B}| = \mu_0 I \left( \frac{\sin \phi_1 - \sin \phi_2}{4\pi \|\mathbf{P3}\|} \right). \quad (2.54)$$

This result is then used to calculate the vector field in the original reference frame:

$$\mathbf{B} = |\mathbf{B}| \frac{\mathbf{P3} \times (\mathbf{E_o} - \mathbf{S_o})}{\|\mathbf{P3} \times (\mathbf{E_o} - \mathbf{S_o})\|}. \quad (2.55)$$

The contributions from each filament that make up the coil or coils are summed at the sample point  $\mathbf{P}$  in order to calculate the total magnetic field. The contributions of the secondary coil will not be in phase with the primary coil and therefore when summing this should be taken into account. The MATLAB code used to calculate the contribution of a filament is included as Appendix E.

### 2.3.4 Calculation of resistances

IPT coils are electrically short loop antenna; as long as they remain below  $\frac{1}{10}\lambda$  in length they can be modelled using a lumped element equivalent circuit (Fig. 2.1) of an inductor in series with a resistor [22]. The coils series loss resistor  $R_{Tx}$  or  $R_{Rx}$  comprises:

$$R = R_{rad} + R_{skin}G_p, \quad (2.56)$$

where  $R_{rad}$  is the coils radiation resistance,  $R_{skin}$  an isolated conductors skin effect resistance and  $G_p$  the proximity factor to take into account the increase in resistance due to current redistribution caused by other turns in the coils cross section for example figure 2.4.

Calculations for the skin effect resistance of tubes,  $R_{skin}$ , were first published by Dwight in 1918 [32]. W. Mingli and F. Yu have improved the reliability of these calculations by using polynomial approximations when parameters cause poor accuracy in evaluation of the Bessel functions [33]. For calculation of the proximity factor Zeljko Pantic and Srdjan Lukic recently presented Fourier series numerical solutions for the problem of the proximity factor of uniform cross section coils comprised of tubes [34]. This is achieved through treatment of the tubes in the cross section that are not the tube to be solved as current filaments. These current filaments are displaced from the geometric centres of the tubes that generate them according to the current distribution in those tubes such that they have the same effect on the tube to be solved that the original tube would have. Their work is an extension of the solution of the current distribution and proximity effect resistance of a single tube caused by a current filament of Dragan Filipović and Tatijana Dlabac [35].

#### Skin effect

At high frequencies the loss resistance of the coils increases due to increasing unevenness in current distribution through the tubes cross section. The radial modulation in current distribution is referred to as the skin effect; in addition to increasing the turns resistance it also causes the internal inductance of the tubes to increase due increased current concentration. However for all tubes that would be practicable for forming IPT coils the internal inductance is very small with respect to the inductance formed by mutual flux linkage between tubes. The skin depth is given by:

$$\delta = \sqrt{\frac{2\rho}{\omega\mu}}. \quad (2.57)$$

The method of Mingli and Yu [33] is used to calculate the tubes resistance and internal inductance (although the internal inductance value is not used). Their method uses a polynomial approximation for the Bessel functions for tubes that have thin walls with respect to their diameter as evaluation of the Bessel functions with large arguments using infinite series truncation produces unreliable results even with double precision computation. For tubes that are thick walled such that  $ma < 8$  or  $mq < 8$  (where  $a$  is the outer radius of the tube and  $t$  the wall thickness):

$$q = a - t, \quad (2.58)$$

$$m = \sqrt{\frac{\omega\mu}{\rho}}, \quad (2.59)$$

$$R_{DC} = \frac{\rho}{\pi(a^2 - q^2)}, \quad (2.60)$$

$$O = -\frac{\text{ber}'(mq) + j \text{bei}'(mq)}{\text{ker}'(mq) + j \text{kei}'(mq)}, \quad (2.61)$$

$$P = \frac{\text{ber}(ma) + j \text{bei}(ma) + O(\text{ker}(ma) + j \text{kei}(ma))}{\text{ber}'(ma) + j \text{bei}'(ma) + O(\text{ker}'(ma) + j \text{kei}'(ma))}, \quad (2.62)$$

$$Z = jR_{DC}P \left( \frac{ma(a^2 - q^2)}{2a^2} \right), \quad (2.63)$$

$$L_{int} = l \frac{\Im(Z)}{\omega}, \quad (2.64)$$

$$R_{skin} = l \Re(Z). \quad (2.65)$$

The Bessel functions are evaluated as:

$$\text{ber}(x) = \Re(J_0(xe^{\frac{j3\pi}{4}})), \quad (2.66)$$

$$\text{ber}'(x) = \Re(e^{\frac{j3\pi}{4}} J_{-1}(xe^{\frac{j3\pi}{4}})), \quad (2.67)$$

$$\text{bei}(x) = \Im(J_0(xe^{\frac{j3\pi}{4}})), \quad (2.68)$$

$$\text{bei}'(x) = \Im(e^{\frac{j3\pi}{4}} J_{-1}(xe^{\frac{j3\pi}{4}})), \quad (2.69)$$

$$\text{ker}(x) = \Re(K_0(xe^{\frac{j\pi}{4}})), \quad (2.70)$$

$$\text{ker}'(x) = \Re(-e^{\frac{j\pi}{4}} K_{-1}(xe^{\frac{j\pi}{4}})), \quad (2.71)$$

$$\text{kei}(x) = \Im(K_0(xe^{\frac{j\pi}{4}})), \quad (2.72)$$

$$\text{kei}'(x) = \Im(-e^{\frac{j\pi}{4}} K_{-1}(xe^{\frac{j\pi}{4}})). \quad (2.73)$$

Where  $J_0$  is the 0th order Bessel function of first kind,  $J_{-1}$  the -1 order,  $K_0$  the modified Bessel function of second kind 0th order and  $K_{-1}$  the -1 order. These functions are widely available in mathematical software libraries and tables [36]. When the tubes are not thick the polynomial approximations,  $\theta(x)$ ,  $\phi(x)$ , to the Bessel functions are used:

$$\begin{aligned} \theta(x) = & (0.0000000 - j0.3926991) \\ & + (0.0110486 - j0.0110485) \left( \frac{8}{x} \right) \\ & + (0.0000000 - j0.0009765) \left( \frac{8}{x} \right)^2 \\ & + (-0.0000906 - j0.0000901) \left( \frac{8}{x} \right)^3 \\ & + (-0.0000252 + j0.0000000) \left( \frac{8}{x} \right)^4 \\ & + (-0.0000034 + j0.0000051) \left( \frac{8}{x} \right)^5 \\ & + (0.0000006 + j0.0000019) \left( \frac{8}{x} \right)^6, \end{aligned} \quad (2.74)$$

$$\begin{aligned}
\phi(x) = & (0.7071068 + j0.7071068) \\
& + (-0.0625001 - j0.0000001) \left(\frac{8}{x}\right) \\
& + (-0.0013813 + j0.0013811) \left(\frac{8}{x}\right)^2 \\
& + (0.0000005 + j0.0002452) \left(\frac{8}{x}\right)^3 \\
& + (0.0000346 + j0.0000338) \left(\frac{8}{x}\right)^4 \\
& + (0.0000117 - j0.0000024) \left(\frac{8}{x}\right)^5 \\
& + (0.0000016 - j0.0000032) \left(\frac{8}{x}\right)^6,
\end{aligned} \tag{2.75}$$

$$\begin{aligned}
A = & \exp(-\sqrt{2}(1+j)(ma - mq) - \theta(ma) \\
& + \theta(-ma) + \theta(mq) - \theta(-mq)),
\end{aligned} \tag{2.76}$$

$$S = \frac{q}{a}, \tag{2.77}$$

$$\frac{R_{skin}}{l} = R_{DC} \Re \left[ \frac{jmr(1 - S^2) \left(1 + A \frac{\phi(mq)}{\phi(-mq)}\right)}{2 \left(\phi(mr) - A\phi(-mr) \frac{\phi(mq)}{\phi(-mq)}\right)} \right], \tag{2.78}$$

$$L_{intDC} = \frac{\mu}{2\pi} \left[ \frac{q^4}{(a^2 - q^2)^2} \ln \left(\frac{a}{q}\right) - \frac{3q^2 - a^2}{4(a^2 - q^2)} \right], \tag{2.79}$$

$$\frac{L_{int}}{l} = L_{intDC} \Re \left( \frac{4(1 - S^2)^2}{ma(S^4(3 - 4 \ln(S)) - 4S^2 + 1)} \cdot \frac{1 + A \frac{\phi(mq)}{\phi(-mq)}}{\phi(ma) - A\phi(-ma) \frac{\phi(mq)}{\phi(-mq)}} \right). \tag{2.80}$$

### Proximity effect

The proximity effect model used is described in the paper of Zeljko Pantic and Srdjan Lukic [34]. The principle is to unwrap the turns of the coil into a straight cross section and then find the proximity factor of each turn in that cross section. The result figure 2.19 shows that for even very tightly wound coils unwrapping the coil and solving the equivalent length conductor can produce accurate results. To find the proximity factor the authors consider the effect on the current distribution in an electrically thin tube influenced by the  $\mathbf{B}$  field produced by a current filament, so solve this problem they use Fourier series to approximate the solution. The tubes apart from the tube to have its proximity factor found are replaced by equivalent filaments and superposition used to calculate their combined effect on the tube under examination. As the redistribution of current in the tubes effects their equivalent filament position a displacement is calculated for each filament to better represent their proximity influenced current.

The proximity factor,  $G$ , for the tube under test,  $i$ , is calculated by the following equation:

$$G_i = 1 + 2o^4 \sum_{p=1}^{\infty} \frac{\left( \sum_{n=1, n \neq i}^{n=N} \left( \frac{r}{s_{n \rightarrow i}} \right)^p \cos(p\alpha_{n \rightarrow i}) \right)^2 + \left( \sum_{n=1, n \neq i}^{n=N} \left( \frac{r}{s_{n \rightarrow i}} \right)^p \cos(p\alpha_{n \rightarrow i}) \right)^2}{p^2 + o^4}, \tag{2.81}$$

with the correction vector for each tube that is not under test given by;

$$r_{i,corr_x} = -\frac{o^4 r^2}{(1 + o^4)} \left[ \sum_{n=1, n \neq i}^N \frac{\cos(\alpha_{n \rightarrow i})}{s_{n \rightarrow i}} \right], \quad (2.82)$$

$$r_{i,corr_y} = -\frac{o^4 r^2}{(1 + o^4)} \left[ \sum_{n=1, n \neq i}^N \frac{\sin(\alpha_{n \rightarrow i})}{s_{n \rightarrow i}} \right]. \quad (2.83)$$

Where;

$$o = \frac{\sqrt{tr}}{\delta}, \quad (2.84)$$

$\alpha$  is the angle from the centre of the tube,  $i$ , to the filament where the x axis is  $0^\circ$  and the angle increments anticlockwise.  $s$ , is the distance from the centre of the tube to the filament. As the current is assumed to be on the surface of the tubes,  $r$ , is the outer radius of the tubes while,  $t$ , is the tubes wall thickness.  $p$ , is the Fourier series harmonic. The authors solve the first 10 harmonics, with no iteration.  $\delta$ , is simply the skin depth in the material that the tubes are composed of.

To calculate the proximity effect resistance of a turn; firstly filaments are placed in a 2D plane at the centre of the tubes that are not the tube under test. These filaments have a correction vector generated for them assuming the other filaments are in their original locations. These correction vectors are then used to alter the positions of the filaments when calculating the proximity factor of the turn using equation 2.81, the turn being solved remains in its uncorrected position. Once the proximity factor the tube is calculated it is then multiplied by the turn length and the skin effect resistance of 1 m of the same tube to calculate the turns AC resistance. The overall resistance of the coil is found by summing the resistance of all the turns.

### Radiation resistance

The radiation resistance of a coil is a phenomenon of electrical length and therefore for accurate calculation a full wave simulation must be conducted as the current distribution in the coil is no longer constant along the coil's length. For complex coil geometries the radiation resistance is not feasible to determine analytically. Simple structures such as wire loops (magnetic dipole) have had their radiation resistance calculated analytically however therefore the solution for the magnetic dipole can be used to approximate the radiation resistance of more complex coils by assuming each turn is an layered magnetic dipole [22]:

$$R_{rad} = \left( \frac{377}{6\pi} \right) \left( \frac{2\pi}{\lambda} \right)^4 (N\pi r^2)^2. \quad (2.85)$$

As the coils are very electrically small it can be assumed that the phase velocity in the coil is the speed of light. For all coil geometries,  $r$ , is set to the mean radius of the coil. This resistance should be small in relation to the skin and proximity effect resistance of an IPT coil as if it's large the coil will be an effective RF radiator.

### 2.3.5 Simulation tool for skin effect modelling of tubes

To verify the resistance models, collections of tubes with varying wall thickness, spacing and outer diameter must be modelled. Full wave simulation tools like CST MWS are ill suited for precision modelling of the skin effect for verification of aspects of resistance models for a number of reasons. Firstly it has no 2D projection mode, therefore many mesh cells have to be wasted in modelling straight length of conductors. Secondly 'normal' material with at least 5 mesh cells per skin depth must be used when the thickness of the conductor walls are not electrically thick ( $< 5\sigma$ ), rather than the electrical conductor approximation which



can use cells much greater than a skin depth. Thirdly the calculation domain is limited in extent and must be meshed as well as the conductors, for the conductor to have a much greater length than diameter a large spacial volume must be meshed. The end result is that too great a number of mesh cells are required for the simulations to run on even a powerful single computer due to limited memory.

To simulate the tube configurations the software "Fast Henry Inductex v4.25 - 21 March 2014" [37] was utilised with a new MATLAB preprocessor script to generate the meshed tube configurations. This software has infinite calculation domain and only simulates magnetic phenomenon, there is also no need for an explicit current return path inside the simulation domain. Only one filament is created along the length dimension of the tubes as the current distribution along the length of the conductors is presumed to be uniform in this dimension. For the verification work the following settings are used: Tube length = 1 m, tube sides = 360, tube outer radius = 400  $\mu\text{m}$ , 5 mesh cells per skin depth, test frequency = 3.7 MHz,  $\rho = 1.72 \times 10^{-8}$ . These dimensions are primarily selected as a balance between fast simulation times and avoiding edge and radius effects. With these settings a single tube of 1 skin depth wall thickness uses 3478 filaments. The following command line settings are used with Fast Henry "fasthenry filename.inp -iterative -mdirect -pdiag -o2 -lauto -aoff -i0 -t0.001 -b0.01 -c200". Figures 2.5 and 2.6 showing the meshing of a single tube have been prepared to show how the tube cross section is divided into squares that approximate its shape; crosses indicate a mesh cell has been located with its centre at that position, while circles indicate no mesh cell. The meshing algorithm is very simple; firstly the cross section of the tube is drawn, secondly this is divided into grid squares of one mesh cell size, thirdly the contents of each of these squares is evaluated, finally if  $> 50\%$  of the cell is occupied by conductor a filament for that cell is generated. Using this method the area of filaments will always be less than the ideal conductor area, as such the ratio of filament area to conductor area is used as a quality metric, for the example single tube (Figs. 2.5, 2.6) this is 0.992.

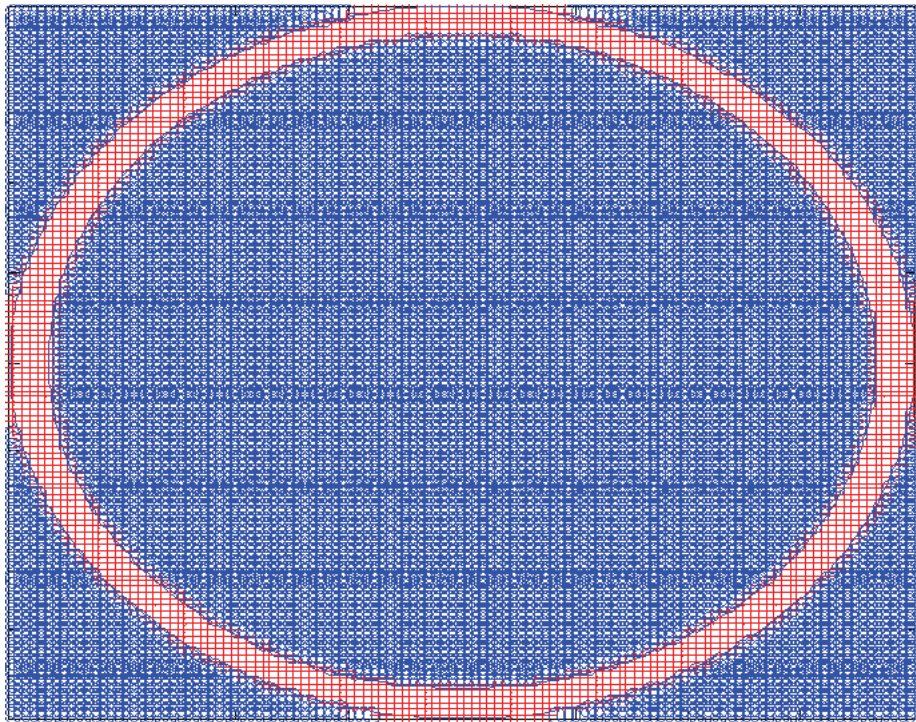


Figure 2.5: Meshing of a single, isolated tube using a simple meshing algorithm.

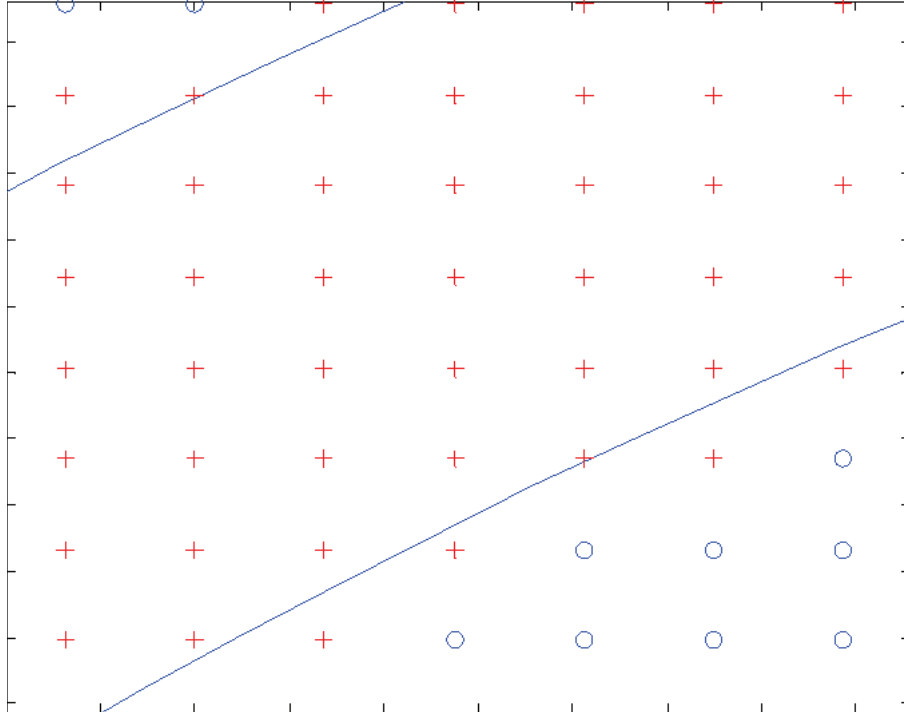


Figure 2.6: Zoomed view of meshing of a single, isolated tube (Fig. 2.5).

## 2.4 Results

### 2.4.1 Inductance

There exist a family of helical reference coils (see Measurement of wireless power transfer coils chapter) that have been used to verify full wave CST simulations. This reference family has a wide range of aspect ratios and number of turns. The measured self inductances are compared with the CST simulations and the modelled self inductances for these coils. There is no reference family for the PSC or VEC types therefore the comparison is only between full wave simulation and modelling. However as the same simulation settings are used as with the helical coils there is a high degree of confidence in the full wave simulations.

| Coil   | CST          | Measurement  | Model        | N | s    | a      | $r_{Max}$ |
|--------|--------------|--------------|--------------|---|------|--------|-----------|
| Coil 1 | 1.23 $\mu$ H | 1.25 $\mu$ H | 1.29 $\mu$ H | 2 | 2 mm | 1.5 mm | 75 mm     |
| Coil 2 | 1.40 $\mu$ H | 1.44 $\mu$ H | 1.47 $\mu$ H | 3 | 2 mm | 1.5 mm | 50 mm     |
| Coil 3 | 1.14 $\mu$ H | 1.17 $\mu$ H | 1.17 $\mu$ H | 4 | 5 mm | 1.5 mm | 35 mm     |
| Coil 4 | 1.10 $\mu$ H | 1.11 $\mu$ H | 1.13 $\mu$ H | 3 | 8 mm | 1.5 mm | 48 mm     |

Figure 2.7: A comparison of the self inductances of helical coils.

| Coil   | CST          | Model        | N | s    | a      | $r_{Max}$ |
|--------|--------------|--------------|---|------|--------|-----------|
| Coil 5 | 1.12 $\mu$ H | 1.15 $\mu$ H | 2 | 2 mm | 1.5 mm | 75 mm     |
| Coil 6 | 1.10 $\mu$ H | 1.14 $\mu$ H | 3 | 2 mm | 1.5 mm | 50 mm     |
| Coil 7 | 407 nH       | 408 nH       | 4 | 5 mm | 1.5 mm | 35 mm     |
| Coil 8 | 573 nH       | 568 nH       | 3 | 8 mm | 1.5 mm | 48 mm     |

Figure 2.8: A comparison of the self inductances of planar spiral coils.

The results for the self inductance for the Helical coils are excellent (Table. 2.7), within 5% for all cases with the closer spaced coils ( $\frac{s}{a} = 3$ ) displaying the greater deviation from CST simulation. For the PSC and VEC types (Fig. 2.8, 2.9) the deviation from the CST simulation is greater with the worst case of +7.8%

| Coil    | CST          | Model        | N | s    | a      | $r_{Max}$ |
|---------|--------------|--------------|---|------|--------|-----------|
| Coil 9  | 1.17 $\mu$ H | 1.24 $\mu$ H | 2 | 2 mm | 1.5 mm | 75 mm     |
| Coil 10 | 1.34 $\mu$ H | 1.43 $\mu$ H | 3 | 2 mm | 1.5 mm | 50 mm     |
| Coil 11 | 913 nH       | 984 nH       | 4 | 5 mm | 1.5 mm | 35 mm     |
| Coil 12 | 921 nH       | 975 nH       | 3 | 8 mm | 1.5 mm | 48 mm     |

Figure 2.9: A comparison of the self inductances of volumetrically efficient coils.

| Coil    | Analytical | Filament length |
|---------|------------|-----------------|
| Coil 1  | 0.9237 m   | 0.9237 m        |
| Coil 2  | 0.9143 m   | 0.9143 m        |
| Coil 3  | 0.8425 m   | 0.8425 m        |
| Coil 4  | 0.8771 m   | 0.8771 m        |
| Coil 5  | 0.8609 m   | 0.8608 m        |
| Coil 6  | 0.7730 m   | 0.7730 m        |
| Coil 7  | 0.4418 m   | 0.4417 m        |
| Coil 8  | 0.5666 m   | 0.5666 m        |
| Coil 9  | 0.8924 m   | 0.8923 m        |
| Coil 10 | 0.8600 m   | 0.8600 m        |
| Coil 11 | 0.7007 m   | 0.7007 m        |
| Coil 12 | 0.7579 m   | 0.7578 m        |

Figure 2.10: Analytically solved lengths of coils compared with summing the total length of filaments that make up the filamentary models.

for the model of Coil 11. The distinguishing features of this coil are that it has the greatest number of turns and therefore the greatest rate of procession about its central axis and also it has a small radius, again introducing sharper angles. This would suggest that the results would converge if the number of filaments making up the paths were increased; however this was found not to change the result.

As in all cases, measurement and modelling reports a greater inductance than CST, an alternative explanation could be that the CST simulations are under reporting inductance, this could be due to the limited calculation domain effectively truncating flux paths (the open boundaries are set to 100 mm from the coils). Regardless of small discrepancies the inductance model has been shown to be a competent predictor of all three coil types self inductance with sufficient accuracy to be used as part of an optimisation procedure.

The length of the coils produced by summing the length of all centre path filaments is compared to the analytical length of the coils obtained from the coil equations (Table. 2.10). The lengths are identical for all coil types, showing that the filament paths are traced correctly.

For mutual inductance calculations the coils are moved coaxially apart and compared with CST simulations with air gaps of 0.01 m to 1 m (z axis displacement) (Figs. 2.12, 2.13, 2.14). A further displacement test (Fig. 2.15) is conducted whereby the helical reference coil 4 is displaced in the x direction while an air gap of 48 mm is maintained between the two coils. The final test is a rotation test (Fig. 2.16) whereby coil 4 is positioned coaxially with another coil 4, a centre to centre distance of 84 mm is maintained while one of the coils is rotated about its x axis (48 mm air gap at 0°) (Fig. 2.11).

The mutual inductance sweeps with respect to distance (Figs. 2.12, 2.13, 2.14) generally have excellent correspondence between the CST simulations and the filamentary model. However in certain cases such as coils 3, 4, 7 and 8 the results differ at distances greater than 0.1 m. These coils have smaller outer radii than others which makes them have the least mutual inductance. The CST simulations for these coils have a decrease in gradient beyond 0.1 m whereas all the other coils have a constant gradient in this region as would be expected from loop approximations to the mutual inductance (equation 2.4) in a log log plot. The decreasing gradient implies that the coils are also capacitively coupled in the full wave simulation, as capacitance between two objects decreases at a lower rate with distance compared to inductive it becomes more apparent at greater distances. Examining the afflicted coils they have greater spacing between the start and end of coils allowing a greater electric field to be developed. The VECs winding pattern cancels

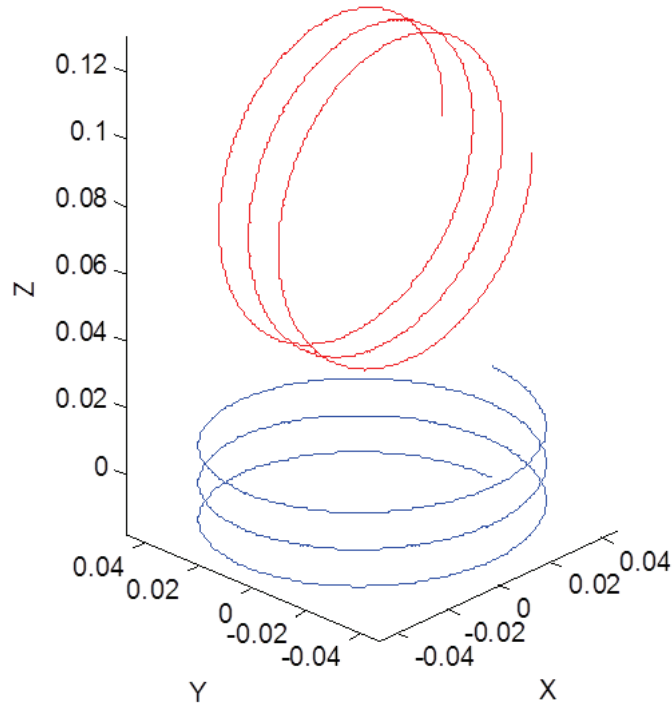


Figure 2.11: Diagram showing coil 4 at centre to centre distance of 84 mm with  $90^\circ$  of rotation about the x axis.

the electric field and therefore they do not show the capacitive effects.

The rotation and displacement tests (Figs. 2.16, 2.15) conducted at one coil radius distance show excellent correspondence between the model and FE simulation. These types of test are useful for establishing the operating parameters of the IPT system (maximum displacement, rotation and distances). To establish these parameters entirely through FE analysis would be extremely time consuming as they are not simple fixed values; for example if the displacement is increased the maximum rotation will be decreased.

In conclusion the inductance calculation method has been verified and shown to produce accurate results for a wide variety of winding patterns in both calculation of the mutual and self inductances of coils. When coils are moved beyond the distances typically employed in efficient inductive power transfer (usually up to a coil diameter [38]) the apparent mutual inductance can increase due to capacitive effects. Capacitive effects are not modelled but are generally unimportant during normal operating of IPT systems. As at the air gaps capacitive effects become important to modelling the mutual inductance the link would be inefficient.

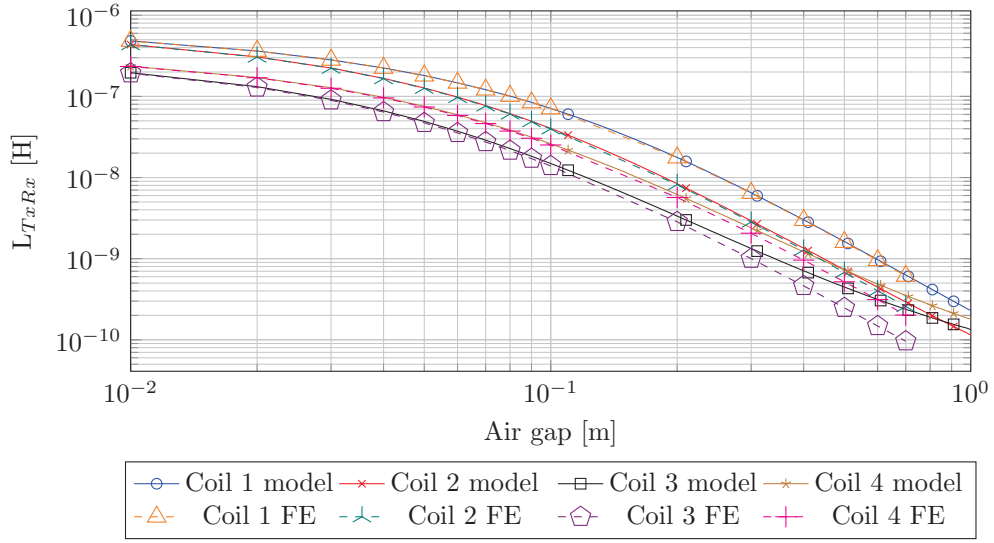


Figure 2.12: Helical coil (Table 2.7) to helical coil mutual inductance with respect to air gap between the coils.

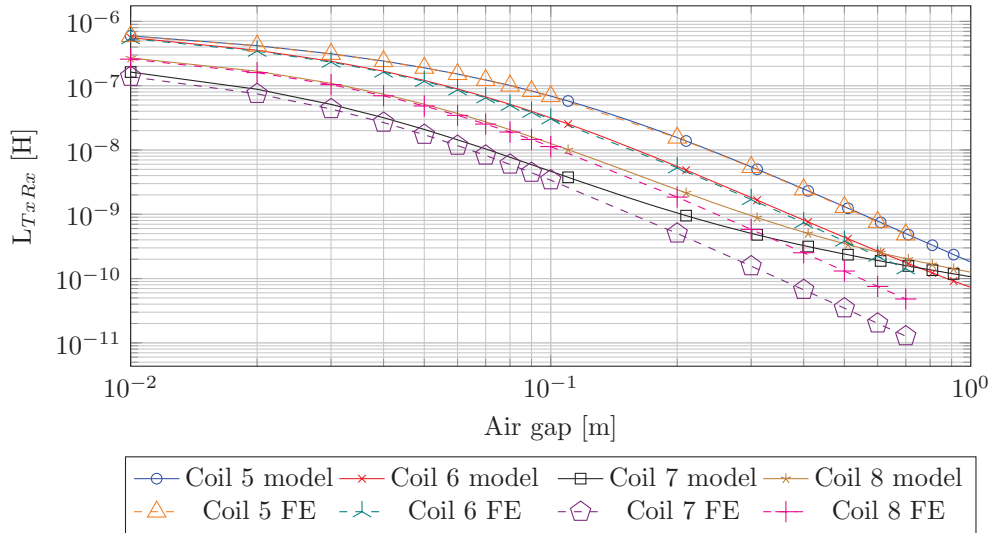


Figure 2.13: PSC (Table 2.8) to PSC mutual inductance with respect to air gap between the coils.

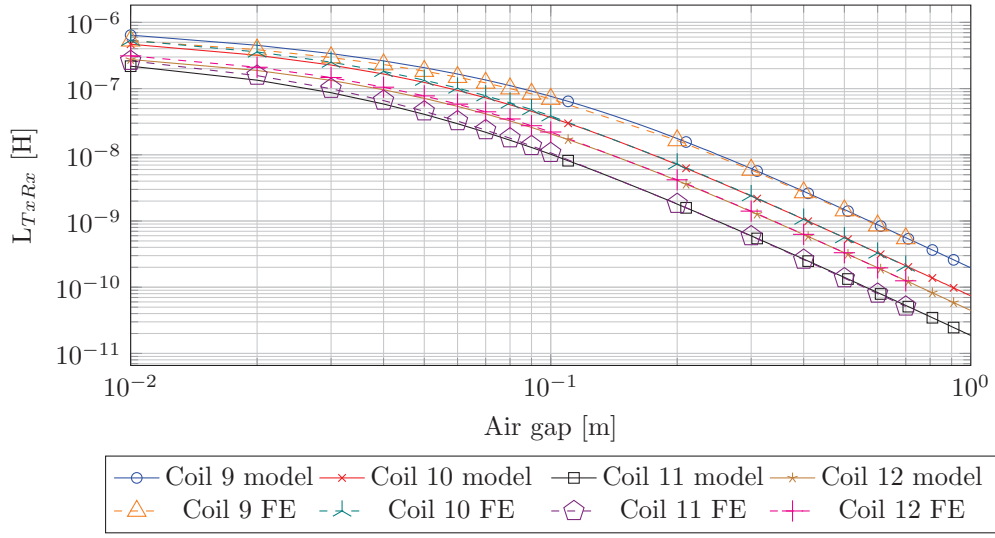


Figure 2.14: VEC (Table 2.9) to VEC mutual inductance with respect to air gap between the coils.

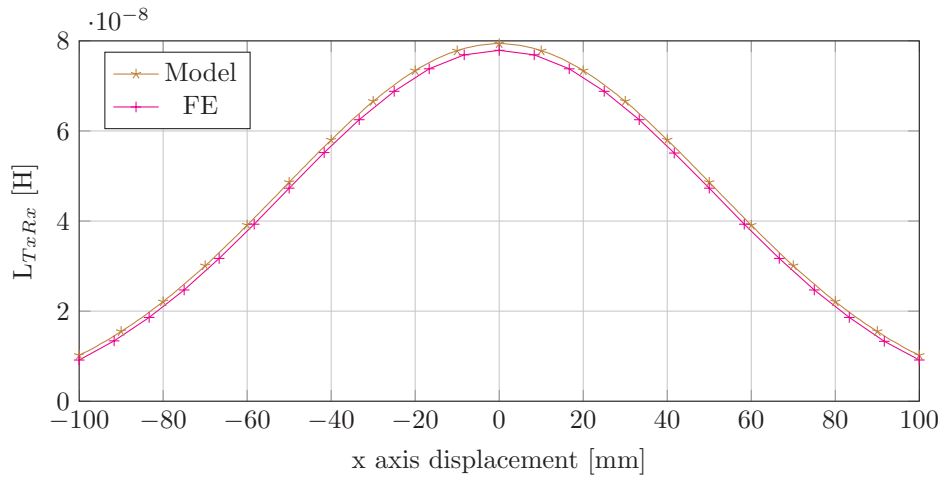


Figure 2.15: Mutual inductance between two coil 4 (Table 2.7) with respect to x axis displacement a fixed 48 mm air gap.

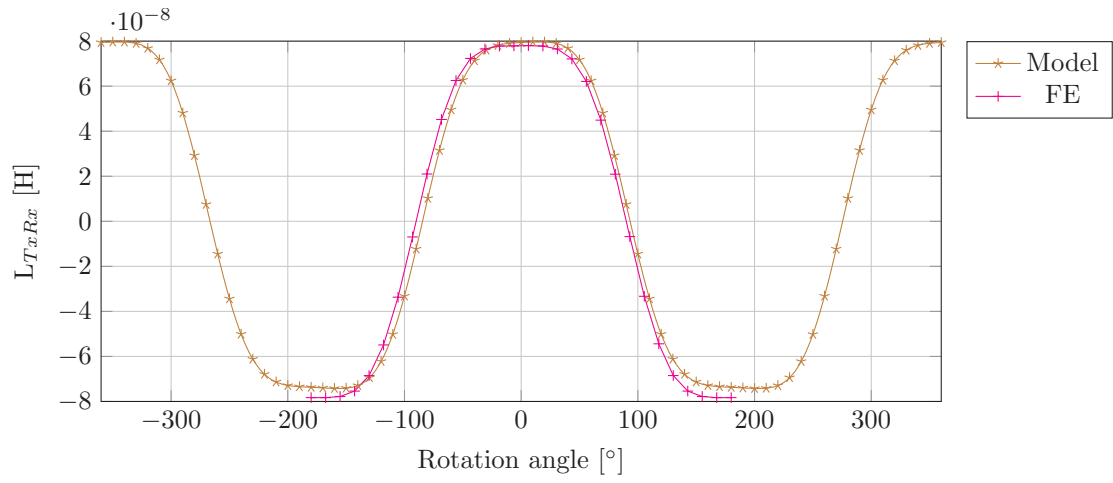


Figure 2.16: Mutual inductance between two coil 4 (Table 2.7) with respect to rotation about the x axis of one of the coils at a fixed 84mm centre to centre distance. This distance is the same as the 48mm air gap at 0° and multiples of 180° rotation in figure 2.15. As only one coil is rotated about its centre and the coils are three dimensional the air gap between the coils is less for other angles, an example of this is shown in figure 2.11. Where the inductance is recorded as negative this is because the polarity of the induced voltage on the rotated coil has reversed.

## 2.4.2 Resistance

### Single tube

As it has no proximity effect the most basic aspect of the resistance model to verify is that of the AC resistance of an isolated copper tube. Simulated tubes of varying wall thickness are compared with the resistance model. The results are normalised to the resistance of a tube of  $5\delta$  at which point the resistance of the tube is considered to converge to the electrically thick case. The internal inductance of the tubes is measured by the same model and therefore this model is also tested here, although it is not used to state the coil's inductances. As internal inductance is not isolated from external inductance in the finite element simulation the equation for the external inductance of a length,  $l$ , of a partial wire [20] is used to subtract external inductance,  $L_{ext}$ , from the finite element total inductance:

$$L_{ext} = \frac{\mu_0}{2\pi} l \left[ \sinh^{-1} \frac{l}{a} - \sqrt{1 + \left(\frac{a}{l}\right)^2} + \frac{a}{l} \right], \quad (2.86)$$

where,  $l$ , is the length of the tube. This equation is valid in the case of the isolated tube as the centre of current of the tube is the same as the wire case.

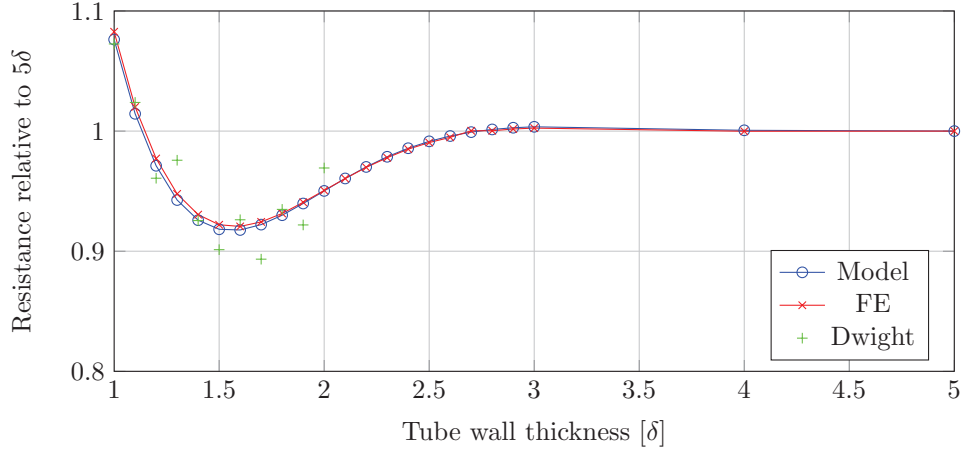


Figure 2.17: Model of skin effect resistance of tubes compared with finite element simulations (FE) conducted in Fast Henry and data from Dwight.

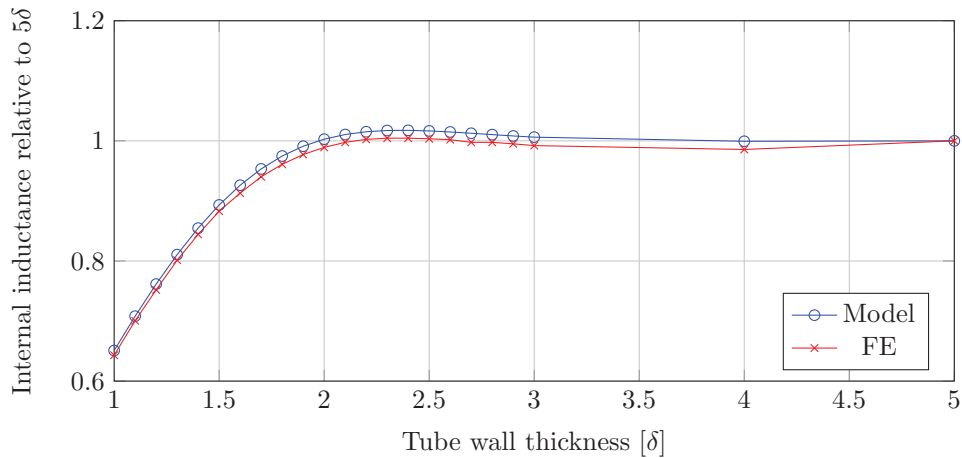


Figure 2.18: Model of internal inductance of tubes compared with finite element simulations (FE) conducted in Fast Henry.



Good correspondence between the resistance model and simulation is observed for both the resistance and internal inductance (Fig. 2.17 and Fig. 2.18), The modelled impedance of  $5\delta$  thickness tube was  $0.208 + j0.199$  and the finite element impedance was  $0.209 + j0.202$  (without external inductances). Of particular note is the optimal wall thickness of  $1.58\delta$ ; this depth offers a lower loss resistance than thicker walls because of the exclusion of the negative current region that is present in thicker tubes [15]. This effect is observable by processing of Dwights original figures [32] [39] some values from which have also been plotted (but are noisy due to Dwights graphs having differing format) and has also noted by Lee and Lorenz [40]. As such if good control over plating depth is available in an application where the coil is formed by plating onto an electrical insulator the depth of this plate should be  $1.58\delta$  for the lowest coil AC resistance at the operating frequency, however if good control is not available the plate should be electrically thick.

## Loops

The resistance model for isolated tubes with differing depths of copper has been verified, however in a real coil the tube is bent into a loop. Due to the differing electromagnetic conditions on the inside and outside edges of the loop as the bend radius decreases relative to the radius of the conductor tube the current in the tube cross section will become increasingly non uniform. The effect of this is that with large conductor radius,  $a$ , and small outer radius,  $r_{Max}$ , the reported resistance may be inaccurate. To this end a loop was simulated in Fast Henry and compared with the same length of tube in the resistance model to find the point the results deviate significantly due to curvature.

The tubes tube outer radius,  $a = 400\mu\text{m}$ , with  $1.58\delta$  wall thickness, the loop is composed of 360 straight line tubes meshed with 5 filaments per skin depth. It is worth noting that the total number of filaments in these simulations are such that almost the full memory of a 128 GB RAM workstation was utilised and as such these simulations represent the limit of the simulation approach that is allowing us to accurately simulate structures between electrically thin and thick. The optimal conductor has a largely uniform current distribution, therefore when curvature occurs the deviation from the equivalent straight conductor resistance should be the greatest. Loop outer radius,  $r_{Max}$  varies between 1.2 mm to 1.2 m.

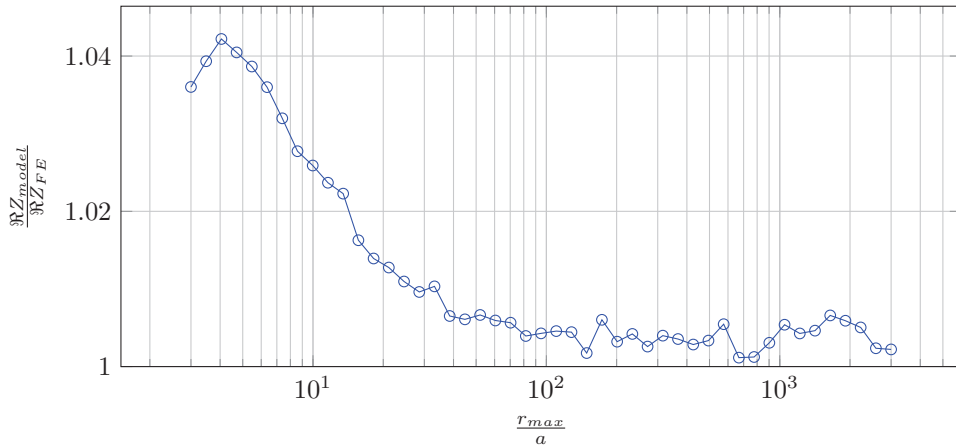


Figure 2.19: Loop radius to conductor radius ratio model and simulation comparison for AC resistance.

Figure 2.19 shows the modelled resistance is within 5% of the FE simulation for all tested  $r_{Max}$  and within 1% for  $r_{Max} > 11.414\text{mm}$  corresponding to a  $\frac{r_{Max}}{a} > 28.535$ . If typical coil geometries are considered (Table. 2.7) the smallest sensible ratio was  $\frac{r_{Max}}{a} = 50$  at smaller  $r_{Max}$  the tube becomes difficult to bend. Therefore it can be expected that the error in resistance calculations caused by the coils curvature will be smaller than 1% for all practically constructable coils.

### Proximity effect between two tubes

With the skin effect resistance model and curvature approximation verified the next stage in development of the resistance model is to find the limitations of the proximity effect model. To this end two tubes ( $400\text{ }\mu\text{m}$  outer radius,  $3.70\text{ MHz}$  test frequency,  $5.8 \times 10^7\text{ S m}^{-1}$  conductivity,  $34.3\text{ }\mu\text{m}$  skin depth ( $\delta$ )) have their resistance modelled and also simulated in Fast Henry (Fig. 2.20). The ratio between the the tubes outer radius,  $a$ , and the space between the tubes,  $s$ , is swept by varying the distance between the tubes from  $1\text{ }\mu\text{m}$  to  $10\text{ mm}$ . By defining the proximity factor as the ratio between the resistance of the tubes including the proximity effect and the resistance of the tubes only including the skin effect, the results are normalised such that they are applicable to all tubes with large outer radius in comparison with skin depth (all IPT coils of good performance). Several skin depths,  $\delta$ , are tested to show the effect of current modulation in the radial direction of the tube. For the simulations the filament tubes used for the skin effect simulations are copied to make two tubes spaced apart by  $s$ , the resistance of the two tubes in parallel is then simulated and the resulted divided by two to obtain the single tube resistance.

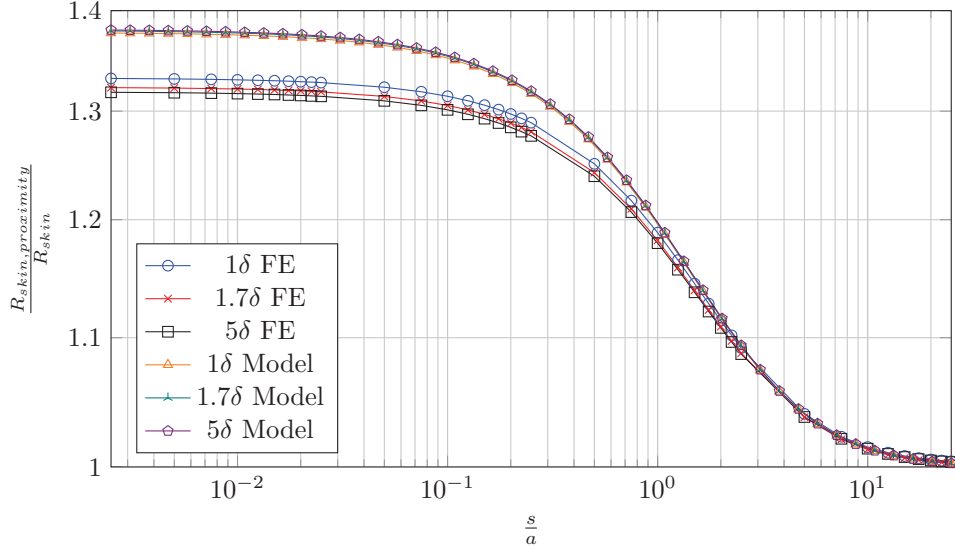


Figure 2.20: Dimensionless proximity factor modelling comparison with finite element simulation.

The results (Fig. 2.20) show a maximum discrepancy between the model and simulation of 0.0619, for  $5\delta$ . Therefore at a worst case for this two tube scenario it would expected the resistance to be over reported by 6.2% by the proximity effect model. However IPT coils are unlikely to have their turns this close together as it results in poor coil quality factor, with more realistic  $\frac{s}{a} > 1$  the proximity factors of simulation and the model are well aligned. The discrepancy when the tubes are closer together is likely caused by two features of the algorithm; firstly the current flowing in the turn is assumed to be at the surface of the tube and secondly there is no iteration to the filament positioning. This results in the centre of current of the tube differing from reality when the tubes are very close. In the FE simulations the proximity factor of electrically thicker tubes is less than electrically thinner tubes, this is likely due to the current been forced to a deeper depth in the tube when the tubes are very close, a phenomenon which cannot occur for thinner tubes. This effect is not modelled in the proximity factor model and therefore all skin depths have the same proximity factor.

### Coils

The CST simulations of coils 1 to 12 (Table. 2.7, 2.8, 2.9) are compared to the results given by the proximity effect model with and without adding radiation losses (Figs. 2.21 - 2.32). Coils 1 to 4 have

also been measured to have properties close to their CST simulations in the real world, therefore it can be assumed that the simulations are accurate (see Measurement chapter).

The results are interesting, all but coil 7 have excellent match to simulation at 1 MHz with the results showing less resistance than simulation beyond 10 MHz. Coil 7 may be anomalous because the very inmost turn is of very small radius and therefore the loop approximation breaks down, it is not optimal to design PSCs in this manner and would be impossible to bend copper tube so sharply so is unlikely to be an issue in actual usage. A more significant issue is that the model is considerably underestimating the resistance of the coils above approximately 10 MHz. If coils 1 - 4 are examined (coils that have actually been constructed) the model deviates at 20 MHz by: -38%, -33%, -18% and -17% respectively. Therefore the coils with the greater filament length (Table. 2.10) generally have the greater deviation from simulation, suggesting radiation losses. However the radiation model, as crude as it is indicates the coils are not radiating appreciably. As skin effect dominated losses are proportional to,  $f^{0.5}$ , and radiation dominated losses,  $f^4$ , by plotting the finite element resistance results of the coils 1 to 4 (Fig. 2.33) on a log scale it is possible to comment on the likely cause of losses. It is observed that the gradient, especially in coils 1 and 2, is increasing from the expected 0.5 at high frequencies. This is consistent with radiation losses becoming significant at lower than expected frequency. Coils 1 and 2 are the helical coils with the greatest deviation between modelled and simulated resistances at high frequencies and also the least turn spacing and greatest outer radii. This would suggest they may be the most effective radiators and this is where the deficiencies lie in the resistance model. Regardless the model is predictive at 6.78 MHz and 13.56 MHz and useful for rapid design.

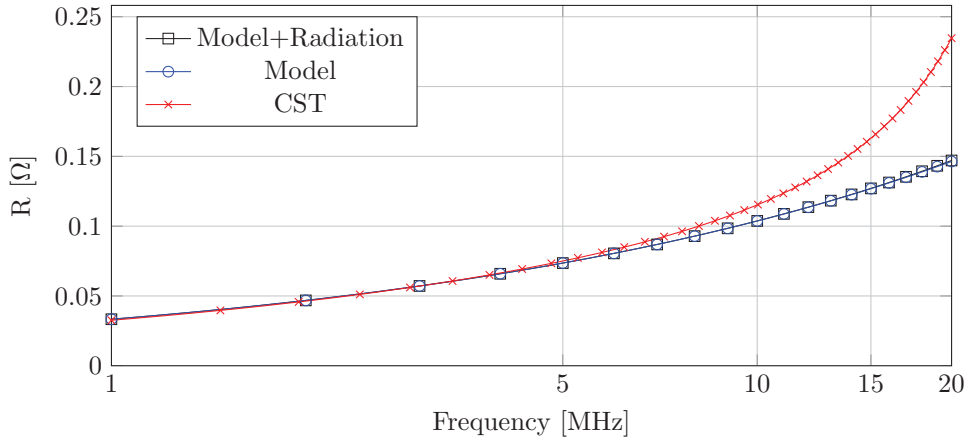


Figure 2.21: CST simulation of coil 1 (Table 2.7) of coils resistance when fit to LCR coil model compared with tube resistance model.

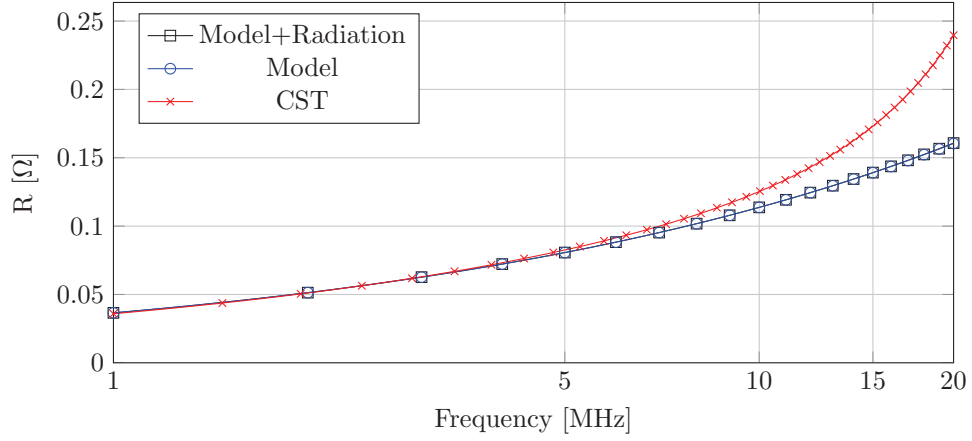


Figure 2.22: CST simulation of coil 2 (Table 2.7) of coils resistance when fit to LCR coil model compared with tube resistance model.

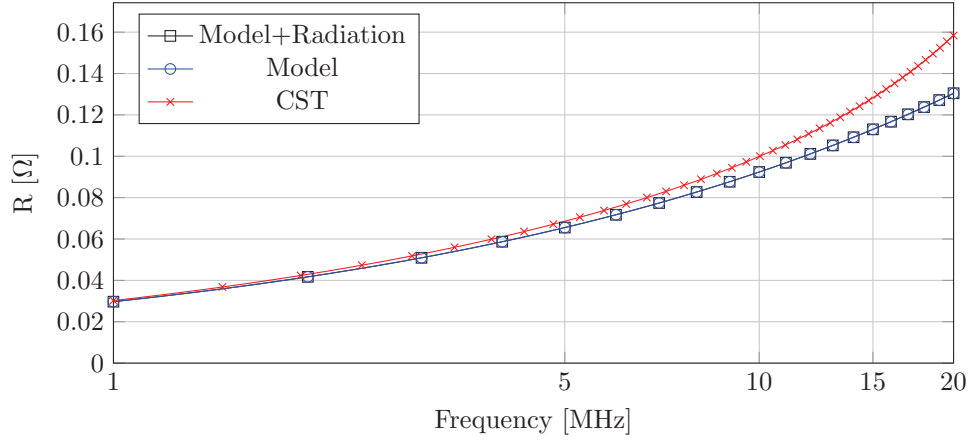


Figure 2.23: CST simulation of coil 3 (Table 2.7) of coils resistance when fit to LCR coil model compared with tube resistance model.

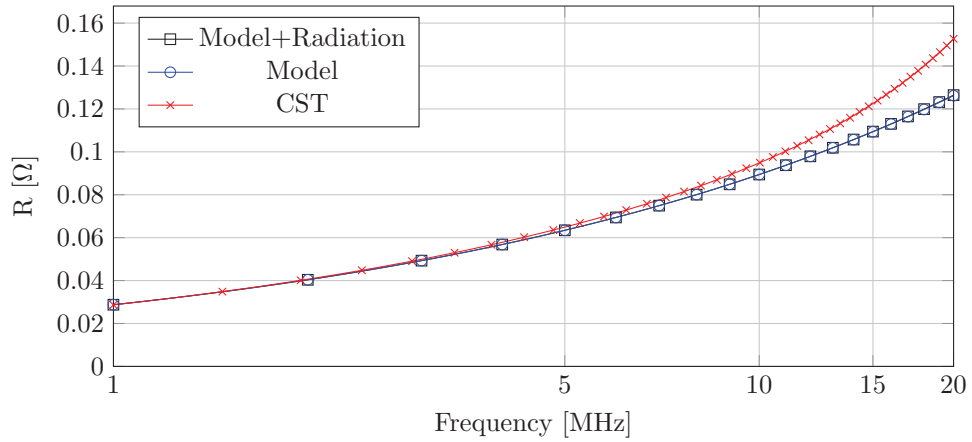


Figure 2.24: CST simulation of coil 4 (Table 2.7) of coils resistance when fit to LCR coil model compared with tube resistance model.

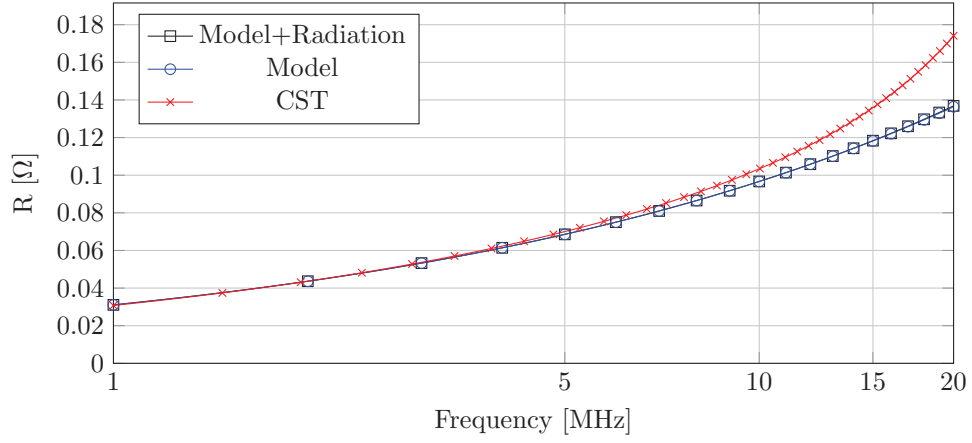


Figure 2.25: CST simulation of coil 5 (Table 2.8) of coils resistance when fit to LCR coil model compared with tube resistance model.

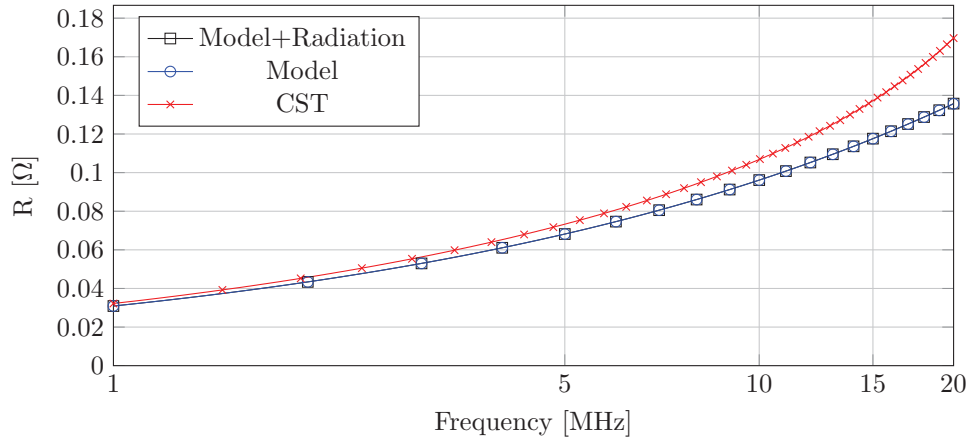


Figure 2.26: CST simulation of coil 6 (Table 2.8) of coils resistance when fit to LCR coil model compared with tube resistance model.

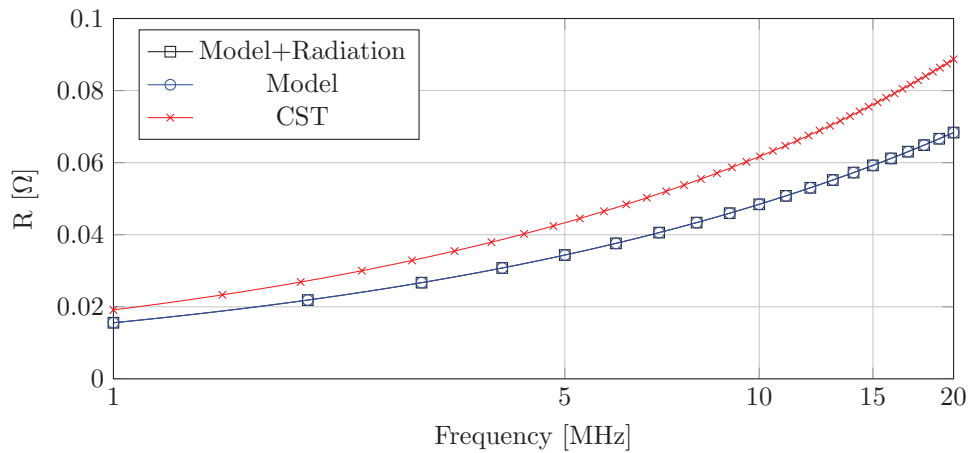


Figure 2.27: CST simulation of coil 7 (Table 2.8) of coils resistance when fit to LCR coil model compared with tube resistance model.

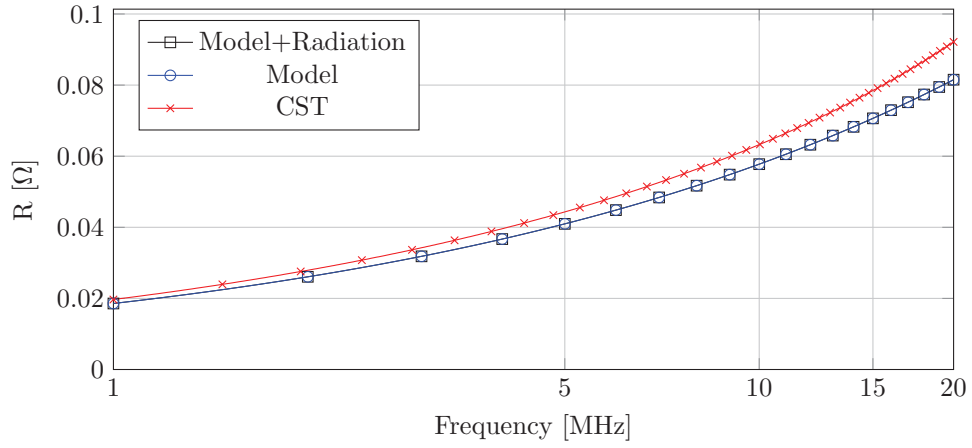


Figure 2.28: CST simulation of coil 8 (Table 2.8) of coils resistance when fit to LCR coil model compared with tube resistance model.

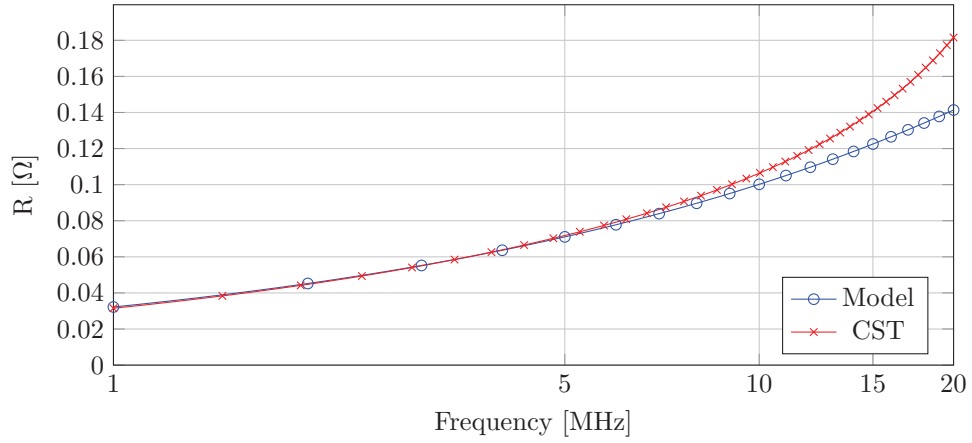


Figure 2.29: CST simulation of coil 9 (Table 2.9) of coils resistance when fit to LCR coil model compared with tube resistance model.

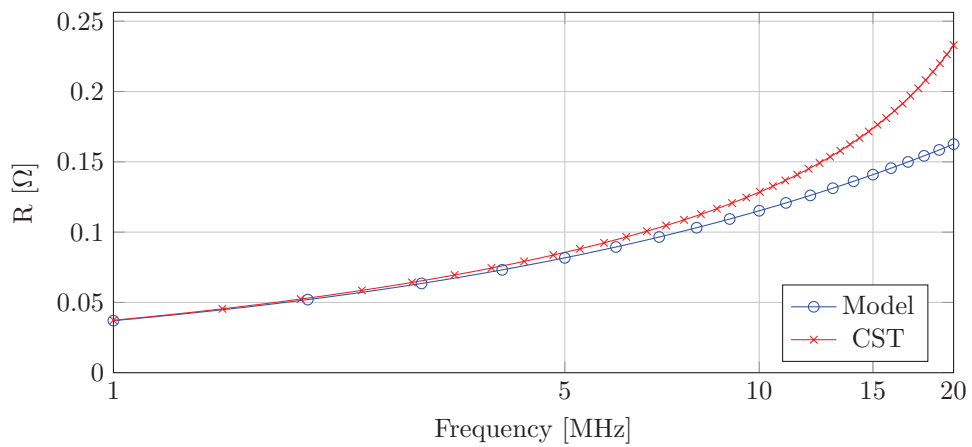


Figure 2.30: CST simulation of coil 10 (Table 2.9) of coils resistance when fit to LCR coil model compared with tube resistance model.

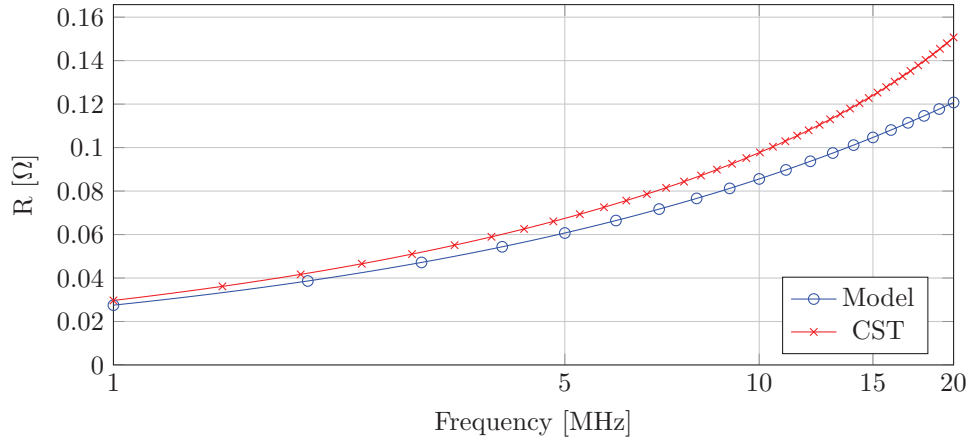


Figure 2.31: CST simulation of coil 11 (Table 2.9) of coils resistance when fit to LCR coil model compared with tube resistance model.

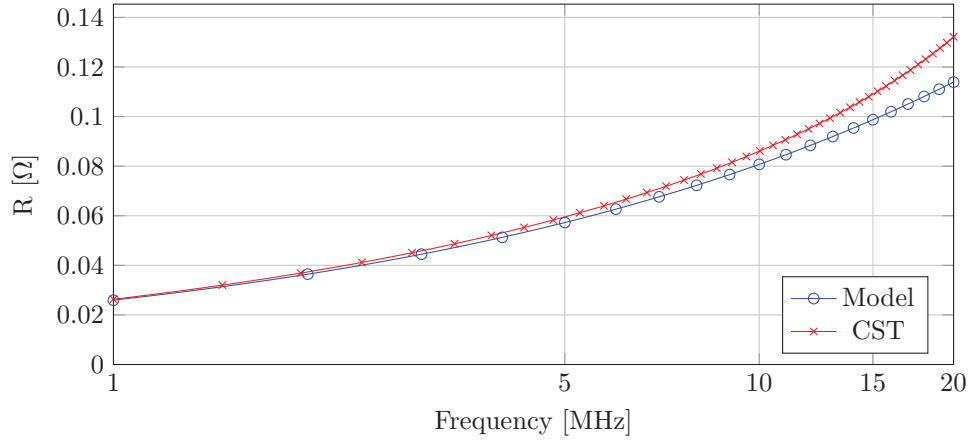


Figure 2.32: CST simulation of coil 12 (Table 2.9) of coils resistance when fit to LCR coil model compared with tube resistance model.

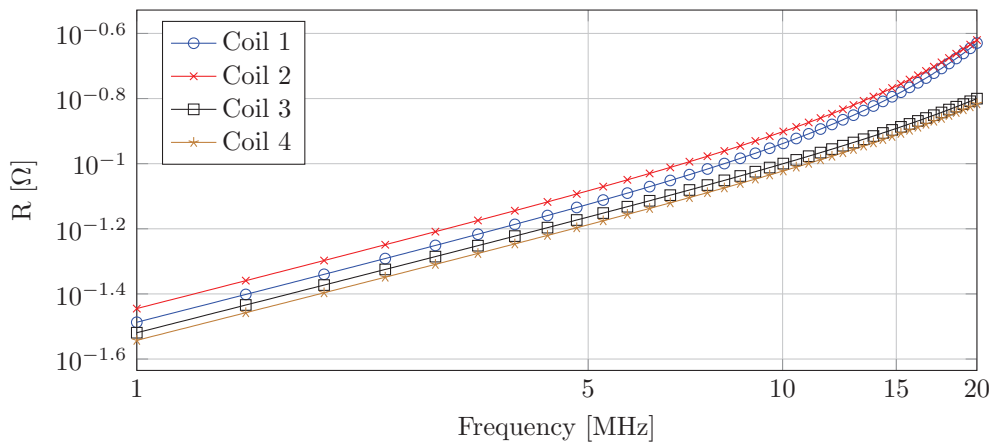


Figure 2.33: CST simulations of coils 1- 4 (Table 2.7) showing that losses beyond 10 MHz begin to be affected by other factors than the skin effect

### 2.4.3 Optimal tube geometry

The two tube simulations conducted for verification of the proximity effect model have been utilised to provide insight into IPT coil design for maximising  $Q$ . As these simulations are only of magnetic effects the  $Q$  for this structure can be defined as:

$$Q_t = \frac{\Im Z_{11}}{\Re Z_{11}}. \quad (2.87)$$

As such for a given space between turns,  $s$ , to turn radius,  $a$ , there is an optimal spacing between turns to maximise  $Q$ . The fractional  $Q$  factor relative to the peak  $Q$  factor has been plotted for the simulated fractional turn spacings for the differing simulated tube thickness, such that the results are relevant for all coils (Fig. 2.34).

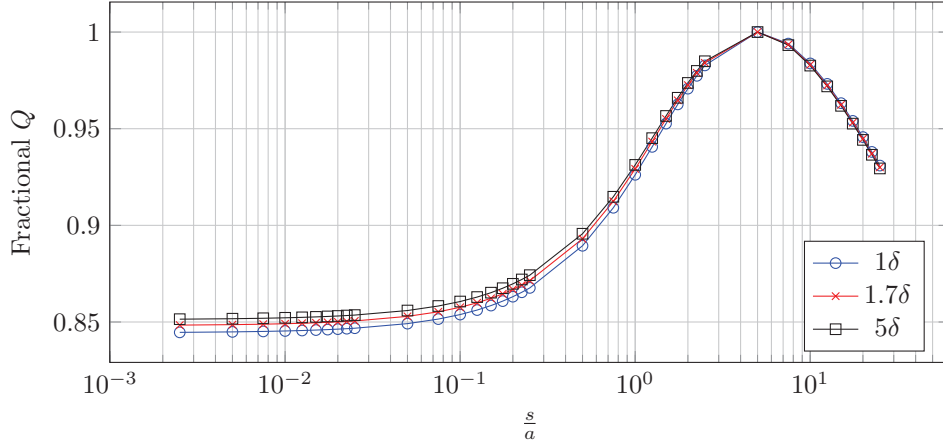


Figure 2.34: FE simulations showing the spacing of tubes for optimal  $Q$ .

The optimal turn spacing for maximal  $Q$  is found to be in all cases  $\frac{s}{a} = 5$ , however at very close spacings the  $Q$  has only decreased to 85% of the maximum value. In most applications the coil has to fit into a defined space and as such any space taken up by air gaps in the winding pattern is reducing the potential space that could be used by conductor. In the simplest case if the turn count is kept constant the tube radius could be increased up to almost  $2.5\times$  to fill the turn spacing. When this is modelled the resistance of the tubes falls to 0.3912 of the optimally spaced value with the smaller tubes, corresponding to an increase in  $Q$  of  $2.5560\times$ . Therefore the optimal spacing for real coils often will be the minimum gap between turns that is manufacturable and avoids arching (due to the large potentials that can exist on IPT coils operated resonantly). Factors that could cause the optimal spacing to deviate from this would be in scenarios where the conductor radius becomes so great that the average turn radius of the coil is greatly reduced. This reduction in the average turn radius would effect the mutual inductance between the coils and could lead to an overall reduction in link efficiency.

### 2.4.4 Magnetic field modelling

To demonstrate the magnetic field plotting method a path to plot the  $\mathbf{B}$  field along is defined (Fig. 2.35) through the centre of coil 4, aligned with the  $z$  axis. Coil 4 has been selected as it has the greatest pitch of the modelled coils and therefore is most sensitive to vector calculation errors. The path extends 100 mm above and below the coil with the centre of the path located at the mid height of the coil. The  $z$  component magnitude of the  $\mathbf{B}$  field has been plot for both CST and the magnetic field model with 1 A of current flowing in the coils (Fig. 2.36), the  $x$  and  $y$  components have not been plot as they are negligible along this



path. The results show almost perfect correspondence, the main difference between the two methods is that the model only took a second to run whereas generating the same result from FE simulation took an hour.

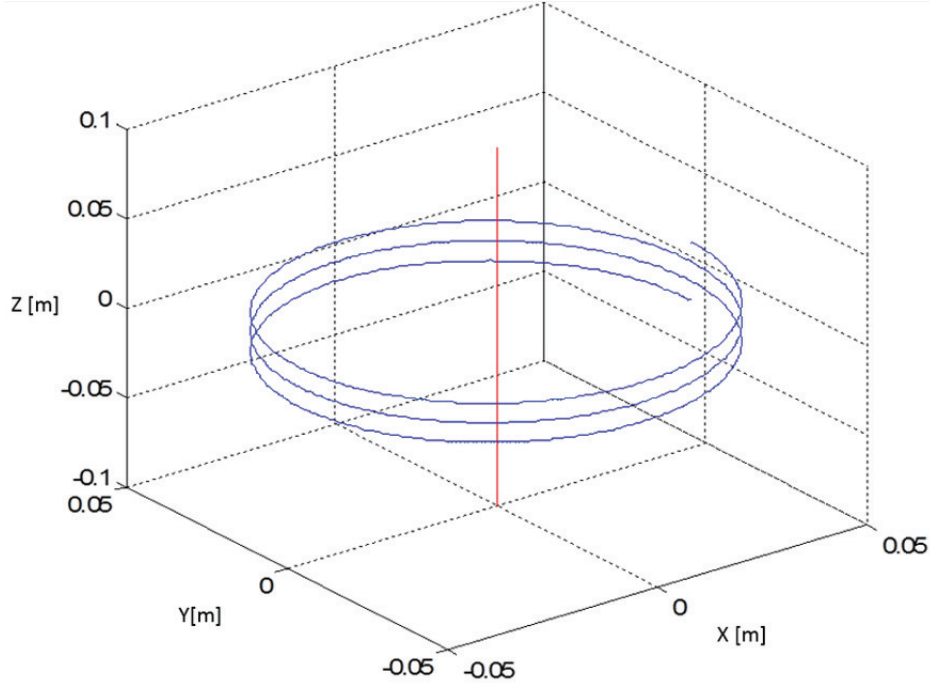


Figure 2.35: Coil 4 (blue) with path the  $\mathbf{B}$  field is plotted along (red) when the coil is excited with 1 A.

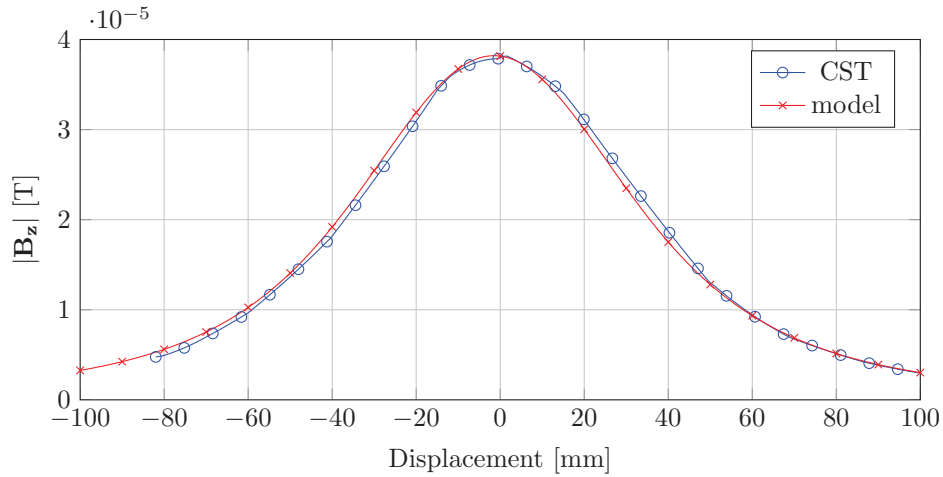


Figure 2.36: Magnetic field along the path shown in figure 2.35.

#### 2.4.5 Full IPT system example

In this section the procedure for modelling an efficiency optimised full IPT system is shown and compared with a CST simulation of the same system. Firstly the design parameters of the system are stated:

- Output power: 100 W
- Operating frequency: 6.78 MHz
- Material conductivity:  $5.8 \times 10^7 \text{ S m}^{-1}$

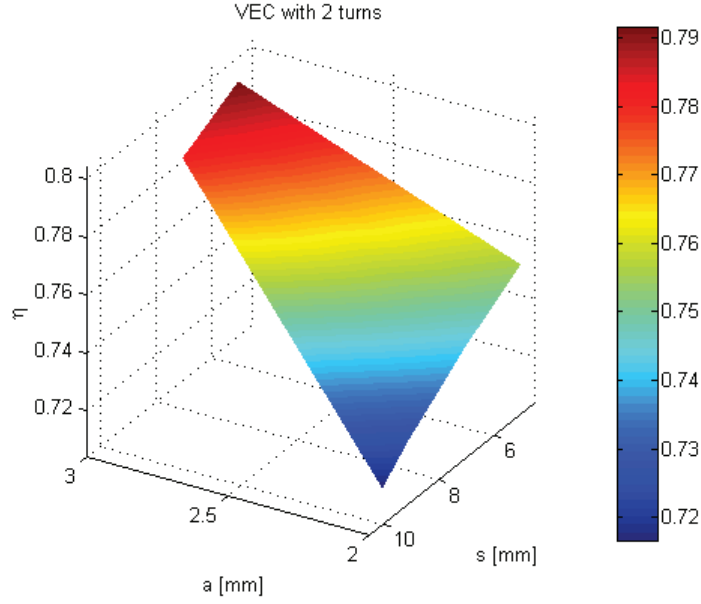


Figure 2.37: Optimisation sweep of two turn VEC showing for this particular parameter sweep that minimal turn spacing and maximum turn radius is desirable.

- Distance between coils,  $D$ : 150 mm
- $r_{Max}$ : 50 mm
- $H_{Max}$ : 25 mm
- Tube outer radius,  $a$ : 2 mm to 20 mm
- Tube spacing,  $s$ : 5 mm to 10 mm
- $N \leq 5$

The optimal VEC is designed within these parameters with the goal of maximising the fractional link efficiency,  $\eta$ , by modelling the magnetic link efficiency of all possible VECs that fit within the design parameters. The optimisation of the two turn case has been illustrated to demonstrate the procedure as this number of turns has the greatest number of possible coils in the parameter space (Fig. 2.37). The optimal coil was found to have the following parameters:

- $N$ : 4
- $s$ : 5 mm
- $a$ : 2 mm
- Height = 16.7 mm
- Model:  $\eta = 0.81$  (found using link efficiency equation acting on modelled parameters), CST:  $\eta = 0.79$  (found via the method of Zargham and Gulak [6])
- Model:  $Q = 920$ , CST:  $Q = 752$
- Model:  $L_{TxRx} = 1.7641 \times 10^{-8}$  H, CST:  $L_{TxRx} = 1.6867 \times 10^{-8}$  H
- Model:  $L = 1.6603 \times 10^{-6}$  H, CST:  $L = 1.5448 \times 10^{-6}$  H

- Model:  $R = 0.076853\ \Omega$ , CST:  $R = 0.08769\ \Omega$
- Model optimal series load:  $(0.7554 - 70.7i)\ \Omega$ , CST: optimal series load  $(0.738 - 66.4i)\ \Omega$  (found via the method of Zargham and Gulak [6], includes effect of 16.2 pF of coil intrinsic parallel capacitance)

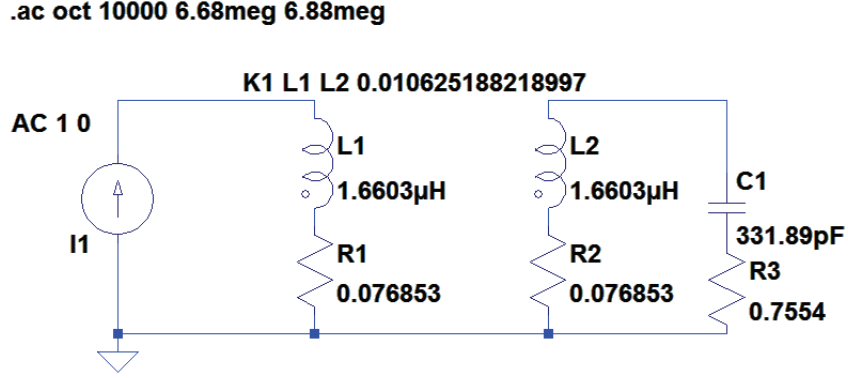


Figure 2.38: Equivalent circuit of optimal VEC magnetic link used to determine secondary current.

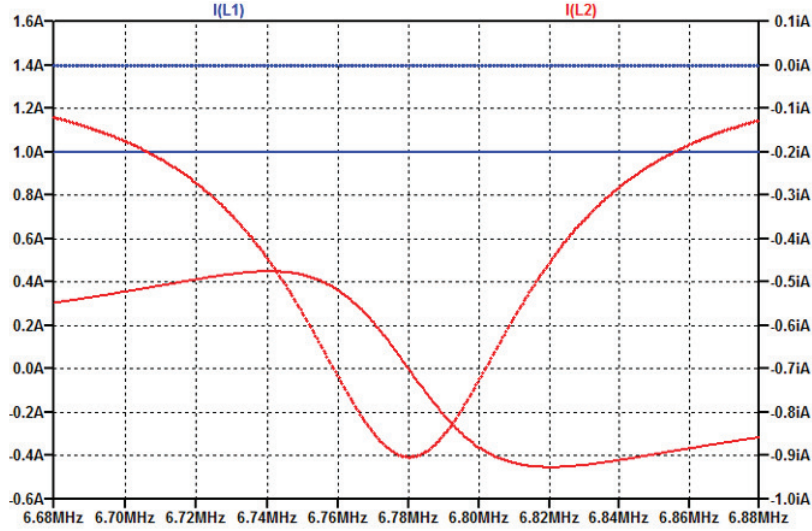


Figure 2.39: Complex Tx and Rx coil current for optimal VEC magnetic link with optimal load.

The link efficiency for the optimal coil is considerably greater than the least efficient coil in the design space which only has  $\eta = 0.72$ . The main deviation between the modelled and full wave simulated system is that the coils effective parallel capacitance is not modelled and changes the required tuning capacitance to operate at resonance, because of this the CST optimal load is used in the CST simulations and the modelled optimal load in further modelling work, if this were not done the resonant frequencies would deviate from 6.78 MHz. Circuit simulations are conducted using the modelled parameters to find the secondary coil current phase and magnitude (with the optimal load connected) relative to that of the primary coil (Figs. 2.38, 2.39). The results of these simulations and of analysis of the currents and voltages of the CST link simulation with the CST optimal load are presented:

- Model secondary current with  $(1 + 0i)$  A primary current at 6.78 MHz:  $(-2.093 + 903.0i)$  mA, CST: not required
- Model primary current to obtain 100 W into optimal secondary load at 6.78 MHz: 12.78 A RMS, CST: 14.07 A RMS

- Model secondary current for 100 W at 6.78 MHz:  $(-0.0268 + 11.5439i)$  A, CST: not required
- Model input impedance at 6.78 MHz:  $(0.7554 + 70.73i) \Omega$ , CST:  $(0.6394 + 66.42i) \Omega$
- Model input voltage for 100 W at 6.78 MHz: 904 V RMS, CST: 935 V RMS

The high input voltage at even a modest power level is a characteristic of high  $Q$  inductive power transfer systems, it was in anticipation of this that the minimum turn spacing was set to 5 mm as to afford sufficient depth of insulation between turns. To provide this large input voltage the transmitter coil is usually matched to its amplifier by using a resonant capacitor. As the primary coil without this resonant capacitor is an inductive load and thus there is a large phase angle between voltage and current the real power delivered at the operating voltage and current is not in excess of that projected by the efficiency.

The final stage in modelling the system is to find the magnetic field while the system is in operation, for systems of this power level this is required to define exclusion zones. To this end a cut plane is defined (Fig. 2.40) at  $x = 0$  such that the plane cuts through the centre of the coils and encompassing the whole CST simulation domain in  $z$  and  $y$  extent. The quantity plot with 10 mm sampling is the vector field magnitude in decibels defined as:

$$\mathbf{B} = \mathbf{B}_{Tx} + \mathbf{B}_{Rx}, \quad (2.88)$$

$$|B_x| = \sqrt{(\Re B_x)^2 + (\Im B_x)^2}, \quad (2.89)$$

$$|B_y| = \sqrt{(\Re B_y)^2 + (\Im B_y)^2}, \quad (2.90)$$

$$|B_z| = \sqrt{(\Re B_z)^2 + (\Im B_z)^2}, \quad (2.91)$$

$$dB|\mathbf{B}| = 10 \log_{10} \left( \sqrt{|B_x|^2 + |B_y|^2 + |B_z|^2} \right). \quad (2.92)$$

In the figures 2.42 and 2.41 the coils centres are  $(0, 0, 0)$  for the transmitter and  $(0, 0, 181 \text{ mm})$  for the receiver, it can be observed that the field is weaker around the receiver coil in comparison to the transmitter due to the lower current magnitude. As the current in the receiver is approximately  $90^\circ$  out of phase with the transmitter so is the  $\mathbf{B}$  field generated by it. The correspondence between the simulation and the model is excellent, the most readily observably deviation is that the CST simulation has slightly jagged contours. The jaggedness is probably caused by the slight disturbance in coil geometry caused by the need to couple a signal from a port into the coils.

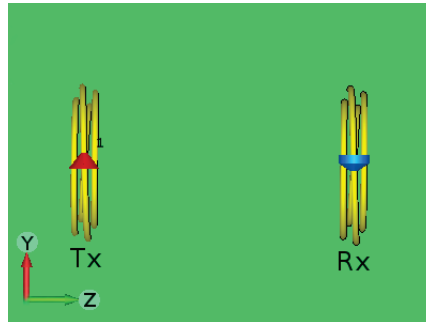


Figure 2.40:  $x = 0$  cut plane from which the field plots are generated, the air gap between the two coils is 150 mm, this is three times the coils radii.

To conclude in this example the total magnetic behaviour of an IPT system has been modelled and optimised using the methods presented in this chapter and the results compared with full wave simulation. The results have been found to be in good agreement with simulation throughout this process, cumulating in accurate calculation of the vector magnetic field of the system while it operates.

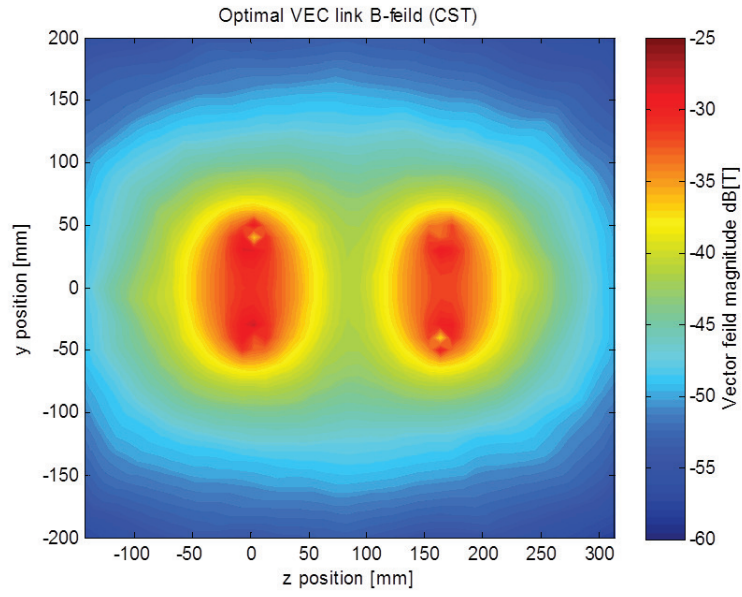


Figure 2.41: Magnetic field strength extracted from CST simulation  $x = 0$  cut plane for optimal VEC system operating into optimal load.

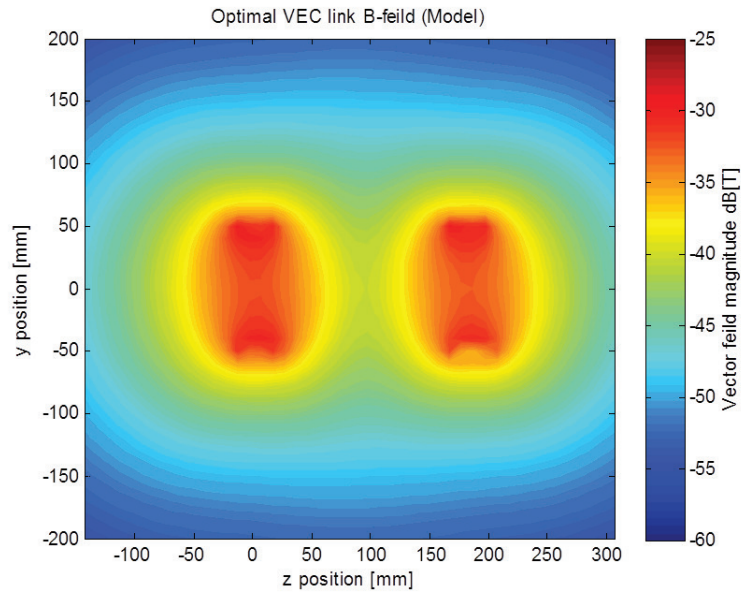


Figure 2.42: Magnetic field strength generated by model  $x = 0$  cut plane for optimal VEC system operating into optimal load.

## 2.5 Conclusion and further work

In this chapter fast sufficiently accurate models have been presented to solve ISM band inductive power transfer systems based on conductive tube, regular cross section coils. Using the presented techniques the circuit parameters of an IPT link can be found. Using the circuit parameters and the system specification the in operation magnetic fields found. This has been demonstrated with a complete design example where an IPT system based around a new coil winding pattern is optimised, modelled and in operation fields found without finite element simulation. The circuit parameters and magnetic field output from the model match those of full field finite element simulations.

A new technique has been used to find the mutual and self inductance of arbitrary coil geometries that is more adaptable than previous methods based on parameter tables. An existing technique has been used to find the proximity effect influenced resistance of the coils with constant cross section. A new technique has been utilised to plot the vector magnetic field of inductive power transfer. Through extensive comparison with finite element simulation some constraints and weaknesses have been identified with the models. It has been found that ignoring the curvature of loop type coils and instead modelling them as constant cross sections is not a significant source of error. However it has also been found that electrically longer coils are exhibiting behaviour similar to radiation loss at a far lower than predicted frequency.

The weakest part of the model is resistance modelling, while the skin effect model matches FE simulation very well introducing proximity effect does result in some limitations in the range of coils that can accurately be modelled. For the proximity effect model coils where the turns are very closely spaced or use longer lengths of copper do not matching simulation. From finite element simulations of the proximity effect of two tubes it is known that the model is not predictive when the turns are very close. This is probably due to the approximations made in that model about separability of current distributions and azimuthal current modulation.

During the example IPT system modelling it was found that the effective receiver coil tuning capacitance was influenced by the self capacity of the receiver coil. In the modelling presented in this chapter no capacitance model is presented, therefore the model cannot currently specify the tuning capacitor accurately. With the currently used coils this is not a significant problem as this value can be adjusted by experiment or found via FE simulation.

## Chapter 3

# Measurement of wireless power transfer coils

In the previous chapter detailed fast coil models were produced and the limitations on their validity was established mostly by comparing to FE simulations. To verify the simulation results it is necessary to perform measurements on actual coils. Measurement of high  $Q$  coils and associated difficulties of doing so are discussed in this chapter.

### 3.1 Introduction

When used in a resonant wireless power transfer system accurate characterisation of the loss of high  $Q$  components is required to calculate the transfer efficiency. For a wireless power transfer system expressed as a generalised two port network the maximum fractional power transfer efficiency,  $\eta$ , is given by Zargham and Gulak [6] as:

$$x = \frac{|Z_{21}|^2}{\text{Re}(Z_{11}) \text{Re}(Z_{22}) - \text{Re}(Z_{12})^2}, \quad (3.1)$$

$$\eta = \frac{x}{(1 + \sqrt{1 + x})^2}. \quad (3.2)$$

In a purely inductively coupled system,  $x$ , reduces to the familiar equation;

$$x = k^2 Q_{Tx} Q_{Rx}, \quad (3.3)$$

where;

$$k = \frac{M_{TxRx}}{L_{Tx} L_{Rx}}. \quad (3.4)$$

It can be observed that generally minimising the real portion of the transfer devices impedance parameters is desirable to improve efficiency, this quantity can be considered to be the self loss of the coil in loosely coupled IPT systems. Therefore in inductively coupled systems maximisation of the coil's quality factor,  $Q$ , is desirable. However for high  $Q$  factor IPT coils the energy loss per oscillatory cycle is by definition much smaller than the reactive energy stored by the coil. From a practical measurement perspective this makes accurate direct measurement of the coil's loss impossible as the measurement uncertainty caused by the reactive impedance is too great.

The aim of this chapter is to introduce methods for measuring high  $Q$  coils; these methods rely on indirect measurement of the coil parameters by exploiting resonance. To begin the definitions of  $Q$  and the

coil model are examined in detail to place bounds on the modelling assumptions made. Full wave simulations of IPT coils include the effects of electrical length and therefore if the results are processed naively (IE. fit to an overly simple LR model) the circuit parameters are reported incorrectly. As such algorithm is developed to fit full wave simulation results to the LCR coil model in an overdetermined manner.

Various conventional methods of examining the electrical impedance of inductive coils are examined using two devices; the vector network analyser (VNA) and the more specialist impedance analyser. Monte Carlo modelling is utilised to show that neither device is capable of measuring the loss of high  $Q$  coils in any configuration directly. The effect of unintentional loading using an unbalanced instrument to measure a coil is shown and corrected by usage of transformer type baluns. Two methods are proposed to measure the  $Q$  of the coils; the first a transmission type measurement using the bandwidth of resonant coupling of a parallel tuned coil and the second a method using the low impedance of a series tuned coil combined with a two port VNA measurement.

To demonstrate the methods a set of four reference coils with known material parameters are constructed; the four coils are of widely varying geometry to show correspondence across the parameter space. Using the reference coils it is demonstrated that the results of the first transmission type method closely match full wave EM simulation in the frequency range where the coils dominant loss is due to the skin effect resistance of the copper.

To find the cause of some observed measurement artefacts and to verify the measurement system a simulation model of this measurement system is developed from measurement and modelling of the components of the measurement system. This model is able to show that the cause of the anti-resonance observed in the results is due to coupling loop to coupling loop coupling. It is also able to show the distance at which the coupling loops should be placed in relation to the coil under test for accurate results.

A second measurement system is proposed that uses the low impedance of the series resonant mode of the coil to read the coils real impedance at resonance. By switching measurement paths, each with an associated series capacitance the frequency of resonance can be varied. By switching the measurement path rather than the capacitor directly the indeterminable series loss from the relay does not effect the measurement result. As the measurement frequency can be changed by relays the coil measurements can be taken automatically under computer control without human intervention. This is important as manually soldering capacitors for each measurement point in the first method takes a significant length of time for each measurement point. New calibration theory is developed to compensate for portions of fixture beyond this tuning capacitor. This measurement system is not completed but significant progress is made in verifying key hypothesis required for measurement systems like it to operated.

### 3.1.1 Literature review

There is a lack of literature on the measurement of IPT coils losses, however this not because this is not an important topic, without this knowledge it is not possible to predict the link efficiency. Frequently papers on IPT systems skirt the issue of measurement of losses by simply not including measurements, skipping ahead to simply reporting the overall system power transfer efficiency. An exception to this is the paper of Ke et al. [41] where litz wire coils are measured. The authors find that the measured  $R_{AC}$  of the coils is similar to that predicted by their models. To perform these measurements they use a HIOKI 3532-50 LCR meter, reporting  $Q$  factors up to 1600 at 340 kHz from a coil with a self inductance of 2.672 mH. For this instrument from its manual [42]:

$$Test\ accuracy = Basic\ accuracy \times C \times D + E, \quad (3.5)$$



where  $C$  is the test speed coefficient,  $D$  the cable length coefficient and  $E$  the temperature coefficient. Under slowest measurement settings, at room temperature and using the leaded test fixture with no extension  $Test\ accuracy = Basic\ accuracy$ . It is assumed that these are the conditions which the coils are measured under. At the test frequency the impedance magnitude of the coil,  $Z_x$ , is  $5.71\text{ k}\Omega$  therefore the following equation is used to calculate basic accuracy:

$$Basic\ accuracy\ Z(\%) \text{ or } \theta(^{\circ}) = \pm \left( A + \frac{B|10Z_x - Range|}{Range} \right). \quad (3.6)$$

By examination of the Basic accuracy table it is found that;  $A = 0.15$ ,  $B = 0.02$  for a calculation of the basic phase accuracy ( $10\text{ k}\Omega$  range). Therefore the base accuracy is:

$$\theta\ accuracy = \pm \left( 0.15 + \frac{0.02 \times |10 \times 5710 - 10000|}{10000} \right) = \pm 0.244^{\circ}. \quad (3.7)$$

For a simple LR inductor model;

$$Q = |\tan(\theta)|, \quad (3.8)$$

therefore the reported angle is  $89.9642^{\circ}$  but the angle could be between  $89.7202^{\circ}$  ( $Q = 205$ ) and  $90.2082^{\circ}$  ( $Q$  unbounded) resulting in the only bound been  $Q > 205$ . Therefore this quality factor of 1600 cannot be reported with any confidence.

A 2011 paper by Lee and Lorenz also includes enough details to calculate the accuracy of the measured quality factor of a coil [15]. They use HP4263A LCR meter to measure an inductance of  $5.1\text{ }\mu\text{H}$  and a resistance of  $0.15\text{ }\Omega$  at  $3.7\text{ MHz}$  ( $Q = 790$ ). However this LCR meter is only capable of measurements up to  $100\text{ kHz}$ .

A third paper that includes measurements of IPT coils is a 2012 paper of Pantic et al. [43]. In this paper a coil with  $R_{AC} = 0.17$ ,  $Q = 480$ ,  $L = 13.0\text{ }\mu\text{H}$  is measured at  $1\text{ MHz}$  using an Agilent 4294A. This instrument is the previous version of the Keysight E4990A that is modelled later in the chapter, the accuracy specifications are only improved for the E4990A. As such the modelling code for the accuracy of the E4990A can be used to produce an optimistic estimate of the 4294A. The estimated accuracy is  $\pm 60\%$  for the improved E4990A version without taking into account additional error sources that are present such as the fixture extension.

In conclusion to the authors knowledge no accurate  $Q$  measurements of IPT coils at MHz frequencies exist due to the limitations of conventional measurement equipment when measuring such high  $Q$  impedances. Frequently these results are simply omitted, when they are included further analysis shows that the instruments used cannot report such values accurately. However these results are important for determination of link efficiency. As such there is a compelling unsatisfied need for methods of measurement of the  $Q$  factor of such coils.

## 3.2 Definitions of Q

### 3.2.1 Energy definition

$Q$  is only strictly defined at resonance,  $\omega_0$  as;

$$Q = 2\pi \frac{E_s}{E_d}, \quad (3.9)$$

where  $E_s$  is the peak stored energy in the resonator and  $E_d$  the energy lost per resonant cycle [44]. When the  $Q$  of a lossy capacitor or inductor is stated it is implicitly resonating with a lossless inductor or capacitor

respectively.

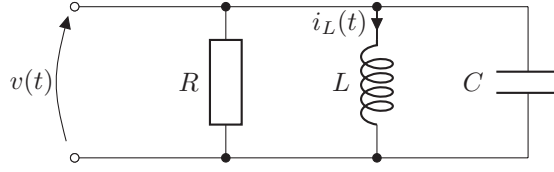


Figure 3.1: Parallel LCR resonator.

For ease of discussion of definitions of  $Q$  the parallel resonator is studied (Fig. 3.1). The coil model (Fig. 3.3) can be transformed into a parallel resonator with equivalent input impedance and  $Q$  to the parallel resonator (see section 3.5). The voltage across the parallel resonator is common to all components:

$$v(t) = |V| \cos(\omega t). \quad (3.10)$$

The electrical energy stored in the capacitor  $E_e$ , follows from definition:

$$E_e(t) = \frac{1}{2} |V|^2 \cos^2(\omega t). \quad (3.11)$$

To calculate the magnetic energy  $E_m$ , stored in the inductor firstly the inductor current is calculated;

$$i_L(t) = \frac{1}{L} \int v(t) dt = \frac{|V|}{\omega L} \sin(\omega t), \quad (3.12)$$

$$E_m(t) = \frac{1}{2} L i_L(t)^2 = \frac{|V|^2}{2\omega^2 L} \sin^2(\omega t). \quad (3.13)$$

By equating the peak magnetic and electric energies the familiar expression for the resonant frequency can be derived:

$$\frac{|V|^2}{2\omega^2 L} = \frac{1}{2} C |V|^2 \therefore \omega_0 = \frac{1}{\sqrt{LC}} \quad (3.14)$$

To calculate the energy lost per resonant cycle,  $E_d$  firstly the instantaneous power loss is defined:

$$P_d(t) = \frac{v(t)^2}{R}, \quad (3.15)$$

$$E_d = \int_0^{\frac{2\pi}{\omega_0}} P_d(t) dt = \frac{|V|^2}{R} \int_0^{\frac{2\pi}{\omega_0}} \cos^2(\omega_0 t) dt = \frac{\pi |V|^2}{R \omega_0}. \quad (3.16)$$

Finally the  $Q$  factor of the parallel resonator can be calculated:

$$Q = 2\pi \left( \frac{|V|^2}{2\omega_0^2 L} \right) \left( \frac{R \omega_0}{\pi |V|^2} \right) = \frac{R}{\omega_0 L}. \quad (3.17)$$

### 3.2.2 Bandwidth definition

If the parallel resonator (Fig. 3.1) is considered to be excited by a current source the two angular frequencies at which the power dissipated in the resonator is -3dB referenced to the maximum power dissipated in the resonator are:

$$|Z(\omega_{-3dB})| = \frac{R}{2}, \quad (3.18)$$

$$\omega_{-3dB} = \frac{\sqrt{2} \sqrt{L^2 + 2CR^2L} \pm \sqrt{L^4 + 4L^3CR^2}}{2CRL}. \quad (3.19)$$

An alternative definition of  $Q$  is:

$$Q_{-3dB} = \frac{\omega}{\Delta\omega}, \quad (3.20)$$

where  $\Delta\omega$  is the -3dB bandwidth of the resonator. This definition is not identical to the energy definition. The usage of this definition in the measurement of IPT coils has the difficulty that  $R$  is a function of  $\omega$  and therefore will have varied within the resonator bandwidth. For electrically small loop antennas  $R \propto \sqrt{\omega}$  in the skin effect dominated loss region and  $R \propto \omega^4$  in the radiation loss dominated region [45]. Therefore we can alternatively express  $R$  for the coil model (fig. 3.3) as:

$$R(\omega) = k\omega^p. \quad (3.21)$$

Where,  $k$ , is a constant defining the  $Q$  factor at  $\omega_0$  and  $p$  the power of proportionality for the dominant effect. By numerical modelling the discrepancy between the energy definition of  $Q$  methods that use the resonator bandwidth has been plot (fig. 3.2) for constant  $R$  with respect to frequency and the two common proportionality. Significant differences between the two definitions only occur at low  $Q$ . Even for the most dispersive modelled case the error is small for the high  $Q$  coils used in IPT systems. With the error mostly attributable to the difference between the two definitions. As IPT coils are expected have  $Q > 10$  the effects of the coils dispersion and difference in definitions of  $Q$  can be safely ignored.

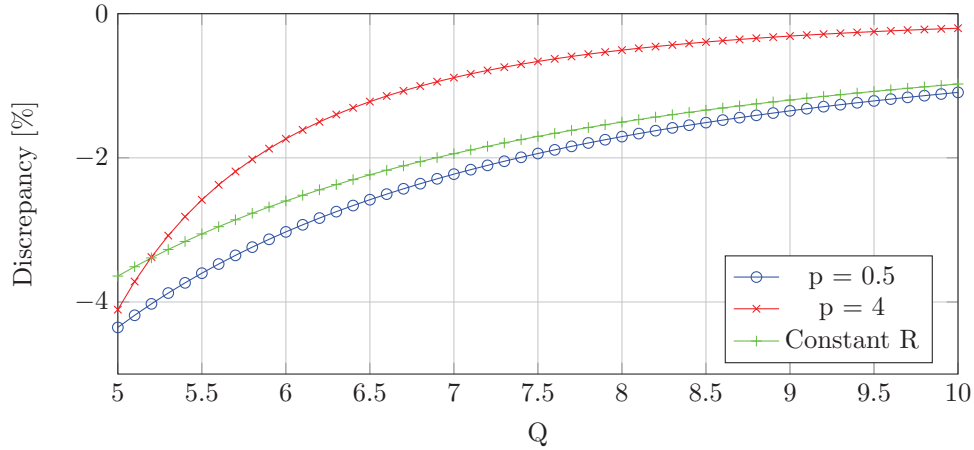


Figure 3.2: Comparison between energy and bandwidth  $Q$  definitions for different proportionalities of  $R$ .

### 3.3 Coil model for inductive power transfer

A frequently used simple model for IPT coils is now introduced (Fig. 3.3). If it is assumed that the reactance of a coil is purely supplied by the coil's inductance then the following two definitions of  $Q$  are identical:

$$Q_{LCR} = \frac{\omega L}{R(\omega)}, \quad (3.22)$$

$$Q_L = \frac{\text{Im}(Z_{11})}{\text{Re}(Z_{11})}. \quad (3.23)$$

However all coils have some parallel capacitance, the impedance of the circuit modified with parallel capacitance,  $C_p$  is:

$$Z_{11} = \frac{R(\omega) + j(\omega L - \omega^3 L^2 C^2 - \omega R(\omega)^2 C)}{1 - 2\omega^2 LC + \omega^4 L^2 C^2 + \omega^4 R(\omega)^2 C^2}, \quad (3.24)$$

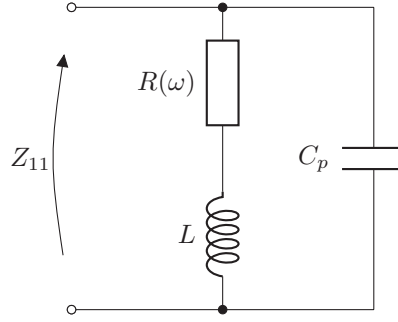


Figure 3.3: Coil model for IPT.

$$\omega_0 = \frac{\sqrt{LC - C^2 R(\omega)^2}}{CL}. \quad (3.25)$$

If the impedance of the  $RLC$  circuit is measured and the simplified model without the parasitic capacitance fitted to it the inductance and resistance are over reported. The capacitance will increase the effective series resistance of the coil and the effective inductance of the coil. The effect on the reported  $Q$  for IPT coils more nuanced; the capacitance causes the  $Q$  to be under reported at frequencies approaching self-resonance, deceptively this can look like the coils radiation corner frequency.

Full wave EM simulation software outputs S-parameters which are transformed into impedance parameters including the coils parallel capacitance, which must be removed from the measurement to obtain the true  $Q$ . While measurement methods for high  $Q$  coils that parallel resonate the coil report the true  $Q$ . Direct measurement of the coil with an impedance analyser will also output only impedance parameters inclusive of the coils capacitance, as per full wave EM simulation.

### 3.4 Capacitance extraction method

When measuring the coil with a resonant method the coils inductive reactive impedance is the additive inverse of the resonating capacitors, for non-resonant methods such as single port S-parameters from an EM simulators complex coil impedance is obtained directly. The problem of fitting the coil model (fig. 3.3) to the impedance data then arises. In the model of the coil it is assumed that the effective inductance of the coil and effective capacitance of the coil does not vary with frequency, however the loss resistance  $R(\omega)$  is a function of frequency. If  $C_p$  is removed from the coil model the imaginary impedance has a linear relationship with angular frequency. Thus an algorithm can be devised to find the capacity that fits. The following curve (Fig. 3.4) is plot from the impedance data:

$$y = \frac{1}{\omega(\frac{1}{\text{Im}(Z_{11})} + \omega C_p)}, \quad x = \omega. \quad (3.26)$$

A least mean squares linear fit to this data is then performed. By selection of the correct value of  $C_p$  the gradient of this fit will be 0, overestimate of  $C_p$  will result in a negative gradient, while underestimate a positive gradient, therefore by use of bisection the estimate of  $C_p$  is refined through successive approximation. Once  $C_p$  is estimated to the required precision the inductance of the coil is given by the y axis intercept of the line of best fit.

Figure 3.4 shows a typical coil capacitance fit plot; it can be observed that the assumptions about static inductance and capacitance are not strictly true. At low frequencies the inductance of the coil is greater than the high frequency asymptote due to increased internal inductance, whereby the skin effect causes a reduction in flux linkage within the coils conductors with increasing frequency (Fig. 3.5). At high

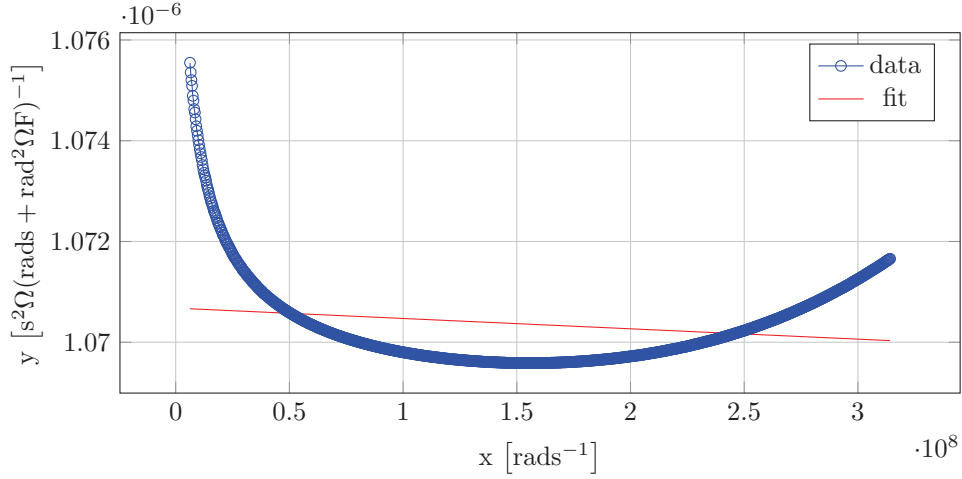


Figure 3.4: Coil capacitance fit plot over a wide frequency range.

frequencies the effective coil capacity starts to increase, this is due to the simplification of the model that the coil has no electrical length. This is not a significant concern for inductive power transfer coils as the coils  $Q$  factor falls as it becomes electrically long, so coils are not likely to be used at frequencies where this effect is significant. For fitting coil capacitance frequency points where the coil deviates from the  $LCR$  model significantly should be discarded.

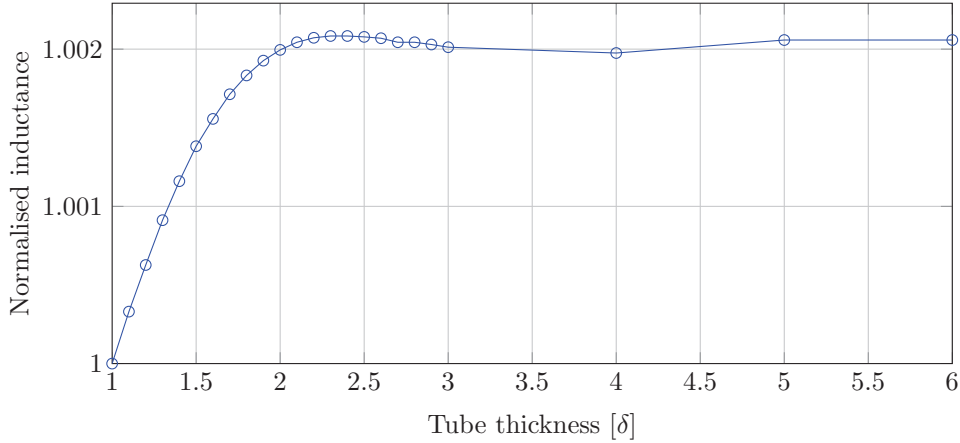


Figure 3.5: Internal inductance variation for straight conductive tube.

### 3.5 Resonator loss relocation

At times it may be more convenient to relocate the series loss resistor of the inductor to be in parallel to  $L$  and  $C_p$  as per figure 3.1 rather than in series with  $L$  as per figure 3.3. By considering only the  $LR$  series circuit a parallel  $L'R'$  circuit that has the same input impedance and  $Q$  can be defined:

$$Z_LR(\omega) = R(\omega) + j\omega L, \quad Z_{L'R'}(\omega) = \frac{j\omega L'R'}{j\omega L' + R'(\omega)}, \quad (3.27)$$

$$Q_{LR} = \frac{\omega L}{R(\omega)}, \quad Q_{L'R'} = \frac{R'(\omega)}{\omega L'} \quad (3.28)$$

$$\therefore R'(\omega) = \frac{R(\omega)^2 + L^2\omega^2}{R(\omega)}, \quad L' = \frac{R(\omega)^2 + L^2\omega^2}{L\omega^2}. \quad (3.29)$$

As  $C_p$  is in parallel with both  $LR$  circuits its value remains unchanged.

### 3.6 Series resonance with additional capacitor

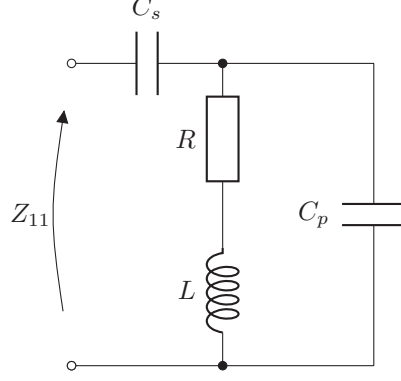


Figure 3.6: Series resonant coil measurement configuration.

In the coil model the parasitic capacitance is modelled as parallel with the coil. This capacitance cannot be removed as it is an inherent property of the relation of electrical potentials within the coil during oscillation. Therefore when series resonating the coil (fig. 3.6) instead of adding capacitance in parallel with the coil the effect of this capacitor must be quantified. The effect of the parallel capacitance is to form a secondary parallel resonance, this results in two frequencies where the imaginary portion of the complex impedance passes through zero:

$$\omega_{0(parallel)} = \frac{1}{2C_p L(C_s + C_p)} (-2C_p(C_s + C_p)(-2C_p L + C_s R^2 C_p + R^2 C_p^2 - C_s L - (-6C_p^2 L C_s R^2 - 4L C_p^3 R^2 + C_s^2 R^4 C_p^2 + 2C_s R^4 C_p^3 - 2C_s^2 R^2 C_p L + R^4 C_p^4 + C_s^2 L^2)^{0.5}))^{0.5}, \quad (3.30)$$

$$\omega_{0(series)} = \frac{1}{2C_p L(C_s + C_p)} (-2C_p(C_s + C_p)(-2C_p L + C_s R^2 C_p + R^2 C_p^2 - C_s L + (-6C_p^2 L C_s R^2 - 4L C_p^3 R^2 + C_s^2 R^4 C_p^2 + 2C_s R^4 C_p^3 - 2C_s^2 R^2 C_p L + R^4 C_p^4 + C_s^2 L^2)^{0.5}))^{0.5}. \quad (3.31)$$

The parallel capacitor also modifies the effective real impedance of the coil;

$$\text{Re}(Z_{11}) = \frac{R}{1 - 2\omega^2 L C_p + \omega^4 L^2 C_p^2 + \omega^2 R^2 C_p^2}. \quad (3.32)$$

At the earlier specified resonance points the effective resistance of the coil is modified from that of a pure parallel or series resonator. For a series tuned IPT coil the effect is to increase the apparent series resistance. If this effect is not taken into account the  $Q$  of the coil will be underestimated by a series tuned resistance measurement method.

### 3.7 Measurement methods

#### 3.7.1 Vector network analyser (VNA)

For a vector network analyser (VNA) the typical accuracy for reflection and transmission phase and magnitude is supplied by the manufacturer. These typical values are for use with specified intermediate frequency

(IF) bandwidth and calibration kits, without typical complications such as test lead flexure. However despite these limitations this data is useful for relative comparison of measurement methods. Although there are methods for computing the measurement uncertainty of derived parameters they require knowledge of the underlying sources of error that are not readily available [46]. Therefore a simple method has been developed to numerically calculate the worst case error using a Monte Carlo process from the manufacturer typical accuracy specifications. For each S-parameter in the derived expression a random phase and magnitude error within the typical error is added. This is repeated 10,000 times for each derived value to be calculated, the worst case error in the derived parameter calculated is then selected. This worst case error is then used to calculate the maximum error % in the derived parameter. This does not give the actual uncertainty as the statistical distribution of the error is not taken into account but does allow simple qualitative assessment of different methods.

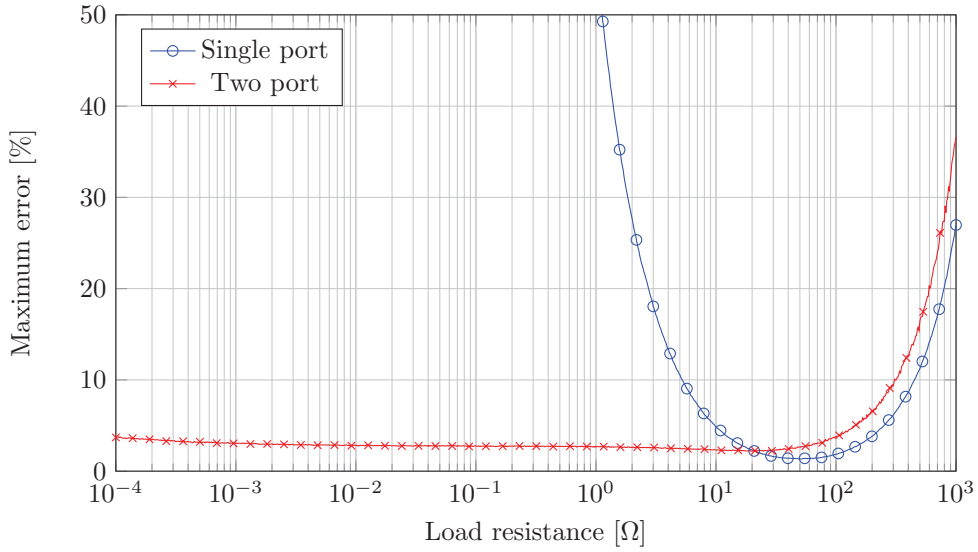


Figure 3.7: Single and two port impedance measurement method comparison for real load.

Using the manufacturer typical uncertainty specifications [47] for the frequency range 100 kHz to 4.5 GHz; the maximum error measuring a real load directly connected to the R&S ZNB4 VNA is plot (Fig. 3.7) for the two different direct measurement methods. The two port method (section 3.7.4) is capable of accurately determining very small values of real load, unlike the single port method (section 3.7.2). The single port method is only marginally advantageous in measuring impedances greater than 50 Ω due to the lack of parallel loading of the component under test by port 2. In both cases (Fig. 3.8, 3.9) accuracy for determination of the loss resistance is significantly degraded by the presence of complex reactance. Therefore for both the single port or two port measurement method resonance must be used to cancel the inductive reactance of the coil.

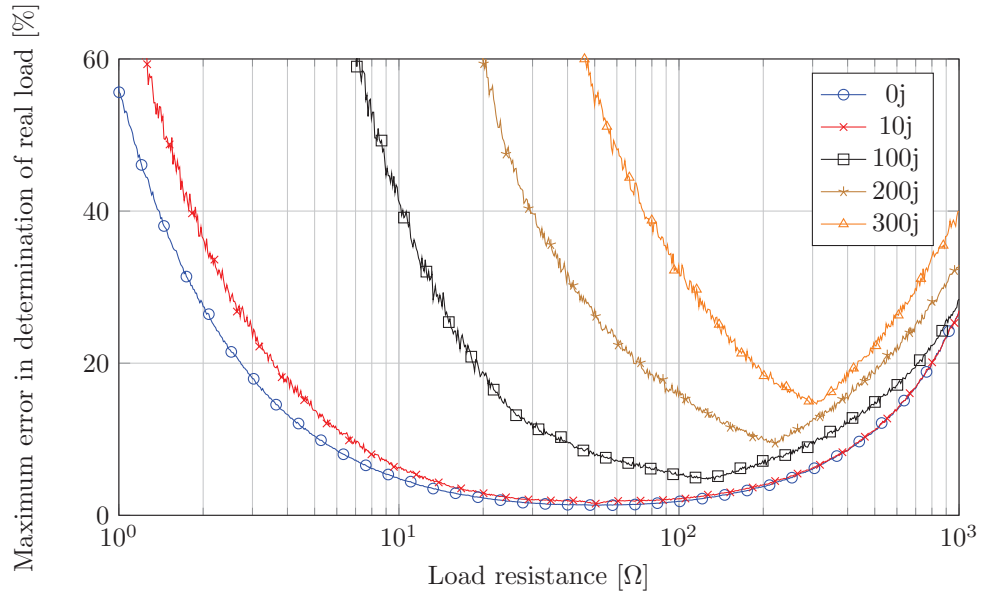


Figure 3.8: Single port direct measurement performance in the presence of reactance.

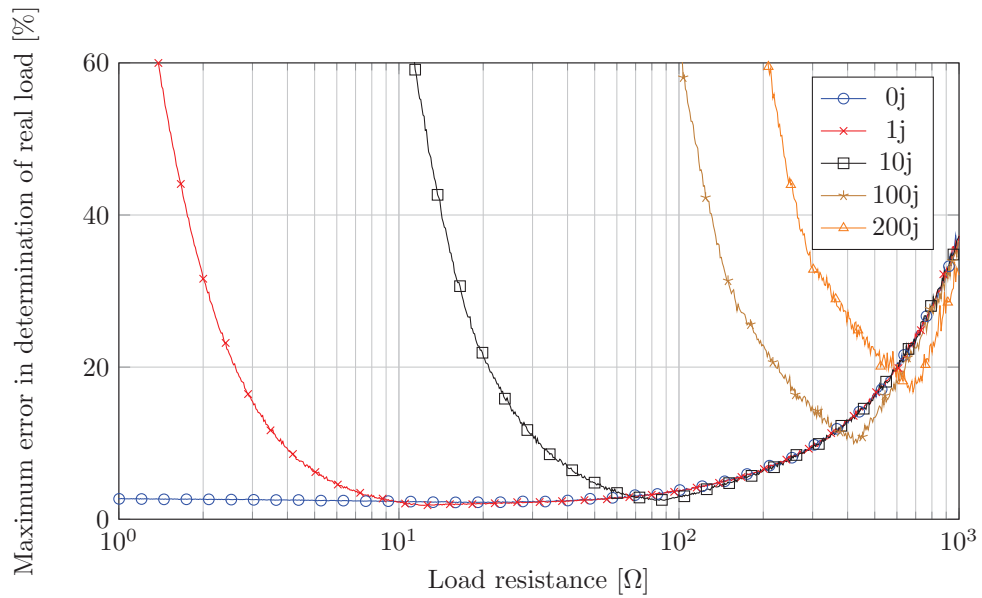


Figure 3.9: Two port direct measurement performance in the presence of reactance.



## Baluns

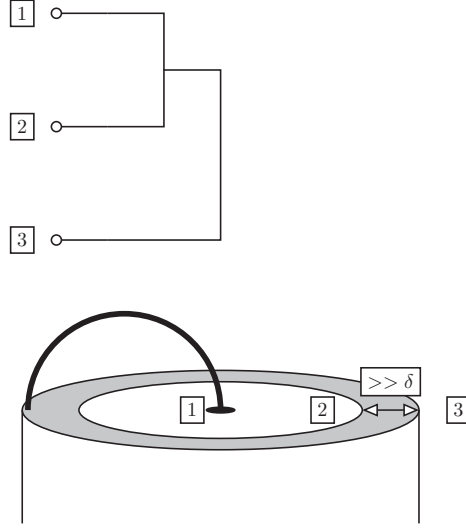


Figure 3.10: Coaxial cable with loop antenna.

An IPT coil is an electrically small loop type antenna, therefore it should be driven from a balanced source to ensure that the current entering the plane from the centre conductor is of equal magnitude and anti-phase to that exiting it. When an IPT coil is directly connected to a coaxial measurement system at frequencies where the coaxial cables shield is electrically thick an unintentional conductor is introduced formed by the outer of the coaxial shield. If a current flows in the outer of the coaxial shield it will alter the coil's measured properties and cause unintentional coupling. This unintentional coupling will electrically load the coil for single and two port measurements. For transmission type measurements not using a balun provides an alternative transmission path via magnetic coupling between the coaxial cables feeding the loop antenna. Unbalanced currents may also cause spurious readings by coupling into the measurement instruments case and ground.

A balun operates by presenting a high impedance to common mode currents. The point of reference is defined as the interface plane to the loop antenna.  $I_1$  is the current from the centre pin,  $I_2$  the current from the inner shield and  $I_3$  the current from the outer shield.  $I_1$  and  $I_2$  are composed of unbalanced,  $U$ , and balanced current,  $B$ ;

$$I_1 = I_1(U) + I_1(B), \quad (3.33)$$

$$I_2 = I_2(U) + I_2(B). \quad (3.34)$$

By application of Kirchhoff's current law;

$$I_3 = I_1 + I_2, \quad (3.35)$$

the definitions are then applied;

$$I_1(B) = -I_2(B), \quad (3.36)$$

$$I_1(U) = I_2(U). \quad (3.37)$$

Therefore;

$$I_3 = I_1(U) + I_2(U). \quad (3.38)$$

The impedance to common mode currents can be increased by introducing an impedance into the shield conductor (choke type balun) or by using a transformer type balun to increase the impedance to common mode currents in the balanced path of  $I_1$  and  $I_2$ .

To provide a high impedance to current flows in the outer of the shield a transformer type balun Mini Circuits T1-1-KK81+ has been employed to connect the VNA to the electrically small measurement loops used in the transmission type measurement. It has  $-3\text{dB}$  bandwidth of 0.15 MHz to 400 MHz in a  $50\Omega$  (Balanced and unbalanced) system. For two port direct measurements of the coil a common mode impedance of  $100\Omega$  and a differential mode impedance of  $50\Omega$  is employed by use of the centre tapped transformer type balun (Mini Circuits ADT1-6T+) (Fig. 3.11) . By having a defined common mode impedance common mode power is absorbed reducing measurement interference from the mode conversion parameters  $S_{dc22}$  and  $S_{cd22}$ . The differential S-parameters [48] and common mode rejection ratio (CMRR) of this balun have been calculated (Figs. 3.12, 3.13, 3.14, 3.15, 3.16, 3.17, 3.18), as the balun is passive and reciprocal parameters that are equal have been highlighted.

$$\begin{pmatrix} S_{cc11} & S_{cd12} & S_{cc12} \\ S_{dc21} & S_{dd22} & S_{dc22} \\ S_{cc21} & S_{cd22} & S_{cc22} \end{pmatrix} \quad (3.39)$$

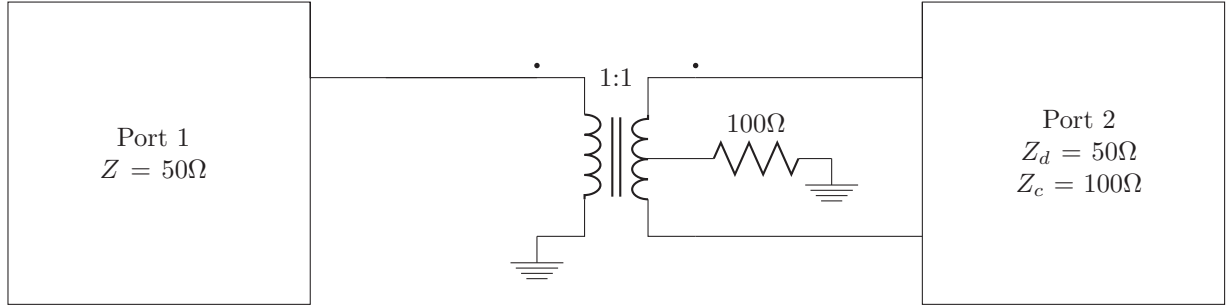


Figure 3.11: Configuration for ADT1-6T+ differential S-parameters.

In an effort to show the effects of unintentional loading a single port direct measurement of a 3 turn volumetrically efficient coil (VEC) has been made with and without the T1-1-KK81+ balun between it and the test lead. To better illustrate the effects of cable loading, 3m long test leads were used. The VEC has 7.25 mm diameter conductors, 310 mm outer diameter and 14.5 mm space between turns. The measured results (fig. 3.19) show that the first self resonance of the coil has been reduced from 23.9 MHz to 15.5 MHz by the loading of the unintentional coupling in the direct measurement without balun. To verify that the coil self resonance is found correctly by the balun method a transmission type measurement was made which found the self resonance to be 23.8 MHz, corresponding to the direct balun measurement. Thus it is verified that the addition of the balun removes the unintentional loading; this also eliminates unintentional coupling as significant current is no longer in the outer of the shield.

The S-parameter data from 1 MHz to 15 MHz has been processed using the capacitance extraction method (section 3.4). This output an inductance of  $3.77\mu\text{H}$  and capacitance of  $20.8\text{pF}$  for the measurement without a balun. For the measurement with the balun the inductance is  $3.80\mu\text{H}$  and capacitance  $12.4\text{pF}$ . This shows that the loading on the coil is primarily capacitive as would be expected by the addition of a short length open terminated additional conductor connected to the coils feed point. An easy technique to test for currents in the shield is to take a measurement with and without the measurement cable running through a high permeability core. A change in measurement result indicates that there are currents in the shield of the cable as the core will increase the impedance to this current (acting as a poor quality choke balun).

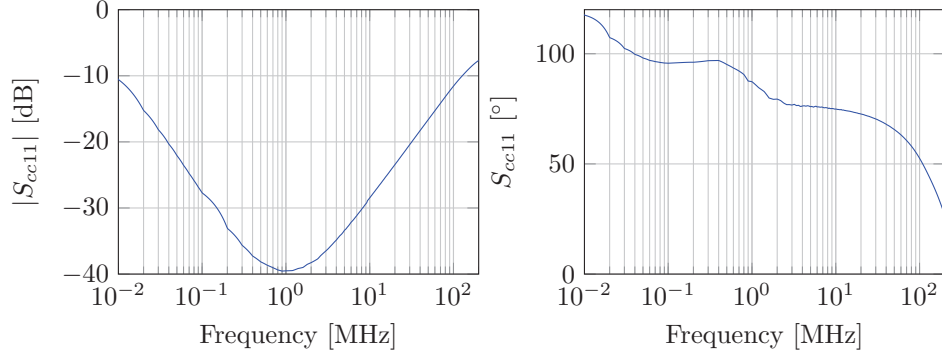


Figure 3.12: ADT1-6T+,  $S_{cc11}$ .

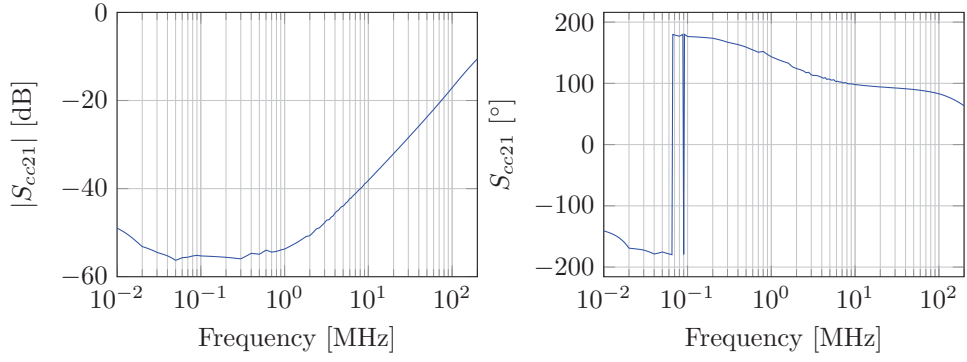


Figure 3.13: ADT1-6T+,  $S_{cc21}$ .

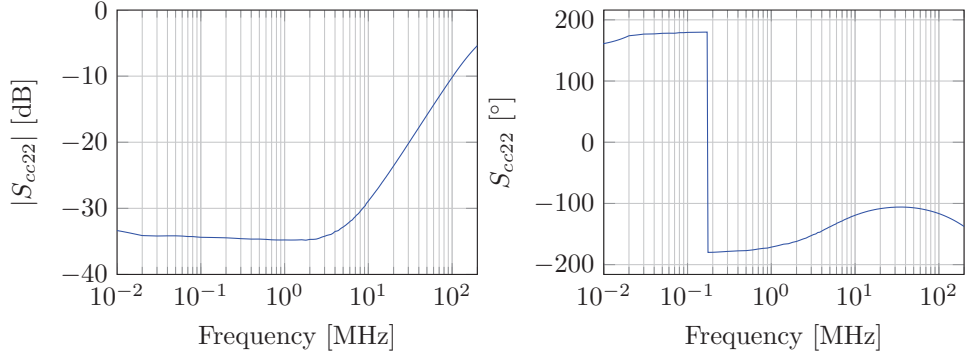


Figure 3.14: ADT1-6T+,  $S_{cc22}$ .

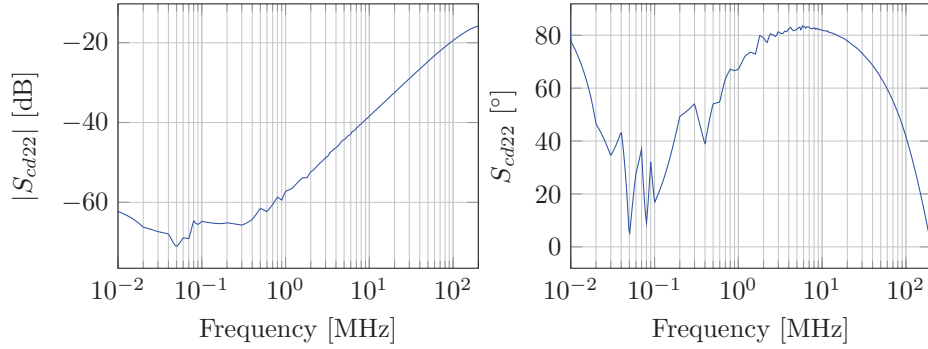


Figure 3.15: ADT1-6T+,  $S_{cd22}$ .

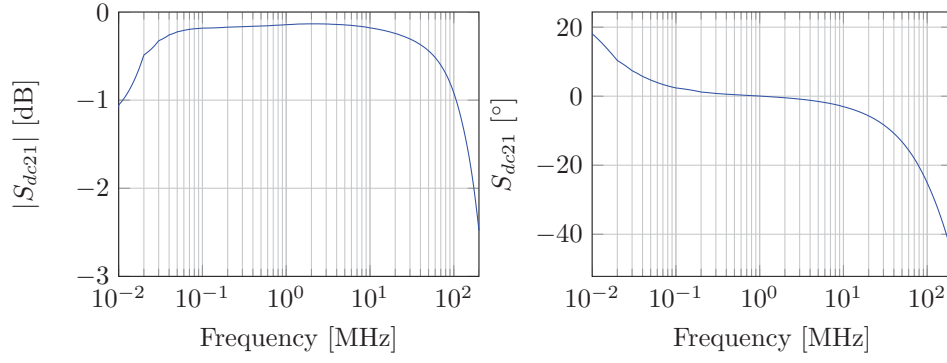


Figure 3.16: ADT1-6T+,  $S_{dc21}$ .

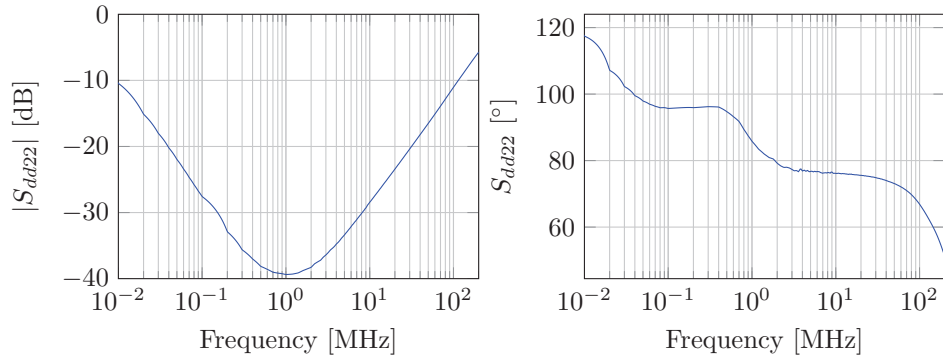


Figure 3.17: ADT1-6T+,  $S_{dd22}$ .

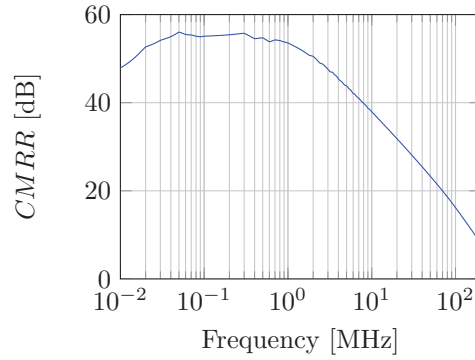


Figure 3.18: ADT1-6T+, CMRR

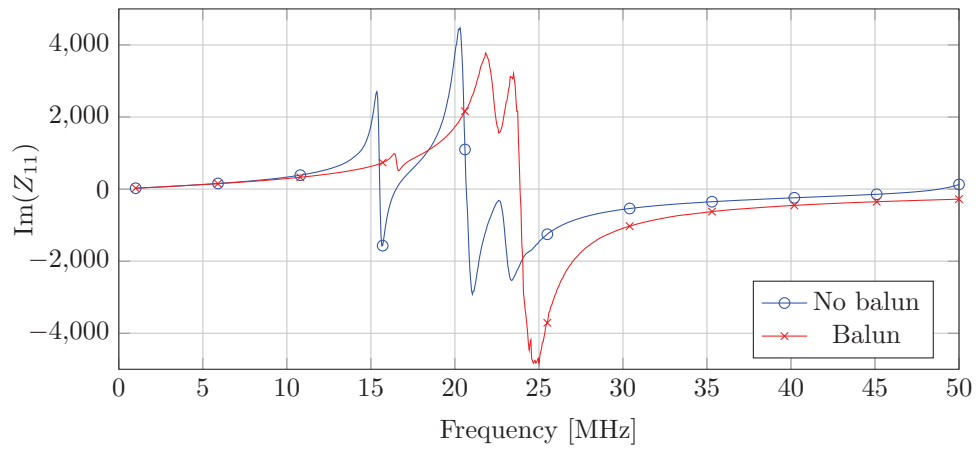


Figure 3.19: Direct single port measurement of a 3 turn VEC with and without balun - note that impedances far from  $50\ \Omega$  will have a large uncertainty.

### 3.7.2 Single port direct measurement

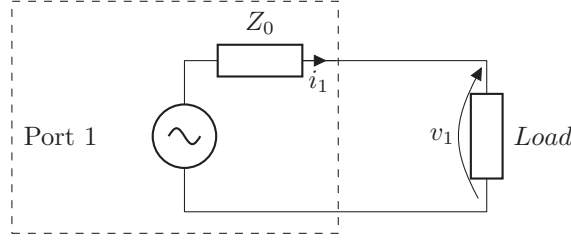


Figure 3.20: Single port measurement without resonance (Balun not shown).

$$Load = Z_{11} = Z_0 \frac{1 + S_{11}}{1 - S_{11}}. \quad (3.40)$$

This simplest application of the VNA unfortunately is not able to produce accurate results for high  $Q$  coils. The reactance of the coil causes the coil to track the outer perimeter of the smith chart due to its high  $|\Gamma|$ . A change in the  $R$  of the coil results in only very small changes in  $\Gamma$ . As the inductive reactance increases the accuracy of the measured resistance falls (Fig. 3.20) This method has been analysed in depth in a paper by Kuhn and Boutz who find in practice a VNA can report a  $Q$  of below 30 with reasonable accuracy using this direct measurement method [49].

### 3.7.3 Single port direct with resonance measurement

The accuracy of the single port method can be improved by series or parallel resonance of the coil under test. At the point of resonance the reactance is zero and as such the VNA can accurately measure resistance in the range  $1 \Omega$  to  $100 \Omega$ . However high  $Q$  coils will have much greater resistance at resonance when parallel tuned and much less resistance at resonance when series tuned. The small range of real impedances that single port methods can resolve still limit this method for high  $Q$  coils in comparison to two port methods.

### 3.7.4 Two port direct measurement

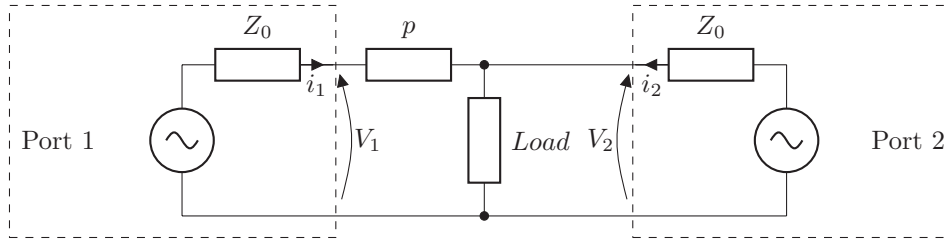


Figure 3.21: Two port measurement without resonance and series impedance,  $p$ , in measurement path.

$$Z_{21} = \frac{2S_{21}Z_0}{(1 - S_{11})(1 - S_{22}) - S_{21}^2}. \quad (3.41)$$

This method is capable of measuring resistances as low as  $0.0001 \Omega$  with better than 5% accuracy (fig. 3.7). It can be considered analogous to a four wire measurement in that it is insensitive to resistance in the test path not directly in series with the test load. By introducing the parasitic impedance,  $p$ , in the test path it is demonstrated that impedances in the test path have no effect on the measured result, assuming the VNA is ideal. S-parameters are independent of excitation amplitude thus the system is excited with 1 V

from port 1 and 2. It is assumed that  $Z_0$  is both the reference impedance and the port impedance and that it is real:

$$V_1 = \frac{p + Load // Z_0}{Z_0 + p + Load // Z_0}, \quad (3.42)$$

$$I_1 = \frac{1}{Z_0 + p + Load // Z_0}, \quad (3.43)$$

$$V_2 = \frac{(Z_0 + p) // Load}{Z_0 + (Z_0 + p) // Load}, \quad (3.44)$$

$$I_2 = \frac{1}{Z_0 + Load // (Z_0 + p)}, \quad (3.45)$$

$$a_1 = \frac{(V_1 + I_1 Z_0)}{2\sqrt{Z_0}}, \quad (3.46)$$

$$b_1 = \frac{(V_1 - I_1 Z_0)}{2\sqrt{Z_0}}, \quad (3.47)$$

$$a_2 = \frac{(V_2 + I_2 Z_0)}{2\sqrt{Z_0}}, \quad (3.48)$$

$$b_2 = \frac{(V_2 - I_2 Z_0)}{2\sqrt{Z_0}}, \quad (3.49)$$

$$S_{11} = \left. \frac{b_1}{a_1} \right|_{a_2=0}, \quad (3.50)$$

$$S_{22} = \left. \frac{b_2}{a_2} \right|_{a_1=0}. \quad (3.51)$$

For calculation of  $S_{21}$  the excitation is from port 1:

$$V_2' = \frac{Load // Z_0}{Z_0 + p + Load // Z_0}, \quad (3.52)$$

$$I_2' = \frac{-V_2'}{Z_0}, \quad (3.53)$$

$$b_2' = \frac{(V_2' - I_2' Z_0)}{2\sqrt{Z_0}}, \quad (3.54)$$

$$S_{21} = \left. \frac{b_2'}{a_1} \right|_{a_2=0}. \quad (3.55)$$

These S-parameters are then substituted into equation 3.41 giving the result:

$$Z_{21} = Load. \quad (3.56)$$

However this measurement method is unable to accurately resolve resistance in the presence of significant reactance (Fig. 3.9). Accuracy is degraded with respect to measurement of high impedances in comparison to single port methods due to the additional parallel resistance of port 2 with the load.

### 3.7.5 Two port direct measurement with resonance

The two port measurement method is capable of measuring very low resistance accurately without the presence of reactance. This can be achieved by series resonance of the coil. The parallel capacitance of the coil modifies the measured series resistance of the coil (equ. 3.32) and the resonance frequencies (equ. 3.30, 3.31). However the value of the series capacitor for each data point is known and the parallel capacitance is static, once multiple frequency points using different value series capacitors have been acquired the capacitance extraction procedure (section 3.4) can be used to find the value of the parallel capacitor.

### 3.7.6 Transmission type measurement

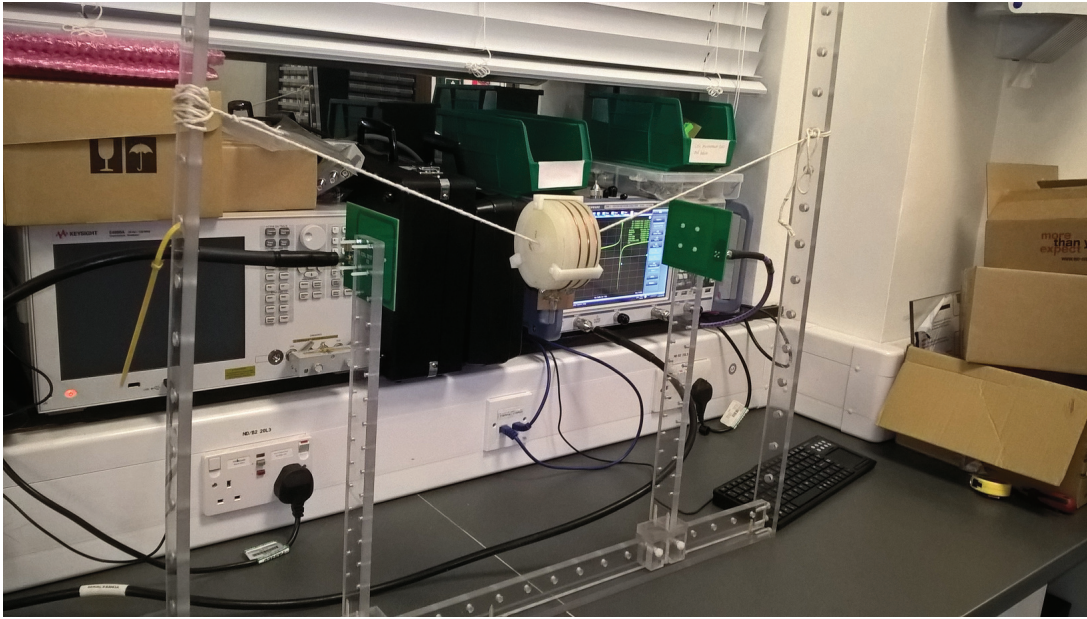


Figure 3.22: Transmission type measurement system showing coupling loops, coil under test and VNA.

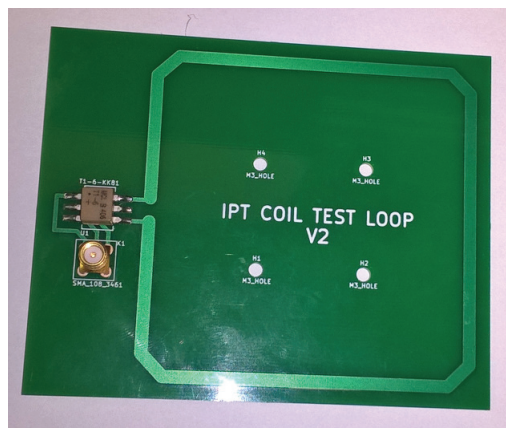


Figure 3.23: Coupling loop used in transmission type measurement.

A measurement method of used for measurement of the  $Q$  of cavity resonators has been adapted for IPT coils. The previously discussed measurements of coil model parameters have used the energy definition (equ. 3.9) however the bandwidth definition (equ. 3.20) can also be used. Energy is coupled into and out of the coil by a pair of loop antenna, via baluns to avoid cable coupling (Fig. 3.23). The coil has an additional



parallel capacitor soldered onto it to cause it to resonate at the test frequency. The coils resonance causes an increase in the transmission coefficient between the two loops, the bandwidth of this resonance giving the  $Q$  at resonance.

| Distance between loops | m loop, loop | k loop, loop          |
|------------------------|--------------|-----------------------|
| 0.09 m                 | 6.78 nH      | $3.39 \times 10^{-2}$ |
| 0.13 m                 | 2.30 nH      | $1.15 \times 10^{-2}$ |
| 0.17 m                 | 1.12 nH      | $5.60 \times 10^{-3}$ |
| 0.21 m                 | 638 pH       | $3.19 \times 10^{-3}$ |
| 0.25 m                 | 382 pH       | $1.91 \times 10^{-3}$ |
| 0.29 m                 | 246 pH       | $1.23 \times 10^{-3}$ |
| 0.33 m                 | 172 pH       | $8.60 \times 10^{-4}$ |
| 0.37 m                 | 124 pH       | $6.21 \times 10^{-4}$ |
| 0.41 m                 | 93.1 pH      | $4.65 \times 10^{-4}$ |
| 0.45 m                 | 64.9 pH      | $3.24 \times 10^{-4}$ |
| 0.49 m                 | 54.2 pH      | $2.71 \times 10^{-4}$ |
| 0.53 m                 | 44.5 pH      | $2.23 \times 10^{-4}$ |
| 0.57 m                 | 32.1 pH      | $1.61 \times 10^{-4}$ |
| 0.61 m                 | 30.8 pH      | $1.54 \times 10^{-4}$ |

Figure 3.24: Mutual inductances of measurement system

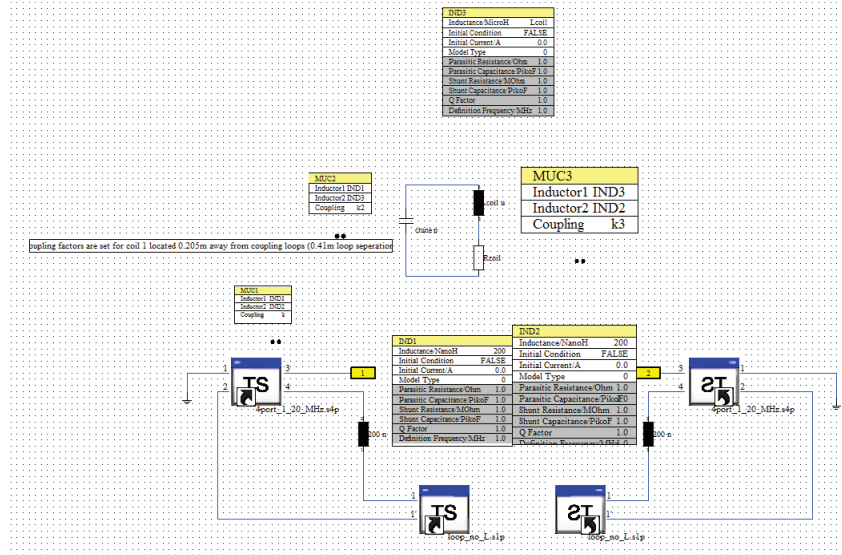


Figure 3.25: Passive frequency domain simulation model of transmission type measurement system.

For verification that this measurement system is capable of measuring high  $Q$  coils and for optimisation of coupling loop position a passive frequency domain simulation model with dispersive elements (Fig. 3.25) has been developed of the measurement system. Known  $LCR$  resonators can be introduced into this virtual measurement system to determine if the measurement system is capable of accurately determining the  $Q$  of the resonators. This model is based upon simulation models and measurements of the system components. Firstly the balun has been measured using a R&S ZNB4 VNA creating a 4 port S-parameter matrix allows it to be de-embedded from measurements. Secondly the loop antenna is simulated in CST-MWS to determine its S-parameters, from this model S-parameters the inductance is removed, resulting in a separate modelled inductance and a frequency variable loss resistance. Simulation is used rather than measurement, as measurement of the loop antennas loss resistance is very difficult even using resonant methods due to its low series resistance been comparable to that of the capacitor used to resonate it. From this the loops self capacity at 20 MHz is found to be negligible. To find the self inductance of the loop antenna a single port measurement of the loop antenna is made with the balun de-embedded. The loop antennas self inductance

is found to be 200 nH, agreeing with simulation.

By separating the series loss resistance and the inductance of the coupling loop the virtual distance between the coupling loops can be changed by modification of the mutual inductance between the loops. To measure the mutual inductance between the loops for different distances between the loops the two port S-parameters of the system are measured at various distances corresponding to stop positions on the coil measurement system. The results are then converted to Z-parameters and  $Z_{21}$  interpreted as mutual inductance.

Figures 3.26- 3.39 show the  $S_{21}$  amplitude and phase of the measured system compared to the model of the system. The model corresponds to measurement for distances between the coupling loop below 0.45 m for frequencies below 15 MHz and for distances below 0.33 m for frequencies up to 20 MHz. Considering the typical thickness's of IPT coils and typical operating frequencies this measurement system is suitable for most ISM band IPT coils. It is likely the loss of relevance of the model beyond these frequencies and distances is due to a coupling mechanism that is not part of the model.

When a coil is introduced to the virtual measurement system the S-parameters of the coil are extracted from simulation. The capacitance fitting procedure is then used to extract the equivalent circuit model. The equivalent circuit consist of a fixed inductance, fixed capacitance and frequency variable resistance. The resistance values are used to make a touchstone file representing the resistance that is imported with the fixed values into the circuit simulation. To calculate the mutual inductance between the coupling loops and the coil the coupling loops and the coil are represented as filamentary structures and modelled using the filamentary procedure detailed in 'Simulation and modelling of wireless power transfer components'.

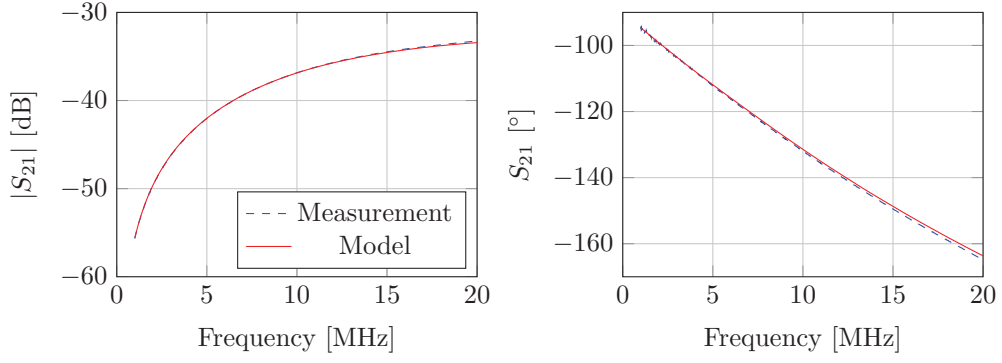


Figure 3.26: 0.09 m distance between coupling loops.

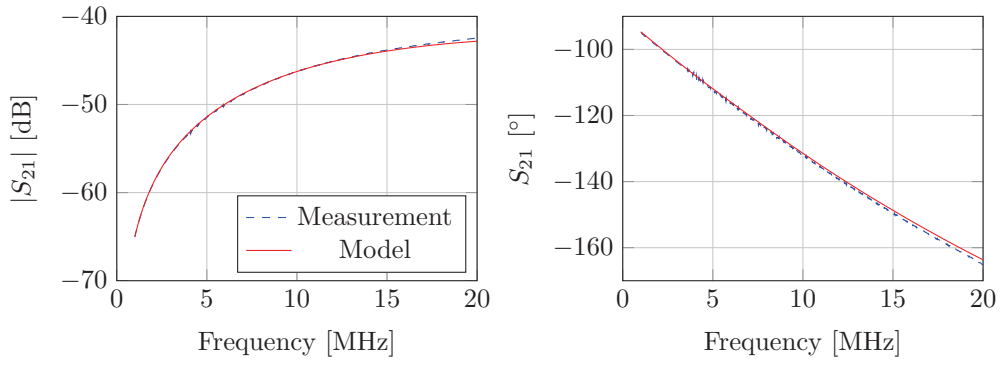


Figure 3.27: 0.13 m distance between coupling loops.

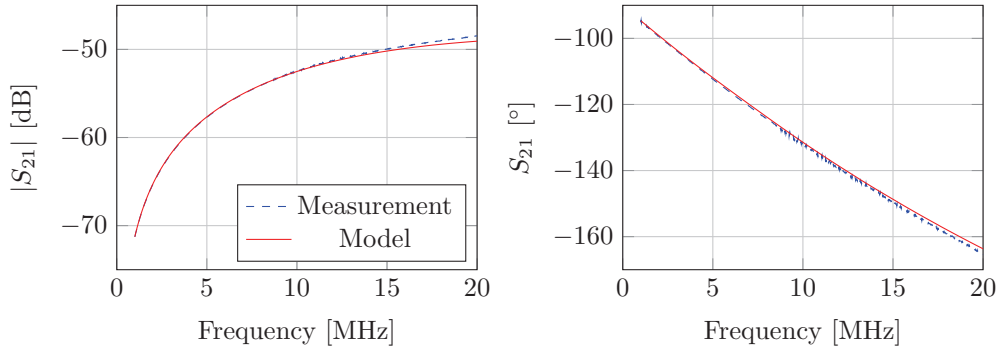


Figure 3.28: 0.17 m distance between coupling loops.

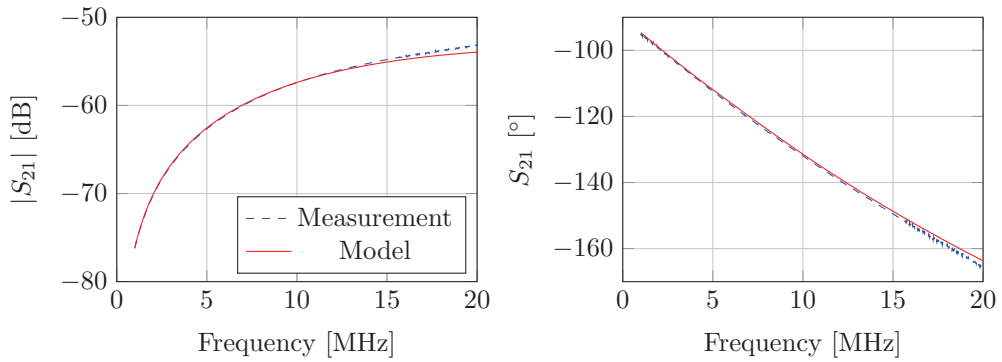


Figure 3.29: 0.21 m distance between coupling loops.

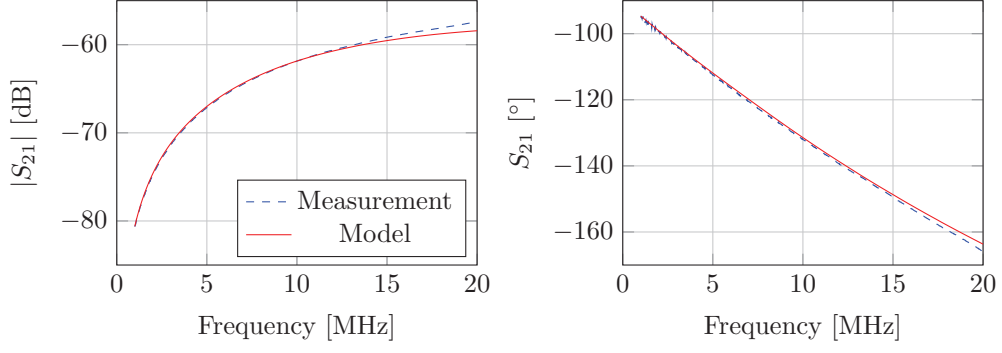


Figure 3.30: 0.25 m distance between coupling loops.

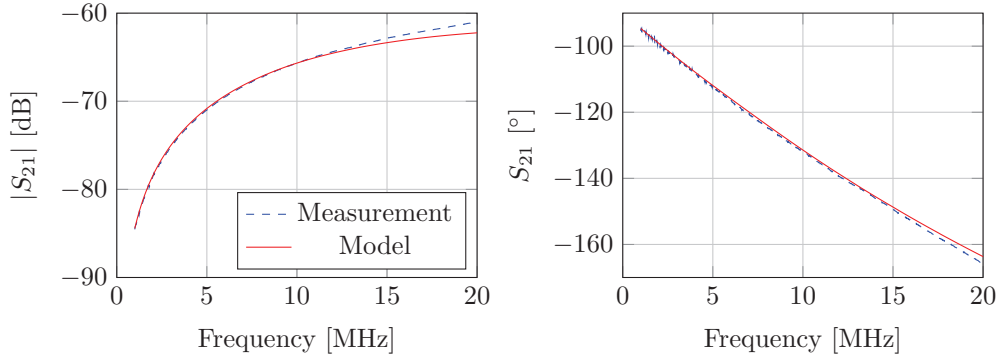


Figure 3.31: 0.29 m distance between coupling loops.

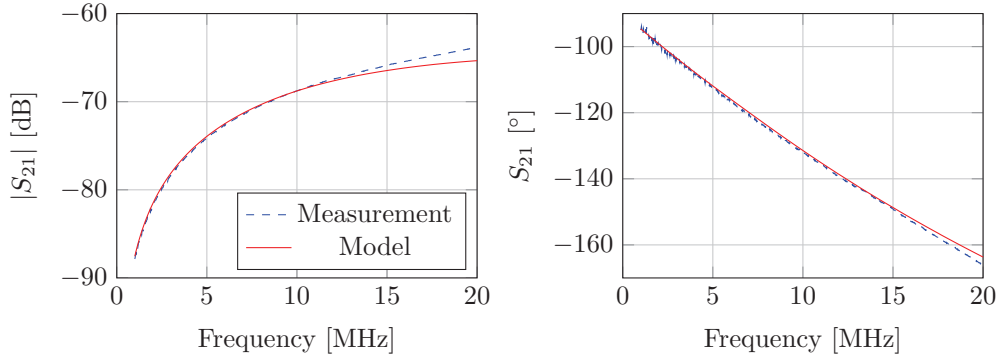


Figure 3.32: 0.33 m distance between coupling loops.

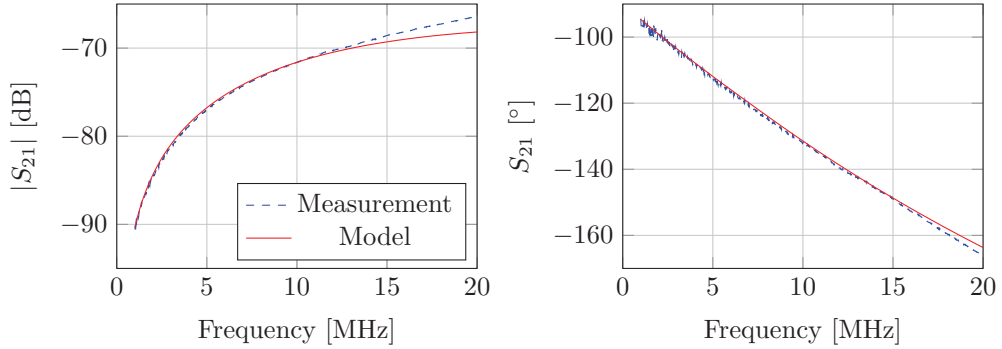


Figure 3.33: 0.37 m distance between coupling loops.

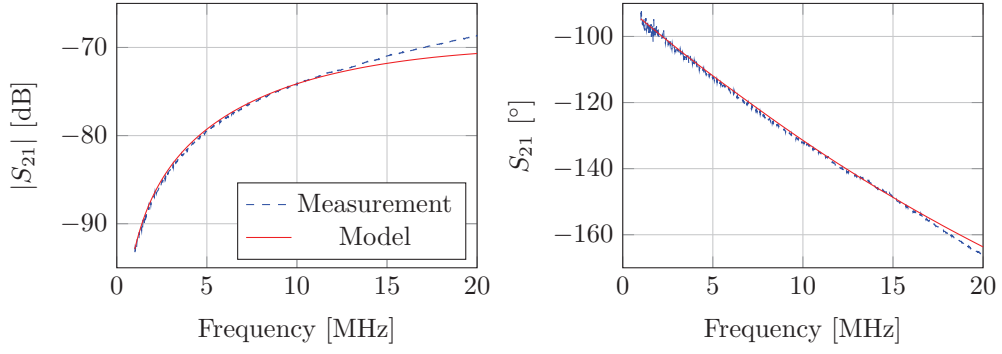


Figure 3.34: 0.41 m distance between coupling loops.

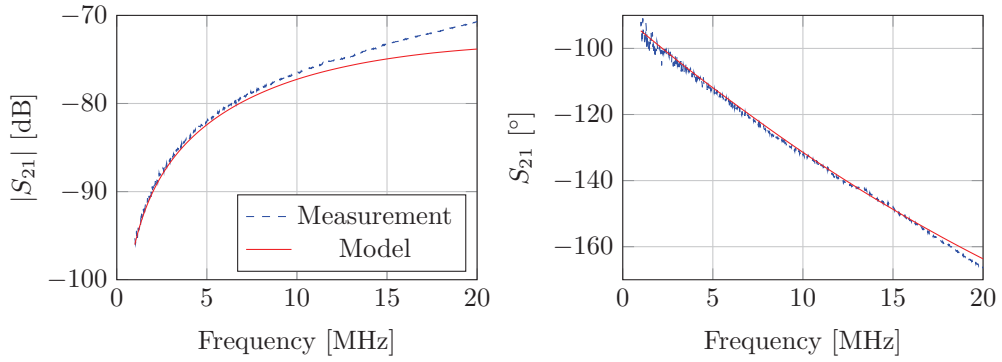


Figure 3.35: 0.45 m distance between coupling loops.

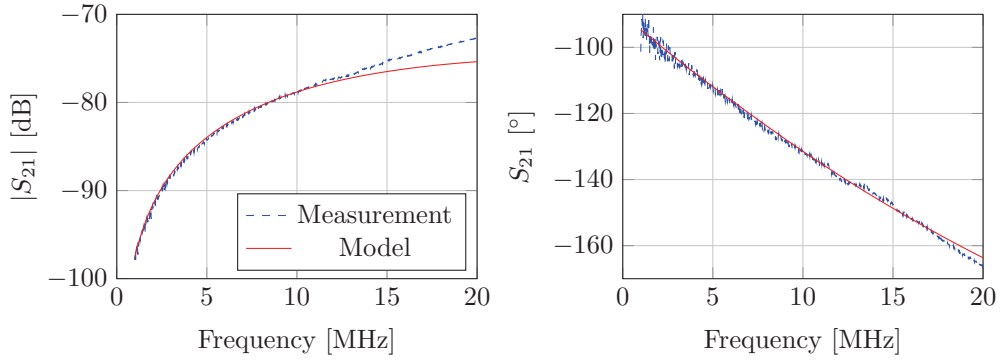


Figure 3.36: 0.49 m distance between coupling loops.

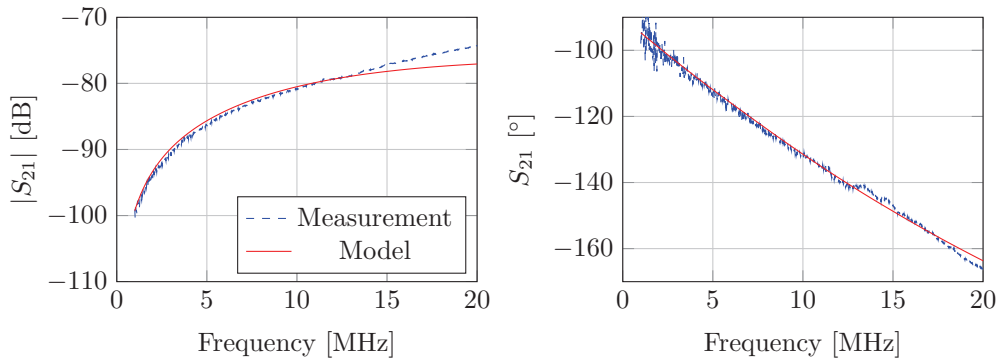


Figure 3.37: 0.53 m distance between coupling loops.

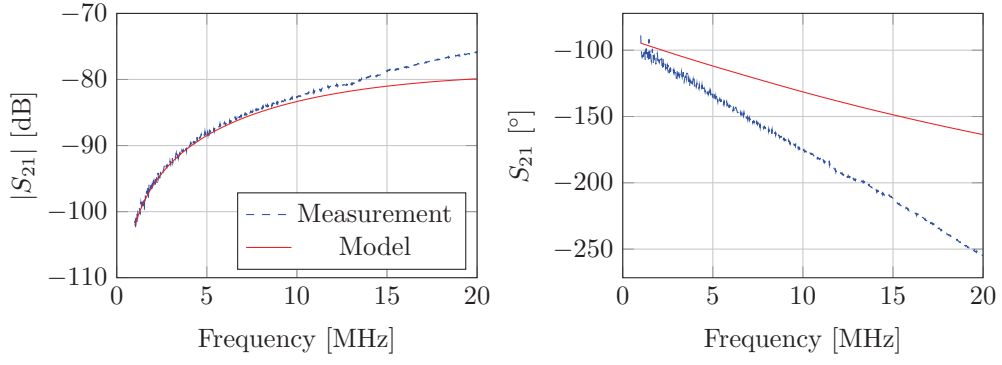


Figure 3.38: 0.57 m distance between coupling loops.

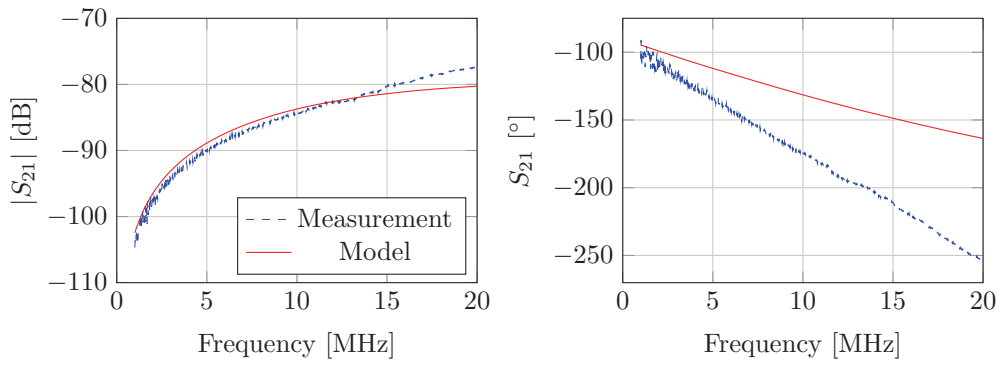


Figure 3.39: 0.61 m distance between coupling loops.

### 3.7.7 Impedance analyser

Impedance analysers are four terminal measurement devices using balanced bridges or RF IV methods to determine the impedance connected between their test terminals. They can measure a much broader range of impedances far away from  $50\ \Omega$ , as they measure current and voltage magnitude and phases rather than  $\Gamma$  with  $50\ \Omega$  reference impedance as per a VNA. However for determination of  $Q$  the requirements placed upon the accuracy of determination of the angle of impedance are extreme, if we consider a  $RL$  series circuit with impedance,  $Z_{11}$ :

$$Z_{11} = R + j\omega L, \quad (3.57)$$

$$Q = \frac{\omega L}{R}, \quad (3.58)$$

$$\theta = \tan^{-1} \left( \frac{\omega L}{R} \right), \quad (3.59)$$

$$Q = \tan \theta. \quad (3.60)$$

For an ideal inductor  $\theta = 90^\circ$ , thus for inductors that have a high  $Q$  a small change in the measured,  $\theta$ , results in a great change in the measured  $Q$ . The Keysight E4990A has the greatest base accuracy specification of any impedance analyser in its frequency range (20 Hz to 120 MHz) as of 2016, with a 5% accuracy for measurement of impedance magnitude from  $200\ \text{m}\Omega$  to  $4\ \text{M}\Omega$ , in the frequency range; 100 Hz to 1 MHz. As per the two port method and the single port method we have plot the accuracy of this instrument (Figs. 3.40, 3.41, 3.42), with the variation that the manufacturer supplies equations that allow direct plotting of expected accuracy without resorting to Monte Carlo methods [50]. The results show that although more capable of measuring impedance in the presence of reactance than a VNA that even in the most accurate 1 kHz to 1 MHz band that the maximum  $Q$  factors that can be reported in the most accurate region of operation are still restricted to less than 150, with reportable  $Q$  limited to around 10 in ISM bands.

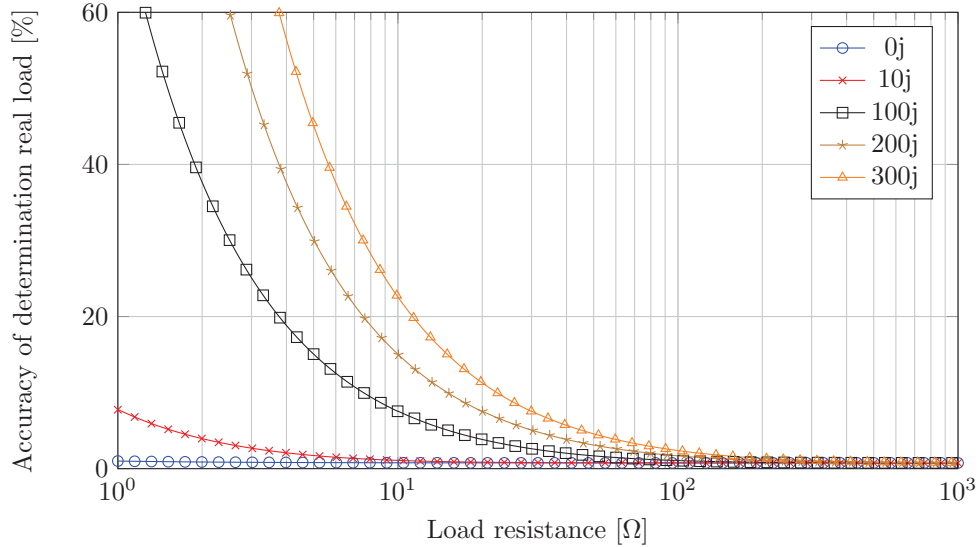


Figure 3.40: E4990A impedance analyser performance measuring real loads in the presence of reactance for the frequency range 1 kHz to 1 MHz.

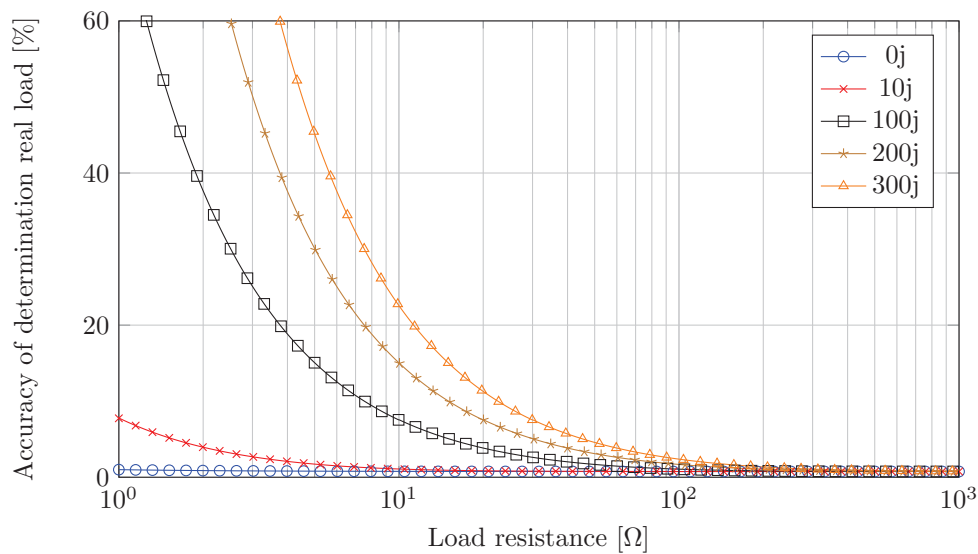


Figure 3.41: E4990A impedance analyser performance measuring real loads in the presence of reactance for the frequency range 5 MHz to 10 MHz.

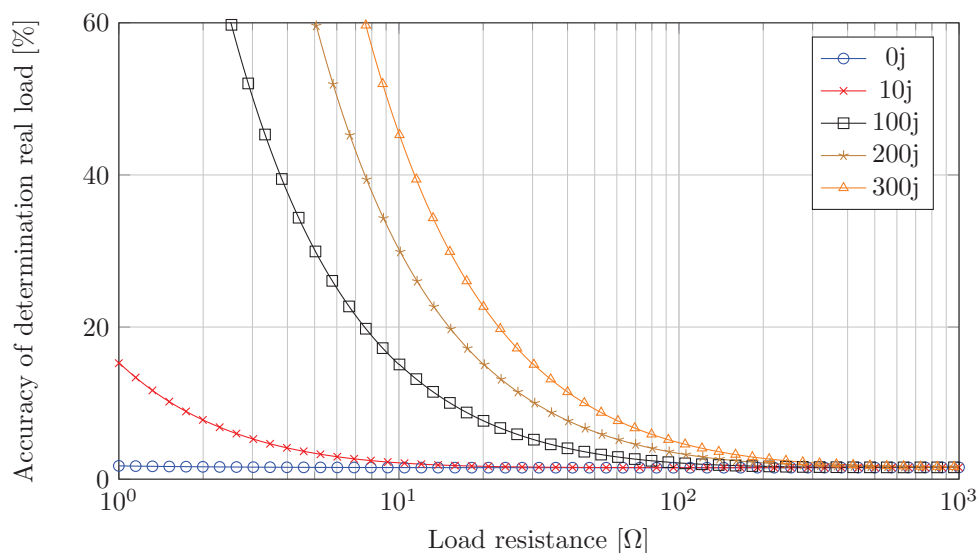


Figure 3.42: E4990A impedance analyser performance measuring real loads in the presence of reactance for the frequency range 10 MHz to 120 MHz.



## 3.8 Reference coil measurements

### 3.8.1 Introduction

In this section four high  $Q$  reference coils (Fig. 3.43) and a coil with  $Q > 1000$  are measured using the transmission type measurement system. The results are compared with full wave EM simulations conducted in CST MWS. The coils have widely varying geometry covering a large range of aspect ratios both in overall height to diameter and in turn spacing to turn diameter. Therefore if simulations match measurement it is reasonable to assume they will match for all expected coil geometries (within electrical length constraints). By ensuring the coils are constructed from materials with well known properties and are accurately constructed on formers it is ensured that the models entered into simulation are the same as those measured in reality. As such the correspondence of these simulations to the transmission type measurements verify the measurement and simulation methods. As their properties electrical properties are verified these coils can be used as references in the development of future measurement systems.

As further verification and to allow the performance of the measurement system to be tested in difficult to configure manners rapidly a measurement model of the transmission type measurement system has been constructed. This model has been developed by measurements of the elements that make up the measurement system. The model has good correspondence to measurements made of the overall measurement system, allowing it to be used to explain characteristics of the actual measurements.

Part of the reason for constructing a model of the measurement system is that merely obtaining one set of coil results that match simulation could be coincidence. This is because when testing the  $Q$  factor of a coil that has only been simulated with an unverified measurement system two hypotheses are tested with only one measurement. The first that the simulation is accurate and the second that the measurement system can measure the coil accurately. The model of the measurement system as it's constructed from independently measured and modelled quantities while having the same characteristics as the actual measurement system acts as a verification of the measurement system independent of the EM simulations.

A crucial difference between the real measurement system and the modelled measurement system is that coils introduced into the modelled measurement system are exactly known. Therefore when a set of results is gathered from the virtual measurement system that correspond to a simulation it is reasonable to assume that the real measurement system would also be able to obtain the same results. This avoids testing two hypotheses with one measurement as the measurement system is partly verified before testing the real coil.

This combination of reference coils, verified simulations and measurement system modelling allows new coils to be tested confidently. Firstly for development of new coils there is confidence in their simulations. Secondly virtual measurements of the coils in the model of the transmission type measurement system can be conducted to check that some unusual characteristic of the coils will not undermine the measurement (for example unusually high  $Q$ ). Thirdly there exists a set of reference coils to check the performance of new measurement systems with.

### 3.8.2 Coil EM simulation models

To ensure that the models in simulation physically match the actual reference coils it is important to characterise the materials used in their construction. The nylon formers relative permittivity will effect the coil's self capacitance; if significantly lossy it will also lower the coils quality factor. A 55 mm diameter, 1.43 mm thick disk of the same nylon used to construct the former has been characterised using a Keysight 16451B dielectric test fixture and E4990A impedance analyser (Figs. 3.45, 3.46). The results are only to 15 MHz which is a slightly lower frequency than the coils are modelled to. This is because it was found beyond this frequency the test fixture began to display resonant effects which it was not possible to fully remove



Figure 3.43: Reference coils.

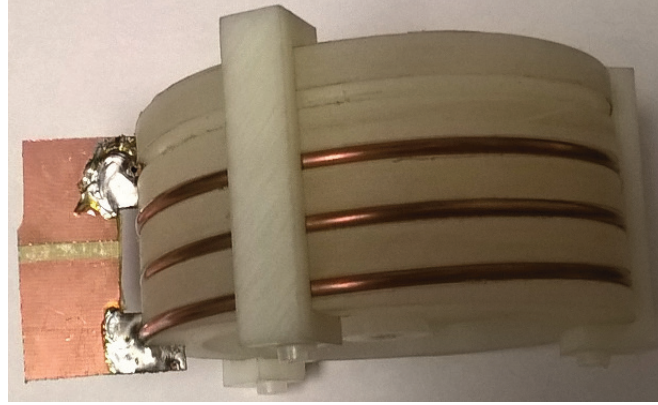


Figure 3.44: Reference coil with capacitor attachment board.

through short, open, load calibration. It may be possible to make higher frequency dielectric measurements using the 16451Bs smaller test terminals, however no sample of the correct size was readily available. From the results we can see the measured  $\tan \delta$  is below the test systems minimum determinable value of 0.01 and that the dielectric constant is at low frequencies constant. Therefore the coil former is modelled as a  $\epsilon_r = 2.12$  lossless dielectric.

The reference coils are 3 mm external diameter tube with 0.9 mm wall thickness, the material is 99.9%+ purity copper. This copper has no guarantee of electrical conductivity and therefore the conductivity of the coils has been measured (Table. 3.51). Taking a mean average of the measured conductivities yields  $\sigma = 4.85 \times 10^7 \text{ S m}^{-1}$  this is less than the international annealed copper standard (IACS) of  $5.8 \times 10^7 \text{ S m}^{-1}$ . As long as the conductivity is taken into account during simulation it does not effect the functionality of the reference coils, although if used for inductive power transfer greater efficiencies can be obtained by using IACS copper (typical at least 99.95%+ purity).

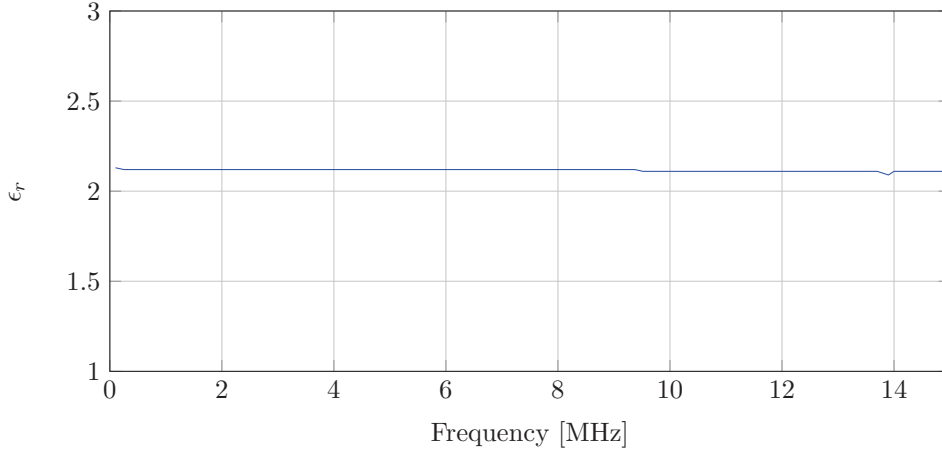


Figure 3.45: Relative permittivity of coil former.

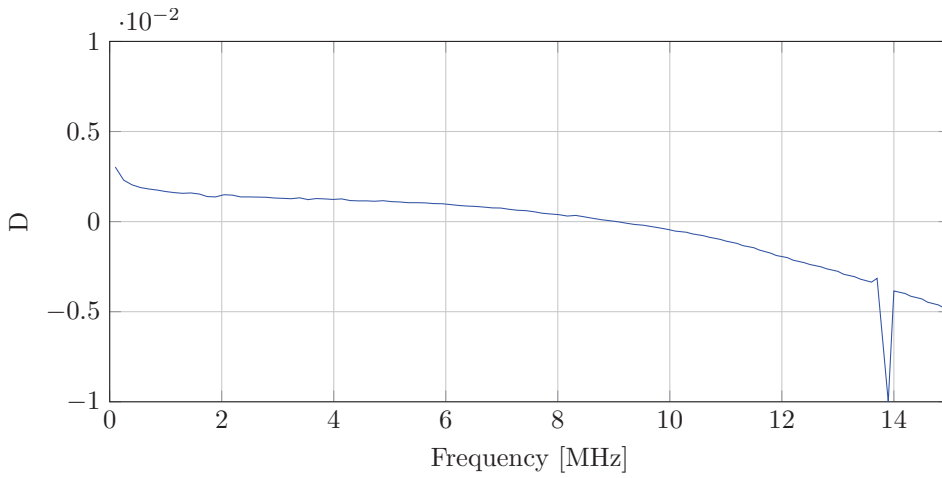


Figure 3.46: Measured loss of coil former dielectric, note the results show lower loss than is discernible with the test equipment. The gap in the data at 14 MHz is an artefact of the resonance associated with cable lengths used to connect the fixture.

### 3.8.3 Results comparison - transmission type measurement

#### Method

When using the transmission type measurement system to determine coil  $Q$  firstly the tuning capacitance is measured using a TTI LCR400 component meter (0.1%) base accuracy (10 kHz test frequency), to take into account manufacturing tolerance. A Keysight E4990A impedance analyser is then used to measure the series loss resistance of the section of circuit board used to connect the tuning capacitor to the coil ends. This measurement is noisy, close to the minimum resistance detectable using the instrument therefore the measured data is fitted to the equation;

$$R(f) = k_1 f^{k_2}, \quad (3.61)$$

which represents the skin effect dominated losses. The loss resistance of the tuning capacitor is obtained from the manufacturer's technical information for a typical capacitor at the tuned frequency of the coil. The measurement and post processing procedure now follows:

1. The VNA is calibrated with the reference plane located at the end of the test leads connecting to the loop antenna (corresponding to the model of the measurement system) over the full frequency range

1 MHz to 20 MHz.

2.  $|S_{21}|$  is then measured and the transmission peak located.
3. The VNA sweep is then adjusted to be centred upon the peak and the span adjusted to just encompass the -3dB points. The VNA is then set to perform a single sweep without averaging to prevent spreading of the resonator bandwidth caused by small changes in the centre frequency between sweeps.
4. The reduction in measured  $Q$  due to the coupling to the resonator is accounted for through the relation [44]:

$$Q_0 = \frac{Q_L}{1 - 10^{\frac{|S_{21}|}{20}}}. \quad (3.62)$$

5. The coils self capacity and inductance is found by plotting  $\frac{1}{\omega_0^2}$  against the measured value of the tuning capacitors for all tested frequencies. The linear line of best fit has a y axis intercept value of the inductance and an gradient of  $C_p L$ .
6. After performing sufficient measurements the coils inductance and self capacity is known and therefore the apparent loss resistance of the coil can be calculated.
7. The actual loss resistance of the coil can then be obtained by subtraction of the capacitor ESR and fixture resistance at  $\omega_0$  from the apparent coil resistance. This can be used to calculate the inductor  $Q$ .

### Measurements of fixtures

Measurements of the tests fixtures for each coil are compared to their fitting equation. As the reference coils have a great variance in height there is a corresponding variance in the length of PCB material that must be traversed and series resistance:

$$ESR_{Fixture1}(f) = 2.866 \times 10^{-4} f^{8.182 \times 10^{-2}}, \quad (3.63)$$

$$ESR_{Fixture2}(f) = 9.353 \times 10^{-6} f^{2.530 \times 10^{-1}}, \quad (3.64)$$

$$ESR_{Fixture3}(f) = 1.831 \times 10^{-5} f^{3.464 \times 10^{-1}}, \quad (3.65)$$

$$ESR_{Fixture4}(f) = 8.787 \times 10^{-5} f^{2.389 \times 10^{-1}}. \quad (3.66)$$

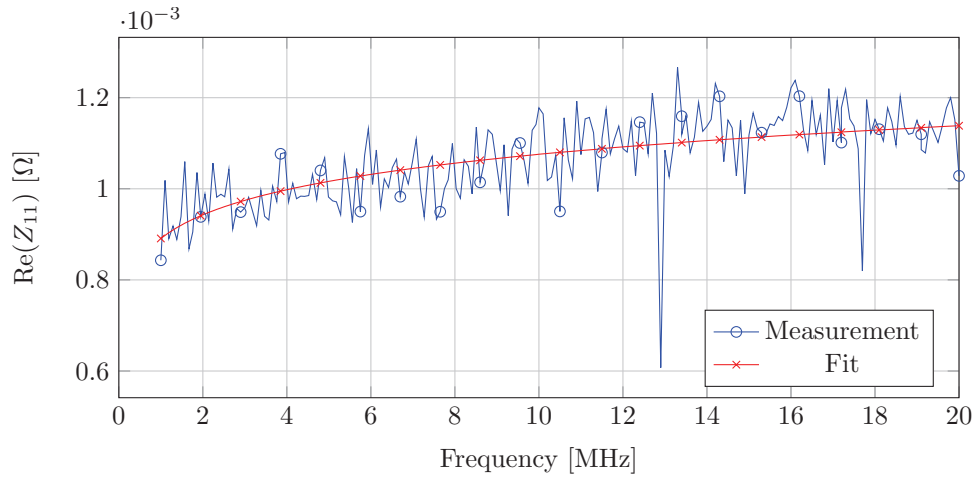


Figure 3.47: ESR of reference coil 1 attachment board.

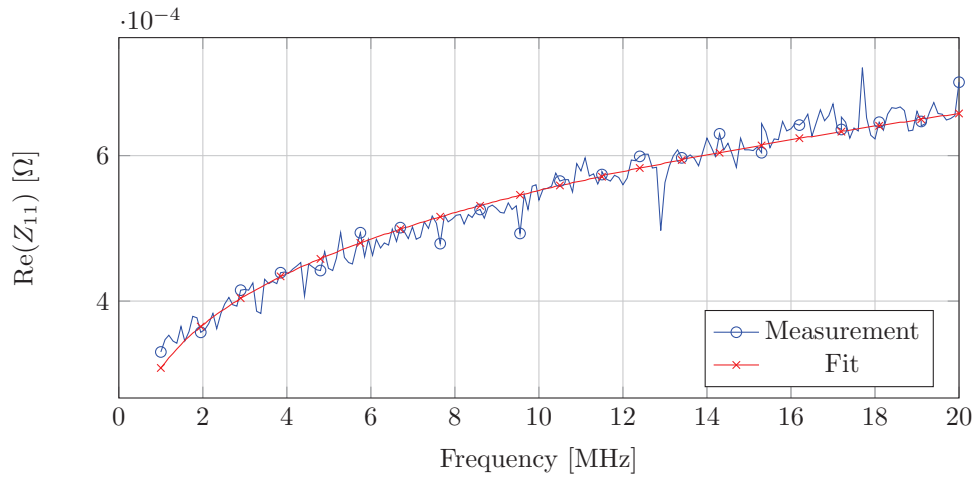


Figure 3.48: ESR of reference coil 2 attachment board.

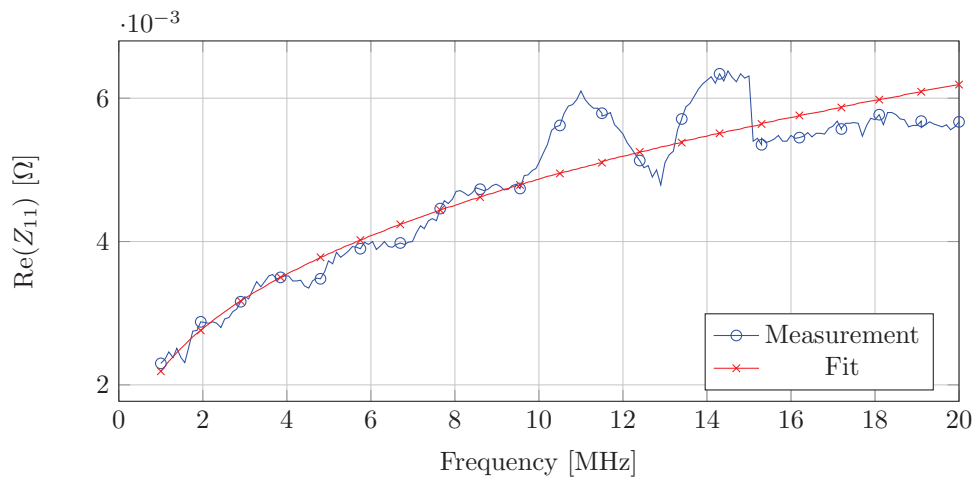


Figure 3.49: ESR of reference coil 3 attachment board.

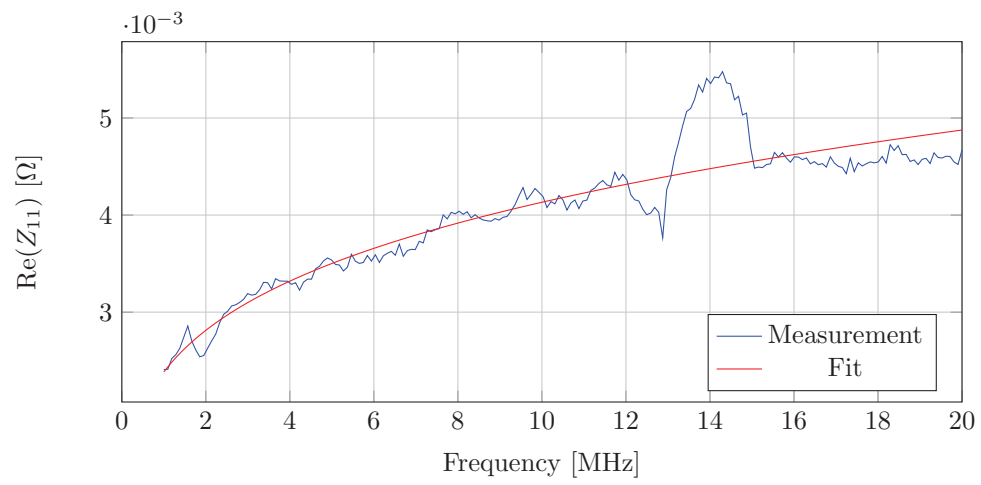


Figure 3.50: ESR of reference coil 4 attachment board.

### Comparison of EM simulation, simulated measurement system and actual measurement

In this section the EM simulations conducted in CST MWS are compared to the circuit simulation of the measurement system and the measurements undertaken using the transmission method. Correspondence for inductance between the EM simulations and measured results are excellent with less than 5% error (Table. 3.51). The correspondence between the measured capacitance and the EM model is poor with error exceeding 50% for coil 3. The EM model seems to underestimate the coil's capacity, in the context of the simulators differences to reality this makes sense. The coil's capacity is a phenomenon of electrical length, if there were no phase retardation along the coil there could be a no potential difference between turns and therefore no capacity [51]. The simulation, having to be contained inside a computers memory has to have a finite calculation domain. As the antenna is very electrically small simulating the near field would require a larger than practicable calculation domain and therefore the calculation domain has been truncated at 100 mm from the coil, therefore electric portions of the outer near field are not simulated correctly. Furthermore the coils have additional capacitor mounting boards added for measurement that bring the ends of the coil (area of peak electric field) in close proximity, adding additional non modelled capacitance. This effect could be taken into account however by measuring the capacitance of the capacitor mounting boards, or measuring the tuning capacitors when they are mounted on the mounting boards. Fundamentally has been made not to focus on the coils self capacitance as it is not important for the performance of IPT coils in ISM bands as coils are operated far bellow their self resonant frequencies to obtain high  $Q$  factor.

For  $Q$  factor, the main focus of this chapter the correspondence of measurement to simulation is to within 11.25% for all measured points and typically within 5% with higher frequencies where the coil is electrically longer having greater discrepancy from simulation. The most likely cause of error at lower frequency is the use of typical values for the tuning capacitor resistance. The modelled measurement system that does not have this limitation displays practically no deviation from the EM simulator results.

| Coil   | Inductance           | Capacitance | N | s    | a      | Length | Rmax  | DC resistance   | $\sigma$                              |
|--------|----------------------|-------------|---|------|--------|--------|-------|-----------------|---------------------------------------|
| Coil 1 | 1.25 $\mu\text{H}$   | 4.78 pF     | 2 | 2 mm | 1.5 mm | 945 mm | 75 mm | 3.60 m $\Omega$ | $4.74 \times 10^7 \text{ S m}^{-1}$   |
| Coil 1 | 1.23 $\mu\text{H}^*$ | 5.28 pF*    | 2 | 2 mm | 1.5 mm | 945 mm | 75 mm | NA              | $4.85 \times 10^7 \text{ S m}^{-1}^*$ |
| Coil 2 | 1.44 $\mu\text{H}$   | 4.76 pF     | 3 | 2 mm | 1.5 mm | 954 mm | 50 mm | 3.18 m $\Omega$ | $5.05 \times 10^7 \text{ S m}^{-1}$   |
| Coil 2 | 1.40 $\mu\text{H}^*$ | 3.83 pF*    | 3 | 2 mm | 1.5 mm | 954 mm | 50 mm | NA              | $4.85 \times 10^7 \text{ S m}^{-1}^*$ |
| Coil 3 | 1.17 $\mu\text{H}$   | 4.22 pF     | 4 | 5 mm | 1.5 mm | 935 mm | 35 mm | 3.34 m $\Omega$ | $4.86 \times 10^7 \text{ S m}^{-1}$   |
| Coil 3 | 1.14 $\mu\text{H}^*$ | 1.84 pF*    | 4 | 5 mm | 1.5 mm | 935 mm | 35 mm | NA              | $4.85 \times 10^7 \text{ S m}^{-1}^*$ |
| Coil 4 | 1.11 $\mu\text{H}$   | 3.30 pF     | 3 | 8 mm | 1.5 mm | 962 mm | 48 mm | 3.42 m $\Omega$ | $4.73 \times 10^7 \text{ S m}^{-1}$   |
| Coil 4 | 1.10 $\mu\text{H}^*$ | 2.14 pF*    | 3 | 8 mm | 1.5 mm | 962 mm | 48 mm | NA              | $4.85 \times 10^7 \text{ S m}^{-1}^*$ |

Figure 3.51: Self inductances and capacitances of measurement system elements, \*model value.

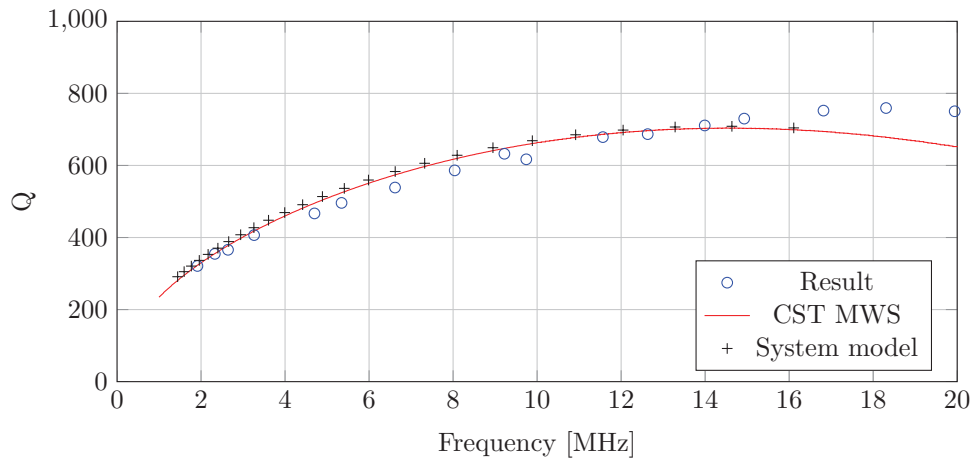


Figure 3.52: Transmission modelling and measurement comparison for reference coil 1.

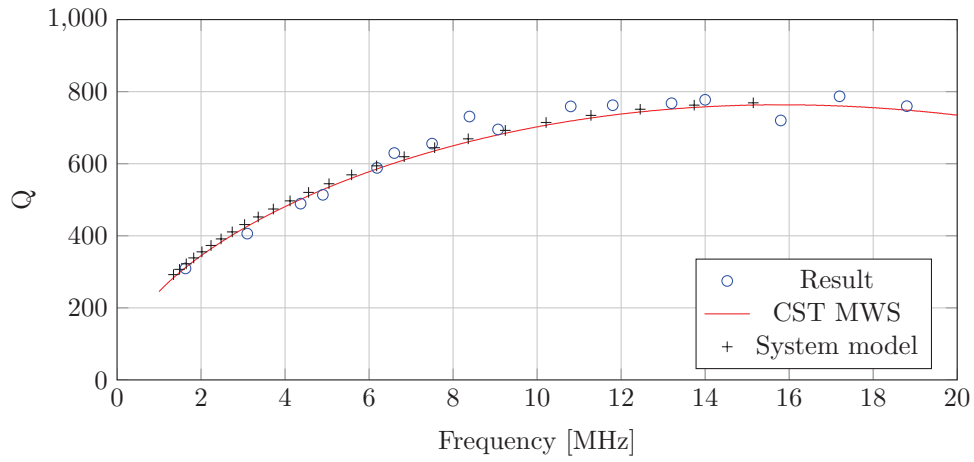


Figure 3.53: Transmission modelling and measurement comparison for reference coil 2.

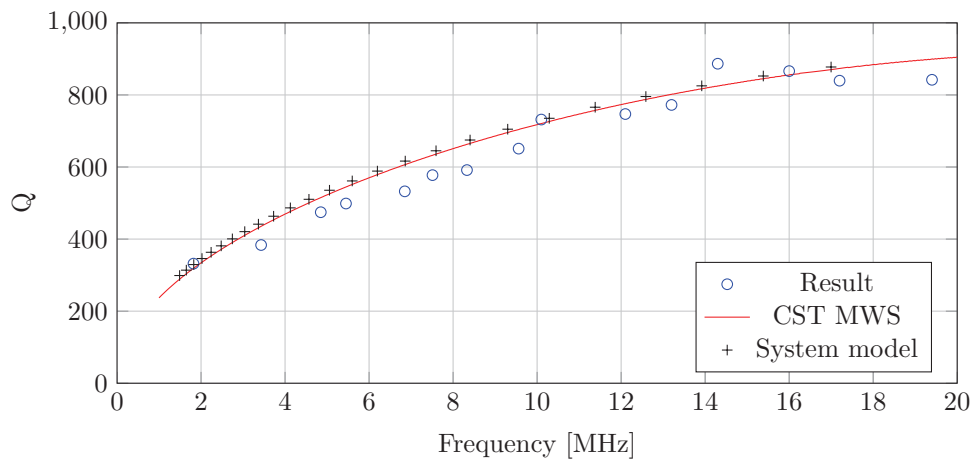


Figure 3.54: Transmission modelling and measurement comparison for reference coil 3.



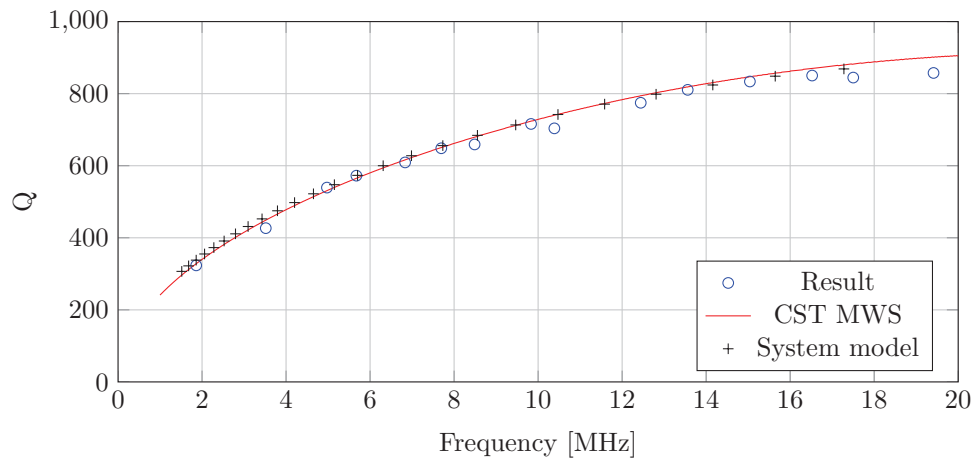


Figure 3.55: Transmission modelling and measurement comparison for reference coil 4.

### Measurement of electrically long $Q > 1000$ coil

A coil designed for maximum  $Q$  at 6.78 MHz has been measured in the same manner as the reference coils. This coil will be referred to as the long coil. The coil is designed to exhibit radiation dominated loss above 6.78 MHz and skin effect dominated loss below. The coil is loosely wound, so that the phase velocity is close to the speed of light. The frequency of maximal  $Q$  is primarily adjusted by altering the length of copper pipe used to construct the coil. As well as been electrically longer than the reference coils in the frequency range 1 MHz to 20 MHz this coil is constructed using larger diameter copper tube, resulting in a greater  $Q$ . However the tube is conventional plumbing pipe and so does not have controlled wall thickness. For this reason there is likely to be dimensional discrepancy between the EM simulation and the actual coil and as such this coil cannot be treated as a reference but instead is utilised as an illustration of the limitations of this measurement system.

The long coil has an outer radius,  $R_{Max}$  of 155 mm, a turn to turn gap  $s$ , of 10 mm. It's composed of 3 turns of 5 mm outer radius copper tubes with nominally 0.7 mm thick walls (manufacturer specification). The total length of the coil is 2.83 m, the measured conductivity of the tube is  $3.89 \times 10^7 \text{ S m}^{-1}$ .

The results have been plotted on a logarithmic frequency axis to show the low frequency skin effect loss dominated region ( $ESR \propto \omega^2$ ) and the high frequency radiation loss dominated region ( $ESR \propto \omega^4$ ) (fig. 3.56). Very good correspondence to simulation is observed in the low frequency region however the slope of high frequency region is only  $\omega^{-1.3}$  showing far less than the expected radiation loss. This could be caused by conducting the experiment in a non anechoic environment with many metallic objects within the near field (capacitive shorting). Regardless this region of operation is not very interesting for inductive power transfer as its below the point of peak efficiency and there is significant electric field close to the coils which interacts more strongly with typical matter than the magnetic field.

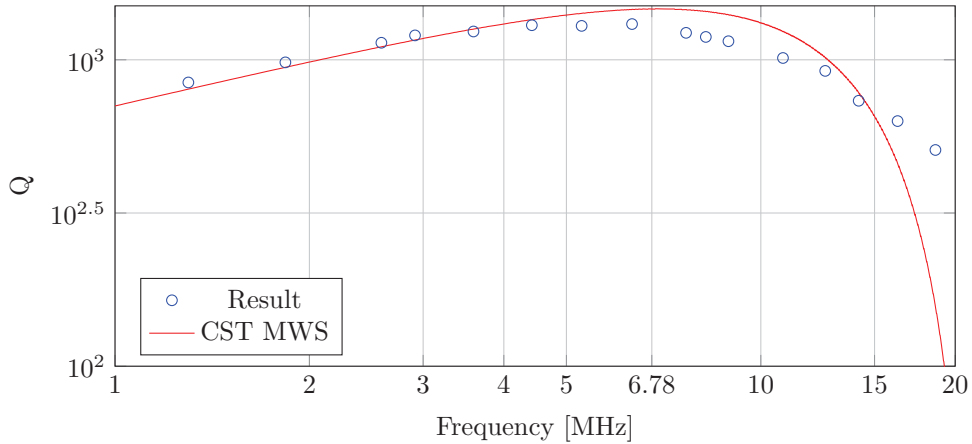


Figure 3.56: Transmission modelling and measurement comparison for long coil.

#### 3.8.4 Varying distance between coupling loops

The model of the measurement system is now used to explore the effect of varying the distance between the coupling loops upon the accuracy of the measurements. For this the model of the measurement system was utilised in conjunction with the modelled mutual inductances (Table 3.1). Fixed tuning capacitors of 470 pF and 120 pF were used to resonate the coils at approximately 6.78 MHz and 13.56 MHz respectively. The distance between the coupling loops was then varied in simulation by varying the coupling factors. The coil under test was always placed centred between the two coupling loops (identical coupling to each loop).

Even at 0.09 m distance the coupling between the loops was insufficient to cause significant shift in

| D [m] | MC1L [H] | MC2L [H] | MC3L [H] | MC4L [H] | kC1L     | kC2L     | kC3L     | kC4L     |
|-------|----------|----------|----------|----------|----------|----------|----------|----------|
| 0.045 | 5.56E-08 | 6.80E-08 | 4.40E-08 | 4.35E-08 | 1.13E-01 | 1.29E-01 | 9.20E-02 | 9.27E-02 |
| 0.065 | 3.63E-08 | 3.73E-08 | 2.88E-08 | 2.85E-08 | 7.36E-02 | 7.05E-02 | 6.03E-02 | 6.08E-02 |
| 0.085 | 2.40E-08 | 2.20E-08 | 1.93E-08 | 1.91E-08 | 4.86E-02 | 4.16E-02 | 4.03E-02 | 4.07E-02 |
| 0.105 | 1.62E-08 | 1.38E-08 | 1.33E-08 | 1.31E-08 | 3.29E-02 | 2.60E-02 | 2.78E-02 | 2.80E-02 |
| 0.125 | 1.13E-08 | 9.08E-09 | 9.39E-09 | 9.31E-09 | 2.29E-02 | 1.72E-02 | 1.97E-02 | 1.99E-02 |
| 0.145 | 8.11E-09 | 6.25E-09 | 6.83E-09 | 6.78E-09 | 1.64E-02 | 1.18E-02 | 1.43E-02 | 1.45E-02 |
| 0.165 | 5.97E-09 | 4.46E-09 | 5.09E-09 | 5.05E-09 | 1.21E-02 | 8.43E-03 | 1.07E-02 | 1.08E-02 |
| 0.185 | 4.49E-09 | 3.28E-09 | 3.88E-09 | 3.85E-09 | 9.11E-03 | 6.20E-03 | 8.12E-03 | 8.22E-03 |
| 0.205 | 3.45E-09 | 2.48E-09 | 3.01E-09 | 2.99E-09 | 7.00E-03 | 4.68E-03 | 6.31E-03 | 6.39E-03 |
| 0.225 | 2.70E-09 | 1.91E-09 | 2.38E-09 | 2.37E-09 | 5.49E-03 | 3.62E-03 | 4.99E-03 | 5.05E-03 |
| 0.245 | 2.15E-09 | 1.51E-09 | 1.91E-09 | 1.90E-09 | 4.37E-03 | 2.85E-03 | 4.00E-03 | 4.05E-03 |
| 0.265 | 1.74E-09 | 1.21E-09 | 1.56E-09 | 1.55E-09 | 3.53E-03 | 2.28E-03 | 3.26E-03 | 3.30E-03 |
| 0.285 | 1.42E-09 | 9.80E-10 | 1.28E-09 | 1.28E-09 | 2.89E-03 | 1.85E-03 | 2.68E-03 | 2.72E-03 |
| 0.305 | 1.18E-09 | 8.06E-10 | 1.07E-09 | 1.06E-09 | 2.39E-03 | 1.52E-03 | 2.23E-03 | 2.27E-03 |

Table 3.1: Modelled mutual inductances and coupling factors of coils to coupling loops. Distance is coil to coupling loop; the coils are placed centrally between the two coupling loops.

the coil resonant frequency. With the resonant frequency within 0.001% of the predicted frequency in all cases. Coil 1 resonates at 6.62 MHz and 12.9 MHz, coil 2 at 6.18 MHz and 12.1 MHz, coil 3 at 6.86 MHz and 13.5 MHz, coil 4 at 6.89 MHz and 13.7 MHz.

The results (Figs. 3.58, 3.59) show that for distances below 0.17m the  $Q$  is under estimated before converging to a value 1% greater than the actual  $Q$ . The under estimated  $Q$  can easily be rationalised by the method used to take into account the coupling treating the coupling as lossless, as the coupling becomes more significant at closer distances the error caused by the approximation becomes greater. Over reporting of the  $Q$  (as slight as it is) was found to be caused by the test loop to test loop coupling, this provides an alternate transmission path which results in an antiresonance after the resonant peak that causes and asymmetrical reduction in the resonant peaks bandwidth, increasing the measured  $Q$ .

To illustrate the anti resonance phenomenon, the measurement of  $|S_{21}|$  for coil 3 has been simulated, when the coupling loops are 0.61 m apart, with and without the coupling factor,  $k$ , between the test loops present ( $1.54 \times 10^{-4}$ ). It can be observed that the antiresonance, that is increasing the apparent  $Q$ , is not present when this coupling is removed (Fig. 3.57). Although interesting and showing the utility of simulating the measurement system, this phenomenon is no liable to be the dominant source of error the real world as component variability results in greater error.

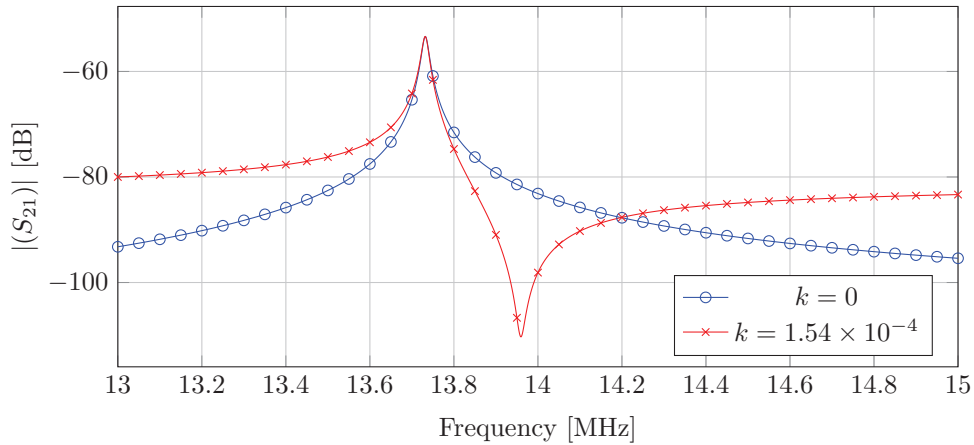


Figure 3.57: Comparison of modelled measurement system with and without test loop to test loop coupling

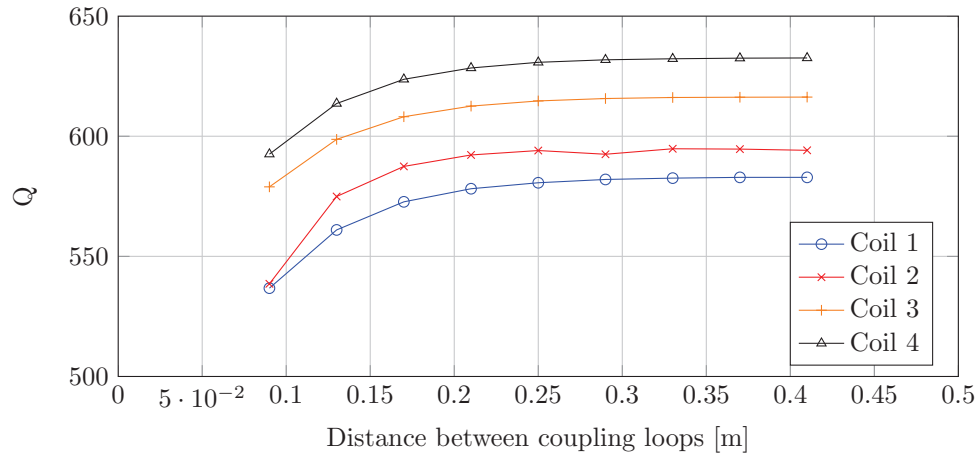


Figure 3.58: Variation in  $Q$  for modelled measurement system with test loop spacing, for 470 pF tuning capacitor. Actual  $Q$  is 574, 585, 607, 623 for coils 1 to 4, respectively.

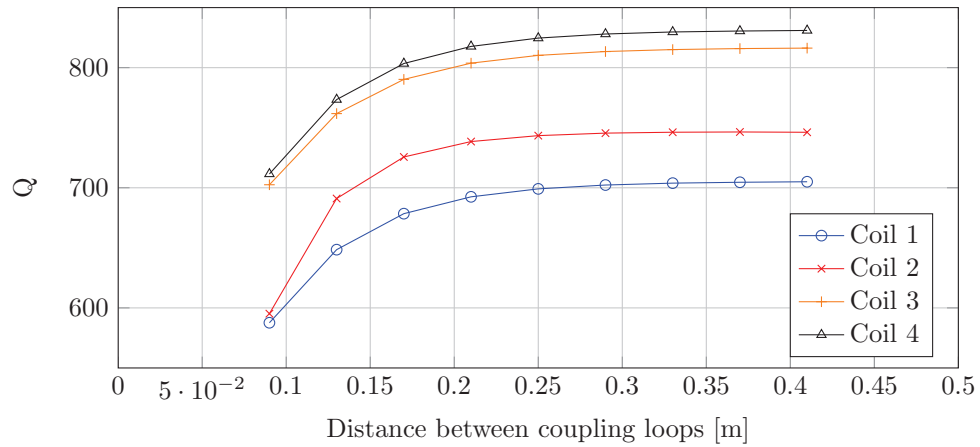


Figure 3.59: Variation in  $Q$  for modelled measurement system with test loop spacing, for 120 pF tuning capacitor. Actual  $Q$  is 698, 739, 808, 821 for coils 1 to 4, respectively.

### 3.9 Automatic measurement system

When using a resonant method to determine coil  $Q$  it is necessary to connect various different values of capacitance to the coil in order to find the coil  $Q$  over a range of frequencies, ideally these connections should not involve soldering and de-soldering capacitors. However specified maximum series resistance of RF relays is of the order of  $0.1\ \Omega$ , this would significantly degrade the measured  $Q$  of a typical IPT coil if it were placed in the measurement path. Furthermore the contact resistance of RF relays is inconsistent between switching cycles and therefore cannot be measured and removed [52]. Equation 3.56 states that a series impedance in the measurement path for a two port measurement and ideal VNA has no effect upon the to measured coil impedance. Therefore if instead of switching in the coil resonant path switching instead occurs in the measurement path the loss of an RF switch in the resonant circuit path is avoided. This is illustrated by figure 3.60 which shows the simplest case of two different resonant capacitors ( $C_1, C_2$ ). The coil is series resonated such that the real impedance at resonance is low, facilitating the use of the two port direct measurement technique.

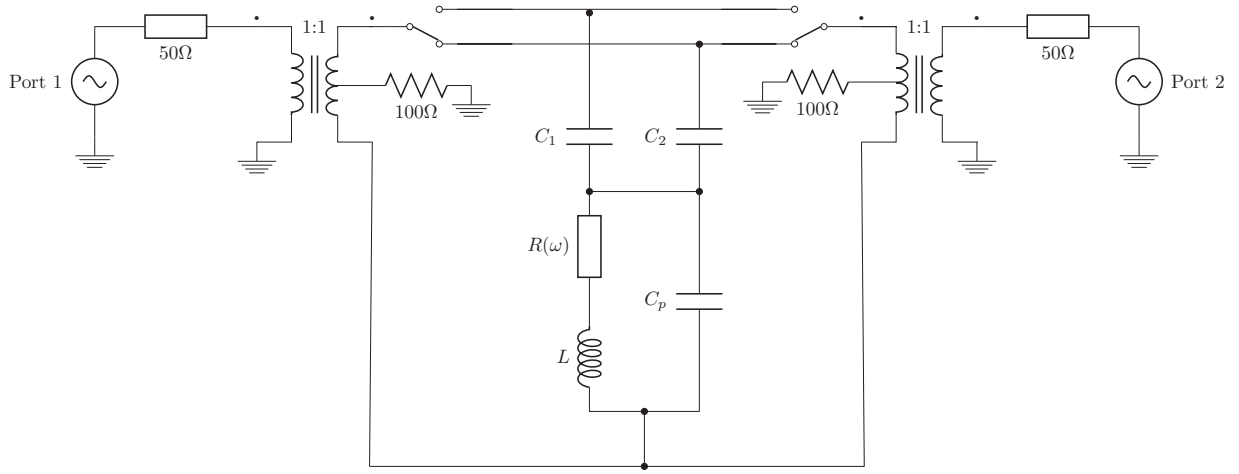


Figure 3.60: Automatic measurement system with two measurement channels.

#### 3.9.1 Connector repeatability

It will be necessary to disconnect and reconnect with test terminals to avoid solder connections to the coil under test. The Cliff Electronic Components CL159830CRA/CL159830CBA terminals were selected for this purpose. It is essential that these test terminals have good repeatability of connection to ensure that compensating the fixture short circuit resistance can be accurate. To this end  $Z_{21}$  and  $Z_{12}$  of a balun connected series test fixture has been measured ten times with a shorting bar in place of a series resonant coil. The shorting bar is disconnected and reconnected for each measurement and the standard deviation of the real part of the mean of  $Z_{21}$  and  $Z_{12}$  plot (fig. 3.61), as can be observed the test terminals have good repeatability. The reference coils have resistances as low as  $40\ \text{m}\Omega$  around  $1\ \text{MHz}$  but are above  $100\ \text{m}\Omega$  by  $10\ \text{MHz}$ , test terminal repeatability could therefore conceivably cause as much as 10% error in results at low frequencies. Repeatability could be improved by solder connection of the coil and calibration standards, however this would defeat the point of developing an easy to use automatic test system. I have decided to use these test terminals even though repeatability is marginally acceptable. If better quality results are required the earlier described transmission type measurement method can be used.

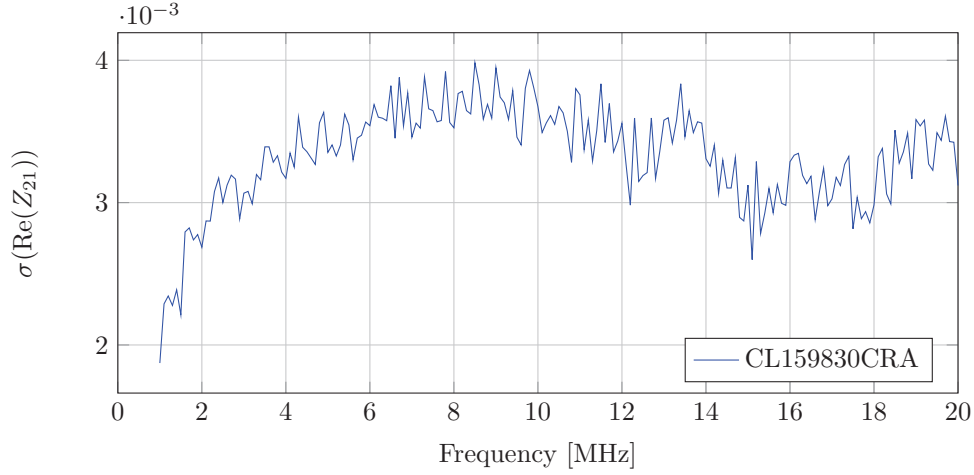


Figure 3.61: Real portion measurement standard deviation for shorting bar in series test fixture.

### 3.9.2 Shielding

A practical problem that has the potential to undermine measurement accuracy is magnetic coupling of PCB traces to the coil under test. To test for this  $S_{21}$  is measured to an AARONIA 50 mm magnetic (H) field probe PBS-H4 placed 50 mm above a test board consisting of a single measurement channel from one of test ports with the other terminated in  $50\Omega$ . The shielding effectiveness is found by comparison to the unshielded case. This test board has provision for shielding cans over the baluns; furthermore a copper sheet can be soldered to the shielding cans providing an electrically thick conductive plane over the entire circuit. The shielding cans alone (which mainly cover the baluns) were found to offer minimal shielding effect. Covering the micro strip with the complete copper plane was found to offer approximately 30 dB of attenuation (Fig. 3.62). This shows that the majority of the coupling to the coil under test is from the PCB tracks and therefore the automatic measurement system should be fully enclosed to prevent inductive coupling to the coil under test. Small openings are necessary for ports but would not significantly reduce shielding.

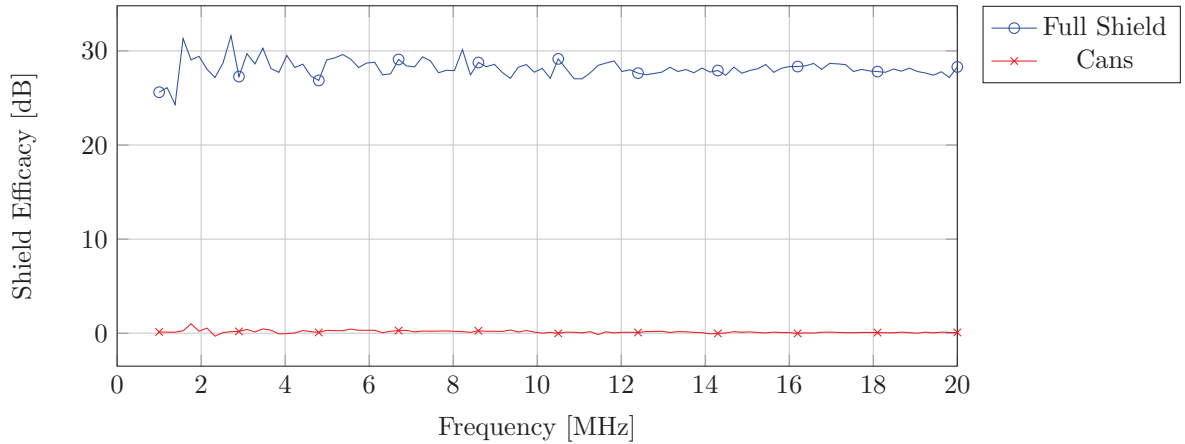


Figure 3.62: Shielding efficacy results showing the majority of the magnetic coupling is between the coil and the PCB tracks.

### 3.9.3 Calibration

Each measurement path has associated inductive, resistive and capacitive residual parasitics that alter the measured impedance. These can be compensated by measuring a short circuit (shorting bar), open circuit (test terminals open) and a known load (characterised resistor). If we represent the measurement fixture as a two port ABCD matrix [53] the equation to correct each measured impedance is:

$$Z = Z_l \frac{1 - \frac{Z_{lm}}{Z_{om}}}{\frac{Z_{lm}}{Z_{om}} - \frac{Z_m - Z_{sm}}{1 - \frac{Z_m}{Z_{om}}}} \quad (3.67)$$

Where  $Z$  is the corrected impedance,  $Z_m$  is the measured impedance,  $Z_{lm}$  and  $Z_l$  are the measured load impedance and actual load impedance respectively,  $Z_{om}$  and  $Z_{sm}$  are the measured short and open impedances. The test standards need only be measured once for each measurement channel and frequency point. The fixture should not have radically changing properties with frequency as its electrically small, therefore it is acceptable to interpolate if the frequency spacing is altered. For testing purposes the fixture residuals are recorded with the same 10,001 points linearly spaced from 1 MHz to 20 MHz as the measured results.

### 3.9.4 Measurement procedure

To measure a coil the short open and load standards have to be measured for each measurement path as the parasitic properties of each measurement path are different. As the fixture does not change and the VNA is calibrated to the fixture this procedure only needs to be done once. The measurements of the standards are used to correct the measured coil impedance. The short comprises a copper shorting bar, the open the two terminals disconnected and the load a  $47\Omega$  resistor that has been characterised using a leaded component fixture and impedance analyser. The following measurement procedure was used for the initial measurements:

1. Firstly the reference plane is relocated to end of test cables, there is no need to de-embed the baluns as they will be compensated for by the SOL fixture correction. It is recommended for a sweep from 1 MHz to 20 MHz at least 10,001 points are used to accurately find the resonant frequency and that a 1 kHz IF bandwidth or lower is used to ensure good S-parameter accuracy.
2. Secondly short open and load fixture standards are measured in each measurement path.
3. The device to be tested is then measured in each measurement path.
4. Equation 3.67 is used to compensate each the measurement.

### 3.9.5 Initial measurements

To test if series measurement of a coil is viable a single measurement channel has been constructed and short open load calibration performed to measure reference coil 3 (Table. 3.63). In this case the tuning capacitor is soldered in series with the coil beyond the calibration plane of the fixture.

To save time there are a number of differences between this fixture and the automatic measurement system: Firstly the test terminals are screwed into the PCB rather than soldered, secondly the non-ideality of the load standard is not characterised (it is assumed resistive), thirdly the location of the test terminals has prevented direct connection of the coil under test, finally the short standard is a length of thick wire between the terminals.

Additional short length of wire are used to connect the coil. They have been characterised by measurement without resonant capacitor, however despite their short length their  $Q$  is high and therefore instead of

measuring their loss resistance at high frequency the result at 1 MHz is extrapolated (where the  $Q$  is lower) assuming the losses are due to skin effect. It is assumed the additional wire does not increase the effective coil capacitance.

Taking into account all these limitations the results (Fig. 3.63) are quite promising with the coil resonant frequency found correctly and measurements of coil resistance often within 15% of that simulated. As has been previously shown this far exceeds what is possible using an impedance analyser. The results are expected to improve with the final automatic system due to its less compromised construction reducing uncertainties, however test terminal repeatability is likely to be a persistent issue at lower frequencies.

| Tuning Capacitor | $f_0$     | $f_0$ (Corrected) | $f_0$ (Predicted) | R $f_0$         | R CST           |
|------------------|-----------|-------------------|-------------------|-----------------|-----------------|
| 1446 pF          | 3.795 MHz | 3.868 MHz         | 3.872 MHz         | 65.1 m $\Omega$ | 60.7 m $\Omega$ |
| 856.6 pF         | 4.933 MHz | 5.027 MHz         | 5.025 MHz         | 84.3 m $\Omega$ | 69.5 m $\Omega$ |
| 455.0 pF         | 6.745 MHz | 6.874 MHz         | 6.880 MHz         | 91.9 m $\Omega$ | 81.9 m $\Omega$ |
| 313.3 pF         | 8.120 MHz | 8.273 MHz         | 8.275 MHz         | 103 m $\Omega$  | 90.8 m $\Omega$ |
| 120.7 pF         | 12.94 MHz | 13.18 MHz         | 13.19 MHz         | 157 m $\Omega$  | 122 m $\Omega$  |

Figure 3.63: Initial series coil measurements of coil 3 using single channel prototype.

### 3.9.6 Two channel prototype

#### Introduction

The basic series resonant measurement technique with one channel has been demonstrated. The next phase is to repeat the work but with a measurement system with two channels (Figs. 3.60, 3.64). This system has been constructed with far more mechanical stability than the single channel PCB used for the initial series resonant measurements. The test terminals have been arranged in such a manner that they have the same reference plane as a Keysight leaded component 16047E test fixture. A set of reference standards have been constructed that are compatible with the two channel prototype and also the 16047E test fixture, this allows the test standards to be characterised, minimising residual errors. There are four standards; open, short load and verification (insert Fig. 3.64). The additional verification standard allows comparison between the automatic measurement system prototype and the Keysight E4990A impedance analyser.

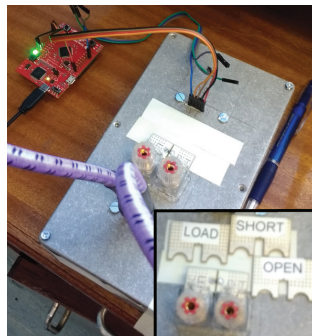


Figure 3.64: Two channel measurement system prototype, controlled by microprocessor development board. Insert shows reference standards.

This two channel prototype uses Pickering 103GM-1-A-5/2D relays to switch between measurement channels. The relays are controlled by serial connected relay drivers to a microcontroller development board (TI EK-TM4C123GXL) that is controlled via a MATLAB program that also controls the R&S ZBV4 VNA. Thus measurements are performed and processed automatically.



## Testing

The measurement standards have been measured using a Keysight E4990A and 16047E test fixture (Figs. 3.65, 3.66, 3.67). The Short, Open and Load standards are then measured (Figs. 3.68, 3.69, 3.70) by the prototype for both channels (a total of 6 measurements), for these measurements the tuning capacitors are replaced by short circuits. These measurements are used to correct measurements of the Verification standard conducted using the two test channels (Fig. 3.71).

It can be observed that the measurements for both channels correspond closely to the measurement conducted using the impedance analyser, displaying slightly more trace noise (However this could be reduced by smoothing or lower IF bandwidth or averaging). Crucially however the prototype has the capability to switch test channels and operates in a balanced manner. The uncorrected measurements from the prototype are unusual because one of the channels is phase reversed, this has no effect on the results after correction.

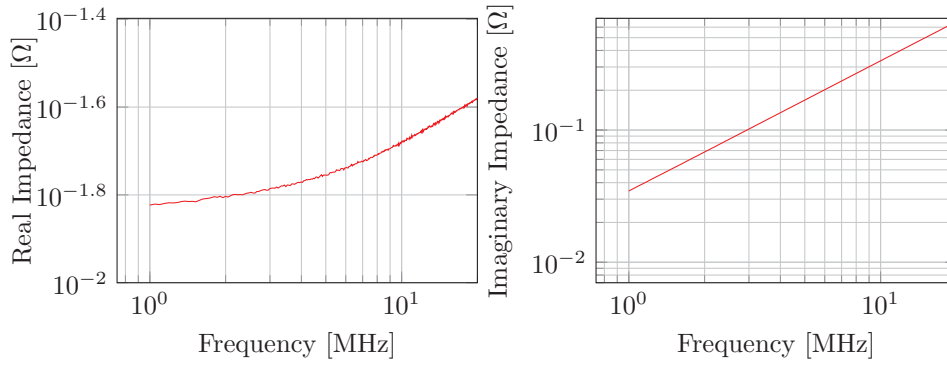


Figure 3.65: Measurement of Short standard using calibrated impedance analyser.

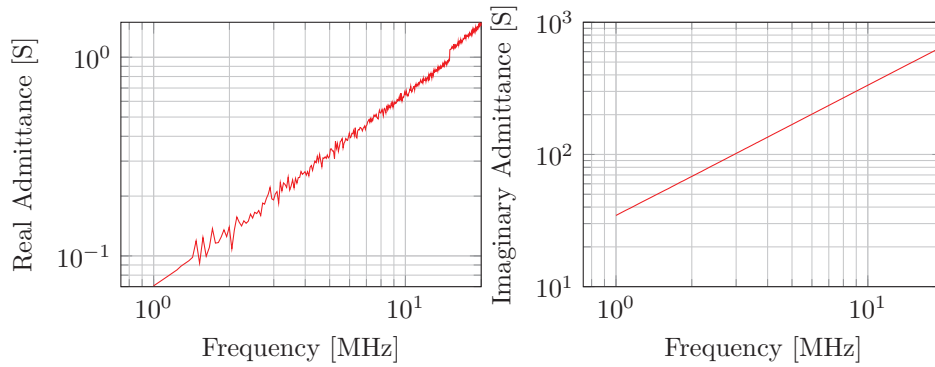


Figure 3.66: Measurement of Open standard using calibrated impedance analyser.

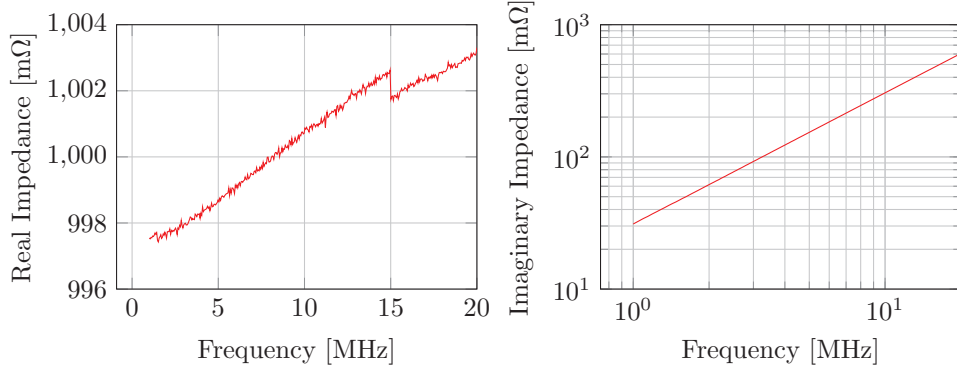


Figure 3.67: Measurement of Load standard using impedance analyser.

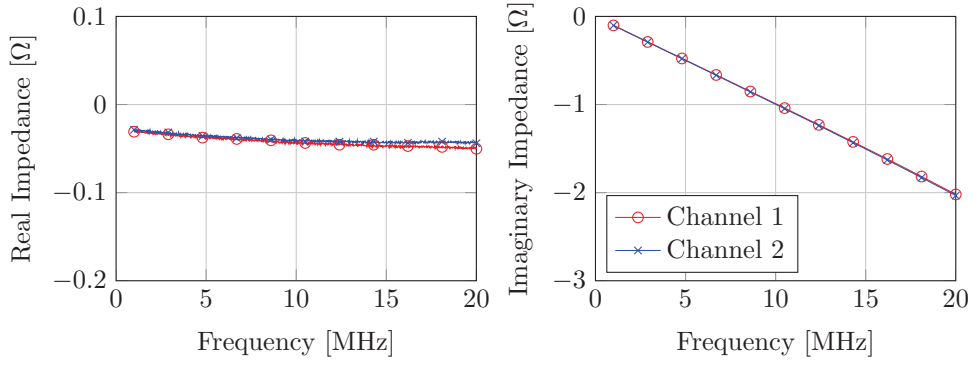


Figure 3.68: Measurement of Short standard using two channel prototype with no error correction.

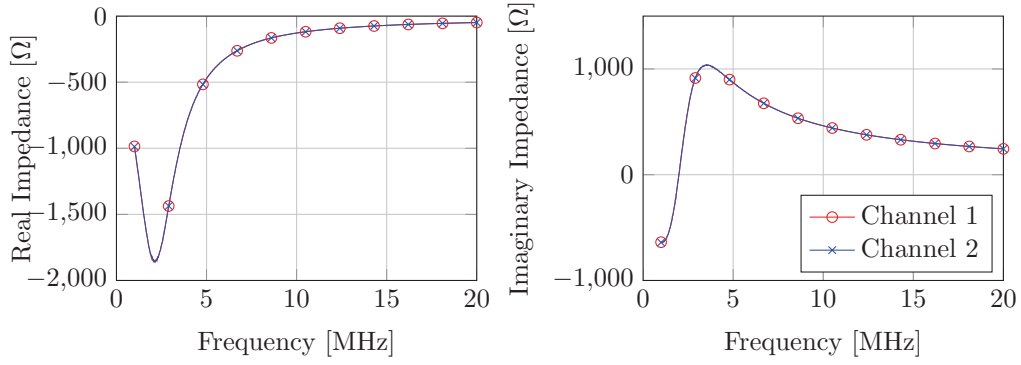


Figure 3.69: Measurement of Open standard two channel using using prototype with no error correction.

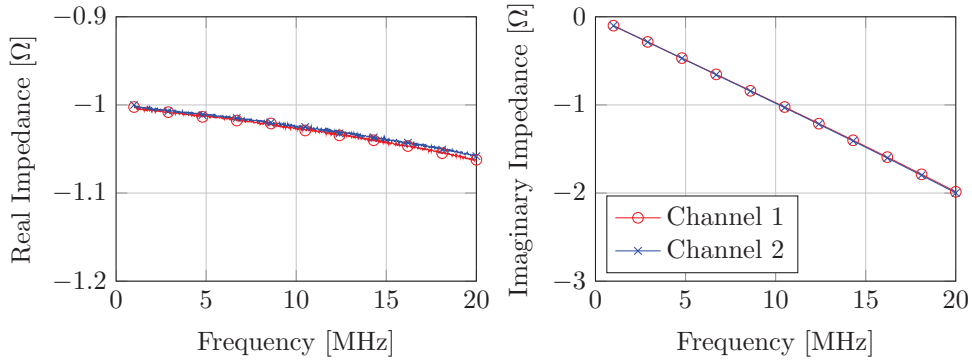


Figure 3.70: Measurement of Load standard using two channel prototype with no error correction.

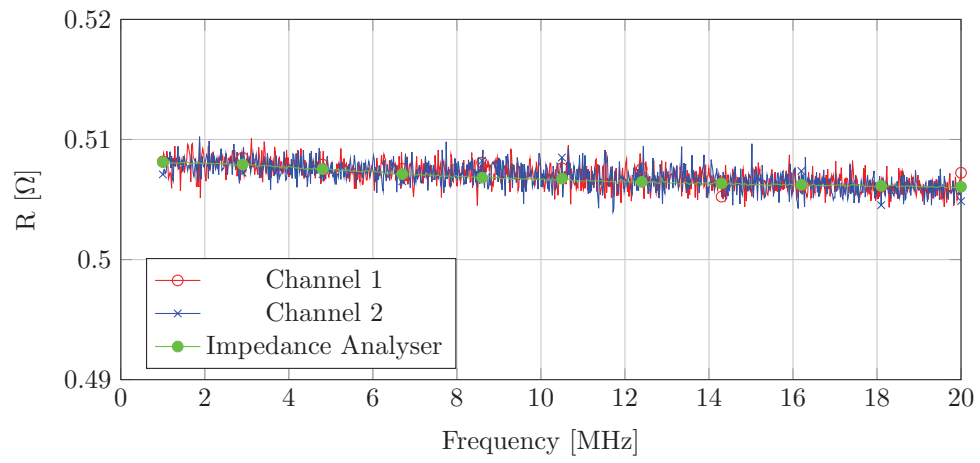


Figure 3.71: Measurements of Verification standard. This shows that the two terminal measurement system can resolve resistances similar to that of a coil at resonance while switching its measurement channel.

## Problems with progressing to full switched coil measurements

When measuring a coil in an automatically switched manner the calibration measurements are performed with a short in place of the capacitor of the channel under calibration, while the other channels still have their capacitors in place. For the measurements all the shorts replaced with capacitors. The coil is measured and the measurements where the capacitor was replaced with a short used to compensate the result. Unexpectedly the result from this was approximately three times greater than expected.

The issue I think is that the capacitor is within the fixture (behind the calibration plane). Specifically I suspect shunt capacitance causes a voltage divider effect. Correcting these measurements remains an unresolved issue.

### 3.9.7 Calibration theory

#### Problem Statement

Standard impedance analyser short open load calibration has been found to be insufficient to correct the fixture (Fig. 3.73) for series resonant coil measurements. This is because of the tuning capacitor embedded inside the fixture as per figure 3.72. When then fixture is measured with the Short, Open and Load (SOL) standards connected we are producing a correction for the overall matrix  $\mathbf{X}$ . However a portion of the fixture lies beyond the capacitor (Matrix  $\mathbf{C}$ ).

When the SOL standards are measured with the series capacitor installed they are not accurately measured due to the series impedance of the capacitor. If the standards are measured with the capacitor replaced by a short and standard compensation theory used to correct results with the capacitor present the compensated results are not accurate. This is because part of the fixture ( $\mathbf{C}$ ) lies beyond the capacitor ( $\mathbf{B}$ ).

An alternative approach is proposed to make six measurements for each measurement channel. The issue of been unable to accurately determine the SOL standards with the capacitor present is avoided. Firstly the overall fixture matrix is determined in both cases, with the capacitor connected and without the capacitor connected. From these results the matrix  $\mathbf{B}$  is found and used to construct the matrix used to correct the result  $\mathbf{ABC}$ .

When taking a two port measurement the measured quantity is a two port S-parameter matrix of the fixture and load connected in shunt to the two the ports; the impedance of the fixture with connected load is given by  $Z_{21}$  of the transformation of this matrix to Z-parameters. This quantity shall be referred to as  $Z_{IN}$  as it represents the input impedance of  $\mathbf{X}$ .  $Z_{IN}$  can be transformed back into  $50\ \Omega$   $Z_0$  S-parameters to give  $\Gamma_{in}$  of figure 3.72.

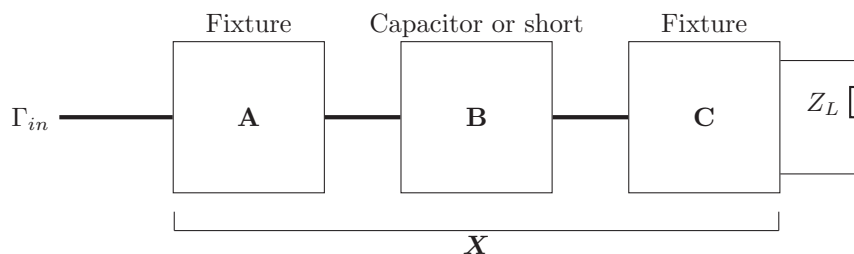


Figure 3.72: Fixture and device under test

For clarity all diagrams in this section are drawn single ended and not differential. Although we measure a quantity using a differential excitation the S-parameter matrix we are fundamentally measuring using the VNA is single ended and therefore it is simpler to consider the fixture as single ended, even though internally it's differential.

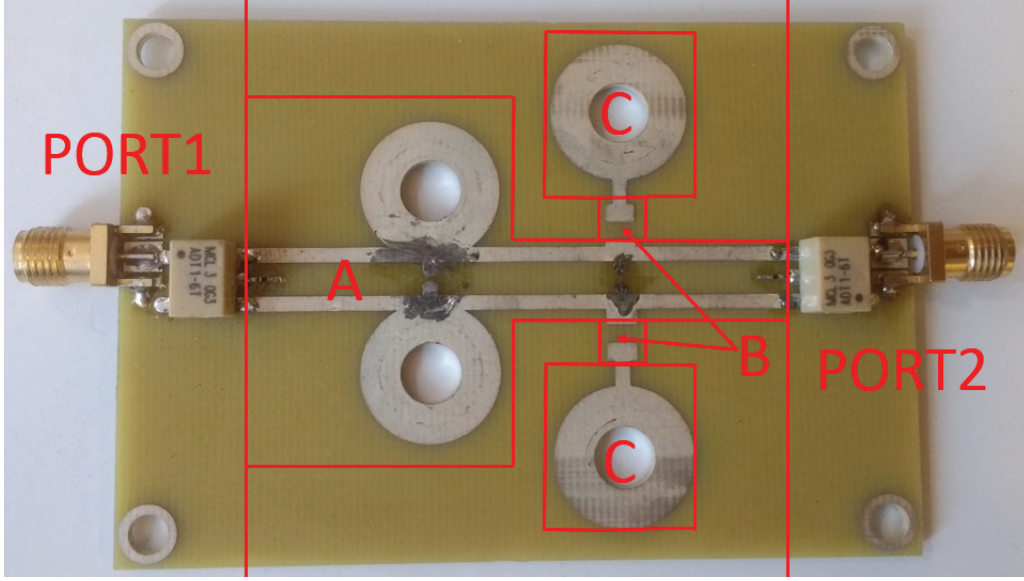


Figure 3.73: Example of a simple fixture that the model of figure 3.72 can be applied to

### Method of finding matrix $\mathbf{X}$

In order to find the constituent matrices  $\mathbf{A}$ ,  $\mathbf{B}$  and  $\mathbf{C}$  the first step is to find  $\mathbf{X}$ . To do this we employ the method of Ou and Caggiano [54] to find the S-parameters of a two port network by measurement with Short Open and Load standards. However their method assumes an ideal matched load is available while our load standard is complex in nature. To allow the usage of any load standard we use the same correction equations but with the reference impedance at each frequency point set to the load standards impedance (complex reference impedance). When the coefficients have been calculated we convert back to a conventional  $50\Omega$  reference impedance. Measurements undertaken are:  $\Gamma_S$  (Short standard connected),  $\Gamma_\infty$  (Open standard connected),  $\Gamma_L$  (Load standard connected). The first stage in the calculation is to transform the measured reflection coefficients,  $\mathbf{S}$ , to reference impedance  $Z_L$  using the general transform (functional on N-port systems, with differing per port reference impedance):

$$\mathbf{S}' = \mathbf{D}^{-1} \cdot (\mathbf{S} - \mathbf{R}) \cdot (\mathbf{I} - \mathbf{R} \cdot \mathbf{S})^{-1} \cdot \mathbf{D}, \quad (3.68)$$

where  $\mathbf{I}$  is the identity matrix,

$$\mathbf{R} = \begin{pmatrix} \Gamma(Z_1) & 0 & \cdots & 0 \\ 0 & \Gamma(Z_2) & \cdots & 0 \\ \vdots & \vdots & \ddots & \vdots \\ 0 & 0 & \cdots & \Gamma(Z_n) \end{pmatrix}, \quad (3.69)$$

$$\Gamma(Z_n) = \frac{Z_n - Z_{n,before}}{Z_n + Z_{n,before}}, \quad (3.70)$$

where  $Z_{n,before}$  is the port reference impedance before normalisation and  $Z_n$  is the new port reference impedance. In our case the previous port reference impedance is the standard  $50\Omega$  and the new port reference impedance is  $Z_L$  at the particular frequency point we are renormalising. Finally the  $\mathbf{D}$  matrix is given by:

$$\mathbf{D} = \begin{pmatrix} D_1 & 0 & \cdots & 0 \\ 0 & D_2 & \cdots & 0 \\ \vdots & \vdots & \ddots & \vdots \\ 0 & 0 & \cdots & D_n \end{pmatrix}, \quad (3.71)$$

$$D_n = \sqrt{\frac{Z_n}{Z_{n,before}}} \cdot \frac{1}{Z_n + Z_{n,before}}. \quad (3.72)$$

Once the reflection coefficients for the Short, Open and Load standards have been transformed to the reference impedance of the load standard we can then find  $\mathbf{X}$ :

$$\mathbf{X}_{S_{11}} = \Gamma_L, \quad (3.73)$$

$$\mathbf{X}_{S_{22}} = \frac{\Gamma_S + \Gamma_\infty - 2\Gamma_L}{\Gamma_\infty - \Gamma_S}, \quad (3.74)$$

As  $S_{21} = S_{12}$  for our passive fixture:

$$\mathbf{X}_{S_{21}} = \sqrt{\frac{2(\Gamma_\infty - \Gamma_L)(\Gamma_L - \Gamma_S)}{\Gamma_\infty - \Gamma_S}}. \quad (3.75)$$

There is a choice of root in the above equation, to select the correct root examine the angle of  $\Gamma_L$  (after normalisation to  $Z_L$ ) at the lowest available frequency. If the angle is positive the positive root is selected, if negative the negative. This method assumes the phase has not wrapped from DC, therefore data below the first resonance must be captured.

### Method of finding constituent matrices $\mathbf{A}$ , $\mathbf{B}$ and $\mathbf{C}$

By transforming  $\mathbf{X}$  and its constituent matrices into its cascade parameter representation:

$$\mathbf{X} = \mathbf{A} \cdot \mathbf{B} \cdot \mathbf{C}. \quad (3.76)$$

Matrix  $\mathbf{B}$  has a known cascade parameter representation, in the case of a short it is simply the identity matrix and in the case of a the tuning capacitor;

$$\mathbf{B}_C = \begin{pmatrix} 1 & \epsilon_{sr} + \frac{1}{j\omega C} \\ 0 & 1 \end{pmatrix}, \quad (3.77)$$

and for the short;

$$\mathbf{B}_S = \begin{pmatrix} 1 & 0 \\ 0 & 1 \end{pmatrix}. \quad (3.78)$$

Therefore;

$$\mathbf{X} = \begin{pmatrix} a_A & b_A \\ c_A & d_A \end{pmatrix} \cdot \mathbf{B} \cdot \begin{pmatrix} a_C & b_C \\ c_C & d_C \end{pmatrix}, \quad (3.79)$$

The SOL standards are measured with the short of the capacitor installed to produce six results per measurement channel, this is insufficient information to solve for the coefficients  $a_A, b_C$  etc. as the equations are linearly dependent. However we can make some assumptions about the nature of  $\mathbf{C}$ ; we know that its electrically short and has some series inductance and resistance, however the greatest measurement disruption would be caused by a voltage divider effect, caused by shunt capacitance. Therefore we approximate

$\mathbf{C}$  as a shunt component therefore;  $a_C = 1, d_C = 1$ . Then subtract the result of the short,  $\mathbf{X}_S$ , from the result with the capacitor in place,  $\mathbf{X}_C$ :

$$\begin{pmatrix} a_{X_C} - a_{X_S} & b_{X_C} - b_{X_S} \\ c_{X_C} - c_{X_S} & d_{X_C} - d_{X_S} \end{pmatrix} = \begin{pmatrix} (\epsilon_{sr} + \frac{1}{j\omega C})c_C a_A & (\epsilon_{sr} + \frac{1}{j\omega C})a_A \\ (\epsilon_{sr} + \frac{1}{j\omega C})c_C c_A & (\epsilon_{sr} + \frac{1}{j\omega C})c_A \end{pmatrix}, \quad (3.80)$$

By inspection:

$$c_A = \frac{d_{X_C} - d_{X_S}}{(\epsilon_{sr} + \frac{1}{j\omega C})}, \quad (3.81)$$

$$a_A = \frac{b_{X_C} - b_{X_S}}{(\epsilon_{sr} + \frac{1}{j\omega C})}, \quad (3.82)$$

$$c_C = \frac{c_{X_C} - c_{X_S}}{d_{X_C} - d_{X_S}}. \quad (3.83)$$

The network is reciprocal therefore  $ad - bc = 1$  allowing the calculation of the remaining coefficient of matrix  $\mathbf{C}$ ;

$$b_C = 0. \quad (3.84)$$

Now in both the short and capacitor case we have the complete  $\mathbf{X}$ ,  $\mathbf{B}$  and  $\mathbf{C}$  matrices. We can now find  $\mathbf{A}$  as;

$$\mathbf{A} = \mathbf{X} \cdot \mathbf{C}^{-1} \cdot \mathbf{B}^{-1}. \quad (3.85)$$

### Correcting the measurement result

To correct the measurement result we collapse the two port network  $\mathbf{X}_C$  with connected coil impedance  $Z_L$  to a single port result  $Z_{IN}$ . The input impedance to this matrix is found by solving from the Z-parameter definitions:

$$Z_{11}I_1 + Z_{12}I_2 = V_1, \quad (3.86)$$

$$Z_{21}I_1 + Z_{22}I_2 = V_2. \quad (3.87)$$

The presence of the load forces the following constraints:

$$V_2 = -\frac{I_2}{Z_L}, \quad (3.88)$$

$$Z_{IN} = \frac{V_1}{I_1}. \quad (3.89)$$

Solving the equations for  $Z_L$ :

$$Z_L = \frac{Z_{12}Z_{21}}{Z_{11} - Z_{IN}} - Z_{22}. \quad (3.90)$$

$Z_{12}$ ,  $Z_{21}$ ,  $Z_{11}$  and  $Z_{22}$  are found by conversion of the earlier calculated fixture matrices  $\mathbf{A} \cdot \mathbf{B} \cdot \mathbf{C}$ , while  $Z_{IN}$  is from the the measured  $Z_{IN}$  with the coil connected at the frequency point where the measured imaginary impedance is 0.

### Simulated example

To illustrate the calculation flow and errors that can be corrected using the described techniques an example has been solved (Fig. 3.74). To show that series loss and reactance has no effect on the result elements  $L_1$

and  $R_1$  are added to the switched path. Matrix  $\mathbf{A}$  is represented by the lumped elements  $L_2$ ,  $C_1$ ,  $R_2$ . The tuning capacitor represented by matrix  $\mathbf{B}$  is  $C_2$ , in the case of  $\mathbf{X}_C$  the capacitor is present, in the case of  $\mathbf{X}_S$  it is replaced with a short. The final parasitic component is  $C_3$ , a shunt capacitance, representing matrix  $\mathbf{C}$ . The load  $Z_L$  represents the coil.

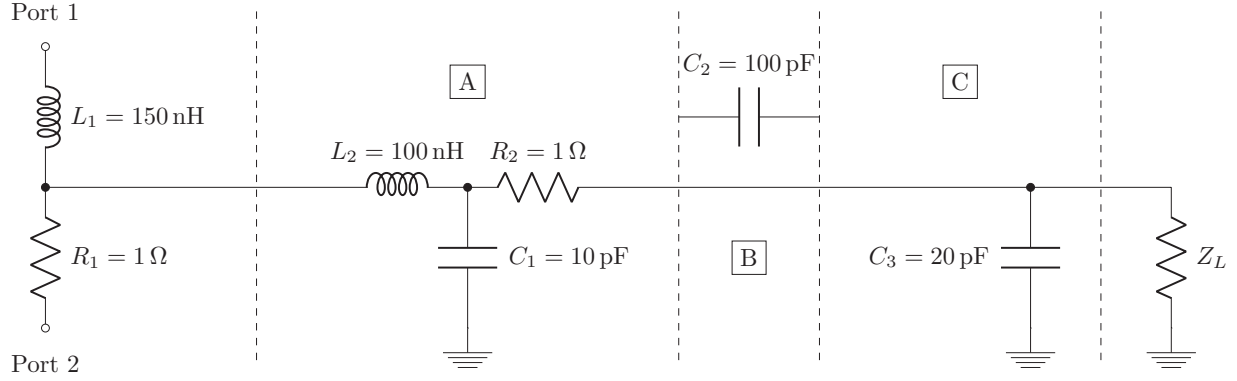


Figure 3.74: Simulated example showing correctable parasitic elements, for what each element corresponds to physically see figure 3.72 and 3.73

Firstly  $Z_{21}$  is found (Figs. 3.75 - 3.79) for both the  $\mathbf{X}_S$  (short in place of tuning capacitor) and  $\mathbf{X}_C$  results (tuning capacitor in place) with the SOL standards connected. The matrices  $\mathbf{X}_C$  and  $\mathbf{X}_S$  are then found (Figs. 3.81 - 3.86) using these results. The next step is to de-embed the constructed  $\mathbf{A} \cdot \mathbf{B} \cdot \mathbf{C}$  from the result of  $\mathbf{X}_C$  with the coil connected (Fig. 3.80) giving the true coil impedance (Fig. 3.93). The real part of the coils impedance will be most accurate at the first zero crossing of the uncorrected imaginary impedance of  $\mathbf{X}_C$ .

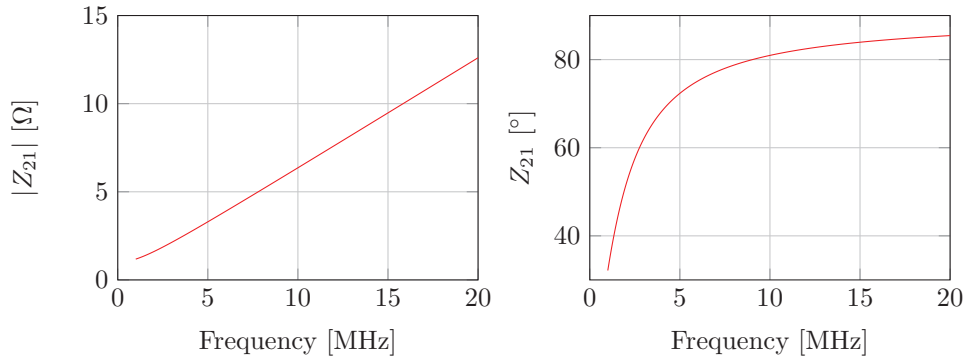


Figure 3.75: Uncorrected measurement of  $\mathbf{X}_S$  with Short circuit termination



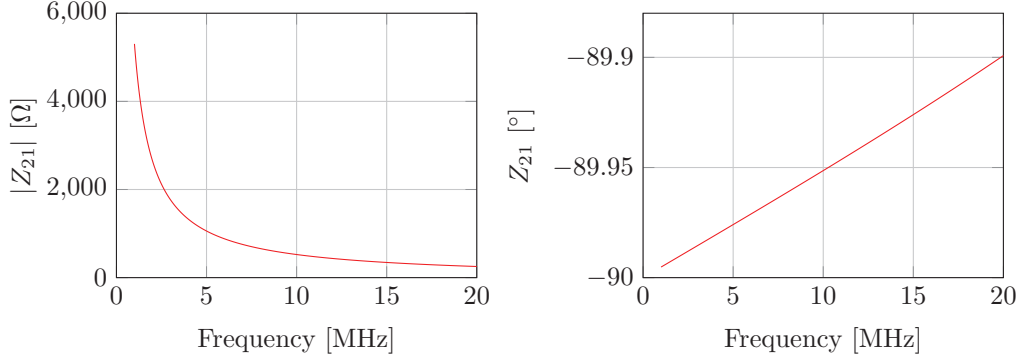


Figure 3.76: Uncorrected measurement of  $\mathbf{X}_{\mathcal{S}}$  with Open circuit termination

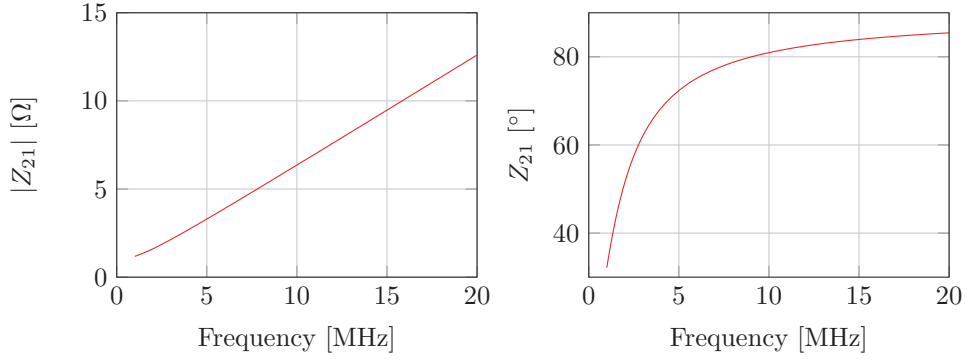


Figure 3.77: Uncorrected measurement of  $\mathbf{X}_{\mathcal{S}}$  with Load circuit termination

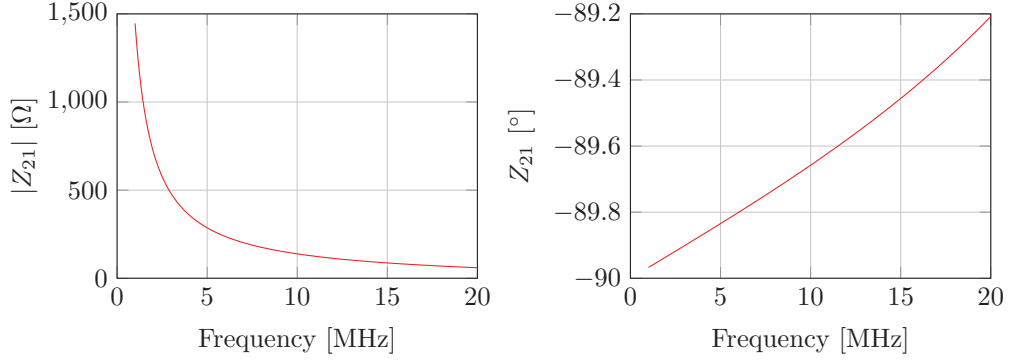


Figure 3.78: Uncorrected measurement of  $\mathbf{X}_{\mathcal{C}}$  with Short circuit termination

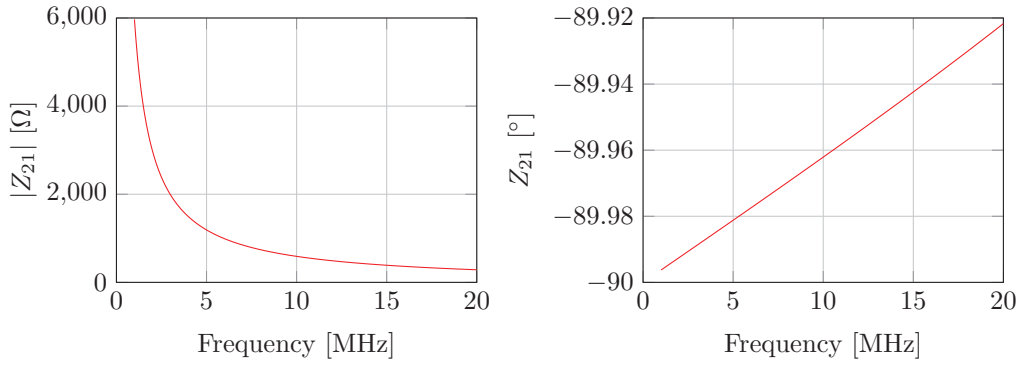


Figure 3.79: Uncorrected measurement of  $\mathbf{X}_{\mathcal{C}}$  with Open circuit termination

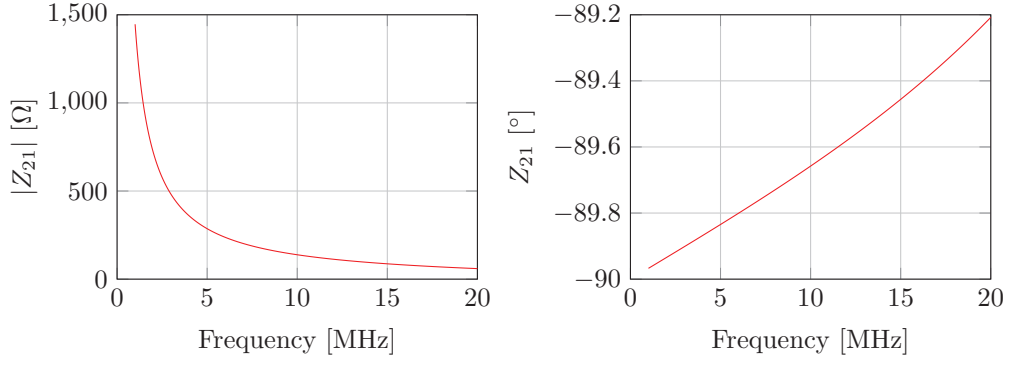


Figure 3.80: Uncorrected measurement of  $\mathbf{X}_C$  with Load circuit termination

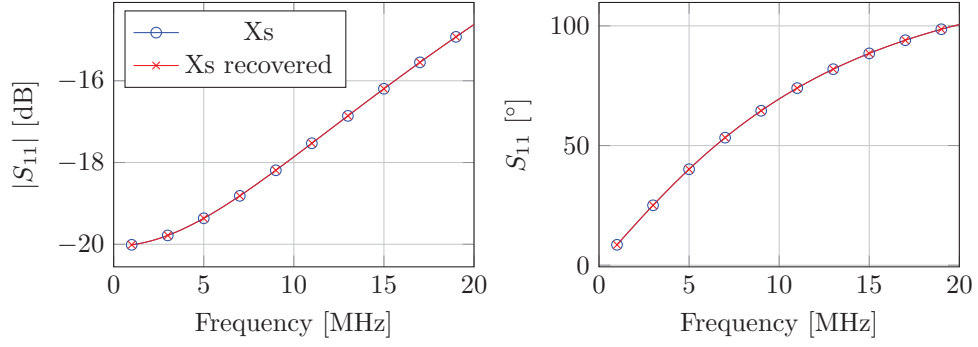


Figure 3.81:  $S_{11}$  parameter of  $\mathbf{X}_S$  recovered from SOL standard measurements compared with  $S_{11}$  of original  $\mathbf{X}_S$

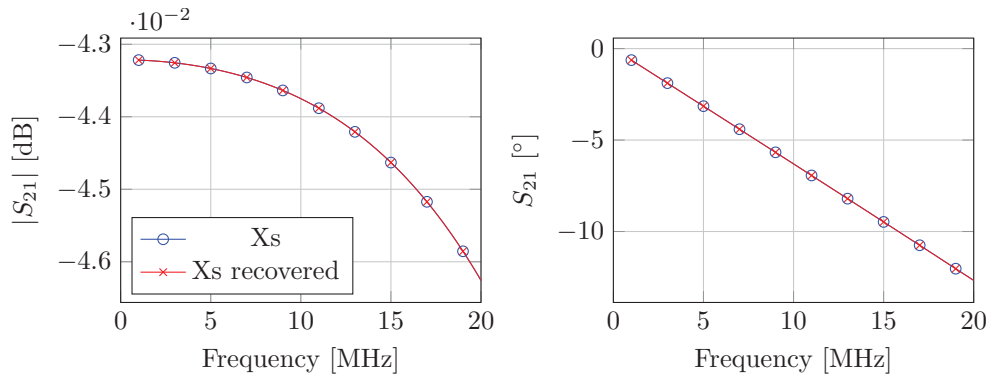


Figure 3.82:  $S_{21}$  parameter of  $\mathbf{X}_S$  recovered from SOL standard measurements compared with  $S_{21}$  of original  $\mathbf{X}_S$

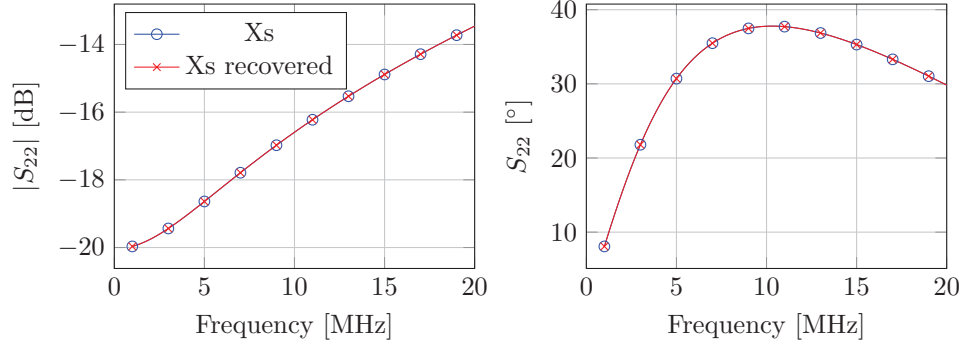


Figure 3.83:  $S_{22}$  parameter of  $\mathbf{X}_S$  recovered from SOL standard measurements compared with  $S_{22}$  of original  $\mathbf{X}_S$

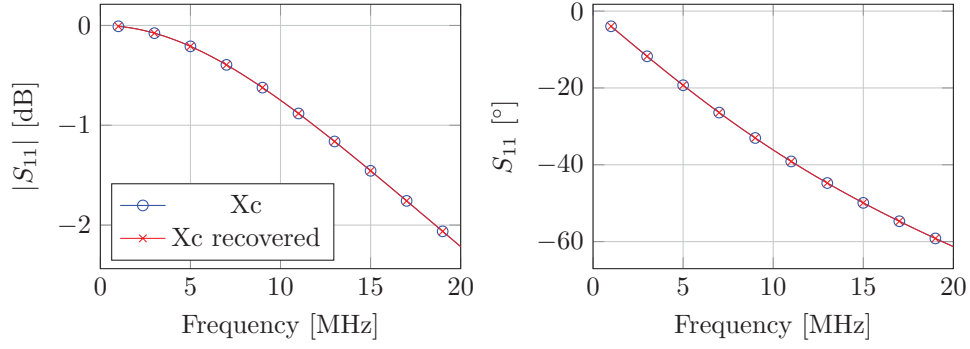


Figure 3.84:  $S_{11}$  parameter of  $\mathbf{X}_C$  recovered from SOL standard measurements compared with  $S_{11}$  of original  $\mathbf{X}_C$

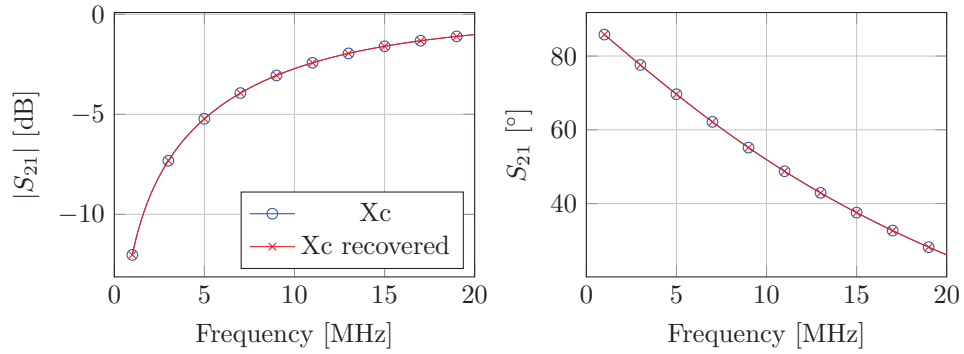


Figure 3.85:  $S_{21}$  parameter of  $\mathbf{X}_C$  recovered from SOL standard measurements compared with  $S_{21}$  of original  $\mathbf{X}_C$

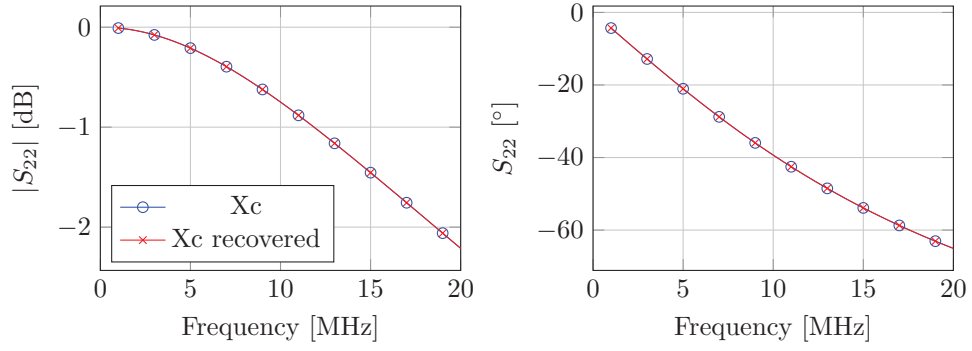


Figure 3.86:  $S_{22}$  parameter of  $\mathbf{X}_C$  recovered from SOL standard measurements compared with  $S_{22}$  of original  $\mathbf{X}_C$

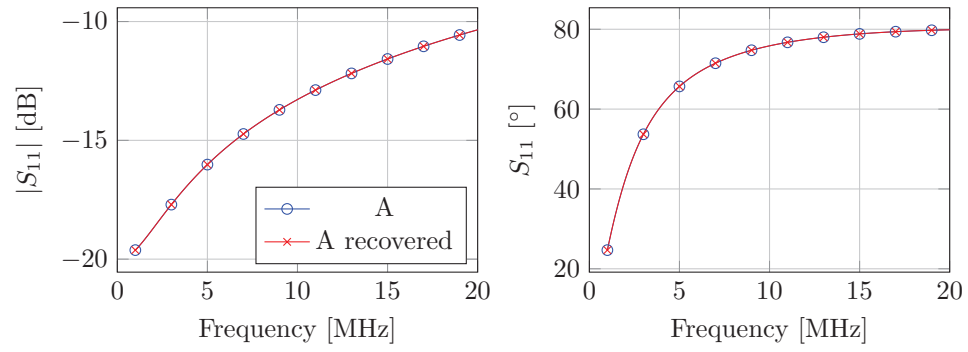


Figure 3.87:  $S_{11}$  parameter of network  $\mathbf{A}$  (Fig. 3.72) recovered from SOL standard measurements of  $\mathbf{X}_C$  and  $\mathbf{X}_S$

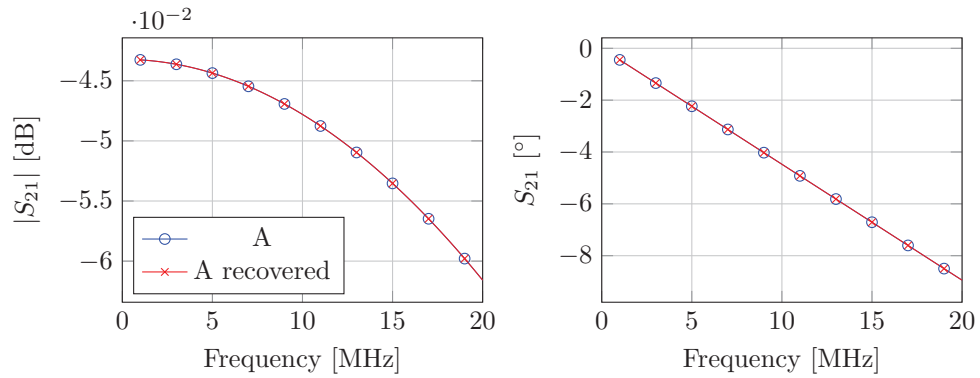


Figure 3.88:  $S_{21}$  parameter of network  $\mathbf{A}$  (Fig. 3.72) recovered from SOL standard measurements of  $\mathbf{X}_C$  and  $\mathbf{X}_S$

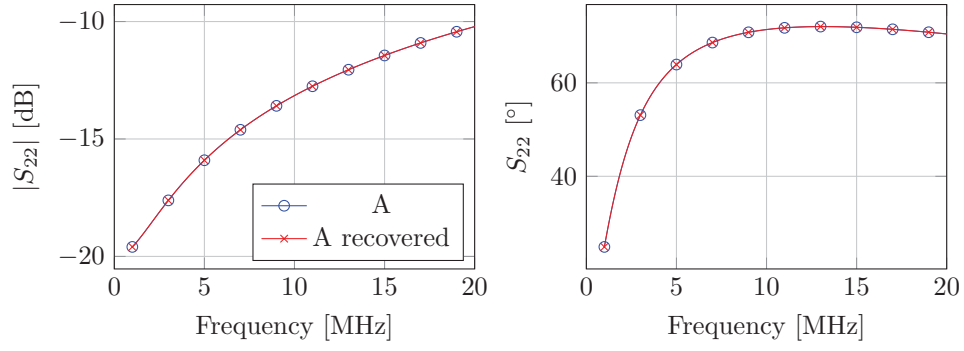


Figure 3.89:  $S_{22}$  parameter of network **A** (Fig. 3.72) recovered from SOL standard measurements of  $\mathbf{X}_C$  and  $\mathbf{X}_S$

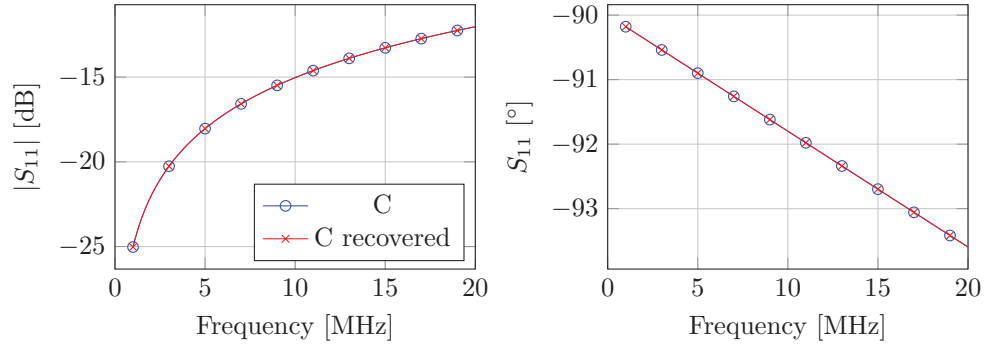


Figure 3.90:  $S_{11}$  parameter of network **C** (Fig. 3.72) recovered from SOL standard measurements of  $\mathbf{X}_C$  and  $\mathbf{X}_S$

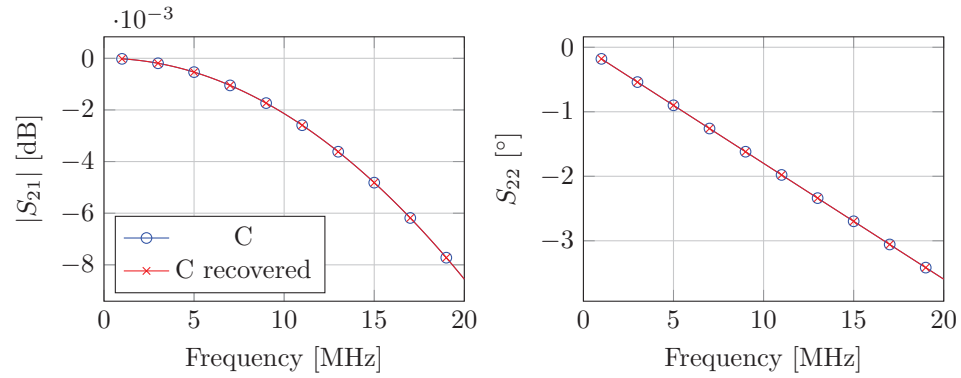


Figure 3.91:  $S_{21}$  parameter of network **C** (Fig. 3.72) recovered from SOL standard measurements of  $\mathbf{X}_C$  and  $\mathbf{X}_S$

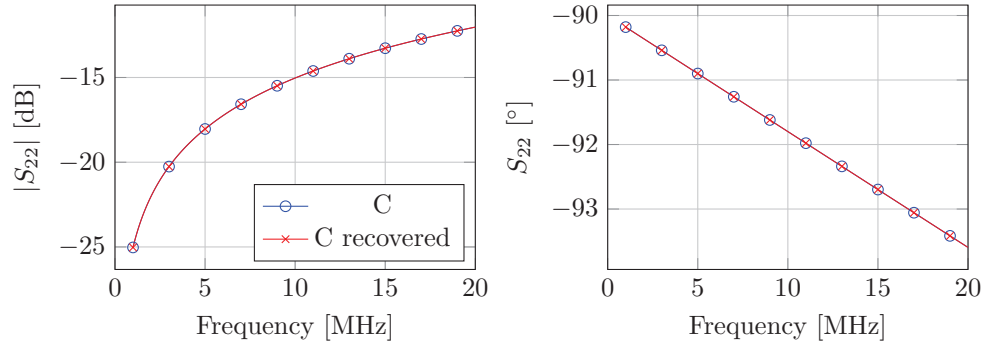


Figure 3.92:  $S_{22}$  parameter of network  $C$  (Fig. 3.72) recovered from SOL standard measurements of  $\mathbf{X}_C$  and  $\mathbf{X}_S$

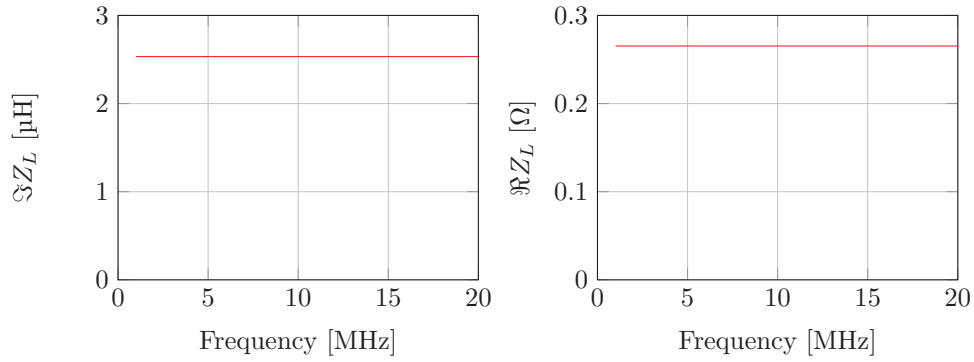


Figure 3.93: Final recovered impedance connected to the output network  $\mathbf{X}_C$  reconstructed by de-embedding the network  $\mathbf{X}_C$ . The impedance is the same as simulated  $0.2653 \Omega$  in series with  $2.533 \mu\text{H}$ . The real portion of this result is most accurately determined at the first zero crossing of Fig. 3.80.

### 3.10 Conclusion

A system for the measurement of coil  $Q$  factor in the frequency range 1 MHz to 20 MHz has been developed. The coil  $Q$  is measured by means of the resonant bandwidth of loop antenna inductively coupled to the parallel tuned coil. The measurements produced by the system have been verified by two means. Firstly they have been compared with full wave finite element simulations of the coils. Where a simple  $LCR$  circuit is fit to the simulation results in an overdetermined manner as to determine the reported  $Q$ . Secondly the measurement system has been modelled and then known resonators introduced into the model. The results from this model indicate that the measurement system is accurate under a wide range of operating parameters and for coil  $Q$  of many thousands.

A significant effort has been put into the development of an automatic measurement that can switch the coils tuning frequency without soldering. Many significant features were verified as functional. Firstly the concept of measurement path switching not effecting measurement results was verified, secondly the ability to measure a series resonant coil was verified. Ultimately the inclusion of the tuning capacitor within the fixture proved the downfall of this method. However some small changes may result in a working measurement system that is faster than the transmission resonance method.

## Chapter 4

# Artificial magnetic conductors applied to wireless power transfer

The thesis thus far has focused on air-cored inductive power transfer systems. However, in the real world, the flux path outside the magnetic link is often compromised by conductors. This can often result in unacceptable link efficiency degradation unless some form of magnetic shielding is implemented. In this chapter an engineered magnetic shield is developed. The magnetic field model of the second chapter shows that in many scenarios the magnetic field outside the coil gap extends for considerable distance from that coils. This can be used to define proximity limits. If proximity limits must be exceeded then some form of magnetic shield is required. In testing the developed shield the transmission method from the measurement chapter is used to measure the  $Q$  of the completed structure.

### 4.1 Introduction

Inductive power transfer (IPT) systems operating at MHz frequencies (usually 6.78 MHz or 13.56 MHz) do not typically use coupling factor,  $k$ , enhancing magnetic cores. They achieve efficient links over distances comparable to the coil diameters by using high  $Q$  coils yielding a high  $k^2 Q_{Tx} Q_{Rx}$  product despite coupling factors below 0.05. Such systems display excellent misalignment and positional tolerance [16]. This is partly due to poor magnetic flux confinement. A particular area of concern is the flux behind the coils (Fig. 4.1). There are many scenarios where the high  $Q$  of the coils could be degraded by media placed behind them. For example, in a car charging pad scenario the  $T_x$  coil has conductive soil beneath it and the  $R_x$  coil has the conductive car chassis above it. In this scenario image currents generated upon the coil side surface of the conductive media act in opposition to the circulating currents in the respective coils. Thus reducing the self and mutual inductance of the coils and increasing the coils series resistances. Furthermore magnetic flux outside the gap between the coils is undesirable for electromagnetic compliance.

A backing material for the coils that, theoretically, results in increased link efficiency is an artificial magnetic conductor (AMC) [55]. Ideally an AMC reflects any incident EM wave with no attenuation and with no phase shift, contrasting with a perfect electrical conductor which causes a  $\pi$  phase shift in the reflection. As the AMC has an in phase reflection the image currents at the surface are in phase with the currents of the coil. This increases the self and mutual inductances of the coils improving link efficiency. The AMC does not allow transmission of incident waves, thus satisfying the field blocking requirement. To this date no AMC has been reported in the literature operating at frequencies used for inductive power transfer. An AMC been demonstrated with a centre frequency of 55 MHz and a fractional bandwidth of 0.39 by Liu et al. [56] however the depth is  $0.067\lambda$  and the element length  $0.0572\lambda$ : if the structure was



scaled to 6.78 MHz this would result in an unacceptably large structure. The work of Daniel. J. Gregoire et al. [57] has yielded surfaces with bandwidths of 0.8 and thickness of  $0.0223\lambda$ . This was achieved by loading with active negative inductance elements. For usage in wireless power transfer systems, however, it may be difficult to create negative inductors that can synthesize the required large voltages and currents.

An alternative solution would be to introduce conductive planes behind the coils, accepting the reduction in link efficiency, which could be improved upon by introducing a ferrite slab between the coil and the conductive plane. This ferrite slab will redirect the magnetic flux such that the image currents in the conductive plane are less well coupled to the coils and also increase the coils mutual and self inductance through improved flux linkage.

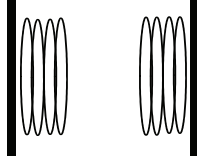


Figure 4.1: IPT coils over backing plates.

## 4.2 High impedance ground plane as artificial magnetic conductor (AMC)

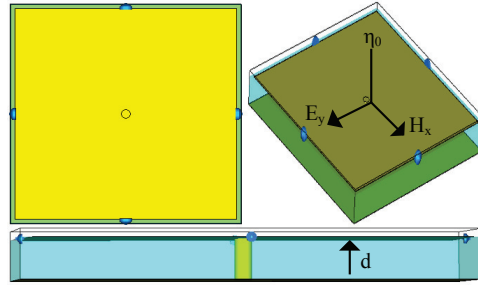


Figure 4.2: Unit cell of developed AMC.

In the most simple case a high impedance ground plane presents a impedance,  $\eta$ , to an incident TEM wave of impedance,  $\eta_0$ , with angular wave number,  $k$ , that causes an in phase reflection of the incident wave. For an infinite plane slab of finite depth,  $d$ , of a medium with effective permeability and permittivity backed with perfect electrical conductor (PEC) at the slab free space interface the reflection coefficient,  $\Gamma$ , at the surface is positive for high  $\eta$ . At the slab free space interface;

$$\Gamma_{slab} = \frac{\eta - \eta_0}{\eta + \eta_0}. \quad (4.1)$$

The phase factor due to phase shift caused by double transit through the dielectric and reflection by the PEC backing is  $e^{-j2kd}$ . Therefore at the surface:

$$\Gamma = \frac{\text{reflected}}{\text{transmitted}} = \frac{\frac{\eta - \eta_0}{\eta + \eta_0} - e^{-j2kd}}{1 - \frac{\eta - \eta_0}{\eta + \eta_0} e^{-j2kd}}. \quad (4.2)$$

For for a high impedance surface  $\lim_{|\eta| \rightarrow \infty} \Gamma = 1$ . For a PEC ground plane:

$$\lim_{|\eta| \rightarrow \eta_0} \Gamma = -e^{-\frac{j4\pi d}{\lambda}} = -e^{\frac{j\pi d}{\lambda}}. \quad (4.3)$$

Therefore for  $d \ll \lambda$  were,  $d$ , in this case represents the distance of observation from the PEC plane the reflection coefficient is  $-1$ . High impedance ground planes are also artificial magnetic conductors as the tangential electric field to the surface at the operating frequency is unable to cause large surface currents due to the high impedance and therefore the boundary condition  $H_x = 0$  is approximated by the surface. TE and TM plane waves at an oblique incidence angle to a surface ( $\theta$ ) have an angle dependent impedances [58] [59];

$$\eta_0^{TE} = \frac{\eta_0}{\cos \theta}, \quad (4.4)$$

$$\eta_0^{TM} = \eta_0 \cos \theta. \quad (4.5)$$

A physically realisable structure for a high impedance surface, developed by Sievenpiper [60], consists of frequency selective surfaces (FSSs) made out of metal patches with a grounded substrate backing. Vias optionally connect them to the rear ground plane, slightly increasing the effective substrate inductance and suppressing surface waves due to shorts caused by the vias being less than a quarter wavelength apart. The effective medium model [60] allows for conversion from material and geometric parameters into an equivalent LCR model of the high impedance surface. The plane wave behaviour of the surface can then be modelled as an impedance at the end of a transmission line with the impedance of the impinging EM wave [61]. Due to the long wavelengths the reflection coefficient at the transmission line LCR model interface is the parameter of interest for usage in IPT systems.

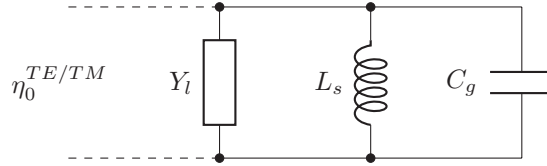


Figure 4.3: Transmission line model of AMC.

The patches lie on the surface of the dielectric, therefore one side of the patches is air. For a substrate with non unity permeability and permittivity the effective permeability,  $\mu_{eff}$ , and permittivity,  $\epsilon_{eff}$ , of the medium they are in is:

$$\epsilon_{eff} \sim \frac{\epsilon_r + 1}{2}, \quad (4.6)$$

$$\mu_{eff} \sim \frac{\mu_r + 1}{2}. \quad (4.7)$$

The admittance of a grid of square patches given by [58] can be expanded upon to include the effects of a substrate with non unity relative permeability:

$$k_{eff} = \omega \sqrt{\mu_0 \mu_{eff} \epsilon_0 \epsilon_{eff}}, \quad (4.8)$$

$$\alpha = \frac{k_{eff} D}{\pi} \ln \left( \frac{1}{\sin \frac{\pi w}{2D}} \right), \quad (4.9)$$

$$Y_g^{TE} = \frac{j2\alpha(1 - \sin^2 \theta)}{\eta_0}, \quad (4.10)$$

$$Y_g^{TM} = \frac{j2\alpha}{\eta_0}. \quad (4.11)$$

Where  $\theta$  is the angle of incidence of the plane wave to the surface and,  $D$ , the unit cell length. As can be observed the grid is capacitive,  $C_g$ , which can be approximated as constant with respect to frequency. The substrate with PEC backing and vias from the centre of the patches has admittances,  $Y_s$ , given by

Luukkonen et al. [62]. The equations have been modified here to include permeability:

$$Y_s^{TE} = -j \frac{\sqrt{\epsilon_0} \sqrt{\epsilon_r - \sin^2 \theta}}{\sqrt{\mu_0 \mu_r}} \cot(\omega h \sqrt{\epsilon_0 \mu_0 \mu_r} \sqrt{\epsilon_r - \sin^2 \theta}), \quad (4.12)$$

$$Y_s^{TM} = -j \sqrt{\frac{\epsilon_0 \epsilon_r}{\mu_0 \mu_r}} \cot(\omega h \sqrt{\epsilon_0 \epsilon_r \mu_0 \mu_r}). \quad (4.13)$$

Such substrate is inductive represented by,  $L_s$ , with linear dependency on permeability and depth,  $h$ , for thin substrates. The effective medium model allows for the grid, substrate and loading admittances to be connected in parallel [61] such that,  $\Gamma$ , can be found;

$$\Gamma = \frac{1 - (Y_s + Y_g + Y_l)\eta_0}{1 + (Y_s + Y_g + Y_l)\eta_0}. \quad (4.14)$$

Lumped admittances,  $Y_l$ , can be used to lower the resonant frequency of the system such that the impedance maximum is lower in frequency. Excessive capacitive loading reduces the fractional bandwidth of the reflectors to the point at which the AMC behaviour is no longer displayed [63].

### 4.3 Survey of existing applicable metamaterials research

| $F_0$<br>(GHz) | Fractional<br>B.W. | Loading   | Depth<br>(mm) | $\epsilon_r$ | $\mu_r$                        | Cell area<br>(mm <sup>2</sup> ) | Ref.       |
|----------------|--------------------|---|---------------|--------------|--------------------------------|---------------------------------|------------|
| 0.00566        | 0.0723             | ferrite substrate and<br>cell to cell capacitance | 50            | 1            | 125                            | 2704                            | [our work] |
| 0.263          | 0.800              | cell to cell NIC                                  | 25.4          | 1.05         | 1                              | 5630                            | [64]       |
| 0.320          | 0.769              | ferrite substrate                                 | 33.0          | 1            | $30 - 1j(x, y), 1 - 0.003j(z)$ | 2090                            | [65]       |
| 0.442          | 0.056              | cell to cell capacitance                          | 6.4           | 4.8          | 1                              | 1600                            | [66]       |
| 1.13           | 0.532              | -   | 30.5          | 1.07         | 1                              | 114                             | [67]       |
| 1.48           | 0.100              | cell to cell capacitance                          | 3.5           | 4.8          | 1                              | 64                              | [68]       |
| 1.77           | small              | cell to cell varactors                            | 1.6           | 4.2          | 1                              | 336                             | [69]       |
| 2.53           | 0.0346             | -   | 2.54          | 6            | 1                              | 369                             | [70]       |
| 2.60           | 0.123              | -   | 15.5          | NA           | 1                              | 31                              | [71]       |
| 2.60           | small              | cell to cell capacitance                          | 0.762         | 3.2          | 1                              | 25                              | [61]       |
| 2.84           | 0.155              | -   | 3.2           | 4.8          | 1                              | 625                             | [72]       |
| 3.16           | 0.700              | ferrite substrate                                 | 100           | 10.73        | 0.47                           | 1225                            | [73]       |
| 3.35           | 0.0806             | surface patterning                                | 1.52          | 4.5          | 1                              | 70.6                            | [74]       |
| 4.25           | 0.0158             | surface patterning                                | 1.27          | 10.2         | 1                              | 17.64                           | [75]       |
| 5.80           | 0.073              | -   | 1.52          | 3.38         | 1                              | 134                             | [76]       |
| 6.00           | 0.125              | -   | 2.4           | 2.55         | 1                              | 70.6                            | [77]       |
| 8.00           | 0.150              | inductive vias                                    | 1             | 10.2         | 1                              | 4                               | [78]       |
| 25.0           | 0.175              | cell to cell NIC                                  | NA            | NA           | NA                             | NA                              | [79]       |

Table 4.1: Table of existing high impedance surfaces.

There has been only a small body of work where metamaterials have been applied in IPT systems to directly interact with the magnetic field. Most examined papers have used negative refractive index materials to refocus the divergent magnetic field emanating from the coils. In the work of Huang et al. [80] simulated a negative index material placed between the  $T_x$  and  $R_x$  coils. Expressions are developed for the effect of finite lenses on IPT systems and it is shown that such structures can improve coupling sufficiently to make up for their additional ohmic losses. In the work of Wang et al. [81] a 2D negative index slab is placed equidistant between the  $T_x$  and  $R_x$  coils of a non-resonant four coil IPT system to great advantage. Power transfer efficiency is improved from 17% to 47% by use of the metamaterial slab. In recent years further variations on this technique have been published by Cho et al. [82], Li et al. [83], Rajagopalan

et al. [84] and Senior et al. [85]. No work using high impedance ground planes with IPT has yet been located, possibly due to the prohibitive dimensions a traditional high impedance ground plane would have to operate at such low frequencies. However a recent paper of Besnoff et al. discusses the development of a metamaterial exhibiting zero effective volume permeability at MHz frequencies [86], however this structure has no potential to improve efficiency beyond the free space case and does not provide the almost complete shielding the AMC potentially offers.

Work has been done on frequency selective surfaces applied to IPT systems to redirect RF 850 MHz to 950 MHz energy around an IPT shielding structure [87] and to block RF interference caused by switching transient excitation of an IPT coil [88]. However these structures have both been designed to minimally interact with the actual IPT frequency and operate at three orders of magnitude higher frequency than the IPT systems they are designed to operate with.

The developed surface has a centre frequency  $50\times$  lower than the lowest centre frequency high impedance ground plane found in the literature, while remaining thin and with reasonable cell size in comparison to the IPT coil (to couple the coil with the surface rather than one cell). A table has been compiled of existing high impedance surfaces showing the significant miniaturisation achieved (Table. 4.3). The bandwidth of a surface is specified as the range of frequencies where the phase of the reflection at the surface is:  $+\frac{\pi}{2} > \phi > -\frac{\pi}{2}$ .

Loading is defined as any modification of the surface beyond the basic mushroom structure (demonstrated by Sievenpiper et al.). At low frequencies this can take the form of a magnetic substrate or lumped components between the cells such as negative impedance converters (NIC) or capacitors. At higher frequencies this generally takes the form of effective lumped components formed by FSS patterning. Broadband operation has been demonstrated at VHF frequencies using NICs configured to primarily provide negative inductance [64] however stability is problematic for large values of negative inductance. There is a general trend towards smaller cell sizes at high frequency to maintain a surface that obeys the effective medium approximation; additionally large cell sizes are problematic for electrically small antenna where the current distribution may rapidly change with respect to the surface cell size. The optimal FSS design among the common varieties (Hilbert, Peano) has been shown to be the Sievenpiper mushroom type structure as it has the broadest bandwidth of the common high impedance surface structures [70]. The work of Parron et al. shows a different approach using spiral resonators to form the effective artificial dielectric above the ground plane [71].

## 4.4 Initial simulation case study

An AMC has been designed with a plane wave centre frequency of 6.78 MHz. The unit cell is 52 mm square with a 50 mm surface patch connected to ground with a single central via. To lower the surfaces centre frequency 690.1 pF lumped capacitors connect each cell to the 4 adjacent cells. The substrate is a 5 mm thick slab of 61 ferrite, with  $\mu_r = 125$  [89] to reduce the required thickness. This results in a surface that has elements only  $113 \times 10^{-6} \lambda$  thick with 0.927 fractional bandwidth. Full wave simulations (Figs. 4.4, 4.5) have been conducted in CST MWS 2014 of the reflection phase behaviour of an infinite array of the AMC for plane waves, requiring approximately 350,000 tetrahedral mesh cells. The AMC has angle independent in phase reflection centre frequency that is the same for both TE and TM waves. This is due to the dominance of the lumped capacitor loading and the very thin substrate. There is excellent correspondence to the transmission line model for plane wave simulations.

An IPT scenario is simulated to compare the performance of a  $10 \times 10$  AMC to various thickness of ferrite slab (0 mm, 3 mm and 5 mm) and free space (no shield). Two 152.5 mm outer radius wire loops separated coaxially by 495 mm made of 5 mm diameter annealed copper, centrally positioned 10 mm above a PEC

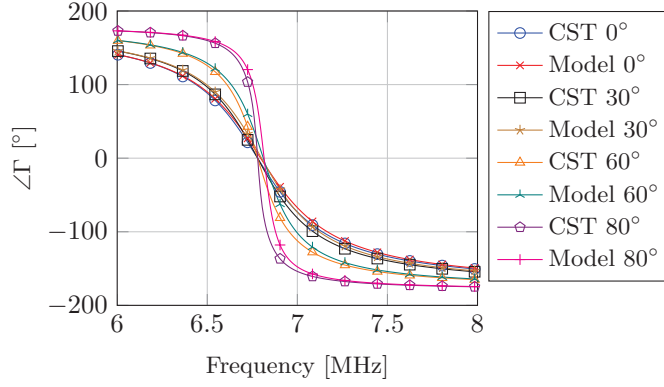


Figure 4.4: Unit cell simulation for TE excitation.

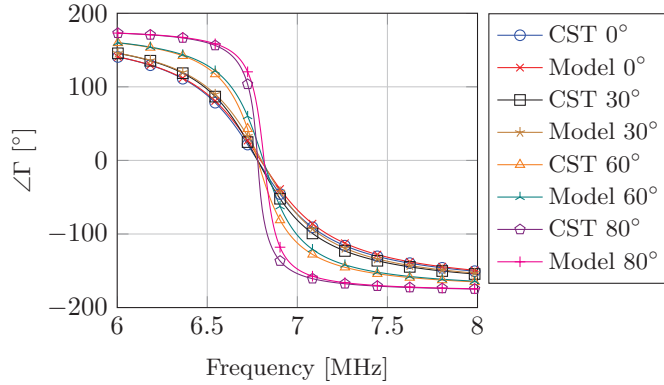


Figure 4.5: Unit cell simulation for TM excitation.

sheet of 520 mm square. The PEC sheet forms the back plane for the AMC and ferrite tests. The tuning capacitor's ESR was  $0.006\ \Omega$  commensurate with the lowest loss multilayer ceramic capacitors commercially available. The positioning of a single AMC and loop is shown in figure 4.6.

The operating frequency of the AMC was found to be much greater than the plane wave case (Figs. 4.4, 4.5), therefore the surface capacitors were increased to 2 nF. This yielded an operating frequency of 12.3 MHz, shown by the resonant peaks in the coils Z-parameters in figure 4.9. The bandwidth of the surface was also clearly greater than the plane wave cases. For scenarios using the AMC, ferrite slabs coating the coil side of the ground plane, just the ground plane and free space the link efficiency has been plot using the method of Zargham and Gulack [6] (Fig. 4.7). The AMC displays a peak fractional link efficiency of 0.77 at 8.1 MHz. The same 5 mm thick ferrite when used as a conventional ferrite covered ground plane results in a peak efficiency of 0.70 at 6.1 MHz. The no shielding case shows a greater efficiency but only at higher frequencies.

As the ferrite loss increases with frequency the peak efficiency of the AMC was 8.1 MHz, lower than the optimal frequency if the ferrite were lossless. To demonstrate this a simulation was conducted with a lossless ferrite model (Fig. 4.8) the peak efficiency was at 11.0 MHz, closer to the AMC operating frequency. It is interesting to note that above 18 MHz the AMC has the worst efficiency, at this point the AMC grid was shorted by the tuning capacitors and acted as a PEC plane in close proximity to the coil. By observing the tangential magnetic field strength at 12.3 MHz at the surface (Fig. 4.6) it simulated the  $H_{x,y} = 0$  boundary condition imposed by an ideal AMC at its operating frequency.

In this simulation case study an AMC (Inclusive of the losses caused by non-ideal ferrite and capacitors) operating at IPT frequencies compared favourably to other solutions to the problem of conductive planes

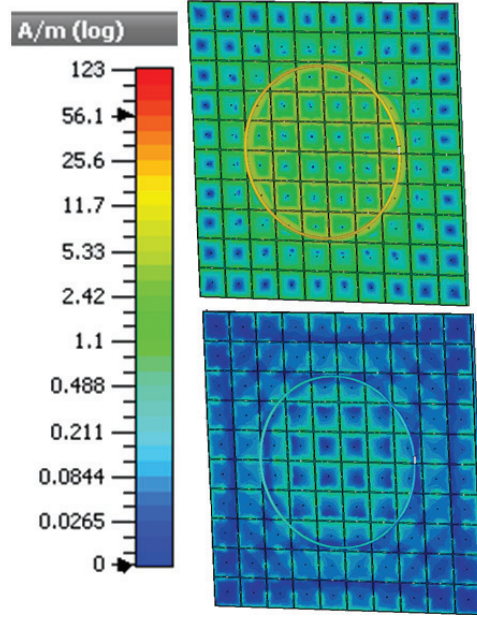


Figure 4.6: 1 MHz (upper) and 12.3 MHz (lower), RMS surface tangential H field strength for 1 W excitation.

behind the coils, which reduce link efficiency. To reduce the operating frequency of the AMC capacitive loading of the grid and ferrite substrate are utilised. The plane wave model of the AMC though very accurate for plane wave behaviour does not correctly predict the AMC centre frequency in an IPT scenario where the coil is very close to the AMC surface (when there is near field coupling). Link efficiencies greater than those in free space are demonstrated while blocking magnetic fields behind the coil. Furthermore the AMC is shown to be superior to the same quantity of ferrite used as a sheet to shield the ground plane.

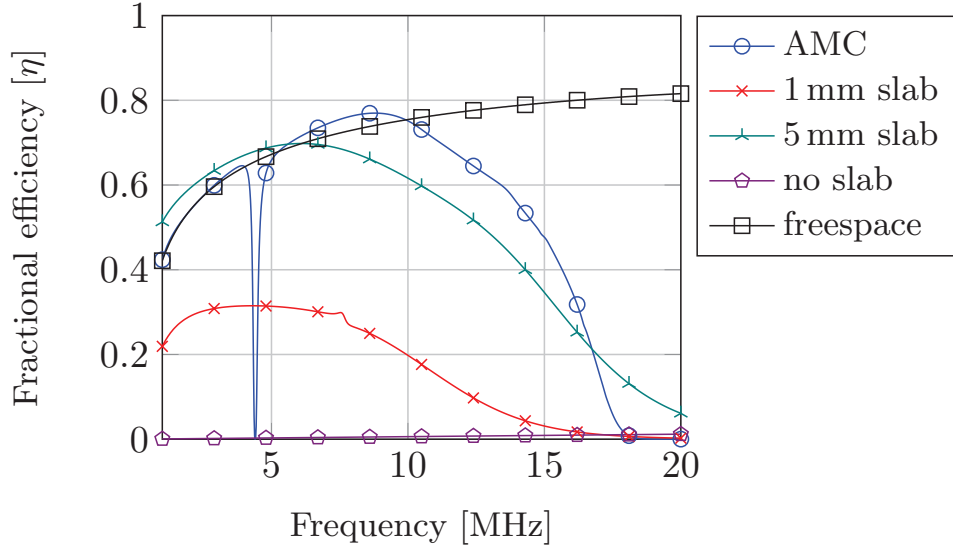


Figure 4.7: Maximum power transfer efficiency of shielding solutions at a coaxial distance between identical wire loops of 495 mm. The wire loops have a conductive sheet positioned 10 mm behind each of them (apart from in the freespace case where this sheet is not present). The depth of ferrite covering this conductive plane is varied for the ferrite cases. In the AMC case this ferrite depth is 5 mm but due to the engineered structure peak efficiency exceeds that of the same depth of ferrite slab. The low efficiency at 4 MHz in the AMC case is not a simulation artefact and instead shows the surface resonance frequency where the AMC is presenting a conductive sheet close to the coils. All simulations were conducted with open boundary conditions spaced 100 mm from the structure.

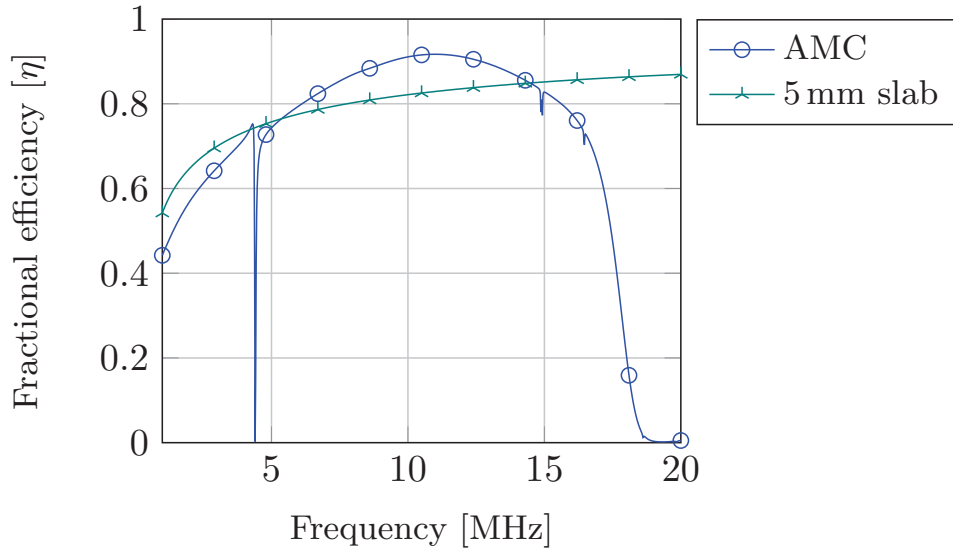


Figure 4.8: Maximum power transfer efficiency of shielding solutions using lossless ferrite model.

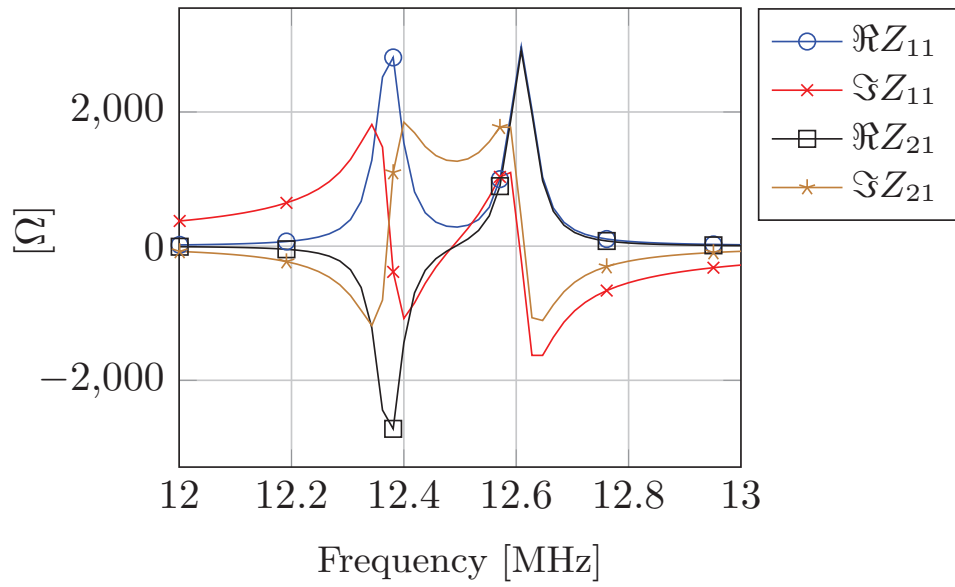


Figure 4.9: Z-parameters of AMC scenario.



## 4.5 Comparison charging pad system

### 4.5.1 Introduction

To confirm the simulation results and to find operating points it is desired to compare the properties of an AMC pad power transfer link with the properties of a link composed of ferrite pads (Fig. 4.11). A magnetic link comprising two ferrite pads has been compared to a magnetic link with identical quantities of ferrite and dimensions using an AMC structure for both pads. The availability of ferrite products in sheet form has constrained the design of this prototype, the only readily available sheet ferrite products are thin stickers designed for 13.56 MHz RFID applications, thicker ferrite block has been constructed from a stack of these sheets. The system is designed for peak power transfer efficiency at 13.56 MHz. A diagram showing the structure of the pads is provided (Fig. 4.10) with the following key:

**A** The pad backing is a made of sheet 120 mm square, 0.3 mm thick IACS annealed copper (electrically thick at operating frequency). The AMC has holes drilled in this backing where the wires used as vias are soldered to the backing; the ferrite pad has no holes or vias.

**B** 1.6 mm thick FR4 board; for the ferrite pads this is a blank spacer (apart from some text), for the AMC this is patterned with a  $5 \times 5$  grid of 22 mm squares with 1 mm diameter holes in their centre, a 2 mm space is left between the patches. The top of the wires used as vias are soldered at the hole locations.

**C** The planar spiral coil is CNC cut from 1 mm thick IACS Annealed copper, it has 3 turns, an outer radius of 50 mm, the turns are 3 mm width and the space between the turns is 3 mm. The coil is positioned centrally above the PCB with a 3 mm gap between the coil base and the PCB.

**D** The coil is held in position using epoxy and a 1 mm thick perspex cover placed on top of the former.

**E** 3D printed (SLS PA2200 Nylon) former that contains a planar spiral coil. This ensures all the pads have identical coil geometry.

**F** For the AMC only 0.8 mm, wires are threaded through holes drilled in the ferrite substrate from the PCB patches to the backing, these act as vias.

**G** layer of 10 stacked Würth WE-FSFS Flexible Sintered Ferrite Sheet 364003 that consists of 0.3 mm thick ferrite layers with a 0.05 mm thick adhesive backing and 0.03 mm thick PET film front, resulting in a 3 mm thick ferrite slab covering the copper backing.

**H** The coil has additional 81 mm of additional conductor length to provide connection points on the underside of the pad.

**I** For the AMC; 5, ATC ATC100B102 1 nF capacitors in parallel are soldered between each patch to the adjacent patch, resulting in a 5 nF patch to patch capacitance with a combined ESR of  $1.2 \text{ m}\Omega$ . The Ferrite pad lacks these capacitors.

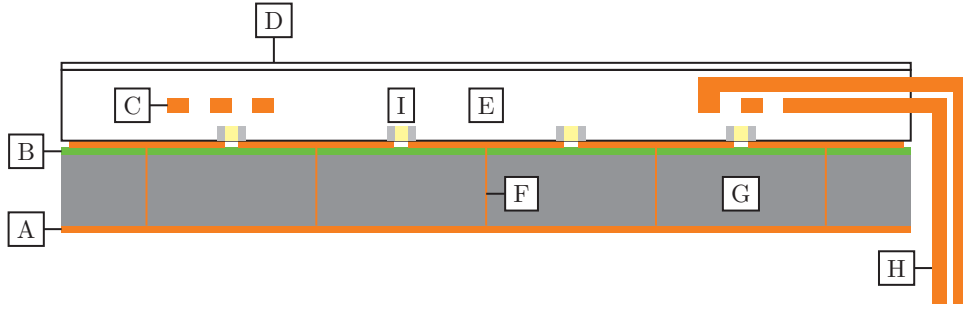


Figure 4.10: Cross section showing charging pad structure (AMC type shown), not to scale.

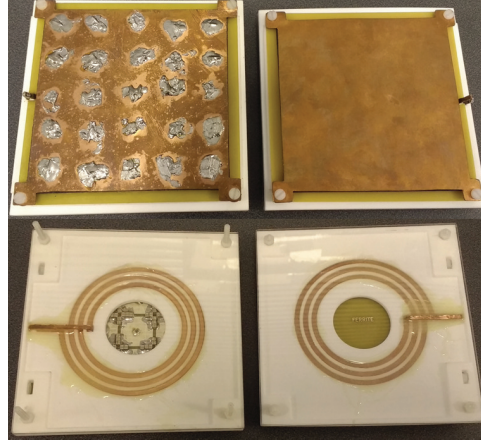


Figure 4.11: AMC (L) and Ferrite (R) charging pads.

## 4.5.2 Results

### Simulation permeability fit

For the simulations a fit has to be performed to the manufacturer supplied data for the ferrite sheet 364003 [90] for  $\mu'$  and  $\mu''$  to obtain the closest fit to manufacturer data at 13.56 MHz a 5th order polynomial fit with an error limit of 0.005 (Figs. 4.12, 4.13) has been used. The manufacturer does not provide data for loss below 10 MHz it is presumed that this is because the loss is below the measurement sensitivity of the employed equipment. The fit has a loss peak in this region, as a result simulation results below 10 MHz should have exaggerated losses. Furthermore below 5 MHz  $\mu'$  is exaggerated from approximately 110 to a peak of 160, this may exaggerate low frequency coupling and inductive effects slightly. In the region of most interest, 10 MHz to 20 MHz, fit is excellent.

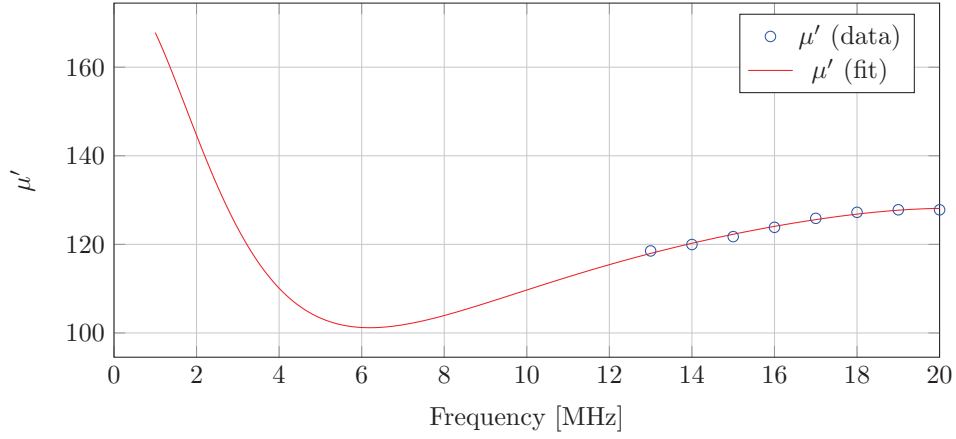


Figure 4.12: Real portion of permeability fit. Note extrapolated data is inaccurate due to polynomial fit, this has been taken into account in results discussion.

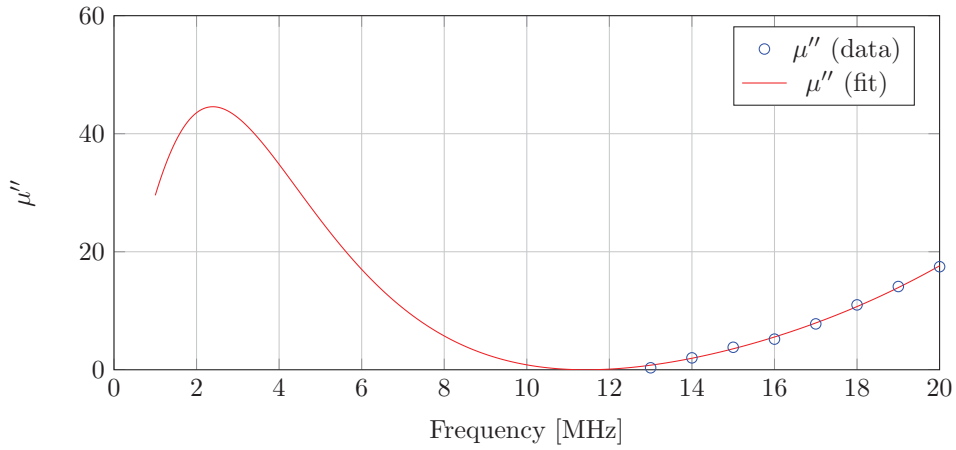


Figure 4.13: Imaginary portion of permeability fit. Note extrapolated data is inaccurate due to polynomial fit, this has been taken into account in results discussion.

### Pad Z-parameters

The impedance of the unloaded pads is important to verify the AMC tuning and accuracy of the simulation models, it is also part of the full Z-parameter matrix of the link that allows link efficiency calculation. As shown in the measurement chapter, for large ratios between real and imaginary components the impedance analyser (Keysight E4990A) cannot accurately determine the smaller component. The pads are measured using this instrument through a transformer type balun, Mini Circuits model T1-1-KK81+. The calibration plane was moved beyond the balun using a SOL calibration. As the maximum ratio of imaginary to real impedance measured is 100 the real impedances are not meaningless as would be typical for higher  $Q$  air coils. A verification plot of an  $10.969\ \Omega$  resistor measured using this technique is in Appendix 2.

The complex impedance has been plotted as effective inductance  $L = \frac{\text{Im}(Z_{11})}{\omega}$  as a device to increase readability. Theory suggests the AMC surface should induce a narrow band increase to the effective inductance. The low frequency values of inductance are: ferrite measured =  $1.43\ \mu\text{H}$  at 1 MHz, ferrite simulated =  $1.58\ \mu\text{H}$  at 10 MHz, AMC measured =  $1.06\ \mu\text{H}$  at 1 MHz and AMC simulated =  $1.66\ \mu\text{H}$  at 10 MHz. As can be observed (Fig. 4.14) the simulation result is reasonably predictive of the ferrite pad inductance, with a lower low-frequency value of inductance but a sharper rise in effective inductance. This is indicative of the charging pad having greater inter-turn capacitance than simulation and the substrate having slightly lower permeability than simulation. Alternatively the coil could have been further away from the ferrite

than in simulation. The AMC results while showing the same general behaviour of a resonant peak differ in that the frequency has changed from 16.37 MHz to 18.556 MHz. Furthermore the peak inductance is an order of magnitude lower (Fig. 4.15). The difference in resonant frequency can be explained by the lower than expected substrate permeability or greater substrate distance. The peak magnitude has a number of possible explanations; firstly lower pad quality factor and secondly non exact capacitor values.

To test the capacitor value hypothesis a simulation has been conducted with each capacitor pseudo randomly varied by up to 5% (the tolerance of the capacitors used in the AMC prototype) using a uniform distribution pseudo random sequence and the result compared to the exact value result (Fig. 4.17). This results in negligible frequency shift and amplitude alteration in the effective inductance peak and suggests the surface performance is not sensitive to capacitor variation, the most likely culprit therefore is additional loss in the structure that has not been captured by simulation.

The plots of the real portion of the pads self impedances (Fig. 4.16) would appear to confirm the earlier hypothesis that losses are greater than simulation in the produced charging pads. In all cases the real world pads display greater than expected real impedance, even the ferrite pad displays far greater real impedance compared to simulation. As the ferrite pad contains nothing unusual, yet has much greater series resistance than expected this suggests that the simulation treatment of the ferrite is not correct or the slab of ferrite does not have the expected properties. To eliminate the remote possibility the coils themselves are the fault the conductivity of the coils copper was verified by DC resistance measurement and found to be as expected  $1.72 \times 10^{-8} \Omega \text{ m}$ .

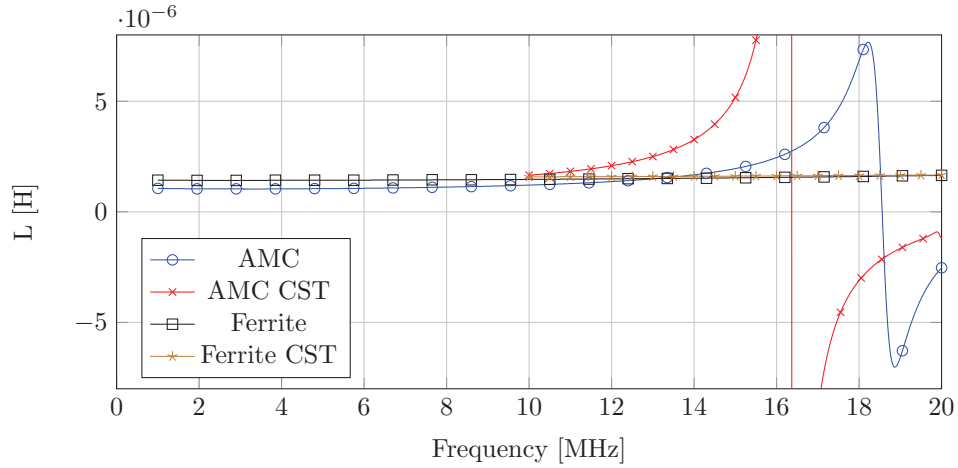


Figure 4.14: Effective self inductance of simulated (CST) and measured charging pads, truncated vertical scale for readability.

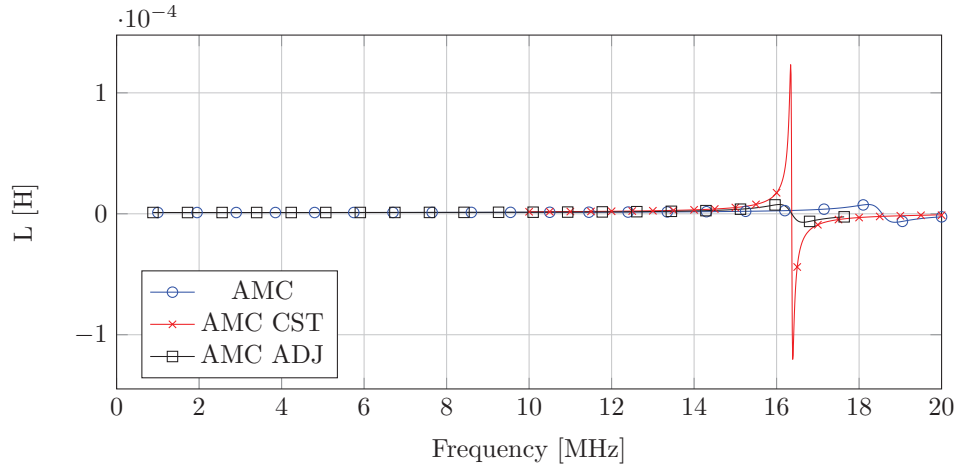


Figure 4.15: Effective self inductance of simulated (CST) and measured charging pads. The ADJ plot has the resonant frequency relocated to the same frequency as simulation for comparison of amplitude.

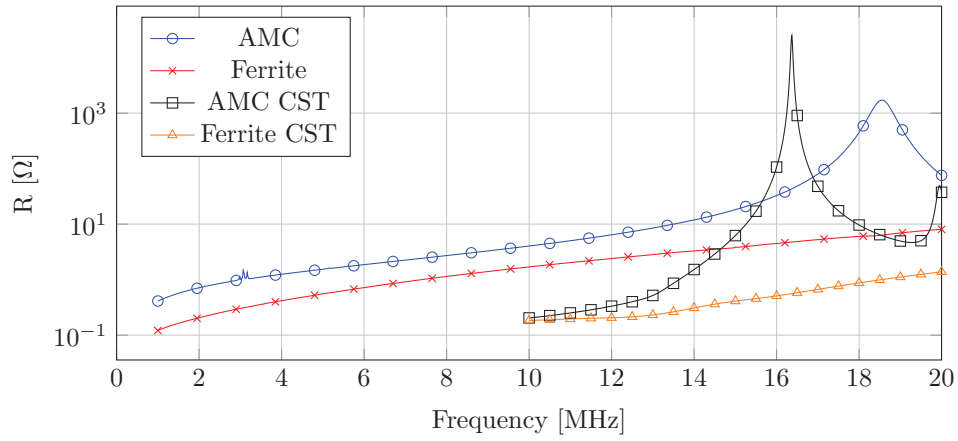


Figure 4.16: Effective resistance of simulated (CST) and measured charging pads.

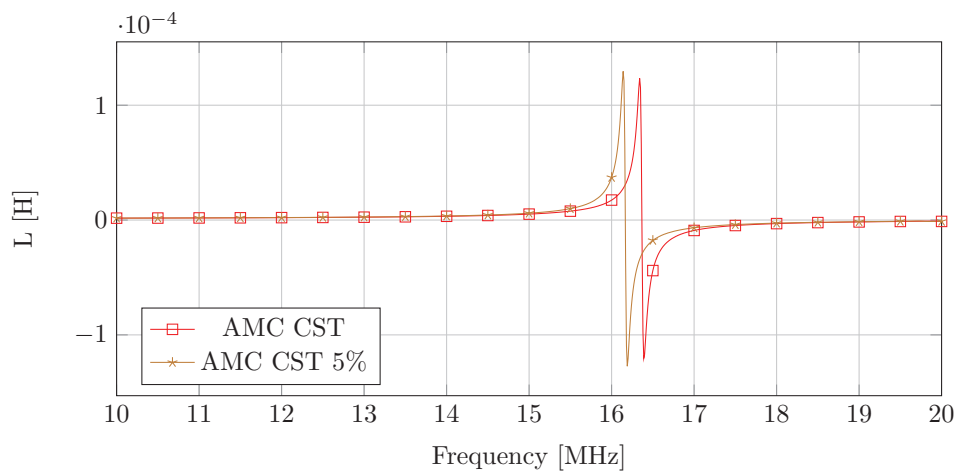


Figure 4.17: Effective self inductance of simulated (CST) AMC charging pads with identical tuning capacitors and 5% tolerance tuning capacitors.

### Pad Resonant $Q$

The AMC pad impedance measurements cannot be simply be mapped to an LCR resonator to ascribe  $Q$ , as per a conventional inductive coil. To confirm the hypothesis that the deviations from simulation are caused by increased losses within the structure the pad resonant  $Q$  was measured. A single-sided coupling loop PCB was constructed and positioned 15 mm above the pads (Fig. 4.18). The coupling loop PCB has two loops with Mini Circuits T1-1-KK81+ baluns used to connect to the VNA, as per chapter 3 the  $Q$  was measured using the bandwidth of the transmission peak between the two loops. To tune the pad ATC100A and 100B series capacitors were placed in parallel with the coil at point H on figure 4.10. The capacitors have high enough  $Q$  that they negligibly reduce the  $Q$  of the pads.

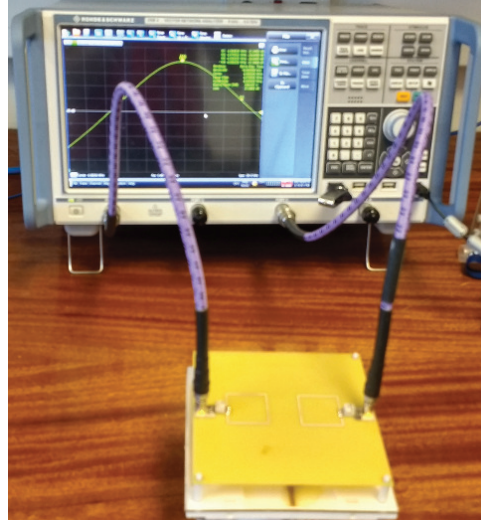


Figure 4.18: Charging pad resonant  $Q$  measurement.

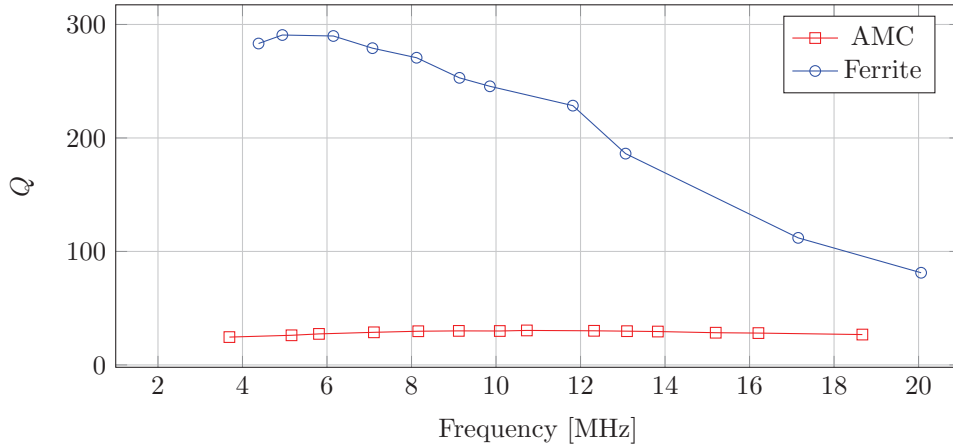


Figure 4.19: Measured pads resonant  $Q$

The measured resonant  $Q$  (Fig. 4.19) is much lower than the simulated resonant  $Q$  (Fig. 4.20). This is for both pads therefore the much greater than expected loss is due to a common element to the AMC and the ferrite pad. The most likely culprit is the ferrite substrate. To confirm this hypothesis, in subsequent sections, a sample of this material is measured.

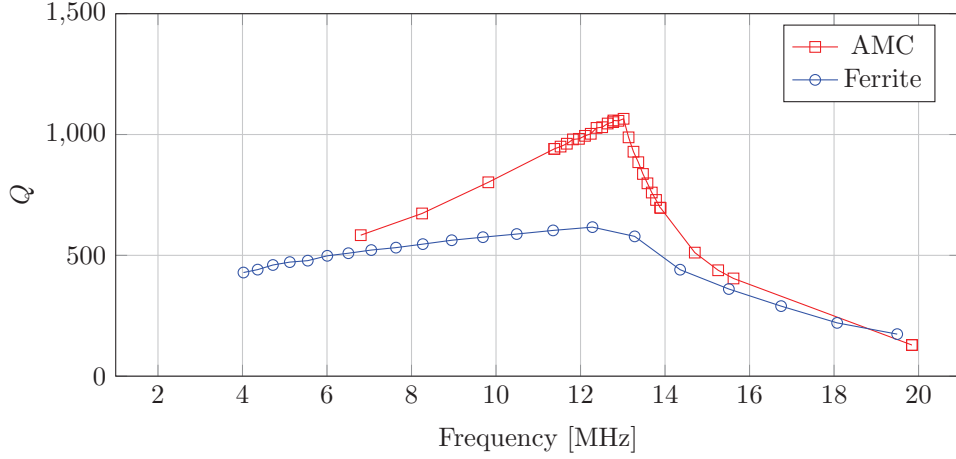


Figure 4.20: Simulated pads resonant  $Q$

### Capacitance fitting

By examination of the change in the first self resonant frequency with loading capacitance effective values of inductance and capacitance can be ascribed to the pads. The AMC was found to have an effective inductance of  $0.992 \mu\text{H}$ , an effective capacitance of  $51.5 \text{ pF}$  with a  $R^2$  value of  $0.997$ . The ferrite pad was found to have an effective inductance of  $1.44 \mu\text{H}$  and an effective capacitance of  $6.09 \text{ pF}$  with a  $R^2$  value of  $0.99999$ .

Although it has previously been noted that the AMC behaviour cannot be fully described by a simple LCR model due to the presence of multiple resonances, when the pad impedance data is truncated to the first resonant peak it still has reasonable fit to an LCR model. using the capacitance extraction method (measurement chapter) on the measured impedance data truncated to  $12 \text{ MHz}$ , before the first resonant peak. This gives the result of  $1.421 \mu\text{H}$  with  $5.52 \text{ pF}$  for the ferrite pad and  $1.02 \mu\text{H}$  with  $38.5 \text{ pF}$  for the AMC. The AMC impedance is more complex than simple LCR resonant impedance and therefore the fit is not as good as the ferrite pad.

The broad correspondence of these two results, for both pads, show that the impedance data is consistent with the resonant  $Q$  results. This way confidence in the resonant  $Q$  results is increased.

### Transmission with respect to distance

The effective coupling factor,  $k$ , has been plotted, from simulated and measured results, (Figs. 4.21, 4.22, 4.23, 4.24, 4.25, 4.26, 4.27, 4.28, 4.29) at varying distances for the AMC and ferrite pad based wireless power links. From the impedance parameters the effective coupling factor is:

$$k = \frac{\Im Z_{12}}{\Im Z_{11}}. \quad (4.15)$$

For a system composed purely of inductively coupled coils the coupling factor is constant with frequency. This behaviour is displayed by the ferrite pads where only a small increase in effective coupling factor is observed. However for the AMC system a massive increase in effective coupling factor is observed near the operating frequency. If we examine the results we see that the effective coupling factor for the AMC pads is greater than the ferrite pads beyond  $10 \text{ MHz}$ . The simulation results for the ferrite pads correspond to the measured results below  $15 \text{ MHz}$ , above this point the effective coupling is greater than simulation. This is likely because the coil former was not simulated and therefore the pads have greater effective capacitance than simulation resulting in this discrepancy. The AMC although displaying the same general resonant

behaviour has a lower peak magnitude than in simulation. Nonetheless peak effective coupling factor is still far in excess of the ferrite pads. The cause of this increase in coupling will be investigated by examining fields in simulation under optimal load conditions.

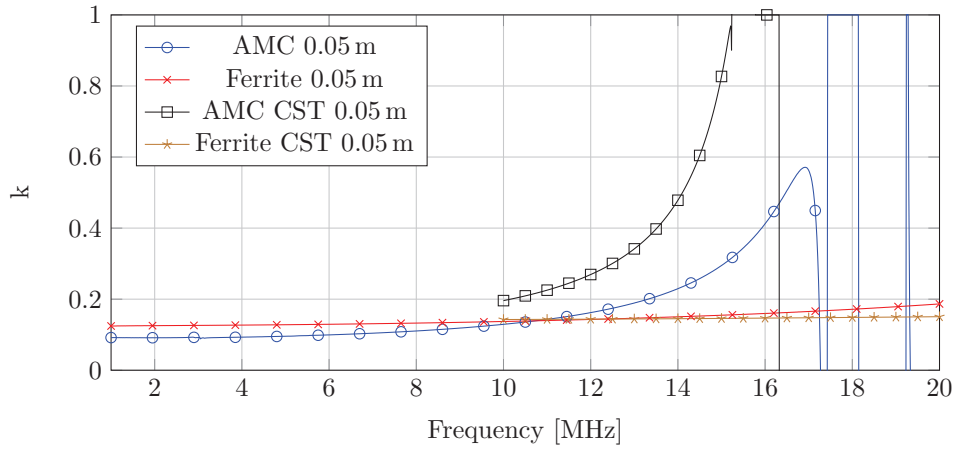


Figure 4.21: Measured and simulated pads effective coupling factor,  $k$ , with 0.05 m air gap between coils.

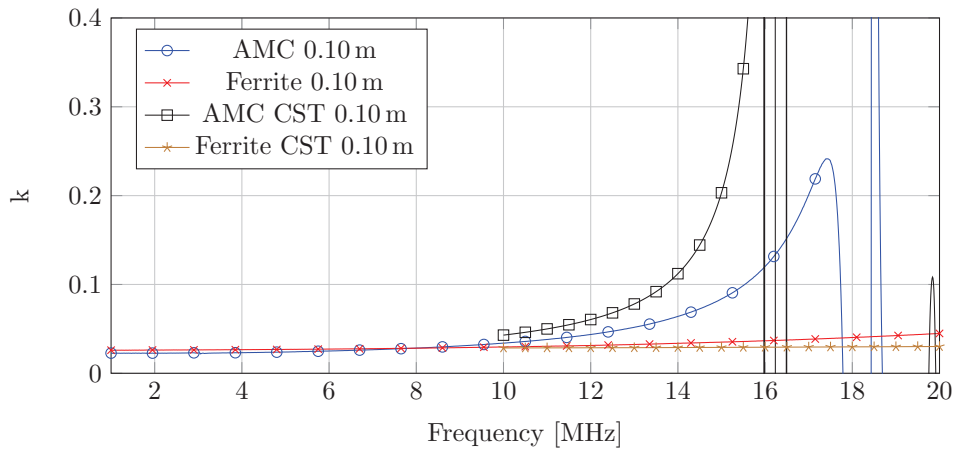


Figure 4.22: Measured and simulated pads effective coupling factor,  $k$ , with 0.10 m air gap between coils.

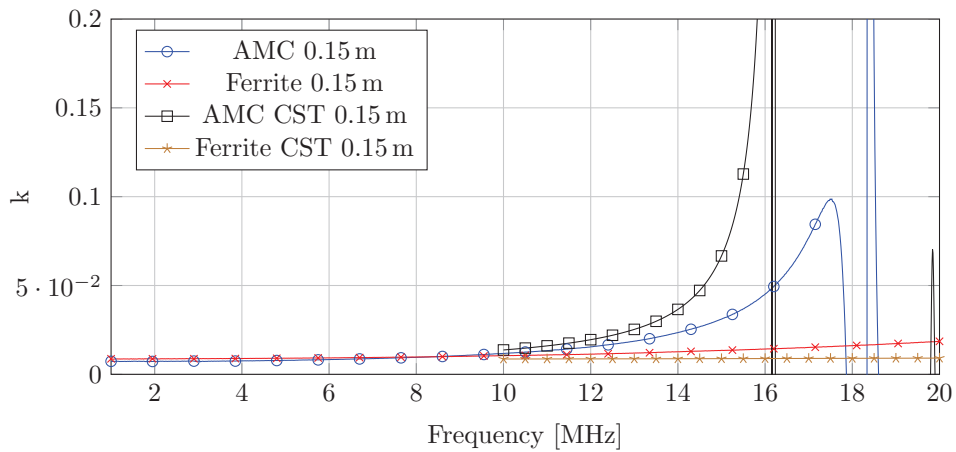


Figure 4.23: Measured and simulated pads effective coupling factor,  $k$ , with 0.15 m air gap between coils.



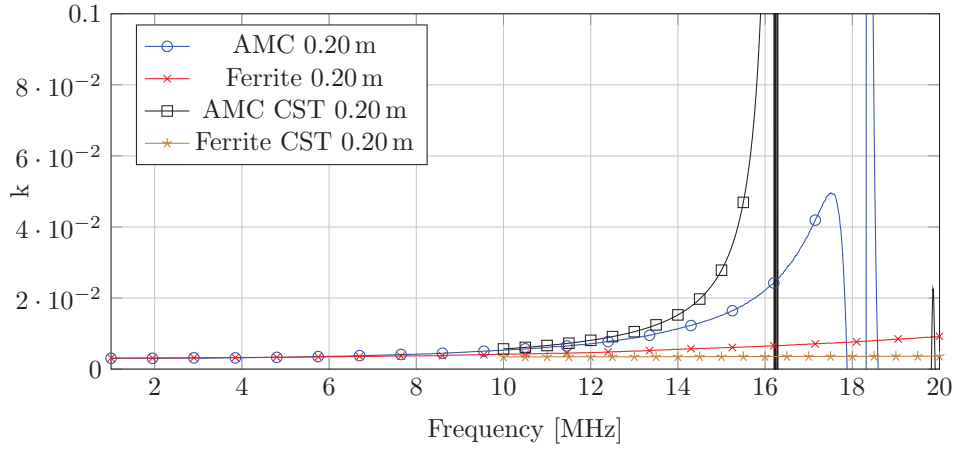


Figure 4.24: Measured and simulated pads effective coupling factor,  $k$ , with 0.20 m air gap between coils

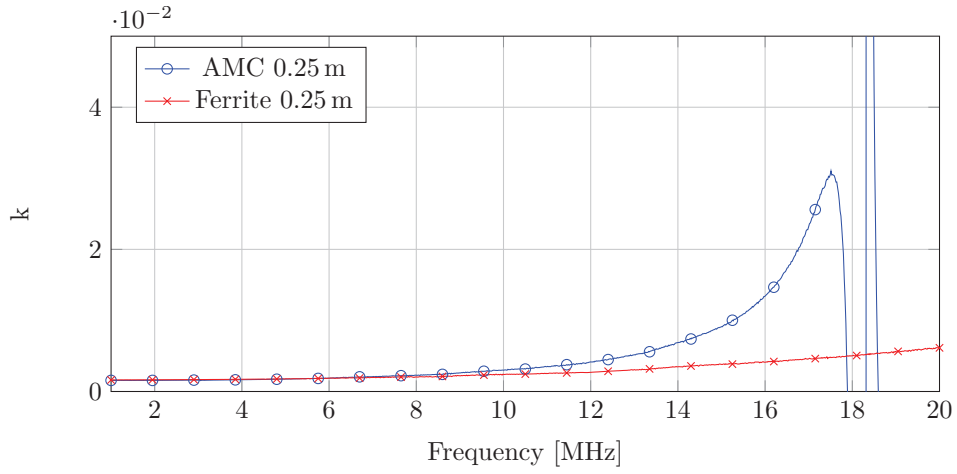


Figure 4.25: Measured effective coupling factor,  $k$ , with 0.25 m air gap between coils

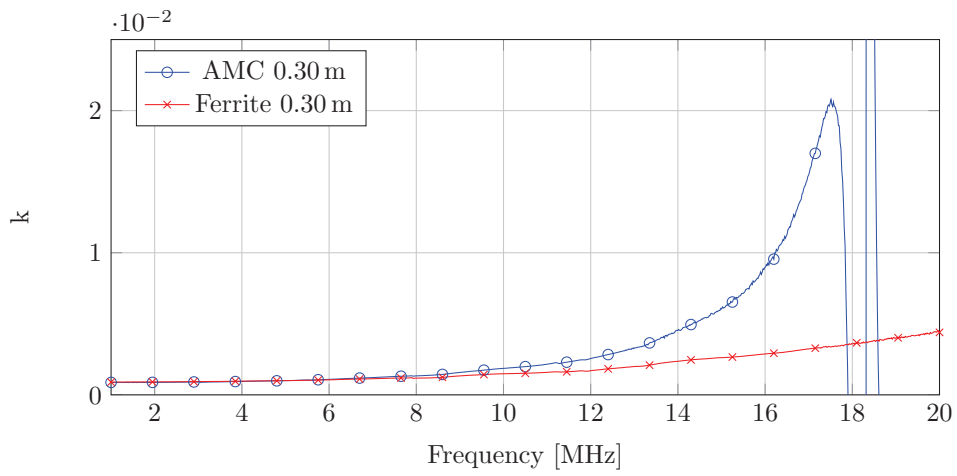


Figure 4.26: Measured effective coupling factor,  $k$ , with 0.30 m air gap between coils

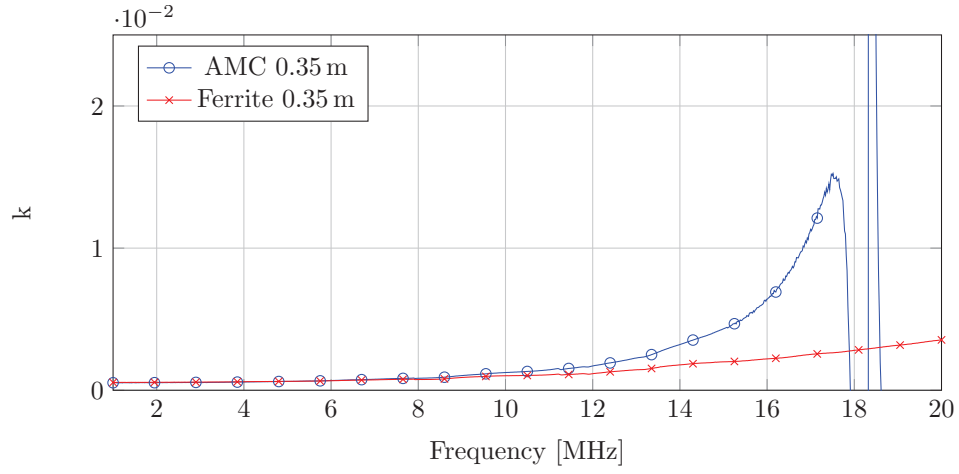


Figure 4.27: Measured effective coupling factor,  $k$ , with 0.35 m air gap between coils

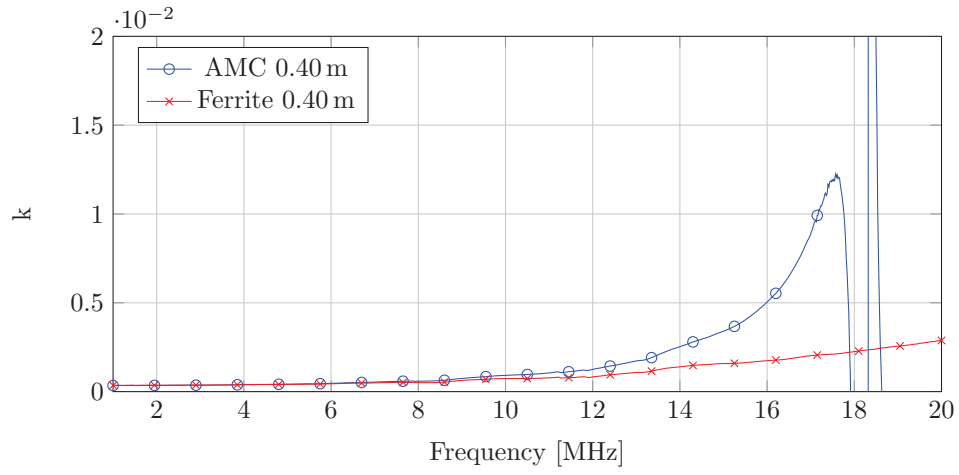


Figure 4.28: Measured effective coupling factor,  $k$ , with 0.40 m air gap between coils

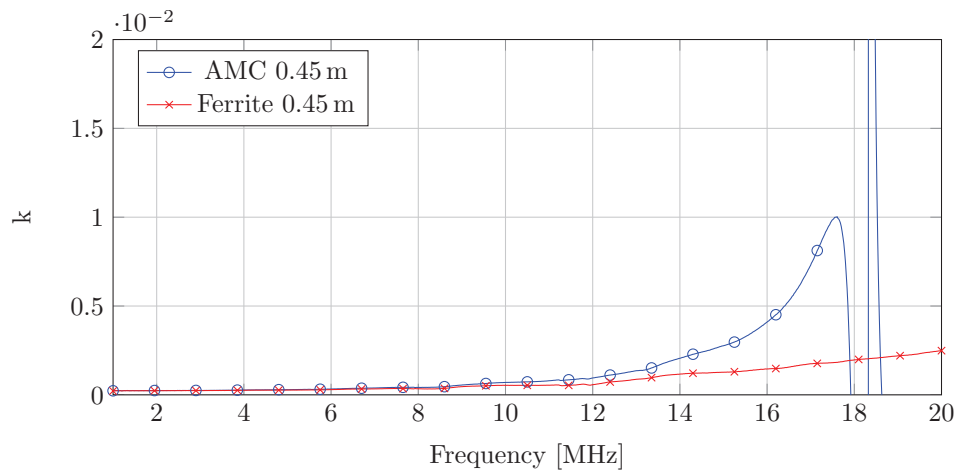


Figure 4.29: Measured effective coupling factor,  $k$ , with 0.45 m air gap between coils

### Unmatched 50 $\Omega$ efficiency

Calculating the theoretical maximum fractional transfer efficiency,  $\eta$ , of the system in the real world is exceptionally difficult. In theory all needed are the two port parameters of the wireless link [6]. However if the expressions are examined, as they are in the measurement chapter (chapter 3), it is observed that the efficiency is sensitive to the real parts of  $Z_{11}$  and  $Z_{22}$ .

No method can accurately determine the real parts of  $Z_{11}$  and  $Z_{22}$  for the AMC using a VNA. This is because the magnitude of the imaginary part of the impedance is far greater than the real. Furthermore the measured impedances are not close to the 50  $\Omega$  reference impedance of the VNA, reducing measurement accuracy. Although the resonant  $Q$  has been found there is no equivalent circuit to fit the the AMC to as to calculate the real portion of  $Z_{11}$ . An impedance analyser has better impedance measurement performance than a VNA but still typically struggles with  $Q$  greater than 100 and is only a single port instrument, thus is not capable of measuring the full link.

One method that yields efficiency results is to connect the ideal secondary load to the secondary pad and measure the power dissipated in the secondary load for the power absorbed by the primary pad. Effectively running a mock IPT system. However this method requires construction of many AC loads featuring low inductance resistor topologies and as such is very laborious and cannot be done over the entire frequency range in reasonable time. The secondary load with this method has to iteratively chosen as the true two port matrix representing the system is unknown yet required to calculate the optimal load. Iterating the secondary load for each frequency point takes considerable time (variable capacitors lack the quality factor to be usable in this application). Later in the chapter such measurements are taken for two operating frequencies.

Instead of been able to present useful efficiency data for optimal secondary load links over the desired frequency range results are presented for the power transfer efficiency when operating in unmatched 50  $\Omega$  RF system. This is simply  $S_{21}$  (Figs. 4.30, 4.31), 4.32, 4.33, 4.34, 4.35, 4.36, 4.37, 4.38). This data shows that the at frequencies beyond 10 MHz the AMC has a greater transmission coefficient magnitude than the ferrite pads. However it also illustrates the naivety of operating these systems using conventional 50  $\Omega$  RF amplifiers and receivers as the efficiencies are far lower than when operating with a matched load as illustrated in the Measured efficiency section later in this chapter.

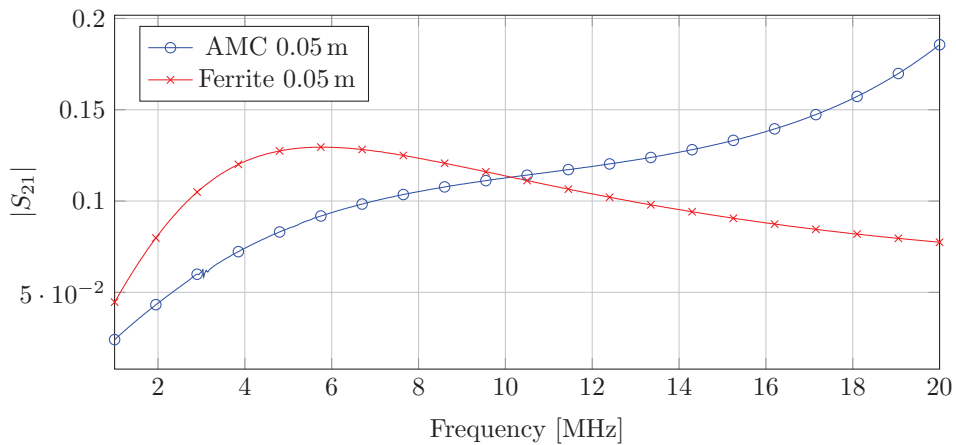


Figure 4.30: Measured transmission coefficient, with 0.05 m air gap between coils

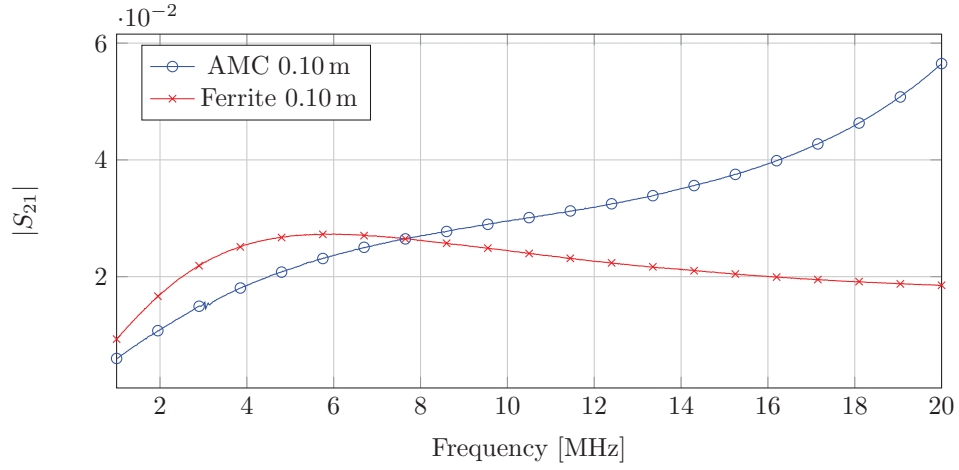


Figure 4.31: Measured transmission coefficient, with 0.10 m air gap between coils.

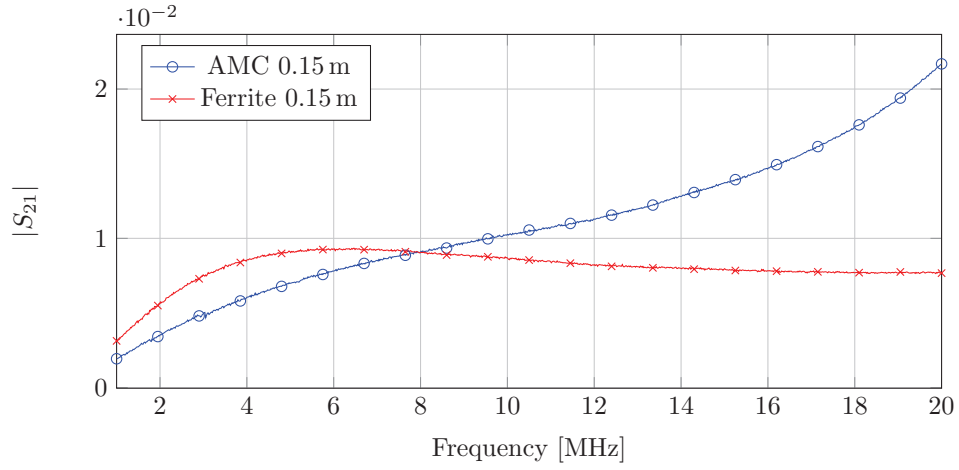


Figure 4.32: Measured transmission coefficient, with 0.15 m air gap between coils.

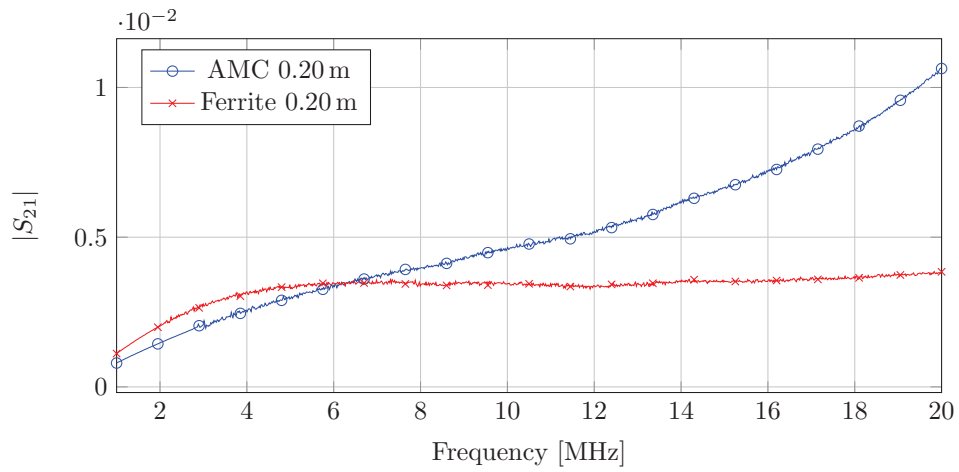


Figure 4.33: Measured transmission coefficient, with 0.20 m air gap between coils.

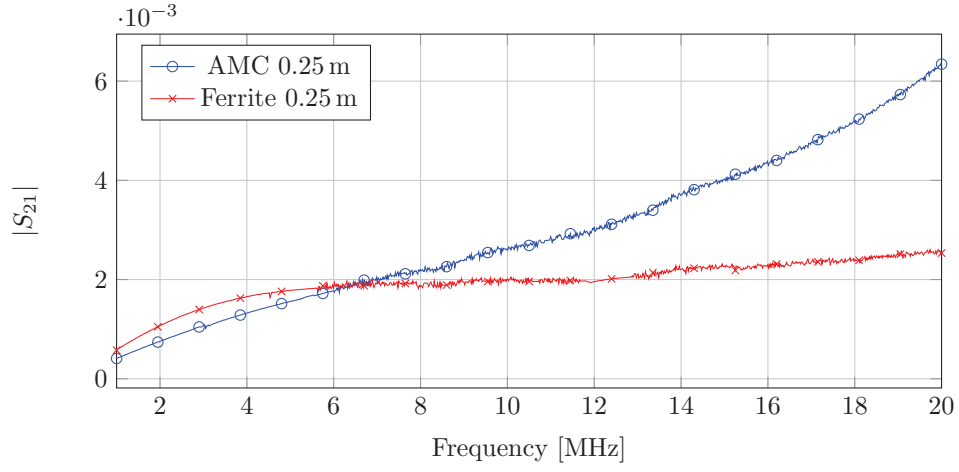


Figure 4.34: Measured transmission coefficient, with 0.25 m air gap between coils.

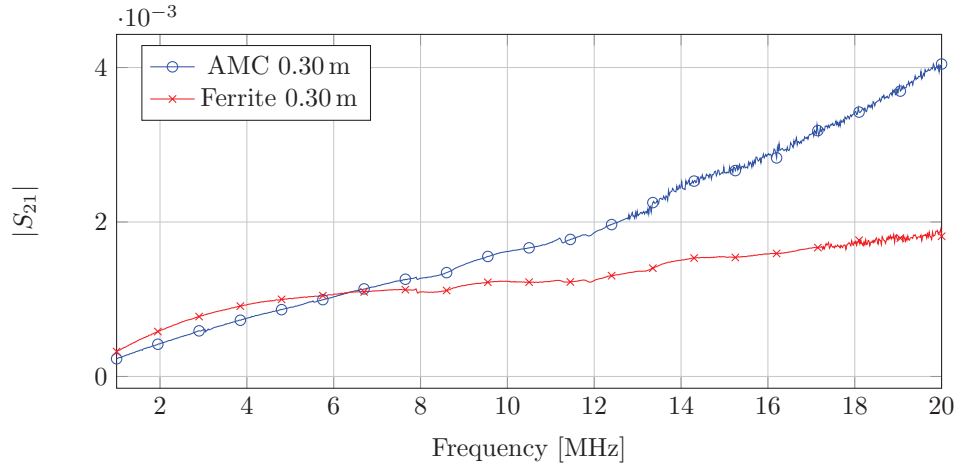


Figure 4.35: Measured transmission coefficient, with 0.30 m air gap between coils.

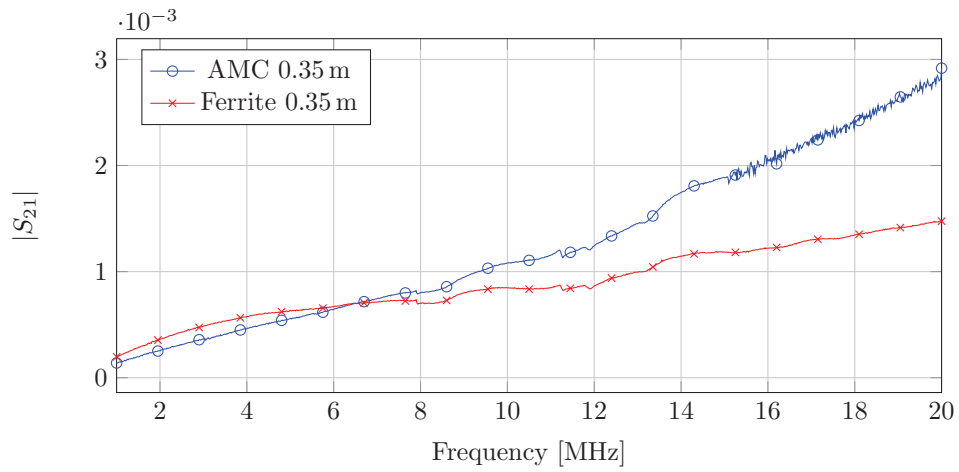


Figure 4.36: Measured transmission coefficient, with 0.35 m air gap between coils.

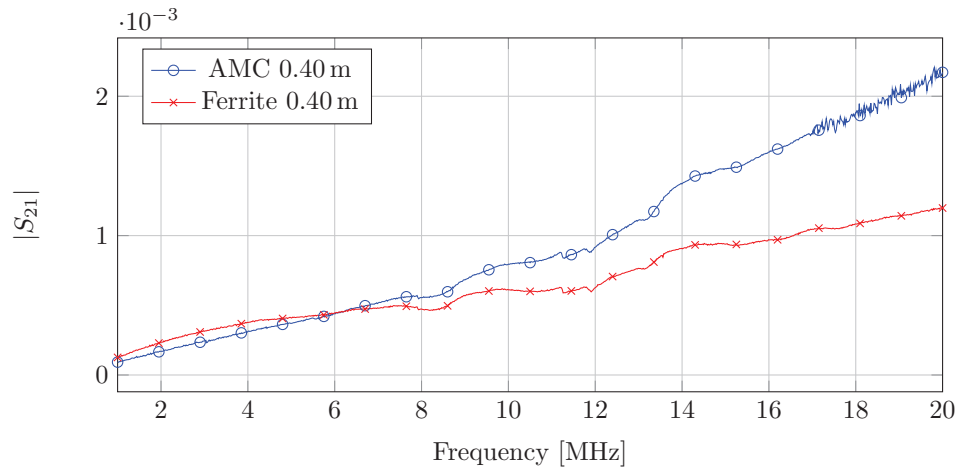


Figure 4.37: Measured transmission coefficient, with 0.40 m air gap between coils.

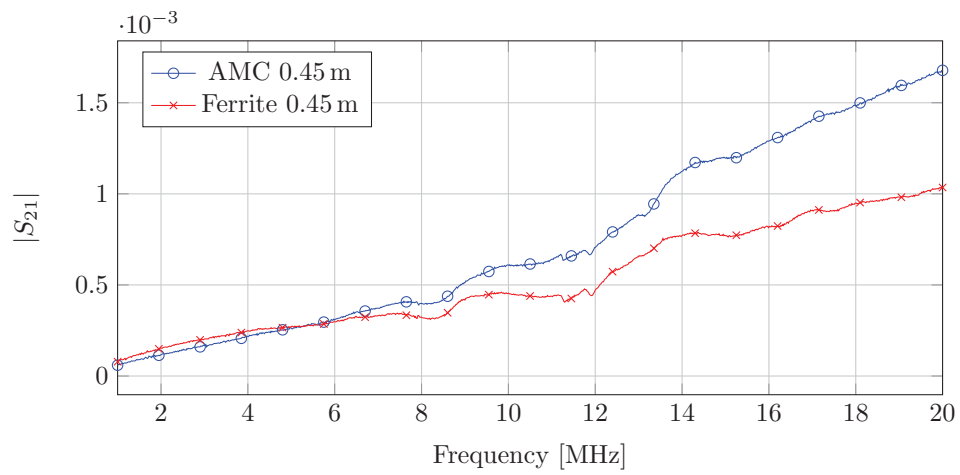


Figure 4.38: Measured transmission coefficient, with 0.45 m air gap between coils.

### Measurements of 364003 material

To investigate why results differ from simulation measurements of the magnetic properties of the substrate material used in the AMC and ferrite pads were conducted. A square core with rectangular cross section consisting of stacked ferrite sheets was constructed, with one to ten stacked sheets. To measure the cores a single turn of copper tape is threaded through the core forming a single turn inductor with impedance,  $Z_m$ , the copper tape has a fixture impedance of,  $Z_f$ . As per [91] the concept of magnetic path length makes calculation of the properties of this type of core trivial:

$$\mu_r = \frac{(Z_m - Z_f)L_c}{j\omega\mu_0 A_c} + 1, \quad (4.16)$$

where;

$$\mu_r = \mu' - j\mu''. \quad (4.17)$$

The average path length,  $L_c$ , is;

$$L_c = 2(A + B) \quad (4.18)$$

where,  $A$ , is the outer dimension and,  $B$ , the inner while,  $H$  is the height of the core including the glue and backing depth. The cross sectional area,  $A_c$ , is:

$$A_c = \frac{H(A - B)}{2}. \quad (4.19)$$

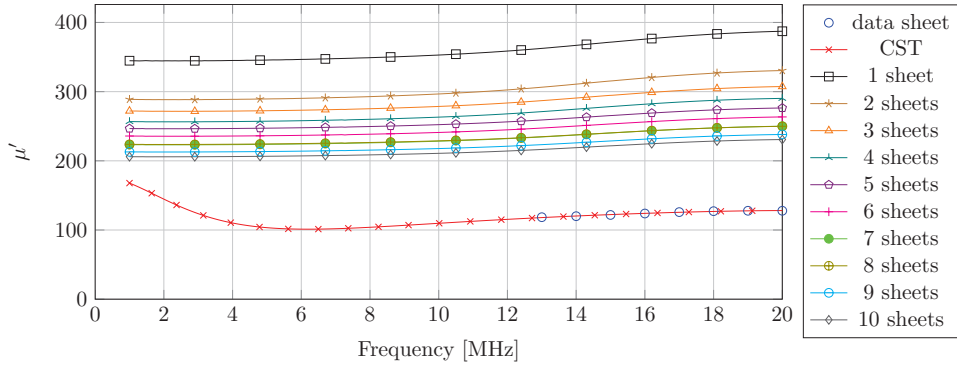


Figure 4.39:  $\mu'$  comparison between measurement of ferrite sheet stacks, simulation and data sheet values. Note CST results are inaccurate below 10 MHz due to the polynomial fit.

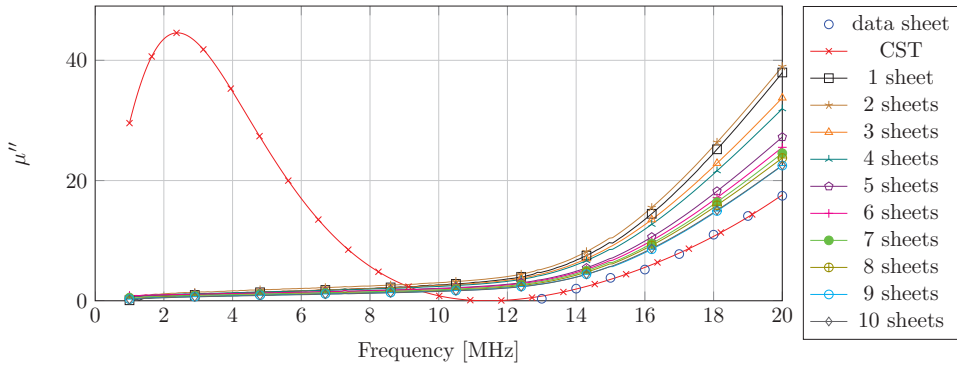


Figure 4.40:  $\mu''$  comparison between measurement of ferrite sheet stacks, simulation and data sheet values. Note CST results are inaccurate below 10 MHz due to the polynomial fit.

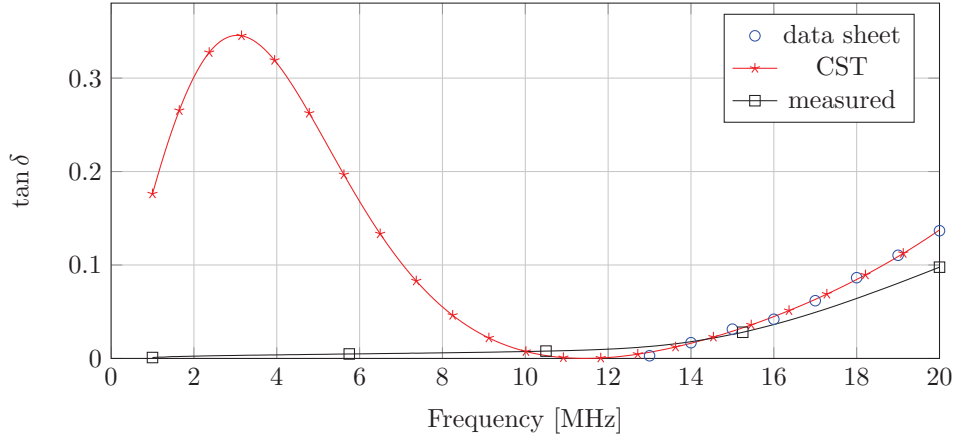


Figure 4.41: Loss tangent comparison between measurement of 10 stacked ferrite sheets, simulation and data sheet values. We have omitted the loss tangent data for the stacks less than 10 sheets deep for clarity as it practically overlaps the 10 stack data.

The permeability of the measured ferrite is much greater than in the manufacturer supplied data and simulation (Fig. 4.39, 4.40) with decreasing effective permeability as more ferrite sheets are stacked. This decrease in effective permeability is due to the effective reluctance of the ferrite falling by effect of the glue filled gaps between layers. The loss tangent data (Fig. 4.41) at first appears to be quite a good fit to the simulation data, but if the region 10 MHz to 14 MHz is considered it is observed that the loss tangent in simulation is underestimated. It is in this region where maximum power transfer efficiency is simulated, this could go some way towards explaining discrepancies between simulation and measurement. However this does not explain the discrepancy in resonant  $Q$  (Fig. 4.19, 4.20) for both the AMC and ferrite pads which should match simulation in the range 14 MHz to 20 MHz, as the loss tangent fit in this region is excellent.

The increased losses are not just caused by ferrite but must instead be at least partly be caused by a common factor between the two pad types, the remaining unexamined factor could be the dielectric former which is not included in simulation. This is composed of SLS PA2200 Nylon, and general purpose epoxy for which we do not have loss information.

### Measured efficiency

An experiment has been devised that allows the measurement of link efficiency. The pads are positioned coaxially with a 70 mm air gap between the coils, in simulation the fractional link efficiency,  $\eta$ , is greater than 0.88 at this distance (Table 4.47) at 12.9 MHz. To measure  $\eta$  the  $T_x$  pad was excited using a conventional 50  $\Omega$  output impedance signal generator connected to the coil via a Mini-Circuits T1-1-KK81 balun. A small PCB was connected to the  $R_x$  pad with a series tuning capacitor and load resistor. The input power to the  $T_x$  pad was measured using a current clamp and differential voltage probe. While the output power was measured using a conventional single ended oscilloscope probe to measure the voltage across the load resistor.

The input power to the link was measured using a Keysight N2891A differential voltage probe ( $\pm 2\%$ ) and Keysight N2783B current probe ( $\pm 1\%$ ,  $\pm 10$  mA). Not taking into account phase distortion effects upon measurements with imaginary power flow; this results in an uncertainty of  $\pm 27.5\%$ . However the majority of the uncertainty is due to offset error of the current probe, thus to avoid this error contribution the current probe was AC coupled. To improve the signal to noise ratio of the current probe at low input currents the ERES function of the Lecroy HDO4104 oscilloscope was used. This function trades signal bandwidth for improved bit depth, this was set to +2 bits reducing bandwidth to 76 MHz.

The usage of a differential voltage probe at the transmitter pad eliminated the problem of ground loops



causing inaccurate input power reading. To measure the output power a Lecroy PP018 is used to measure the voltage across a load resistor. The inductance of the load resistor and resistance of the load resistor at the operating frequency was measured using a Keysight E4490A impedance analyser. The same lead length was used when measuring the load resistors in the impedance analyser fixture as the efficiency test. This allowed compensation for the lead inductance by assumption that, the inductance is in series with the resistance and the resistors have no further parasitic elements. The oscilloscope probe is attached to the load via a BNC socket to reduce pick up of magnetic fields by the oscilloscope probe via the ground lead loop.

The tuning capacitor was a fixed 97.45 pF (measured) ATC100B series capacitor (C0G) for both pad sets. The operating frequency was set to maximise the voltage across the load resistor (peak power transfer). The test frequency ranged from 12.75 MHz to 13.4 MHz with larger resistor values operating at higher frequency. This frequency range should only cause small variation in link efficiency (Fig. 4.51) as the peak link efficiency is tracked. The compromise of fixed capacitance had to be made due to the infeasibility of operating at fixed frequency without a variable capacitor. However variable capacitors are not available with sufficient  $Q$  to avoid noticeable degradation of link efficiency.

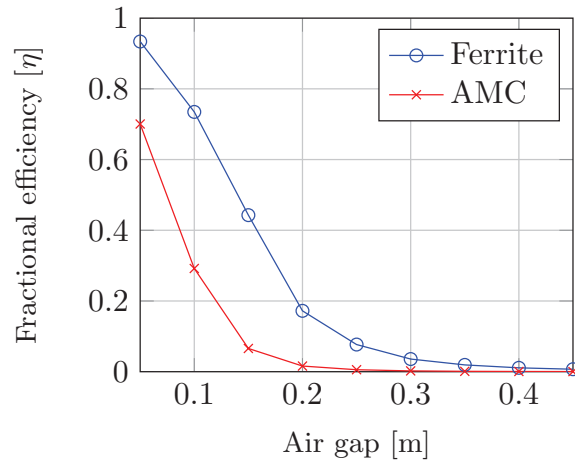


Figure 4.42: Predicted fractional power transfer efficiency for 12.9 MHz, from link efficiency equation. Using resonant measurements of pad  $Q$  and measured,  $k$ .

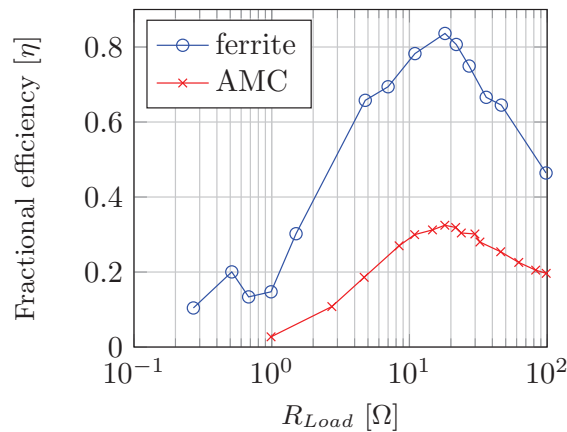


Figure 4.43: Measured fractional power transfer efficiency comparison between ferrite and AMC wireless power links at 70 mm air gap and approximately 12.9 MHz operation. Measurement made by load sweeps, on real link, with voltage and current monitoring.

The ferrite pad link had a peak efficiency of 84% at 18.1  $\Omega$  while the AMC had a peak efficiency of only

32% at  $18.0\ \Omega$  (Fig. 4.43). This result is consistent with the low  $Q$  measured using the single sided coupling device and the measured coupling factors. Using the magnetic link efficiency,  $\eta$ , equation;

$$\eta = \frac{k^2 Q_{Tx} Q_{Rx}}{(1 + \sqrt{1 + k^2 Q_{Tx} Q_{Rx}})^2}, \quad (4.20)$$

the predicted efficiencies based upon these measurements have been plot with respect to distance for the same 12.9 MHz operating frequency (Fig. 4.42). The data used to generate this plot is the single sided resonant  $Q$  (Fig. 4.19) in addition to the measured coupling factors (Figs. 4.21, 4.22, 4.23, 4.24, 4.25, 4.26, 4.27, 4.28, 4.29). It is clear that at this frequency due to the much lower than predicted  $Q$  factor the AMC had no advantage over the ferrite pads.

The link efficiency equation predicts at 16.941 MHz where the effective coupling factor is maximal (Fig. 4.44. The AMC should exhibit a peak fractional efficiency of 0.688 and the ferrite pads 0.629 with an air gap of 0.1 m. To attempt to demonstrate a region of operation where the AMC had an efficiency advantage the operating frequency was adjusted to 17 MHz. As the load was swept the Ferrite pad resonated at 16.68 MHz to 16.84 MHz while the AMC resonated in the range 16.71 MHz to 17.75 MHz. However the results (Fig. 4.45) differ greatly from the link efficiency equation predication at 16.941 MHz. Measured peak fractional efficiencies were 0.148, and 0.115, for the Ferrite pads and AMC pads respectively. This fails to show improved efficiencies from using the AMC structure but does appear to show the coupling factor is greater for the AMC case than the ferrite case. The likely reason for the discrepancy between the link efficiency prediction and the measured link efficiency is an inaccurate coupling factor measurement due to such a measurement been taken close to the pads self resonances.

If the  $Q$  measurements are assumed to be correct (using a variation of a method established to be reliable in the measurement chapter) the link efficiency equation can be rearranged to give the coupling factor,  $k$ :

$$k^2 Q^2 = \frac{4\eta_{max}}{(\eta_{max} - 1)^2}. \quad (4.21)$$

The derived the coupling factor in the ferrite case was 0.0078 and the AMC case was 0.033. This demonstrates an effective coupling factor for the AMC that is 4.2 times greater for the AMC than the ferrite coil. Confirming that as long as the  $Q$  factor of the coils has been measured correctly the coupling factor of the AMC pads must be greater than the ferrite pads. This result compares with an earlier measurement of 0.0382 and 0.194 for the ferrite and AMC respectively. As the ferrite link is a conventional IPT link and therefore can be characterised by the link efficiency equation this suggests that measurements of the coupling factor by direct connection of the VNA were not reliable at this frequency; this is to be expected as we have already shown that this method of connection distorts impedance measurements of the coils (measurement chapter). However improving this measurement is difficult due to the need to move the calibration plane beyond a balun.

Returning to the graphs of output efficiency with respect to load around 16.941 MHz (Fig. 4.45) the distinctly differing natures of the wireless power transfer systems were observed. The ferrite system only displayed a small region of peak efficiency around the optimal load whereas the AMC system displayed a two decade region of peak efficiency with respect to load. A wide range of loads near peak efficiency is characteristic of a system with low  $Q$  and greater coupling factor. The extreme example of such characteristics is conventional transformer that has a very wide efficient load range.

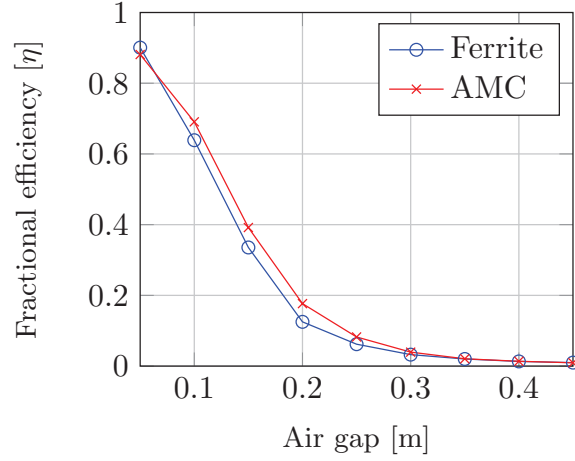


Figure 4.44: Predicted fractional power transfer efficiency for 16.941 MHz, from link efficiency equation. Using resonant measurements of pad  $Q$  and measured,  $k$ .

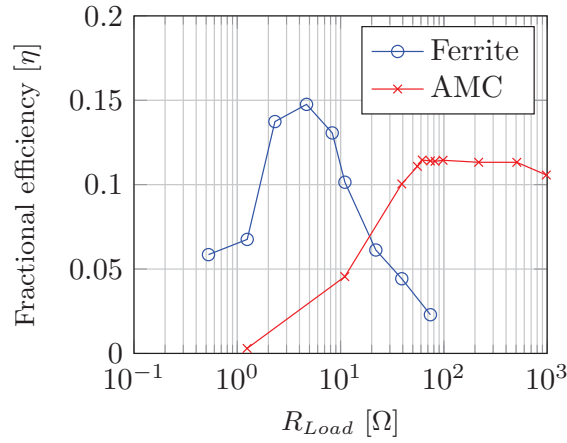


Figure 4.45: Measured fractional power transfer efficiency comparison between ferrite and AMC wireless power links at 100 mm air gap and approximately 16.941 MHz operation. Measurement made by load sweeps, on real link, with voltage and current monitoring.

### Study of optimal loads and comparison to capacitor loaded coils

The charging pads deviate from simulation due to some unknown loss, possibly due to the polymers used to construct the formers. Assuming this loss can one day be found and reduced, a simulation study has been conducted on how an AMC magnetic link would interact with the rectification circuits of complete IPT systems.

Although when measuring the link efficiency of the system increased coupling factor has been demonstrated, strong resonances in the impedance plots may cause the AMC behaviour to be mistakenly categorised as a capacitively loaded coil. As an example in some pager antennas [92], an inductively coupled capacitively tuned loop defines the resonant frequency. To this end the fractional transfer efficiency in simulation and the ideal series load impedance for the AMC pad, the ferrite pad and the ferrite pad with 50 pF of parallel capacitance with respect to distance have been compared (Fig. 4.50, 4.51, 4.52, 4.53) using the method of Zargham and Gulak [6]. These results show the peak link efficiency of the AMC is always greater than the peak efficiency of the ferrite pad which has the same efficiency as the capacitively loaded ferrite pads. The greater the distance between the loops the greater the advantage of using the AMC rather than the ferrite pads.

To examine the viability of operating the AMC with rectifier circuits the optimal series load when operating in variable frequency and fixed frequency modes has been found (Fig. 4.46, 4.47, 4.48, 4.49). Of particular importance is minimising the required variation of imaginary impedance, as this would necessitate adjustment of rectifier phase angle or variable capacitance, both of which are difficult without degrading  $Q$ . When operating in variable frequency mode the AMC displays  $-7.2\%/+13.4\%$  complex impedance variation about the mean compared to  $-1.07\%/+2.84\%$  for the ferrite pad. However when operating in fixed frequency mode both pads displayed minimal variation in imaginary impedance, always without significant loss in link efficiency. Fixed frequency operation is normal for wireless power transfer systems as the frequency bands regulated to operate in are narrow and the amplifiers and rectifiers used are frequently based on tuned topologies. The real portion of the optimal series load for the AMC pads is greater than for the ferrite pad, but displays the same approximately 30 : 1 variation in impedance over the 0.15 m distance range.

These results show that the AMC consistently displays in simulation better transfer efficiency than the equivalent ferrite pad while having similar optimal secondary load. It will therefore be compatible with the same rectifier topologies as the ferrite pad.

| Distance between loops | AMC Frequency | AMC $\eta$ | AMC $Z_{Load}$             |
|------------------------|---------------|------------|----------------------------|
| 0.05 m                 | 12.22 MHz     | 0.985      | $(46.89 - 160.85i) \Omega$ |
| 0.10 m                 | 12.91 MHz     | 0.939      | $(25.66 - 205.65i) \Omega$ |
| 0.15 m                 | 12.35 MHz     | 0.807      | $(3.761 - 176.65i) \Omega$ |
| 0.20 m                 | 12.79 MHz     | 0.624      | $(2.021 - 198.64i) \Omega$ |

Figure 4.46: AMC optimal frequency tuning.

| Distance between loops | Ferrite Frequency | Ferrite $\eta$ | Ferrite $Z_{Load}$         |
|------------------------|-------------------|----------------|----------------------------|
| 0.05 m                 | 12.91 MHz         | 0.978          | $(18.88 - 129.75i) \Omega$ |
| 0.10 m                 | 12.36 MHz         | 0.891          | $(3.590 - 124.64i) \Omega$ |
| 0.15 m                 | 12.39 MHz         | 0.682          | $(1.107 - 124.76i) \Omega$ |
| 0.20 m                 | 12.40 MHz         | 0.392          | $(0.481 - 124.80i) \Omega$ |

Figure 4.47: Ferrite optimal frequency tuning.

| Distance between loops | AMC Frequency | AMC $\eta$ | AMC $Z_{Load}$             |
|------------------------|---------------|------------|----------------------------|
| 0.05 m                 | 12.90 MHz     | 0.984      | $(64.02 - 185.91i) \Omega$ |
| 0.10 m                 | 12.90 MHz     | 0.939      | $(15.57 - 205.10i) \Omega$ |
| 0.15 m                 | 12.90 MHz     | 0.801      | $(5.076 - 205.56i) \Omega$ |
| 0.20 m                 | 12.90 MHz     | 0.623      | $(2.153 - 206.08i) \Omega$ |

Figure 4.48: AMC fixed 12.9 MHz tuning.

| Distance between loops | Ferrite Frequency | Ferrite $\eta$ | Ferrite $Z_{Load}$         |
|------------------------|-------------------|----------------|----------------------------|
| 0.05 m                 | 12.90 MHz         | 0.976          | $(18.85 - 129.56i) \Omega$ |
| 0.10 m                 | 12.90 MHz         | 0.888          | $(3.766 - 130.37i) \Omega$ |
| 0.15 m                 | 12.90 MHz         | 0.675          | $(1.158 - 130.17i) \Omega$ |
| 0.20 m                 | 12.90 MHz         | 0.383          | $(0.564 - 130.09i) \Omega$ |

Figure 4.49: Ferrite fixed 12.9 MHz tuning

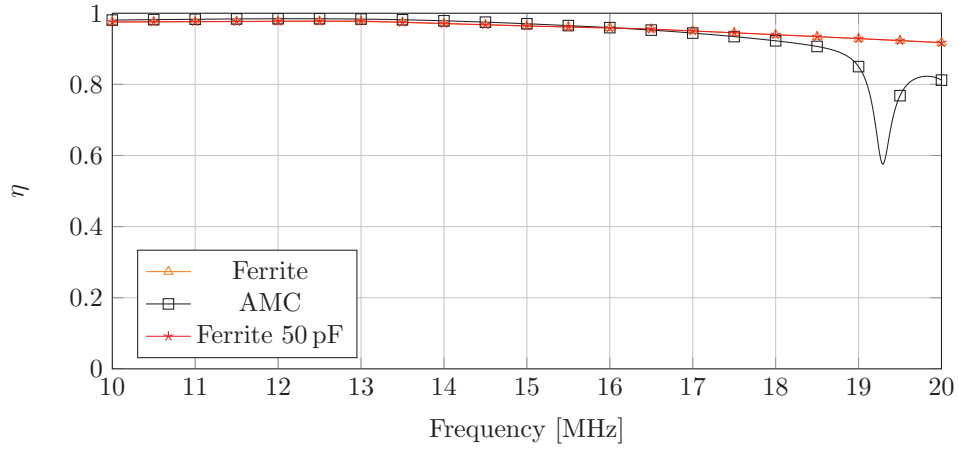


Figure 4.50: Simulated fractional maximum power transfer efficiency with 0.05 m air gap between coaxially aligned coils.

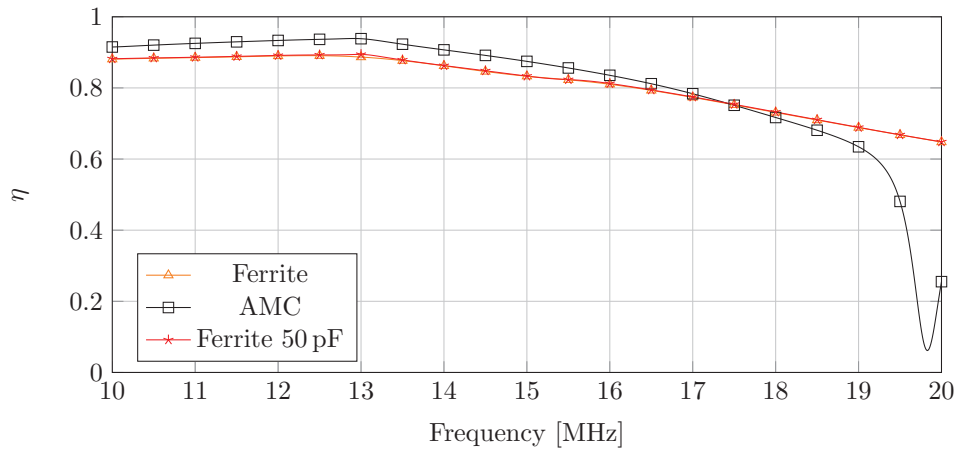


Figure 4.51: Simulated fractional maximum power transfer efficiency with 0.10 m air gap between coaxially aligned coils.

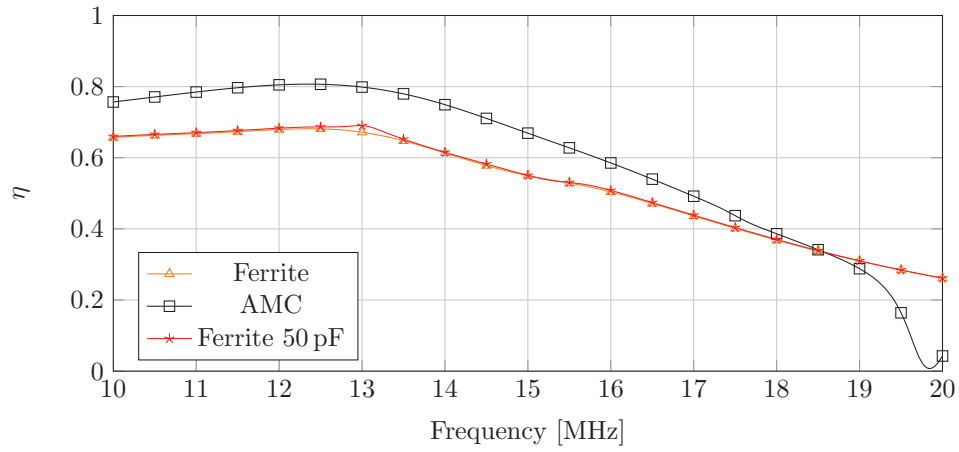


Figure 4.52: Simulated fractional maximum power transfer efficiency with 0.15 m air gap between coaxially aligned coils.

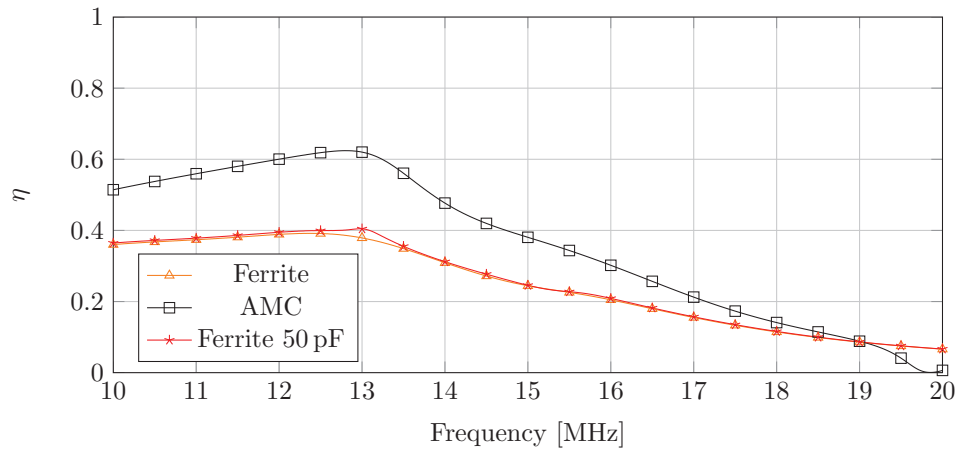


Figure 4.53: Simulated fractional maximum power transfer efficiency with 0.20 m air gap between coaxially aligned coils.

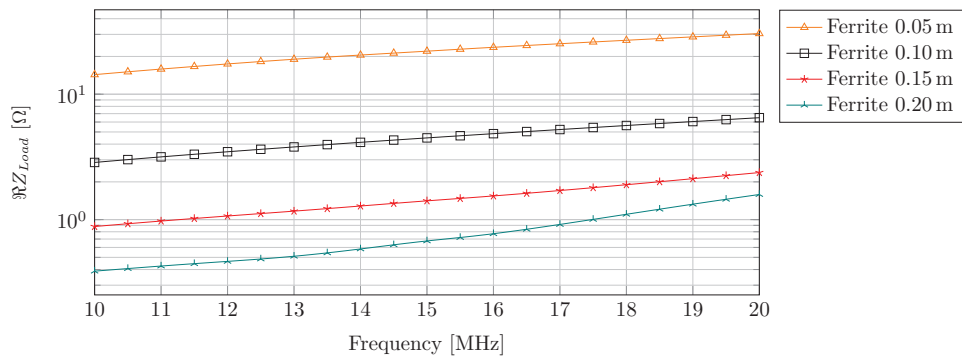


Figure 4.54: Simulated optimal series secondary load real portion for ferrite pad

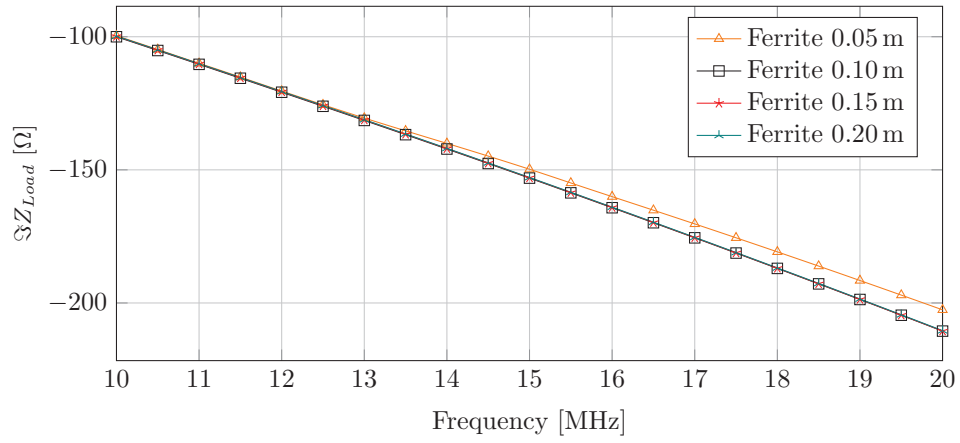


Figure 4.55: Simulated optimal series secondary load imaginary portion for ferrite pad

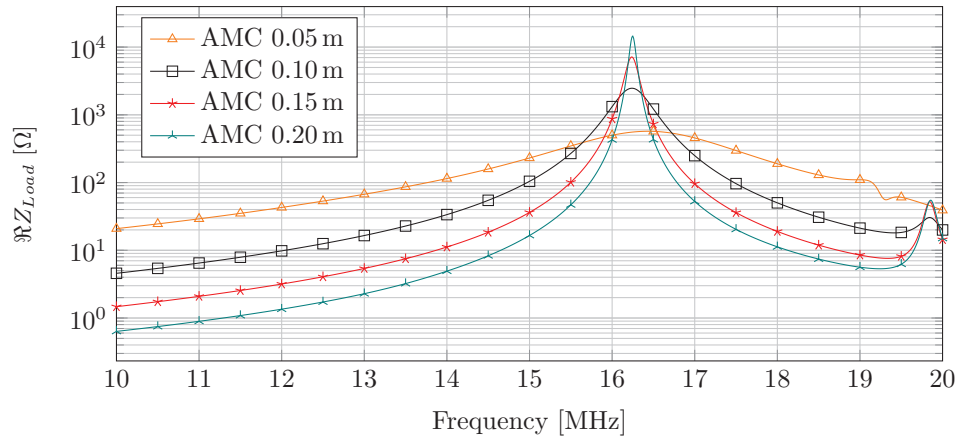


Figure 4.56: Simulated optimal series secondary load real portion for AMC

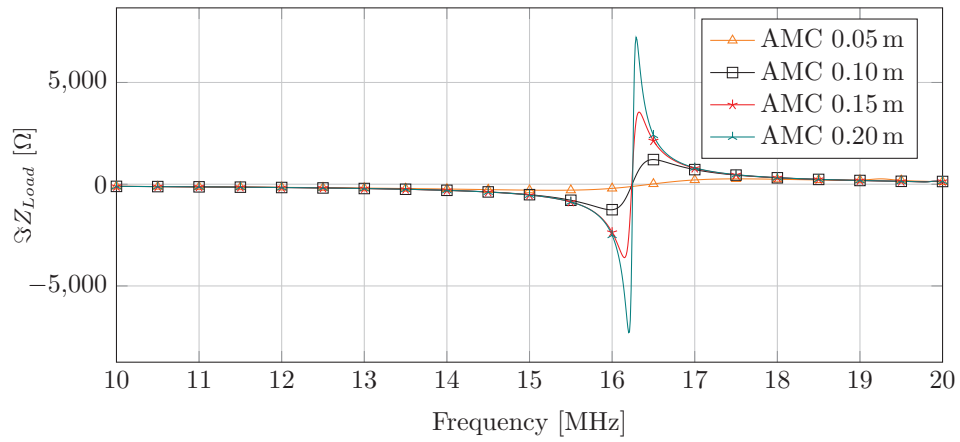


Figure 4.57: Simulated optimal series secondary load imaginary portion for AMC

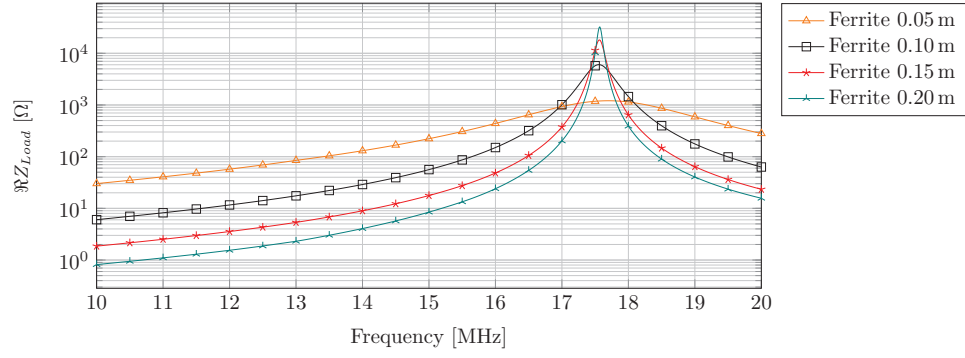


Figure 4.58: Simulated optimal series secondary load real portion for ferrite pad with 50 pF of parallel loading on both pads

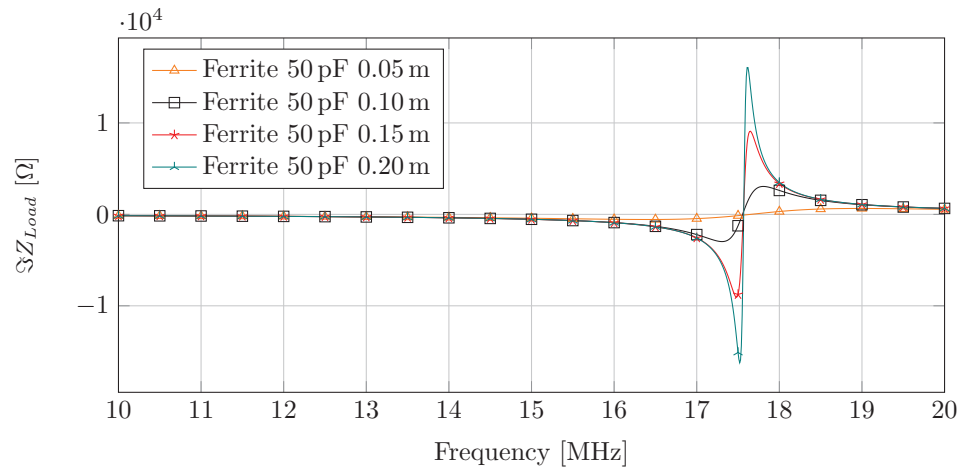


Figure 4.59: Simulated optimal series secondary load imaginary portion for ferrite pad with 50 pF of parallel loading on both pads



### 4.5.3 field simulations

The simulations had fixed input power of 1 W and operating frequency of 12.9 MHz. The optimal load (Fig. 4.48, 4.49) for this frequency was connected to the secondary coil, the coils are coaxially aligned with a 0.1 m air gap between the coils. A cut plane was then defined at the midpoint distance between the two coils tangential to the plane upon which the coils lie. The vector electromagnetic field is captured with 1 mm sampling at the cut plane. The vector magnitude of the E and H field components has been plot (Fig. 4.60, 4.61, 4.62, 4.63). The energy stored in the electric field in both cases was far less than the magnetic as:

$$u_{EM} = \frac{\varepsilon}{2} |\mathbf{E}|^2 + \frac{1}{2\mu} |\mathbf{B}|^2, \quad (4.22)$$

where  $u_{EM}$  is the energy stored. The AMC displayed considerably greater magnetic energy than ferrite pad. This results suggests that energy is mainly transferred through the magnetic field and that the AMC is increasing the magnetic coupling between the two coils.

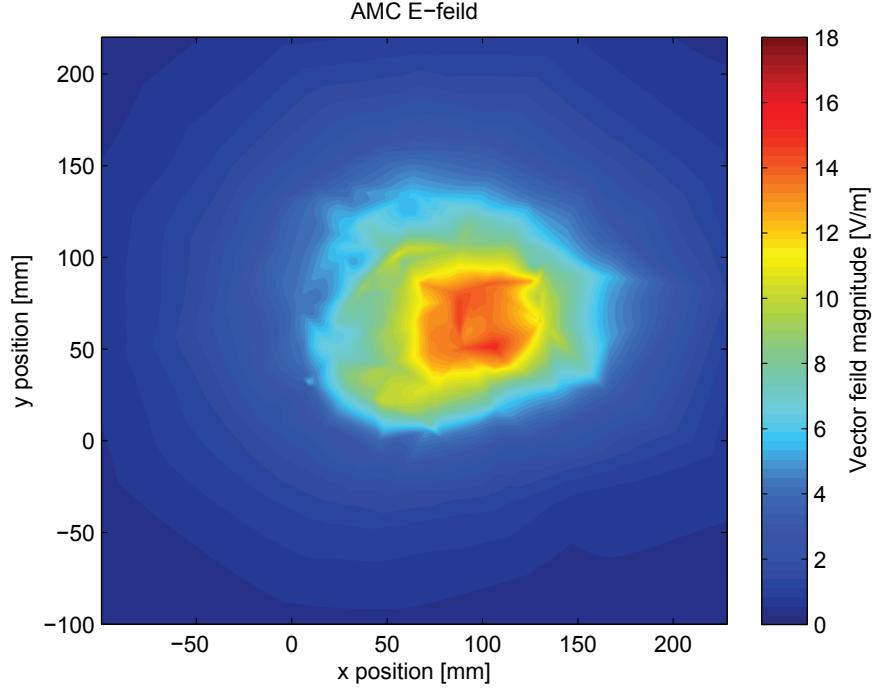


Figure 4.60: AMC cut plane E-field vector magnitude. This is comparable to the ferrite case.

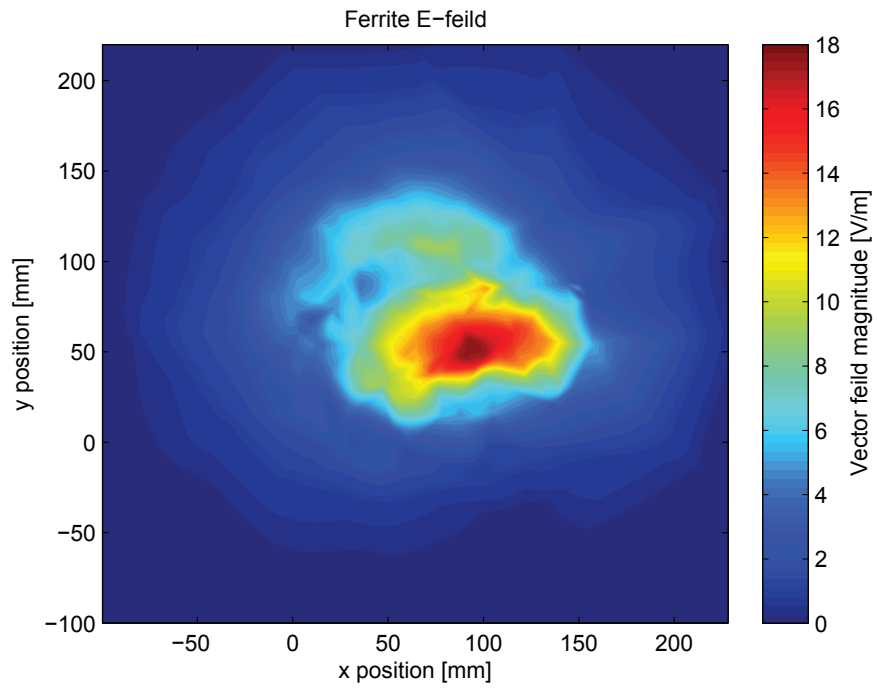


Figure 4.61: Ferrite cut plane E-field vector magnitude. This is comparable to the AMC case.

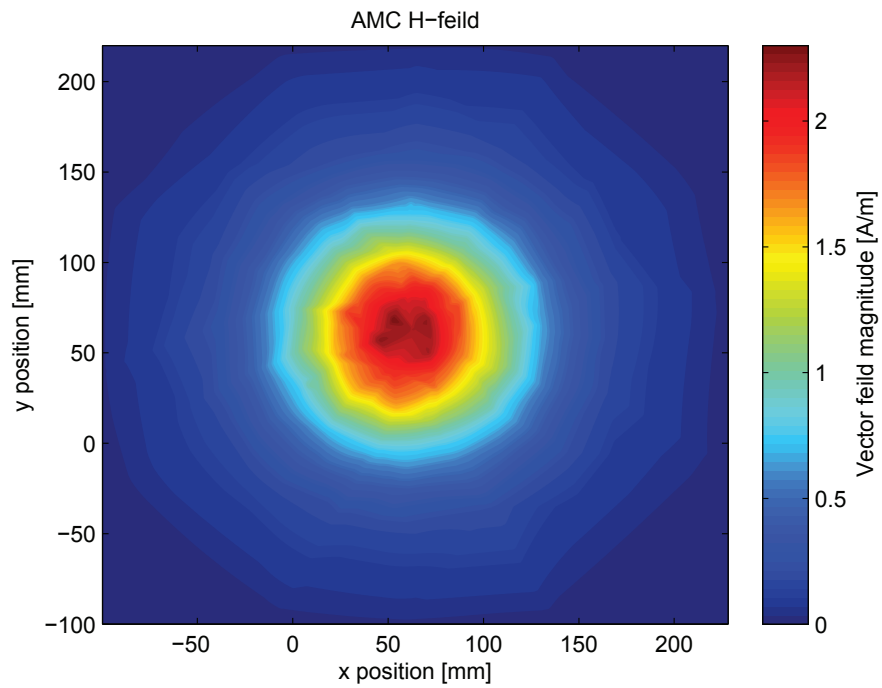


Figure 4.62: AMC cut plane H-field vector magnitude. Showing much greater magnitude than the ferrite case of figure 4.63.

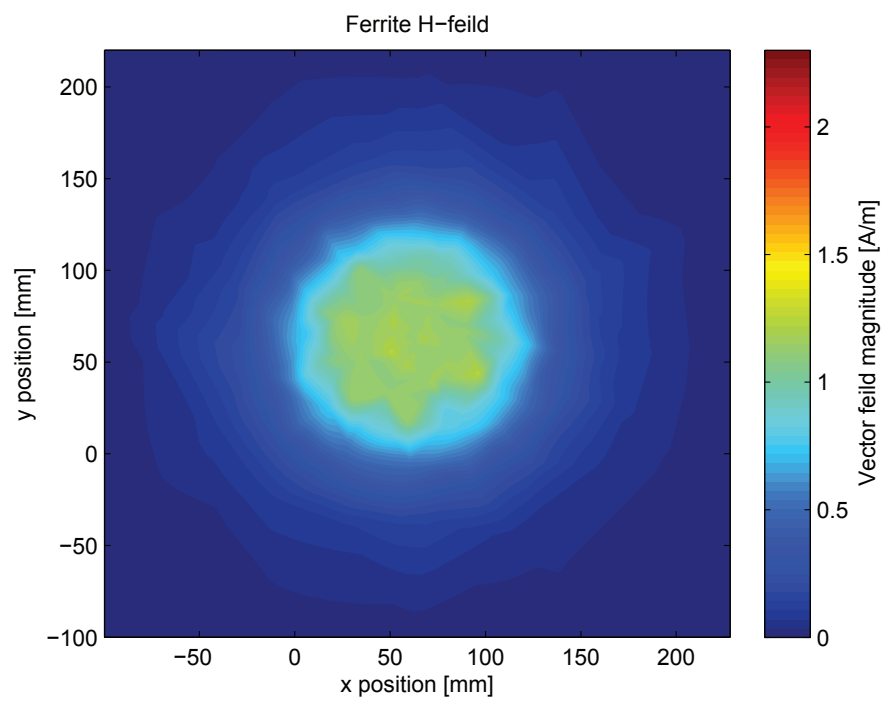


Figure 4.63: Ferrite cut plane H-field vector magnitude. Considerably less than the AMC case (Fig. 4.62.

#### 4.5.4 Conclusions and further work

In this chapter an AMC structure suitable for ISM band wireless power transfer has been developed. This AMC has unique combination of a ferrite substrate and lumped capacitor loading to produce a surface with cells only  $113 \times 10^{-6} \lambda$  thick. Plane wave behaviour formula have been modified to include the contribution of a permeable substrate. Simulations show the unit cell of the proposed AMC structure conform to the modelled characteristics. However this plane wave model is insufficient to predict the operating frequency when used in an IPT scenario. It was then demonstrated in simulation that the structure could improve the link efficiency.

With the justification for the structure and a viable design clear a prototype AMC wireless power link designed for 13.56 MHz was constructed, as well as a conventional dimensionally identical ferrite backed ground plane using the same quantity of ferrite. This AMC link while displaying many of the simulated characteristics such as peaking self and mutual effective inductance also deviated significantly from simulation in having much greater than expected loss. The ferrite link also had greater than expected loss which was found to be partly attributable to the ferrite substrate deviating from the manufacturers specifications. The AMC displayed a greater effective coupling factor than the ferrite pad link at the operating frequency. Many other possible explanations were eliminated as causes of the increased losses.

Finding the system fractional transfer efficiency over the full desired frequency range was not possible at this stage due to their high  $Q$  factors. However when the fractional efficiency as part of a  $50 \Omega$  system without matching networks and found the AMC had better efficiencies over all tested air gaps beyond 10 MHz.

By experimental load sweep the peak fractional efficiency of the two systems was found. Two operating points were examined 0.07 m air gap at 12.9 MHz and 0.10 m air gap at 16.9 MHz. In both cases the Ferrite pads were more efficient than the AMC pads. However these tests provided more evidence that the coupling factor was greater for the AMC pads, resulting in the AMC pads having a greater flexibility in the range of loads close to optimal. The optimal loads with respect to distance for the AMC and Ferrite pads in simulation were studied. The optimal loads are similar for both pads. The AMC can operate at a fixed frequency without a complex variable optimal load with minimal loss in efficiency. This results means the AMC should operate with existing ISM band rectifier circuits.

Finally fields have been examined when the AMC is operating in simulation, finding that the magnetic coupling is increased and the boundary condition that the tangential magnetic field strength at the surface is reduced, consistent with the theory of the structure.

## Chapter 5

# Long range inductive power transfer system

The work in this chapter presents a long range (up to 6 m) IPT system prototype designed for powering mW level for the internet of things (IOT). This work was developed early in the PhD before the analysis of the previous chapters but is presented last to allow the system to be described within the framework of the analysis of coil design and coil measurement. Examples have been selected where later work would aid the development of a new version of this system.

### 5.1 Introduction

In this chapter an inductive link is established between a large planar, 1 m by 1 m, square transmit coil,  $T_x$ , and a small planar, 170 mm by 170 mm, square receiver coil,  $R_x$ , demonstrating highly asymmetrical coil configurations that real-world applications such as sensor networks impose. High  $Q$  factor  $T_x$  and  $R_x$  coils required for viable power transfer efficiencies over such distances are measured using a resonant method. A Class-E amplifier is used to drive the transmitter coil. The applicability of the Class-E amplifier in very low magnetic coupling scenarios and at the high frequencies of operation required for high  $Q$  operation is demonstrated by its usage as the  $T_x$  coil driver.

Attempts to transmit power using electromagnetic fields beyond 1 m have tended to use the far field, rather than near field region [93][94]. However such operation involves radiating energy and is intrinsically inefficient, unless the receiver intercepts a significant portion of the radiated energy. This limits such systems to the use of antennas with narrow beam patterns. The technology presented here uses loop antennas which have very broad magnetic field distributions allowing power transfer to receivers over a wide area [95]. Unlike in far field systems coils are kept electrically small, to keep radiation losses to a minimum, avoiding significant radio emission [23].

An alternative for ultra low power sensors may be ambient RF harvesting systems. They are capable of tens of  $\mu\text{W}$  with cm scale antennas [96]. Although they are able to operate in many urban environments without an explicit power source, many applications are not achievable at this power level. Greater power levels are possible by use of an explicit RF source. Hubregt J. Visser has developed a directional radiative system, capable of delivering hundreds of  $\mu\text{W}$  to the load at a distance of 1 m [94]. Inductive coupling has been recently demonstrated with watt level received power at distances over 0.6 m [16]. Another IPT system has been demonstrated transmitting power with 15% efficiency over 2 m [97], using a 1 m by 1 m,  $T_x$ , and 1 m by 1 m,  $R_x$ , coil at a frequency of 513 kHz.

It has been shown in the introduction and measurement chapters that when optimising the coils of an

inductive power transfer system within a given dimensional constraint, the most important parameter is the  $Q$  factor. The link efficiency,  $\eta$ , is given by [13]:

$$\eta = \frac{k^2 Q_{Tx} Q_{Rx}}{(1 + \sqrt{1 + k^2 Q_{Tx} Q_{Rx}})^2}, \quad (5.1)$$

where the coupling factor,  $k$ , is given by:

$$k = \frac{L_{TxRx}}{\sqrt{L_{Tx} L_{Rx}}}. \quad (5.2)$$

The coil's self inductance,  $L_{Tx}$ ,  $L_{Rx}$  is proportional to the number of turns squared, while the mutual inductance between the  $T_x$  and  $R_x$  coils,  $L_{TxRx}$ , is proportional to the turns product of the two coils. Therefore,  $k$  is effectively set by the coil diameter and varies little with changes in the number of turns. The link efficiency is constant and high until  $k^2 Q_{Tx} Q_{Rx} \ll 1$  (Eq. 5.1) whereupon the link efficiency ultimately falls with the 6th power of distance (consistent with behaviour of reactive near field). Usually the coil's dimensions are constrained by the operating scenario and are not available as a design parameter. As such, maximising  $Q$  factor by selection of appropriate operating frequency and minimising the coil's loss resistance are key to obtaining high link efficiency [16].

For coupling to be mostly due to the magnetic field and to minimise radiative emissions it is desirable to operate within the reactive near field. This imposes a maximum operating frequency constraint upon the system dictated by the maximum desirable transmission distance. The transition between near and far field operation is not a sudden shift in the structure of the fields but a more gradual transition, a commonly accepted limit,  $r$ , on the near field for electrically short antennas is [98]:

$$r = \frac{C}{\omega}, \quad (5.3)$$

Where,  $C$ , is the speed of light in freespace and,  $\omega$ , the angular frequency. This results in a maximum frequency constraint of 3 MHz for 10 m transmission distance. Operating with dissimilar,  $T_x$ , and  $R_x$ , coil sizes causes the optimal transmission frequency for the,  $T_x$ , and  $R_x$ , coils to be at different frequencies. An electrically larger coil will lose more energy to radiation, ( $R_{rad}$ ), in the frequency range of interest than an electrically smaller coil causing the larger coil to have its maximum  $Q$  at a lower frequency than the smaller. Assuming the coil's losses are entirely in their inductive impedance, the coil  $Q$  is given by:

$$Q = \frac{\omega L}{R_{rad} + G_p R_{skin}}. \quad (5.4)$$

Where,  $R_{rad}$ , represents the coil's radiation loss and  $G_p R_{skin}$ , represents the proximity factor and skin effect losses. Simple analysis would suggest choosing an operating frequency to maximise the product  $Q_{Tx} Q_{Rx}$ ; however, as the loss mechanism for the larger of the two coils is radiation this is likely to result in excessive radiative emissions from the,  $T_x$ , coil. Below the peak  $Q$  factor of a coil the skin effect is the dominant loss mechanism:

$$Q(\omega \ll \omega(Q(Peak))) \propto \sqrt{\omega}. \quad (5.5)$$

At frequencies beyond the peak  $Q$  factor of a coil the radiation loss is the dominant loss in the coil:

$$Q(\omega \gg \omega(Q(Peak))) \propto -\frac{1}{\omega^3}. \quad (5.6)$$

Therefore the system operating frequency is constrained by the larger of the two coils [16]; as the increase in the smaller coil  $Q$  with increasing frequency is at a far slower rate than the reduction in the larger coil rate after the peak  $Q$  of the larger coil is reached.

For long range IPT the coupling between primary and secondary is exceptionally weak which allows for a number of useful design approximations to be made:

- The Class-E amplifier load is free-wheeling primary coil with no reflected secondary impedance and thus is given by the measured coil  $Q$  and resonant frequency.
- The impedance match for the secondary coil can be simplified as a match to its own resonant tank by assuming the incoming power is in the form of a current source in parallel to the tank inductor.
- Optimisation of coil  $Q$  for planar coils can be done by first finding the optimum turn spacing for the two turn case (balancing proximity effect against inductance caused by adjacent turns) and then increasing the number of turns to the point at which the radiation losses cause a reduction in  $Q$ .
- The design of the transmitting amplifier and coil is decoupled from the design of the receiving coil and receiver power conversion circuit due to the low overall efficiency of the system resulting in the majority of the effective primary resonant tank resistance been the,  $T_x$ , coil's loss resistance.

## 5.2 Design

### 5.2.1 Transmit coil

The maximum operating frequency is 3 MHz due to the requirement to operate in the reactive near field. While the,  $T_x$ , coil must fit within a 1 m square dimensional constraint and be of planar construction. The  $T_x$  coil is therefore designed to maximise  $Q$  within these restrictions. For ease of construction we chose the coil consists of from plumbing pipe joined with Yorkshire solder joints. The resistance of the Yorkshire joints was tested at DC and found to be approximately the same resistance as an equivalent length of tube. This is expected as the solder layer in the joint if properly soldered is of the order of 10  $\mu\text{m}$  thick. The largest commonly available copper plumbing pipe is 28 mm diameter is selected. As this offers the largest cross section this will also present the smallest loss resistance. At this point the only two remaining parameters are the number of turns of the coil and the turn spacing, assuming that the velocity of propagation is the speed of light in the  $T_x$  coil going beyond 2 turns will result in a coil that is electrically too long and thus unacceptably radiative at the operating frequency. Both the one turn loop case and the two turn case were simulated in CST MWS. One turn loops were typically found to have lower  $Q$  than two turn coils because there is very little self flux linkage between different sections of the loop greatly reducing the  $Q$ . With the single turn loop eliminated the only remaining design choice is a two turn square planar spiral for which the turn spacing is optimised to 56 mm for maximum  $Q$  by simulation sweeps.

### 5.2.2 Amplifier

The Class-E amplifier was designed using the design method of Rabbs [19] driving the unloaded primary coil. The ratio between the,  $T_x$ , coil resonant frequency and the operating frequency of the circuit are adjusted until the design value of the capacitance across the MOSFET in the amplifier was equal to the high voltage asymptote of its  $C_{DS}$ , removing the need for this capacitance to be augmented with an additional discrete capacitor. The technique of semi resonant matching to eliminate the series output inductor from Class-E amplifiers is described in the paper of Pinuela et al. [16].

### 5.2.3 Miniaturised receiver coils

As described in chapter 3, direct measurement of coil parameters via the reflection coefficient using a traditional network analyser is not generally possible for  $Q$  greater than 30 [49]. Therefore measurement

of coil parameters was performed using a transmission-type resonant measurement [99] with 2 pF coupling capacitors to minimally load the resonators (fig. 5.1). An estimate of resonator loading was obtained using the peak transmission coefficient [44].

$$Q_L(f_0) = \frac{f_0}{f_2 - f_1} \quad (5.7)$$

$$Q_0(f_0) = \frac{Q_L(f_0)}{1 - |S_{21}(f_0)|} \quad (5.8)$$

Where  $Q_L$  is the loaded  $Q$  factor obtained from the resonator bandwidth,  $|S_{21}(f_0)|$  the magnitude of the resonant peak,  $f_2$ , is the upper  $-3dB$  point and  $f_1$ , the lower  $-3dB$  point. Inductance of the coils varies little with frequency and therefore was found by measurement of the resonant frequency with a large resonant capacitor to minimise the effects of the coil self capacitance. The capacitors used to resonate the coils (American Technical Ceramics) have  $Q$  in excess of 10,000 at the frequencies of interest and were therefore assumed to be lossless.

When this method was applied to the,  $T_x$ , coil the reported  $Q$  differed greatly from simulation, this ultimately started the investigation that lead to the measurement chapter. The weakness of this method in comparison to the method verified in the measurement chapter is two fold. Firstly no baluns are used and therefore common mode current can easily flow along the outer of the coaxial cables connected to the coil, causing unexpected losses. Secondly as the parasitic capacitance between port 1 and 2 is comparable to the coupling capacitance the unintentional coupling between ports 1 and 2 is much greater than if magnetic coupling loops are used.

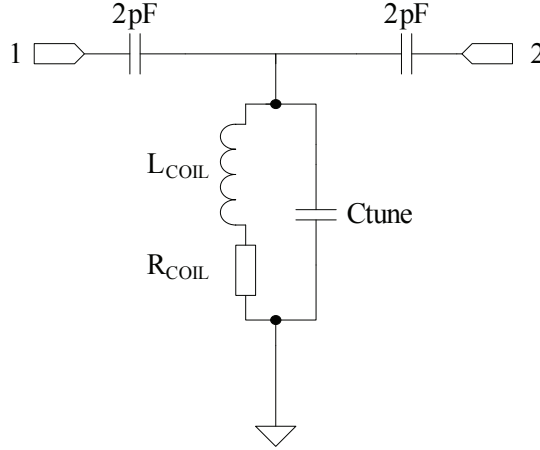


Figure 5.1: Transmission type coil measurement method used for long range IPT system development.

A series of 20 mm outside diameter,  $R_x$ , coils were constructed, aiming to maximise the  $Q$  factor at 3 MHz, the target frequency of operation of the IPT system. This frequency of operation was primarily dictated by the need to avoid spurious radio emission from the,  $T_x$ , coil, caused by the transmission wavelength approaching its electrical length. Coil parameters (turns, turn spacing) were optimised in an EM simulator (CST Microwave Studio) before construction and via empirical models [100, 101, 30]. The number of turns and conductor diameter for the,  $R_x$ , coil was constrained by manufacturing capability. It was found that PCB coils, due to the small conductor cross-sectional areas, had poor  $Q$  compared to copper wire coils. The wire coils were constructed by threading enamelled wire through a former, composed of 100  $\mu$ m thick flexible PCB material, with holes drilled at each wire corner; a thin ferrite, TDK IRJ04 ( $\mu = 40$ , depth = 0.5 mm) was then stuck to the reverse side of the coil to reduce the effect of metallic planes behind the coil. The ferrite had little measurable effect on the coil  $Q$  factor.

The results (Fig. 5.2) compare favourably with published research by other groups, achieving almost 2x



the  $Q$  factor of optimised PCB coils at 3 MHz of 40 mm diameter [100]. Litz wire was found to offer a small advantage in  $Q$  factor over equivalent diameter solid wire; the lack of dramatic improvement is likely due to the reduced conductor area available in such finely stranded insulated wire due to the space occupied by insulation.

#### 5.2.4 170 mm receiver coil

The 20 mm coils only harvest 1 mW within a meter of the transmitting coil and are of limited use for a long range system. Therefore as a more practical alternative a 170 mm diameter,  $R_x$ , coil was developed for the long range wireless power transfer system using a 3D printed ABS former loaded with 3 overlaid parallel connected litz wires (Fig. 5.4). Due to its greater  $Q$  factor (280 at 3 MHz) and 72x greater area than the miniaturised coils, it was found to be able to harvest greater than 1 mW up to 7 m from the  $T_x$  coil. To obtain an estimate of the power transferred, not taking into account the environment the coil is placed in, the mutual inductance has been estimated via the loop areas,  $A_{Tx}$ ,  $A_{Rx}$ , of the antennas using [30]:

$$L_{TxRx} = \frac{\mu_0 A_{Tx} A_{Rx}}{2D^3} \quad (5.9)$$

Where  $A_{TX}$ ,  $A_{RX}$  are the sum of the areas of the turns for the Tx and Rx coils respectively and  $D$ , is the on axis displacement of the coils.

Table 5.1: Miniaturised 20 mm diameter receiver coils

| Coil       | Spacing (mm) | Conductor                            | Turns | Inductance ( $\mu H$ ) | Q(3 MHz) |
|------------|--------------|--------------------------------------|-------|------------------------|----------|
| Litz wire  | 0.5          | Litz wire<br>0.025 mm x 160          | 11    | 1.11                   | 97       |
| Solid wire | 0.5          | 0.321 mm diameter<br>copper wire     | 11    | 1.25                   | 68       |
| PCB        | 0.25         | 0.4 x 0.035 mm Cu track<br>with HASL | 15    | 2.07                   | 30       |

Table 5.2: Long range IPT system coils. <sup>1</sup>Simulation result.

| Coil | Diameter (m) | Spacing (mm) | Conductor                | Turns | Inductance ( $\mu H$ ) | Q(3 MHz)          |
|------|--------------|--------------|--------------------------|-------|------------------------|-------------------|
| Rx   | 0.17         | 1.5          | 3 strands of 1.3 mm litz | 6     | 9.70                   | 280               |
| Tx   | 1            | 30           | 28 mm Cu pipe            | 2     | 7.63                   | 2890 <sup>1</sup> |

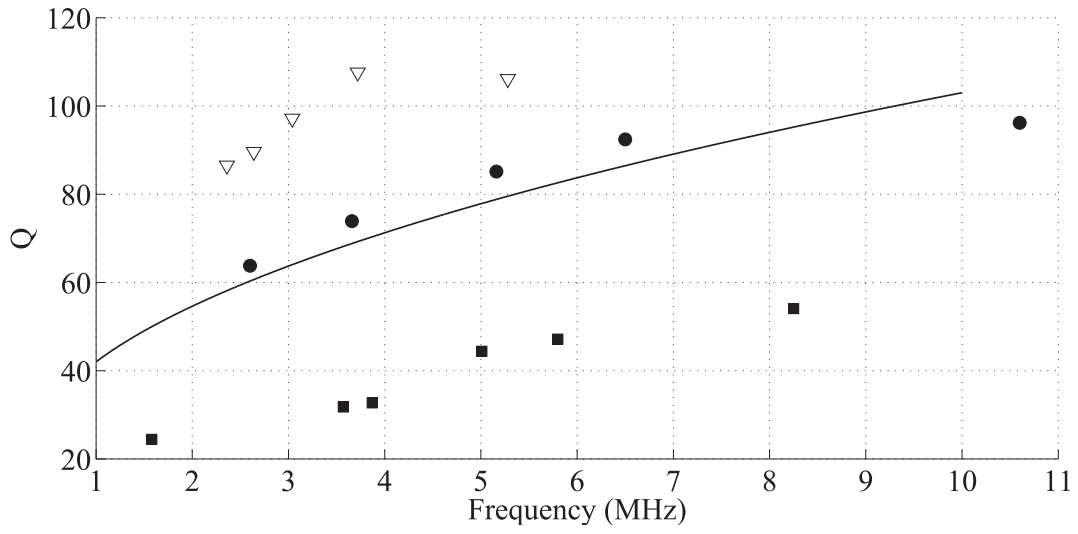


Figure 5.2:  $Q$  factor measurements and simulation results for 20 mm coils. Simulation of solid wire coil —, Litz wire coil ▽ (measurement), Solid wire • (measurement), PCB coil ■ (measurement).

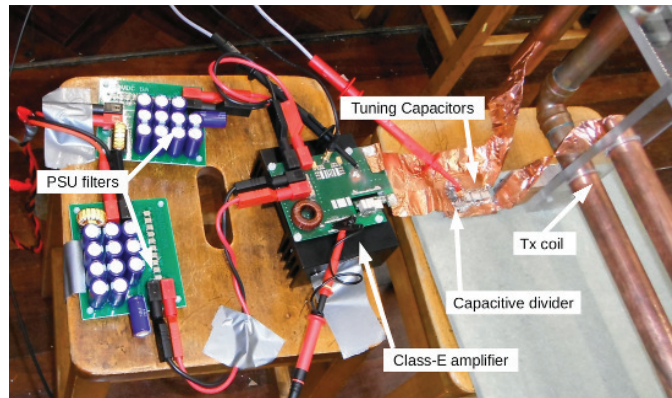


Figure 5.3: Class-E amplifier and connection to  $T_x$  coil.



Figure 5.4: 170 mm and 20 mm  $R_x$  coils.



Figure 5.5: 1 m  $T_x$  coil and Class-E amplifier.

### 5.3 Long range IPT approximations

In a conventional IPT system, where efficiency is  $> 50\%$ , the,  $R_x$ , coil reflected impedance makes up the majority of the primary tank impedance formed between the,  $T_x$ , coil and its tuning capacitor [16]. As this varies with position and  $R_x$ , load, the Class-E amplifier must be re-tuned for optimal efficiency. However, with a long-range system, the,  $R_x$ , coil is so weakly coupled that it has negligible effect on the  $T_x$  coil impedance, simplifying both design and operation. Furthermore, the optimal resistive load for the,  $R_x$ , coil can be simplified to the conjugate match of the,  $R_x$ , tank at the operating frequency:

$$Z_{tank} = \frac{1}{\frac{1}{R_{Rx} + j\omega L_{Rx}} + j\omega C_T}, \quad (5.10)$$

where,  $R_{Rx}$ , is the series loss resistance of the,  $R_x$ , coil,  $L_{Rx}$ , the inductance of the,  $R_x$ , coil and  $C_T$ , the turning capacitance used to resonate the  $LC$  tank at the systems operating frequency. As this model makes use of the coil's loss resistance, the  $Q$  factor measurements of the coils can be verified by checking that the calculated impedance match is optimal. The match should be resistive at resonance, since the tank presents a real impedance. The free wheeling coil current can be found using the coil voltage and the impedance of the  $T_x$  coil (from inductance and  $Q$  factor measurements) or by approximating the coil as line segments of current (as in the modelling chapter) and measuring the magnetic field at a known close location to the  $T_x$  coil (e.g. 1 m away on axis).

The mutual inductance,  $L_{TxRx}$ , can be found at a specific location by measuring the magnitude of the magnetic field component the,  $R_x$ , coil primarily links with,  $|B_v|$  and the sum of the loop areas of the,  $R_x$ , coil,  $A_{Rx}$ :

$$L_{TxRx} = \frac{A_{Rx}|B_v|}{I_{Tx}} \quad (5.11)$$

This methodology allows for prediction of system efficiency in real-world environments where the magnetic field strength is modified by conductive objects.

### 5.4 Results

The, 1 m by 1 m,  $T_x$ , coil and 170 mm by 170 mm,  $R_x$ , coil were displaced from 2 m to 10 m, on axis, in a large laboratory with the coils located far away from any boundary and with no objects placed between the coils. The laboratory contained a number of non-removable conductive objects, such as the flooring (steel backed) and the bench supports (steel bar). This is reflected in the magnetic field strength readings in table 5.3 which are greater than would be expected at 6 m and beyond. This shows that in real-world environments, range may be greater than expected for long-range systems. Magnetic field readings were taken using a 50 mm Aaronia PBS1 magnetic field probe and Agilent FieldFox Handheld spectrum analyser, orientated such that the component of the field in the direction of displacement was measured. To measure the received power for the system, the,  $R_x$ , coil was first was tuned to the excitation frequency of the,  $T_x$ , coil and then impedance matched with a 51 k $\Omega$  1206 surface mount resistor. The  $R_x$  coil was then positioned at the locations the magnetic field probe readings had previously been taken with the system operated at the same, 98 W DC power input to the Class-E amplifier. The voltage at the load was then measured to determine the power transferred to the load from the,  $T_x$ , coil, using a Fluke 190 Scopemeter connected to the tuning capacitors, via a short stub of coaxial cable to avoid adding additional loop area to the  $R_x$  coil. To test the maximum power input to the system, a 246 W DC power input test was run, where 10.9 mW was transferred to the receiver coil located 6 m away on axis. The limiting factor to power transfer was found to be the 1000 V rating of the MOSFET used in the Class-E amplifier, due to the high impedance of the free-wheeling  $T_x$  coil. The miniaturised Litz wire 20 mm by 20 mm coil harvested 832 mW at 1 m for

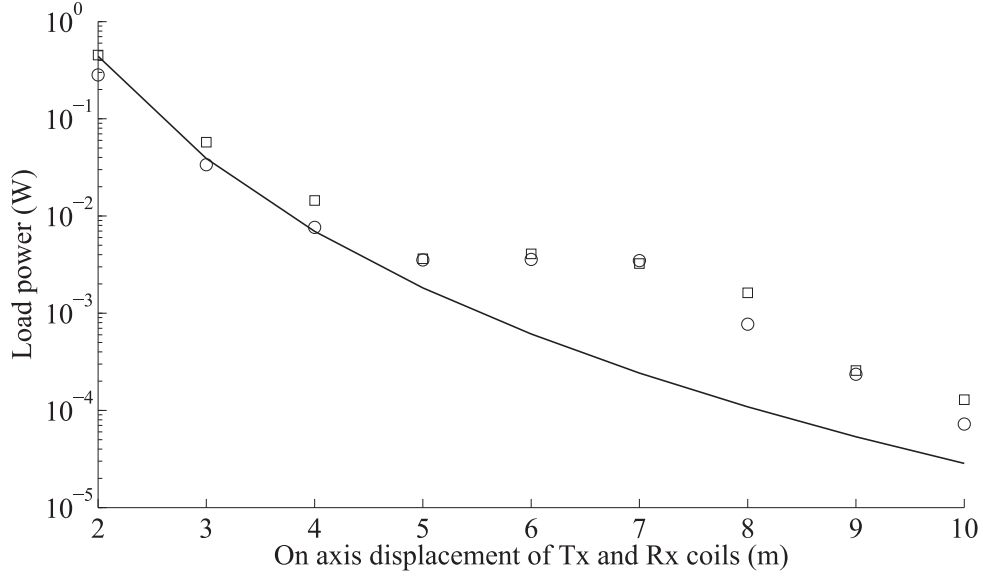


Figure 5.6: Load power transferred to 170 mm by 170 mm  $R_x$  coil from 1 m by 1 m  $T_x$  coil with 98 W DC power input to  $T_x$  amplifier. Simulation using round loops approximation —, Prediction using local magnetic field strength  $\square$ , Measured power at  $R_x$  coil  $\circ$ .

Table 5.3: long-range IPT system results

| Distance<br>(m) | Pin<br>(W) | Pout<br>(mW) | Tx voltage<br>(kVpp) | B field<br>( $\mu T$ ) | Clock<br>(MHz)   |
|-----------------|------------|--------------|----------------------|------------------------|------------------|
| 1               | 97.9       | NA           | 4.06                 | 2.91                   | 2.87126          |
| 2               | 97.9       | 282          | 4.06                 | 0.331                  | 2.87126          |
| 3               | 97.9       | 33.6         | 4.06                 | 0.117                  | 2.87126          |
| 4               | 97.9       | 7.53         | 4.06                 | 0.0588                 | 2.87126          |
| 5               | 97.9       | 3.52         | 4.06                 | 0.0294                 | 2.87126          |
| 6               | 97.9(246)  | 3.57(10.9)   | 4.06(8.19)           | 0.0322(NA)             | 2.87126(2.87721) |
| 7               | 97.9       | 3.47         | 4.06                 | 0.0278                 | 2.87126          |
| 8               | 97.9       | 0.771        | 4.06                 | 0.0197                 | 2.87126          |
| 9               | 97.9       | 0.235        | 4.06                 | 0.0078                 | 2.87126          |
| 10              | 97.9       | 0.072        | 4.06                 | 0.0056                 | 2.87126          |

98 W of DC power input to the  $T_x$  amplifier.

## 5.5 Conclusion

A practical long-range IPT system has been demonstrated. While showing low efficiency, useful amounts of power of 10 mW at distances up to 6 m from the  $T_x$  coil to compact, 170 mm by 170 mm, receivers was recovered. This system makes use of recent advances in IPT technology, using a quasi-resonant,  $T_x$ , coil with a Class-E driver, MHz transmission frequency, quasi-resonant primary and resonant secondary coils [16]. Novel coil constructions, with the aim of maximising  $Q$  factor, have been developed for the link. The system performance has been demonstrated in a real-world environment, showing the validity of using magnetic field measurements for performance prediction.

In addition, by using a 246 W power input it was demonstrated that greater  $T_x$  coil power levels are possible. Although ultimately the maximum drain-source voltage the MOSFET can withstand in the Class-E amplifier constrains the output power. Although efficiency is very low, many sensors can be powered at the same time from the same transmitter and distributed around a room, increasing overall system efficiency

and providing an alternative solution to energy harvesters or RF power beaming for power supplies in remote applications.

The long range system has a transmitter and receiver coil separated by distances up to 10 m, however the receiver coil is only 170 mm square. This large aspect ratio makes conventional finite element analysis of the complete system infeasible. The modelling chapter includes a method for calculation of the magnetic field generated by a coil. In this chapter the magnetic field generated by the transmitter coil dictates the power that can be received. Using the magnetic field modelling work received power could have been predicted taking into account the shape of the transmitter coil. This would improve power transfer predictions within 1 m of the coil when its shape becomes important.

The measurement chapter describes techniques to measure high  $Q$  coils, they would have allowed measurement of the ( $Q \approx 3000$ ) transmitter coil in this chapter. While in this chapter simulation results had to be relied on as reliable measurements could not be made of a coil with such high  $Q$ , at the time the work was completed. As the technique described in this chapter makes no provision to increase the common mode impedance of the measurement system, the reportable  $Q$  is limited to a few hundred.

# Chapter 6

## Conclusions and further work

This thesis has been concerned with the modelling, measurement and design of inductive links for wireless power transfer systems. An inductive power transfer system consists of two or more coils linked by magnetic flux. In order to optimise the design as a whole, *i.e.* to maximise the power transfer efficiency or meet some specific magnetic field strength constraint, it is necessary to be able to model the coil behaviour in the system. Without accurate measurements of the coils models cannot be verified. Design aspects of this thesis focus on practical implementation of inductive power transfer systems, where shielding is required and upon a novel long range operating mode as an alternative to harvesting and RF power beaming.

### 6.1 Overview and main findings

#### Introduction

Inductive power transfer (IPT) systems using air core coils can be modelled as loosely coupled transformers. As they have low coupling factor,  $k$ , efficient operation is not possible unless specific conditions are met. The first of these conditions is that the receiver load is resonant. If a non resonant load is used the leakage inductance causes a large current flow through the transmitter coil loss resistance resulting in excessive transmitter coil power dissipation and poor efficiency. Although non resonant receiver operation does not result in additional receiver power dissipation. The second condition is that the coils have high  $Q$  factor: The greater the  $Q$  factor of the coils the greater the efficient range of the system. Maximum quality factor and therefore maximum link efficiency occurs, in most scenarios, at MHz frequencies.

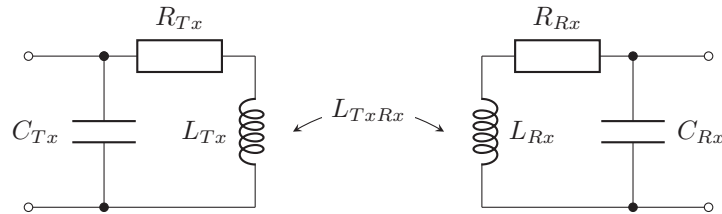


Figure 6.1: Transformer model of inductive link including coils self capacitance.

#### Modelling and simulation of inductive links

Copper tubing has been found to be a good material to wind into high  $Q$  coils. Current flows mainly on the outside of the tubing, by hollowing out the middle of the tube resistance is not increased. Coils made from these tubes, below their first self resonant frequency, which lies beyond the efficient frequency range,

have a relatively simple equivalent circuit (Fig. 6.1). This circuit consists of a resistance, with a value that increases with frequency, in series with a fixed inductance all in parallel with a small capacitance. The equivalent circuit is a simplification of the coils behaviour, even before the first self resonant frequency. At low frequencies the current flowing through the coils penetrates deeper into the tube's cross section, the results in the effective inductance. At frequencies approaching the self resonant frequency of the coil the effective capacitance increases due to increasing phase delay along the coils length. However both of these effects are not significant for the design of IPT systems.

The frequency variation of the resistance is mostly caused by the area of the tubes cross section in which the current flows reducing as the frequency of operation increases. Primarily this is due to two effects termed the skin effect and the proximity effect. The skin effect causes the depth of penetration of current to reduce with increasing frequency, while the proximity effect causes current to favour one side of the tube over the other. The skin effect is caused by the magnetic field produced by the current flowing in the tube, while the proximity effect is caused by the magnetic fields produced by the current flowing in adjacent tubes.

Both the skin and proximity effects have been modelled by other authors for tubular coils with constant cross section, however the verification work that was undertaken on these models was at below 1 MHz. The verification work undertaken in this thesis found that the skin effect model of W. Mingli and F. Yu [33] correctly predicted the skin effect for IPT frequency tubes. The proximity effect model of Zeljko Pantic and Srdjan Lukic [34] however has a number of scenarios where it underestimates coil resistance. When the coils turns are very closely spaced and secondly when the total length of the coils turns exceeds  $\frac{\lambda}{30}$ . Common IPT coils are within these limitations.

The inductive elements of the model can be modelled by division of their forms into straight filamentary finite elements. By finding the sum of the mutual inductance between all the elements generated by both coils the mutual inductance can be found. If a single coil is modelled as two paths of filaments radially spaced apart by the tubes geometric mean-distance the coil self inductance is given by the sum of mutual inductances between the two filament paths. This approach, while not taking into account the high frequency current redistribution in the tubes, predicts the inductive properties all tested coil types. When a transmitter and receiver coil are positioned many coil diameters apart electric field coupling becomes dominant over magnetic field. Mutual inductance calculations are not able to describe the complete behaviour. Under such coupling conditions the magnetic link is not efficient this is not a concern in the design of IPT systems.

With fast-running models of both the inductive effects and resistive effects an IPT system can be quickly optimised for link efficiency by exhaustive parameter sweeps. Finding an optimised IPT system would take weeks if traditional finite element simulations were used. Efficiency optimised IPT systems generally have few turns (but more than one), of closely spaced larger diameter conductors. This geometry gives the greatest possible conductor cross sectional area within the coil dimensional constraints.

The magnetic field generated by an IPT system (Fig. 6.2) in operation, can be computed by knowing the currents in the transmitter and receiver coils and application of the Biot-Savart law to filamentary models of the transmitter and receiver coils. The resistive loss equivalent circuit parameters calculated using skin effect and proximity effect models in conjunction with the inductive element modelling allow for the calculation of the currents in the transmitter and receiver coils.

In many scenarios a transmitter or receiver coil must fit within a given height and outer radius. Assuming coils maximise the use of this volume; a helical winding pattern with its constant outer radius can be considered to be coupling factor maximising, while a planar spiral winding with its much greater possible conductor radius within a given height constraint is  $Q$  factor maximising. An alternative coil winding pattern is the volumetrically efficient coil whereby the coil winding processes radially around a circular axis. With a fixed turn spacing and height constraint, increasing the turn count of this winding pattern does not reduce the average turn radius as much as the planar spiral coil or reduce the coil cross section as much as a helical coil. The volumetrically efficient winding provides a compromise between the two winding types,



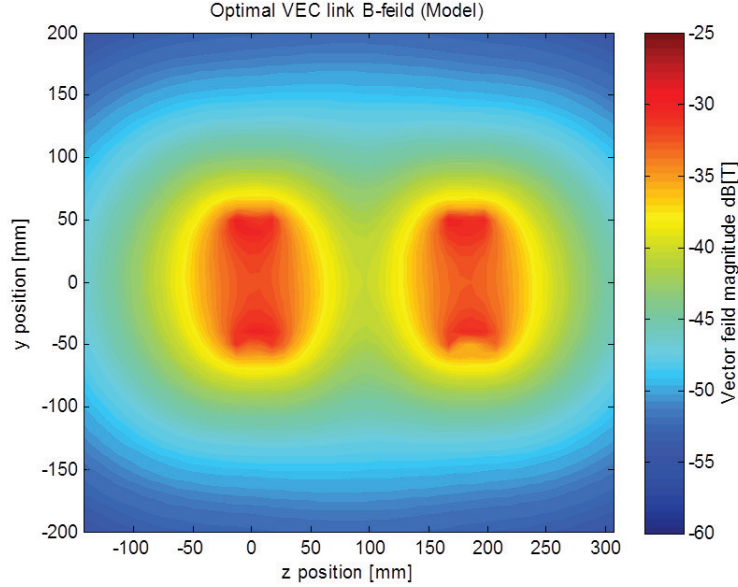


Figure 6.2: Magnetic field strength generated by model  $x = 0$  cut plane for optimal VEC system operating into optimal load.

balancing  $Q$  and coupling.

### Measurement of wireless power transfer coils

When an individual circuit component is ascribed  $Q$  it is assumed the component is resonating with its lossless dual. This results in two definitions of  $Q$ ; a circuit based definition whereby the impedance of the component defines the  $Q$  and a bandwidth definition whereby the half power bandwidth of the resonator defines the  $Q$ . For  $Q > 10$  both definitions are for practical purposes equivalent, although they are never equal, with the bandwidth definition asymptotically approaching the circuit definition.

To measure the  $Q$  factor of low loss IPT coils they must be resonated to cancel their reactance. No measurement device exists that can directly resolve the effective series resistance of an IPT coil in the presence of reactance. IPT coils also present an additional incompatibility with most measurement equipment in that they cause common mode currents in coaxial lines. The additional loading causes the self-resonant frequency and  $Q$  factor to be underestimated. An effective device to reduce these common mode currents is the transformer type balun; it must be added to test fixtures to produce accurate results.

One method that can measure the  $Q$  factor of IPT coils at MHz frequencies with  $Q$  in excess of 1,000 is the transmission method. In this method the transmission bandwidth of the IPT coil under test and a parallel connected low loss capacitor is measured, giving a single frequency point where the  $Q$  factor is known. If this test is repeated with different capacitor values the complete  $Q$  with respect to frequency can be built up. Unfortunately due to the unpredictable loss of RF relays been comparable to that of IPT coils at the frequencies of interest, this switching process cannot be made automatic through use of a switched capacitor bank. The effective capacitance and inductance of the coil can be found by observing the resonant frequencies of the coil with multiple values of capacitance.

An alternative method for finding the coil  $Q$  is to measure the impedance of a coil when resonating in series with a capacitor. At the resonant frequency the coils reactance is cancelled, presenting the loss resistance. A vector network analyser fixture can be constructed allowing it to measure such low impedances by connecting both ports together and measuring the impedance in shunt. This method can measure the  $Q$  of IPT coils even with baluns degrading the measurement. However the greater promise of this measure-

ment technique is that losses before the shunt connection do not directly effect the measurement. Therefore switching the measurement path, with an associated measurement path capacitance allows changing of the measurement frequency without introducing the switch loss into the measurement.

### Artificial magnetic conductors applied to wireless power transfer

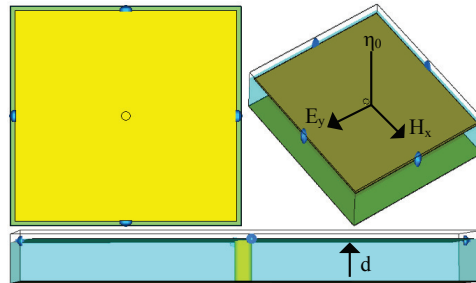


Figure 6.3: Unit cell of developed AMC.

To provide magnetic shielding engineered ground plane structures used for antennas typically operating in the GHz range can be miniaturised to operate with IPT coils. These engineered ground plane structures are termed artificial magnetic conductors, so called because of their ideal electromagnetic boundary condition which is analogous to the electrical conductors observed in nature. They consist of square patches joined at their centre by a conducting rod to a conductive plane (Fig. 6.3) in a regular grid pattern. Miniaturisation can be carried out by lowering their tuning; via increasing the substrate inductance and grid capacitance. The substrate inductance scales with the permeability of the substrate, by using a permeable substrate the required substrate thickness for a given substrate inductance is decreased. The grid capacitance can be increased by loading adjacent with discrete capacitors. AMC structures in simulation display considerable link efficiency advantages over conventional ferrite-covered ground planes using the same quantity of ferrite. However prototypes thus far constructed display excessive loss; as a result they do not meet the link efficiency predicted in simulation.

### Long range inductive power transfer system

The conventional radiative RF solution for transmitting power to remote sensors distributed around a room is limited in the amount of power that can be transmitted within regulatory emission limits. IPT systems as they are not effective radiators can avoid these regulations but still provide power to objects within 6 m of the transmitter. The system operates in an usual regime where the coupling between transmitter and receiver is very low. The link efficiency is low but the power received by the sensors is much greater than could be received by other means. This type of system is designed in a different way to a conventional IPT system. The transformer model (Fig. 6.1) is eschewed in favour of an approach based upon the harvesting of energy from a magnetic field. As metallic objects in a room shape the magnetic field, more accurate performance predictions can be obtained by performing a magnetic field survey.

## 6.2 Author's contribution

### 6.2.1 Measurement of wireless power transfer coils

- A major contribution of this thesis is a measurement technique for high  $Q$  IPT coils. At the start of this project there was no suitable method for the measurement of high  $Q$  coils. Frequently in others work measurements were made well outside of instrument specifications, or simply omitted. In

this thesis a measurement method is developed and verified using both a set of reference coils and modelling of the measurement system. This measurement system can measure coils in the frequency range 1 MHz to 20 MHz accurately.

- A related secondary contribution of this thesis is specify how the results from full field electromagnetic simulations of MHz frequency IPT coils should be interpreted in an overdetermined manner. If they are naively read, circuit  $Q$  will not match measured resonant  $Q$  at higher frequencies.
- A minor contribution of this thesis is the progress in developing a new faster measurement system. Some aspects of calibration theory were made more versatile in the development of this system and many key observations were made that will aid the development of future systems.

### 6.2.2 Modelling and simulation of inductive links

- The second major contribution of this thesis is that of a complete model for inductive links that runs quickly. This allows for fast optimisation. The thesis has focused around link efficiency optimisation but any parameter of the IPT system could be optimised (EG. field strength or input impedance).
- A related secondary contribution of this thesis is the modelling of inductances and the magnetic fields produced by coils via filamentary methods. These methods are very adaptable to new coil geometries.
- Minor contributions from this chapter are the new volumetrically efficient coil and verification of existing models.

### 6.2.3 Artificial magnetic conductors applied to wireless power transfer

- A major contribution of this thesis is the design and construction of an AMC that works at IPT frequencies. This is greater than an order of magnitude lower in frequency than has been previously been demonstrated. This structure increases magnetic coupling beyond what is possible using ferrite covered ground planes and has been shown to improve link efficiency in simulation. To achieve this the AMC had to be constructed with a permeable substrate, this has never been attempted in an AMC.
- A minor contribution of this chapter is developing a measurement method that allowed measurement of the link efficiency of the AMC.

### 6.2.4 Long range inductive power transfer system

- A major contribution of this thesis was making the first long range IPT system. Showing that this is a viable solution to the powering mW level devices. This system was further developed by Chris Kwan into a complete system for powering sensors [3].
- A minor contribution from this chapter was developing a methodology based upon magnetic energy harvesting for the design of long range IPT systems. This simplifies the design of long range inductive power transfer systems.

## 6.3 Collaboration

The overall project was my own intellectual effort apart from where literature is referenced and the exceptions I will now list:

- I briefly collaborated with Chris Kwan in a project improving the long range system by adding closed loop control. However this project was largely his, I only assisted with specifications for the receiver circuit, guidance and some measurements. As such I have not included it in the thesis. This project resulted in the publication of a paper [3].
- I also assisted George Kkelis with the measurements for a paper on high frequency rectifiers [102]. Again I have not included this in the thesis.
- At the beginning of my PhD some suggestions for the design of the long range system were made by Manuel Pinuela, David C Yates, Stepan Lucyszyn and Paul D Mitcheson in weekly meetings.
- Manuel Pinuela suggested that the volumetrically efficient coil could have non circular central paths.
- At one point Jonathan Hazel suggested that the tuning frequency of the AMC would be different in the near field to the far field while I had previously been looking for the AMC behaviour in the wrong frequency range. Changing the frequency range allowed me to observe improved link efficiency for the first time.
- Lingxin Lan assisted with designing the circuit boards, writing control code and producing the prototypes for the automatic measurement system.

## 6.4 Suggestions for further work

The particular kind of inductive power transfer subject to examination in this thesis (MHz, high  $Q$ , air cores) is very immature. Although this thesis has made progress in characterisation and modelling of the magnetic link there is still significant work to be done.

### 6.4.1 Inconclusive areas of this thesis

The following is a list of work that was attempted but did not reach as satisfactory conclusion:

- The automatic measurement system has not been completed due to issues with calibration. I am of the opinion that ultimately it is possible to construct an automatic measurement system for IPT coils using the knowledge gained from this system. Key aspects of the system such as the series switching not effecting the result were verified. Problems arose with assigning a tuning capacitor to each measurement path as this capacitor was unexpectedly part of the fixture. The original reason the measurement paths were switched rather than the coil path was because it was not possible to know the resistance of a switch in the measurement path, as the switches lack repeatability. However as the measurement path can have series switches it is in fact possible to disconnect the measurement path, measure the series switch and then reconnect the measurement path without actuating the series switch in the coil path. With this scheme the coil can be tuned by a conventional switched capacitor bank avoiding the problem of in fixture tuning capacitors.
- The AMC prototype displayed unsatisfactory performance I have no way to be certain but this could be due to the gaps in the ferrite substrate. A new prototype could be constructed if low loss ferrite can be obtained in plate form that would test this hypothesis. I tried for a number of years to obtain ferrite in this form but failed before compromising and using the stack of ferrite stickers.
- The VEC displays considerably greater link efficiencies than other coil types only when the turn spacing is very small. Unfortunately this causes the proximity effect model to not correspond to FE results. Ultimately improving this model will require a method of finite elements, a prototype of which

could be regarded as the work with fast henry and coil cross sections. However this runs too slowly for effective optimisation. My opinion is that quasi 2D solving of coil cross sections could be made quick enough to be usable for the originally intended optimisation process if a number of conditions are met. Firstly there would have to be significant algorithmic optimisation due to quasi 2D rather than full 3D calculations, secondly the matrix multiplication steps should be performed on a graphical processing unit (GPU). Ignoring the algorithmic optimisations switching from a single thread CPU code to GPU code should result in greater than order of magnitude speed up.

- Another area of research that was attempted with VEC was to actually produce coils for measurement. These coils were 3D printed, electroless plated and then electroplated with silver. Unfortunately the silver had poor conductivity resulting in the measured  $Q$  been far below predictions. Further research revealed that plating metals with conductivity close to bulk, while possible is difficult. Not able to find a commercial company willing to do this work and with no chemistry knowledge this work stalled.

### 6.4.2 Speculative areas of inductive power transfer development

The following are ideas in inductive power transfer that were not attempted:

- Beyond improving the developed structure and instrumentation thus far only a flat AMC has been developed. In other areas of metamaterial research 3D structures have begun to be explored [103]. There may be additional opportunities for flux confinement by adding side plates to the AMC.
- A method of finding the link efficiency through load sweeps has been developed however it is very laborious, this could be greatly accelerated by an automatically switched variant. Further refinements been to automatically generate a balanced sinusoid excitation and record voltage and current automatically. This would result in only having to change the tuning capacitor and distance manually with the load sweep and data recording fully automatic. This would be a generally useful piece of laboratory apparatus for investigation of wireless power systems.
- In the future coils may be desired with very close turns that are self resonant, in such a circumstance a capacitance model will be required to tune the coils. As such a further area of work would be develop such models, there are some recent papers that act on cross sections and may be usable [104].
- A slower but more accurate approach to proximity effect modelling would be to perform a quasi finite element simulation where the resistance of the coil per unit length is found via the total magnetic interaction of the filaments representing the true cross section of the tubes, similar to the Fast Henry simulations performed but with a more modern code. As the number of elements would be quite small (a few thousand) it should be possible to fit the problem on a modern graphics processor and solve very quickly, unlike the Fast Henry code that can only use a single CPU core. This simulation could also improve the mutual and self inductance calculations by knowledge of the centre of current of the tubes allowing more accurate filament placement.
- Near field beam forming is possible [105] and has not yet been explored for inductive power transfer. Beamforming schemes could reduce shielding requirements.
- Copper tube coils utilise the potential cross section currents could flow in inefficiently. The pipes are typically mm thick yet the current is only flowing in the top 30  $\mu\text{m}$ , due to the skin effect. There are various proposed methods for increasing the skin depth, it would be interesting to pursue these for an IPT coil [106][107][108][109].

# Chapter 7

## Publications

### 7.1 Conference papers

- Lawson, J.; Yates, D.C.; Mitcheson, P.D., "Efficient artificial magnetic conductor shield for wireless power," in Wireless Power Transfer Conference (WPTC), 2015 IEEE , vol., no., pp.1-4, 13-15 May 2015 doi: 10.1109/WPT.2015.7140124
- Kwan, C.H.; Kkelis, G.; Aldhafer, S.; Lawson, J.; Yates, D.C.; Luk, P.C.-K.; Mitcheson, P.D., "Link efficiency-led design of mid-range inductive power transfer systems," in Emerging Technologies: Wireless Power (WoW), 2015 IEEE PELS Workshop on , vol., no., pp.1-7, 5-6 June 2015 doi: 10.1109/WoW.2015.7132845
- Kkelis, G.; Lawson, J.; Yates, D.C.; Pinuela, M.; Mitcheson, P.D., "Integration of a Class-E low DV/DT rectifier in a wireless power transfer system," in Wireless Power Transfer Conference (WPTC), 2014 IEEE , vol., no., pp.72-75, 8-9 May 2014 doi: 10.1109/WPT.2014.6839597
- Christopher H Kwan and James Lawson and David C Yates and Paul D Mitcheson, Position-insensitive long range inductive power transfer, Journal of Physics: Conference Series, volume 557, number 1, 2014
- James Lawson and Manuel Pinuela and David C Yates and Stepan Lucyszyn and Paul D Mitcheson, Long range inductive power transfer system, Journal of Physics: Conference Series, volume 476, number 1, 2013

### 7.2 Patents

- C. Kwan, R. Pinuela, P. Mitcheson, D. Yates, and J. Lawson, Inductive power transfer system, Jun. 2 2016, wO Patent App. PCT/EP2015/072,106. [110]

# Bibliography

- [1] F. Grover, *Inductance Calculations: Working Formulas and Tables*, ser. Dover phoenix editions. Dover Publications, 2004. [Online]. Available: <https://books.google.co.uk/books?id=K3KHi9lltsC>
- [2] J. Lawson, M. Pinuela, D. C. Yates, S. Lucyszyn, and P. D. Mitcheson, “Long range inductive power transfer system,” *Journal of Physics: Conference Series*, vol. 476, no. 1, p. 012005, 2013. [Online]. Available: <http://stacks.iop.org/1742-6596/476/i=1/a=012005>
- [3] C. H. Kwan, J. Lawson, D. C. Yates, and P. D. Mitcheson, “Position-insensitive long range inductive power transfer,” *Journal of Physics: Conference Series*, vol. 557, no. 1, p. 012053, 2014. [Online]. Available: <http://stacks.iop.org/1742-6596/557/i=1/a=012053>
- [4] B. H. Waters, A. P. Sample, P. Bonde, and J. R. Smith, “Powering a ventricular assist device (vad) with the free-range resonant electrical energy delivery (free-d) system,” *Proceedings of the IEEE*, vol. 100, no. 1, pp. 138–149, Jan 2012.
- [5] S. C. Tang, T. L. T. Lun, Z. Guo, K. W. Kwok, and N. McDannold, “Intermediate range wireless power transfer with segmented coil transmitters for implantable heart pumps,” *IEEE Transactions on Power Electronics*, vol. PP, no. 99, pp. 1–1, 2016.
- [6] M. Zargham and P. Gulak, “Maximum achievable efficiency in near-field coupled power-transfer systems,” *Biomedical Circuits and Systems, IEEE Transactions on*, vol. 6, no. 3, pp. 228–245, June 2012.
- [7] B. Deepika, V. Ramya, T. Yamuna, and R. Kalpana, “A numerical analysis of temperature distribution in human eye when exposed to electromagnetic radiation,” in *2015 IEEE International Conference on Electronics, Computing and Communication Technologies (CONECCT)*, July 2015, pp. 1–5.
- [8] G. A. Covic and J. T. Boys, “Inductive power transfer,” *Proceedings of the IEEE*, vol. 101, no. 6, pp. 1276–1289, June 2013.
- [9] Y. D. Chung and C. Y. Lee, “Feasible study of wireless power charging system for eds-based superconducting magnetic levitation train using hts receiver,” in *2015 9th International Conference on Power Electronics and ECCE Asia (ICPE-ECCE Asia)*, June 2015, pp. 2328–2334.
- [10] Anderson, Ed., *Nikola Tesla On His Work With Alternating Currents and Their Application to Wireless Telegraphy, Telephony and Transmission of Power*, 2nd ed. Twenty First Century Books, 2002.
- [11] J. T. Boys and G. A. Covic, “The inductive power transfer story at the university of auckland,” *IEEE Circuits and Systems Magazine*, vol. 15, no. 2, pp. 6–27, Secondquarter 2015.
- [12] G. A. Covic, M. L. G. Kissin, D. Kacprzak, N. Clausen, and H. Hao, “A bipolar primary pad topology for ev stationary charging and highway power by inductive coupling,” in *2011 IEEE Energy Conversion Congress and Exposition*, Sept 2011, pp. 1832–1838.



- [13] G. Vandevoorde and R. Puers, “Wireless energy transfer for stand-alone systems: a comparison between low and high power applicability,” *Sensors and Actuators A: Physical*, vol. 92, no. 13, pp. 305 – 311, 2001, [ce:title]Selected Papers for Euroensors XIV[ce:title]. [Online]. Available: <http://www.sciencedirect.com/science/article/pii/S092442470100588X>
- [14] A. Kurs, A. Karalis, R. Moffatt, J. D. Joannopoulos, P. Fisher, and M. Soljačić, “Wireless power transfer via strongly coupled magnetic resonances,” *Science*, vol. 317, no. 5834, pp. 83–86, 2007. [Online]. Available: <http://science.sciencemag.org/content/317/5834/83>
- [15] S.-H. Lee and R. Lorenz, “Development and validation of model for 95%-efficiency 220-w wireless power transfer over a 30-cm air gap,” *Industry Applications, IEEE Transactions on*, vol. 47, no. 6, pp. 2495–2504, Nov 2011.
- [16] M. Pinuela, D. Yates, S. Lucyszyn, and P. Mitcheson, “Maximizing dc-to-load efficiency for inductive power transfer,” *Power Electronics, IEEE Transactions on*, vol. 28, no. 5, pp. 2437–2447, 2013.
- [17] S. Aldhaher, D. C. Yates, and P. D. Mitcheson, “Design and development of a class ef<sub>2</sub> inverter and rectifier for multimegahertz wireless power transfer systems,” *IEEE Transactions on Power Electronics*, vol. 31, no. 12, pp. 8138–8150, Dec 2016.
- [18] S. Aldhaher, P. D. Mitcheson, and D. C. Yates, “Load-independent class ef inverters for inductive wireless power transfer,” in *2016 IEEE Wireless Power Transfer Conference (WPTC)*, May 2016, pp. 1–4.
- [19] G. Vandevoorde and R. Puers, *Inductive Powering Basic Theory and Application to Biomedical Systems*, 1st ed. Springer, 2009.
- [20] C. R. Paul, *Inductance Loop and Partial*, 1st ed. John Wiley and Sons, 2011.
- [21] R. W. V. Duzer, *Fields and Waves in Communication Electronics*, 3rd ed. John Wiley and Sons, 1993.
- [22] H. J. R. C. Johnson, *Antenna engineering handbook*, 2nd ed. McGraw-Hill Book Company, 1984.
- [23] D. Yates, A. Holmes, and A. Burdett, “Optimal transmission frequency for ultralow-power short-range radio links,” *Circuits and Systems I: Regular Papers, IEEE Transactions on*, vol. 51, no. 7, pp. 1405–1413, 2004.
- [24] H. A. Mantooth, M. D. Glover, and P. Shepherd, “Wide bandgap technologies and their implications on miniaturizing power electronic systems,” *IEEE Journal of Emerging and Selected Topics in Power Electronics*, vol. 2, no. 3, pp. 374–385, Sept 2014.
- [25] C. Zierhofer and E. Hochmair, “Coil design for improved power transfer efficiency in inductive links,” in *Engineering in Medicine and Biology Society, 1996. Bridging Disciplines for Biomedicine. Proceedings of the 18th Annual International Conference of the IEEE*, vol. 4, Oct 1996, pp. 1538–1539 vol.4.
- [26] D. W. Knight. (2013, July) The self-resonance and self-capacitance of solenoid coils. [Online]. Available: <http://www.g3ynh.info/zdocs/magnetics/appendix/self-res.html>
- [27] R. Calder, S.-H. Lee, and R. Lorenz, “Efficient, mhz frequency, resonant converter for sub-meter (30 cm) distance wireless power transfer,” in *Energy Conversion Congress and Exposition (ECCE), 2013 IEEE*, Sept 2013, pp. 1917–1924.



- [28] *Precision Impedance Analyzers 6500B Series Product Specification*, 2nd ed., Online, Wayne Kerr Electronics, 2008. [Online]. Available: <http://www.waynekerrtest.com/specification/6500b%20series%20specification.pdf>
- [29] S.-H. Lee and R. D. Lorenz, "Surface spiral coil design methodologies for high efficiency, high power, low flux density, large air-gap wireless power transfer systems," in *Applied Power Electronics Conference and Exposition (APEC), 2013 Twenty-Eighth Annual IEEE*, March 2013, pp. 1783–1790.
- [30] S. Ramo, J. R. Whinnery, and T. V. Duzer, *Fields and Waves in Communication Electronics*, 3rd ed. New York: John Wiley & Sons, 1994.
- [31] J. C. Maxwell, *A Treatise on Electricity and Magnetism*, 1st ed. Macmillan and Co., 1878, vol. 2, pp. 291–298.
- [32] H. B. v. Dwight, "Skin effect in tubular and flat conductors," *American Institute of Electrical Engineers, Transactions of the*, vol. XXXVII, no. 2, pp. 1379–1403, July 1918.
- [33] W. Mingli and F. Yu, "Numerical calculations of internal impedance of solid and tubular cylindrical conductors under large parameters," *Generation, Transmission and Distribution, IEE Proceedings*, vol. 151, no. 1, pp. 67–72, Jan 2004.
- [34] Z. Pantic and S. Lukic, "Computationally-efficient, generalized expressions for the proximity-effect in multi-layer, multi-turn tubular coils for wireless power transfer systems," *Magnetics, IEEE Transactions on*, vol. 49, no. 11, pp. 5404–5416, Nov 2013.
- [35] D. Filipović and T. Dlabáč, "A closed form solution for the proximity effect in a thin tubular conductor influenced by a parallel filament," *Serbian Journal of Electrical Engineering*, vol. 7, no. 1, Feb 2010.
- [36] I. A. S. Milton Abramowitz, *Handbook of Mathematical Functions*, 9th ed. Dover, 1972.
- [37] (2012, 5) Inductex. Stellenbosch University. [Online]. Available: <http://stbweb02.stb.sun.ac.za/inductex/index.html>
- [38] S. Y. R. Hui, W. Zhong, and C. K. Lee, "A critical review of recent progress in mid-range wireless power transfer," *IEEE Transactions on Power Electronics*, vol. 29, no. 9, pp. 4500–4511, Sept 2014.
- [39] H. B. Dwight, "Skin effect and proximity effect in tubular conductors," *American Institute of Electrical Engineers, Transactions of the*, vol. XLI, pp. 189–198, Jan 1922.
- [40] S.-H. Lee and R. Lorenz, "A design methodology for multi-kw, large air-gap, mhz frequency, wireless power transfer systems," in *Energy Conversion Congress and Exposition (ECCE), 2011 IEEE*, Sept 2011, pp. 3503–3510.
- [41] Q. Ke, W. Luo, G. Yan, and K. Yang, "Analytical model and optimized design of power transmitting coil for inductively coupled endoscope robot," *IEEE Transactions on Biomedical Engineering*, vol. 63, no. 4, pp. 694–706, April 2016.
- [42] *HIOKI INSTRUCTION MANUAL 3532-50 LCR HiTESTER*, HIOKI E.E CORPORATION, 6 2008, equipment Manual.
- [43] Z. Pantic, B. Heacock, and S. Lukic, "Magnetic link optimization for wireless power transfer applications: Modeling and experimental validation for resonant tubular coils," in *2012 IEEE Energy Conversion Congress and Exposition (ECCE)*, Sept 2012, pp. 3825–3832.

- [44] D. Kajfez, *Q Factor Measurements Using MATLAB*, 1st ed. 685 Canton Street, Norwood, MA 02062: Artech House, 2011, ch. 1, p. 23 to 24.
- [45] R. C. Johnson and H. Jasik, *Antenna Engineering Handbook*, 2nd ed. McGraw Hill, 1984, ch. 5, pp. 5–3.
- [46] A. Lewandowski, D. Williams, P. Hale, J. Wang, and A. Dienstfrey, “Covariance-based vector-network-analyzer uncertainty analysis for time- and frequency-domain measurements,” *Microwave Theory and Techniques, IEEE Transactions on*, vol. 58, no. 7, pp. 1877–1886, July 2010.
- [47] *R&S ZNB Vector Network Analyzer Specifications*, Rohde & Schwarz, 10 2014.
- [48] D. E. Bockelman and W. R. Eisenstadt, “Combined differential and common-mode scattering parameters: theory and simulation,” *IEEE Transactions on Microwave Theory and Techniques*, vol. 43, no. 7, pp. 1530–1539, Jul 1995.
- [49] W. Kuhn and A. Boutz, “Measuring and reporting high quality factors of inductors using vector network analyzers,” *Microwave Theory and Techniques, IEEE Transactions on*, vol. 58, no. 4, pp. 1046–1055, April 2010.
- [50] *Keysight Technologies E4990A Impedance Analyzer 20 Hz to 10/20/30/50/120 MHz Data Sheet*, Keysight, 6 2015, rev. 1.
- [51] G. Grandi, M. K. Kazimierczuk, A. Massarini, and U. Reggiani, “Stray capacitances of single-layer solenoid air-core inductors,” *IEEE Transactions on Industry Applications*, vol. 35, no. 5, pp. 1162–1168, Sep 1999.
- [52] B. Gottert, “Quantifying the influence of plastic vapours on different contact materials in sealed miniature relays,” in *Electrical Contacts, 1990. Proceedings of the Thirty-Sixth IEEE Holm Conference on ... and the Fifteenth International Conference on Electrical Contacts*, Aug 1990, pp. 212–217.
- [53] J. M. Torrents and R. Pallas-Areny, “Uncertainty analysis in two-terminal impedance measurements with residual correction,” in *Instrumentation and Measurement Technology Conference, 2001. IMTC 2001. Proceedings of the 18th IEEE*, vol. 3, 2001, pp. 1450–1453 vol.3.
- [54] J. Ou and M. F. Caggiano, “Determine two-port s-parameters from one-port measurements using calibration substrate standards,” in *Proceedings Electronic Components and Technology, 2005. ECTC '05.*, May 2005, pp. 1765–1768 Vol. 2.
- [55] J. Wu, B. Wang, W. Yezunis, and K. H. Teo, “Wireless power transfer with artificial magnetic conductors,” in *Wireless Power Transfer (WPT), 2013 IEEE*, May 2013, pp. 155–158.
- [56] S. Liu, Q. Wu, J. Hua, and M. Chen, “A broadband fractal amc ground plane for low-profile antennas,” in *Millimeter Waves (GSMM), 2012 5th Global Symposium on*, May 2012, pp. 70–73.
- [57] D. Gregoire, C. White, and J. Colburn, “Wideband artificial magnetic conductors loaded with non-foster negative inductors,” in *Antenna Technology (iWAT), 2012 IEEE International Workshop on*, March 2012, pp. 237–240.
- [58] O. Luukkonen, C. Simovski, G. Granet, G. Goussetis, D. Lioubtchenko, A. V. Raisanen, and S. A. Tretyakov, “Simple and accurate analytical model of planar grids and high-impedance surfaces comprising metal strips or patches,” *IEEE Transactions on Antennas and Propagation*, vol. 56, no. 6, pp. 1624–1632, June 2008.

- [59] O. Luukkonen, C. Simovski, G. Granet, G. Goussetis, D. Lioubtchenko, A. V. Raisanen, and S. A. Tretyakov, "Corrections to 'simple and accurate analytical model of planar grids and high-impedance surfaces comprising metal strips or patches'", [jun 08 1624-1632], *IEEE Transactions on Antennas and Propagation*, vol. 58, no. 6, pp. 2162–2162, June 2010.
- [60] D. F. Sievenpiper, "High-impedance electromagnetic surfaces," Ph.D. dissertation, University of California, Los Angeles, 1999.
- [61] K. Whites, B. Glover, and T. Amert, "Easily designed and constructed high impedance surfaces," in *Antennas and Propagation Society International Symposium, 2003. IEEE*, vol. 2, 2003, pp. 407–410 vol.2.
- [62] C. Simovski, P. de Maagt, and I. Melchakova, "High-impedance surfaces having stable resonance with respect to polarization and incidence angle," *Antennas and Propagation, IEEE Transactions on*, vol. 53, no. 3, pp. 908–914, 2005.
- [63] M. Samani and R. Safian, "On bandwidth limitation and operating frequency in artificial magnetic conductors," *Antennas and Wireless Propagation Letters, IEEE*, vol. 9, pp. 228–231, 2010.
- [64] D. Gregoire, C. White, and J. Colburn, "Wideband artificial magnetic conductors loaded with non-foster negative inductors," *Antennas and Wireless Propagation Letters, IEEE*, vol. 10, pp. 1586–1589, 2011.
- [65] R. Diaz, "Magnetic loading of artificial magnetic conductors for bandwidth enhancement," in *Antennas and Propagation Society International Symposium, 2003. IEEE*, vol. 2, 2003, pp. 431–434 vol.2.
- [66] S. Zhu, K. Ford, A. Tennant, and R. Langley, "Miniaturised split ring antenna over loaded amc surface," in *Antennas and Propagation Conference (LAPC), 2010 Loughborough*, 2010, pp. 305–308.
- [67] S. Clavijo, R. Diaz, and W. McKinzie, "Design methodology for sevenpiper high-impedance surfaces: an artificial magnetic conductor for positive gain electrically small antennas," *Antennas and Propagation, IEEE Transactions on*, vol. 51, no. 10, pp. 2678–2690, 2003.
- [68] H. Liu, K. Ford, and R. Langley, "Miniaturised artificial magnetic conductor design using lumped reactive components," *Electronics Letters*, vol. 45, no. 6, pp. 294–295, 2009.
- [69] C. Mias and J. H. Yap, "A varactor-tunable high impedance surface with a resistive-lumped-element biasing grid," *Antennas and Propagation, IEEE Transactions on*, vol. 55, no. 7, pp. 1955–1962, 2007.
- [70] J. Sohn, K. Y. Kim, H.-S. Tae, and H. Lee, "Comparative study on various artificial magnetic conductors for low-profile antenna," *Progress In Electromagnetics Research*, vol. 61, pp. 27–37, 2006.
- [71] J. Parron, J. Gonzalez-Arbesu, F. Fortuny, J. M. Rius, G. Junkin, R. Villarino, and J. Romeu, "Artificial magnetic reflector based on spiral resonators," in *Antennas and Propagation, 2006. EuCAP 2006. First European Conference on*, 2006, pp. 1–5.
- [72] A. Dewantari and A. Munir, "Bandwidth enhancement of artificial magnetic conductor-based microwave absorber using square patch corner cutting," in *Telecommunication Systems, Services, and Applications (TSSA), 2012 7th International Conference on*, 2012, pp. 210–214.
- [73] J. Bell and M. Iskander, "Experimental analysis of an ultrawideband hybrid ebg/ferrite ground plane," in *Antennas and Propagation Society International Symposium, 2008. AP-S 2008. IEEE*, 2008, pp. 1–4.

- [74] S. Raza, M. Antoniadou, and G. Eleftheriades, "A compact low-profile high-impedance surface for use as an antenna ground plane," in *Antennas and Propagation (APSURSI), 2011 IEEE International Symposium on*, 2011, pp. 1832–1835.
- [75] R. Hadarig, M. de Cos, and F. Las-Heras, "Novel miniaturized artificial magnetic conductor," *Antennas and Wireless Propagation Letters, IEEE*, vol. 12, pp. 174–177, 2013.
- [76] R. C. Hadarig, M. de Cos Gomez, Y. Alvarez, and F. Las-Heras, "Novel bow-tie-amc combination for 5.8-ghz rfid tags usable with metallic objects," *Antennas and Wireless Propagation Letters, IEEE*, vol. 9, pp. 1217–1220, 2010.
- [77] S. Abootorabi, M. Kaboli, S. Mirtaheri, and M. Abrishamian, "Using high impedance ground plane for improving radiation in monopole antenna and its unusual reflection phase properties," in *PIERS Proceedings*, 2009, pp. 197–201.
- [78] C. S. R. Kaipa, A. Yakovlev, S. I. Maslovski, and M. Silveirinha, "Mushroom-type high-impedance surface with loaded vias: Homogenization model and ultra-thin design," *Antennas and Wireless Propagation Letters, IEEE*, vol. 10, pp. 1503–1506, 2011.
- [79] D. Kern, D. Werner, and M. Wilhelm, "Active negative impedance loaded ebg structures for the realization of ultra-wideband artificial magnetic conductors," in *Antennas and Propagation Society International Symposium, 2003. IEEE*, vol. 2, 2003, pp. 427–430 vol.2.
- [80] D. Huang, Y. Urzhumov, D. R. Smith, K. H. Teo, and J. Zhang, "Magnetic superlens-enhanced inductive coupling for wireless power transfer," *Journal of Applied Physics*, vol. 111, no. 6, p. 064902, 2012. [Online]. Available: <http://link.aip.org/link/?JAP/111/064902/1>
- [81] B. Wang, K. H. Teo, T. Nishino, W. Yezauris, J. Barnwell, and J. Zhang, "Experiments on wireless power transfer with metamaterials," *Applied Physics Letters*, vol. 98, no. 25, p. 254101, 2011. [Online]. Available: <http://link.aip.org/link/?APL/98/254101/1>
- [82] Y. Cho, S. Lee, S. Jeong, H. Kim, C. Song, K. Yoon, J. Song, S. Kong, Y. Yun, and J. Kim, "Hybrid metamaterial with zero and negative permeability to enhance efficiency in wireless power transfer system," in *2016 IEEE Wireless Power Transfer Conference (WPTC)*, May 2016, pp. 1–3.
- [83] W. Li, P. Wang, C. Yao, Y. Zhang, and H. Tang, "Experimental investigation of 1d, 2d, and 3d metamaterials for efficiency enhancement in a 6.78mhz wireless power transfer system," in *2016 IEEE Wireless Power Transfer Conference (WPTC)*, May 2016, pp. 1–4.
- [84] A. Rajagopalan, A. K. RamRakhyani, D. Schurig, and G. Lazzi, "Improving power transfer efficiency of a short-range telemetry system using compact metamaterials," *IEEE Transactions on Microwave Theory and Techniques*, vol. 62, no. 4, pp. 947–955, April 2014.
- [85] D. E. Senior and P. V. Parimi, "Planar wireless power transfer system with embedded magnetic metamaterial resonators," in *2016 IEEE International Symposium on Antennas and Propagation (APSURSI)*, June 2016, pp. 607–608.
- [86] J. Besnoff, M. Chabalko, and D. S. Ricketts, "A frequency-selective zero-permeability metamaterial shield for reduction of near-field electromagnetic energy," *IEEE Antennas and Wireless Propagation Letters*, vol. 15, pp. 654–657, 2016.
- [87] K. C. Wan, Q. Xue, X. Liu, and S. Y. Hui, "Passive radio-frequency repeater for enhancing signal reception and transmission in a wireless charging platform," *IEEE Transactions on Industrial Electronics*, vol. 61, no. 4, pp. 1750–1757, April 2014.

- [88] P. Wu, F. Bai, Q. Xue, X. Liu, and S. Y. R. Hui, "Use of frequency-selective surface for suppressing radio-frequency interference from wireless charging pads," *IEEE Transactions on Industrial Electronics*, vol. 61, no. 8, pp. 3969–3977, Aug 2014.
- [89] Fair-rite. (2013, Jun.) 61 material characteristics. [Online]. Available: <http://www.fair-rite.com/newfair/materials61.htm>
- [90] *WE-FSFS Flexible Sintered Ferrite Sheet*, Würth, 2 2016, rev. 1.3.
- [91] W. H. W. W. G. Hurley, *Transformers and Inductors for Power Electronics: Theory, Design and Applications*, 1st ed. Wiley, 4 2013.
- [92] P. J. Massey, "New formulae for practical pager design," in *Antennas and Propagation, 2001. Eleventh International Conference on (IEE Conf. Publ. No. 480)*, vol. 1, 2001, pp. 265–268 vol.1.
- [93] B. Strassner and K. Chang, "Microwave power transmission: Historical milestones and system components," *Proceedings of the IEEE*, vol. 101, no. 6, pp. 1379–1396, 2013.
- [94] H. Visser, "Aspects of far-field rf energy transport," in *Microwave Conference (EuMC), 2012 42nd European*, 2012, pp. 317–320.
- [95] K. Finkenzeller, *RFID Handbook*, 2nd ed. New York: John Wiley & Sons, 2003.
- [96] M. Pinuela, P. Mitcheson, and S. Lucyszyn, "Ambient rf energy harvesting in urban and semi-urban environments," *Microwave Theory and Techniques, IEEE Transactions on*, vol. 61, no. 7, pp. 2715–2726, 2013.
- [97] J. Garnica, R. Chinga, and J. Lin, "Wireless power transmission: From far field to near field," *Proceedings of the IEEE*, vol. 101, no. 6, pp. 1321–1331, 2013.
- [98] K. Finkenzeller, *RFID Handbook*, 1st ed. Wiley, 2001.
- [99] D. Kajfez, "Q factor measurements, analog and digital," University of Mississippi, University, 1999. [Online]. Available: <http://www.ee.olemiss.edu/darko/rfqmeas2b.pdf>
- [100] U.-M. Jow and M. Ghovanloo, "Design and optimization of printed spiral coils for efficient transcutaneous inductive power transmission," *Biomedical Circuits and Systems, IEEE Transactions on*, vol. 1, no. 3, pp. 193–202, 2007.
- [101] F. E. Terman, *Radio Engineers' Handbook*, 2nd ed. New York and London: McGraw-Hill, 1947.
- [102] G. Kkelis, J. Lawson, D. C. Yates, M. Pinuela, and P. D. Mitcheson, "Integration of a class-e low dv/dt rectifier in a wireless power transfer system," in *2014 IEEE Wireless Power Transfer Conference*, May 2014, pp. 72–75.
- [103] D. J. Gregoire, "3d artificial impedance surfaces," in *Proceedings of the 2012 IEEE International Symposium on Antennas and Propagation*, July 2012, pp. 1–2.
- [104] H. Li and W. M. Rucker, "An accurate and efficient hybrid method for the calculation of the equivalent capacitance of an arbitrary-shaped coil," *IEEE Transactions on Magnetics*, vol. 52, no. 3, pp. 1–4, March 2016.
- [105] R. A. Kennedy, D. B. Ward, and T. D. Abhayapala, "Nearfield beamforming using radial reciprocity," *IEEE Transactions on Signal Processing*, vol. 47, no. 1, pp. 33–40, Jan 1999.

- [106] H. Shinagawa, T. Suzuki, M. Noda, Y. Shimura, S. Enoki, and T. Mizuno, "Theoretical analysis of ac resistance in coil using magnetoplated wire," *IEEE Transactions on Magnetics*, vol. 45, no. 9, pp. 3251–3259, Sept 2009.
- [107] A. M. Clogston, "Reduction of skin-effect losses by the use of laminated conductors," *Proceedings of the IRE*, vol. 39, no. 7, pp. 767–782, July 1951.
- [108] Y. Iwashita, H. Fujisawa, M. Ichikawa, and Y. Tajima, "Reduction of rf skin loss with thin foils," in *2007 IEEE Particle Accelerator Conference (PAC)*, June 2007, pp. 2134–2136.
- [109] T. Mizuno, S. Yachi, A. Kamiya, and D. Yamamoto, "Improvement in efficiency of wireless power transfer of magnetic resonant coupling using magnetoplated wire," *IEEE Transactions on Magnetics*, vol. 47, no. 10, pp. 4445–4448, Oct 2011.
- [110] C. KWAN, R. PINUELA, P. Mitcheson, D. Yates, and J. Lawson, "Inductive power transfer system," Jun. 2 2016, wO Patent App. PCT/EP2015/072,106. [Online]. Available: <https://www.google.com/patents/WO2016050633A3?cl=zh>
- [111] J. D'Errico, "IpdM: Inter-point distance matrix," <https://uk.mathworks.com/matlabcentral/fileexchange/18937-ipdm--inter-point-distance-matrix>, Feb 2008.

# Appendix A

## Grover $f(\tau^2)$ table

Table A.1: This table is found on Pg. 79 and 80. of [1] and used in the calculation of mutual inductance between loops. Further tables for close loops and very distant loops are available in the same book.

| $\tau^2$ | $f$      | $\tau^2$ | $f$       | $\tau^2$ | $f$        | $\tau^2$ | $f$ |
|----------|----------|----------|-----------|----------|------------|----------|-----|
| 0.01     | 0.021474 | 0.34     | 0.00274   | 0.67     | 0.0006246  | 1        | 0   |
| 0.02     | 0.01735  | 0.35     | 0.0026317 | 0.68     | 0.0005903  |          |     |
| 0.03     | 0.014937 | 0.36     | 0.0025276 | 0.69     | 0.0005571  |          |     |
| 0.04     | 0.013284 | 0.37     | 0.0024276 | 0.7      | 0.0005251  |          |     |
| 0.05     | 0.012026 | 0.38     | 0.0023315 | 0.71     | 0.0004941  |          |     |
| 0.06     | 0.011017 | 0.39     | 0.0022391 | 0.72     | 0.0004642  |          |     |
| 0.07     | 0.010179 | 0.4      | 0.0021502 | 0.73     | 0.0004353  |          |     |
| 0.08     | 0.009464 | 0.41     | 0.0020646 | 0.74     | 0.0004074  |          |     |
| 0.09     | 0.008843 | 0.42     | 0.0019821 | 0.75     | 0.0003805  |          |     |
| 0.1      | 0.008297 | 0.43     | 0.0019026 | 0.76     | 0.0003545  |          |     |
| 0.11     | 0.00781  | 0.44     | 0.0018259 | 0.77     | 0.0003295  |          |     |
| 0.12     | 0.007371 | 0.45     | 0.0017519 | 0.78     | 0.0003054  |          |     |
| 0.13     | 0.006974 | 0.46     | 0.0016805 | 0.79     | 0.0002823  |          |     |
| 0.14     | 0.006611 | 0.47     | 0.0016116 | 0.8      | 0.00025998 |          |     |
| 0.15     | 0.006278 | 0.48     | 0.0015451 | 0.81     | 0.00023859 |          |     |
| 0.16     | 0.00597  | 0.49     | 0.0014808 | 0.82     | 0.00021806 |          |     |
| 0.17     | 0.005685 | 0.5      | 0.0014186 | 0.83     | 0.0001984  |          |     |
| 0.18     | 0.00542  | 0.51     | 0.0013585 | 0.84     | 0.00017959 |          |     |
| 0.19     | 0.005173 | 0.52     | 0.0013004 | 0.85     | 0.00016162 |          |     |
| 0.2      | 0.004941 | 0.53     | 0.0012443 | 0.86     | 0.0001445  |          |     |
| 0.21     | 0.004723 | 0.54     | 0.00119   | 0.87     | 0.00012821 |          |     |
| 0.22     | 0.004518 | 0.55     | 0.0011374 | 0.88     | 0.00011276 |          |     |
| 0.23     | 0.004325 | 0.56     | 0.0010865 | 0.89     | 0.00009815 |          |     |
| 0.24     | 0.004142 | 0.57     | 0.0010373 | 0.9      | 0.00008438 |          |     |
| 0.25     | 0.003969 | 0.58     | 0.0009897 | 0.91     | 0.00007176 |          |     |
| 0.26     | 0.003805 | 0.59     | 0.0009436 | 0.92     | 0.0000594  |          |     |
| 0.27     | 0.003649 | 0.6      | 0.000899  | 0.93     | 0.00004824 |          |     |
| 0.28     | 0.0035   | 0.61     | 0.0008558 | 0.94     | 0.00003798 |          |     |
| 0.29     | 0.003359 | 0.62     | 0.0008141 | 0.95     | 0.00002866 |          |     |
| 0.3      | 0.003224 | 0.63     | 0.0007736 | 0.96     | 0.00002035 |          |     |
| 0.31     | 0.003095 | 0.64     | 0.0007345 | 0.97     | 0.00001312 |          |     |
| 0.32     | 0.002971 | 0.65     | 0.0006966 | 0.98     | 0.00000708 |          |     |
| 0.33     | 0.002853 | 0.66     | 0.00066   | 0.99     | 0.00000249 |          |     |

## Appendix B

### Verification resistor measurement

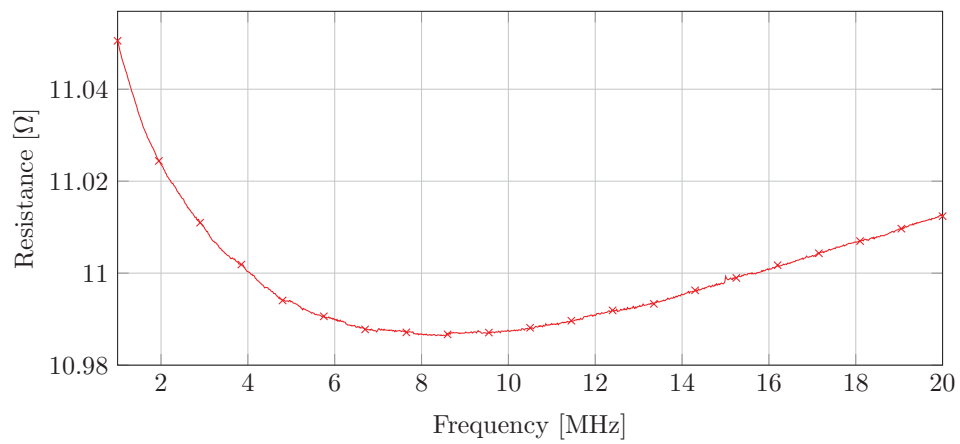


Figure B.1: Measurement of a  $10.967\ \Omega$  resistor through a balun to show that methodology is valid.



## Appendix C

# MATLAB code for inductance calculation

This MATLAB code calculates the inductance between two paths composed of discrete filaments. It relies on the MATLAB package "IPDM: Inter-Point Distance Matrix" by John D'Errico to quickly compute the distances from each vector midpoint to each other vector midpoint [111]. Alternative slower code for this is commented out at the end of the file.

```
function [M12] = BeamsInductance(L1, L2, u)
%BeamsInductance finds the partial inductance between two current paths
%using the concept of the magnetic vector potential
%Inputs:
%   L1 <= [x1 y1 y2; x2 y2 z2...] cords of L1s path
%   L2 <= [x1 y1 y2; x2 y2 z2...] cords of L2s path
%Outputs:
%   M12 <= Mutual partial inductance between them [H]
%James Lawson 2016

%Constants
const = u/(4*pi);

%Generate vectors of lines that make up the paths
dl = [L1; 0 0 0] [ 0 0 0; L1]; %Xm+1 Xm
dl = dl(2:end1,:);
ds = [L2; 0 0 0] [ 0 0 0; L2]; %Xn+1 Xn
ds = ds(2:end1,:);

%Generate midpoints of lines
L1_mid = ([L1; 0 0 0]+[ 0 0 0; L1])/2;
L1_mid = L1_mid(2:end1,:);
L2_mid = ([L2; 0 0 0]+[ 0 0 0; L2])/2;
L2_mid = L2_mid(2:end1,:);

%Generate array of distances between midpoints
m_dist = ipdm(L1_mid, L2_mid);

%Generate array of dot products between each element
dots = zeros(length(dl), length(ds));
for loop=1:length(ds)
    dots(:,loop) = ds(loop,:)*dl';
```

```

end;

%Compute the double path integral to work out the total mutual inductance
M12 = const*sum(sum((dots./m-dist)));

%This is the old implementation using loops that cannot make use of vector
%instructions.
%dl <=> L1 <=> loop
%ds <=> L2 <=> loop2
%Calculate mutual inductance between filiments
%M12 = 0;
%for loop=1:length(dl)
%    for loop2=1:length(ds)
%        R = sqrt(sum((L2_mid(loop,:) L1_mid(loop2,:)).^2));
%        M12 = M12+dot(dl(loop,:), ds(loop2,:))/R;
%    end;
%end;
%M12 = const*M12;
end

```

## Appendix D

# MATLAB code for tube resistance calculation

This MATLAB code calculates the AC resistance of isolated tubular conductors and their internal and external inductances. It is an implementation of the paper by W. Mingli and F. Yu with additional code to evaluate the Bessel functions from the MATLAB implementations.

```
function [Rdc Rac Ldc Lac] = TubeSkin(u, rho, a, t, l, f)
%tubeSkin Calculates the impedance of single straight tubes and solid pipes
%Inputs:
%   u <= absolute permeability of the conductor [H/m] (copper = 1.256629e 6)
%   rho <= resistivity of conductor [Ohm.m]
%   annealed copper IACS = 1.72e 8 [Ohm.m]
%   a <= external radius of tube [m]
%   t <= wall thickness of tube (for solid pipe t == a, result valid) [m]
%   l <= length of pipe [m]
%   f <= frequency to find impedance at [Hz]
%Outputs:
%   Rdc <= DC resistance of the tube [Ohms]
%   Rac <= AC resistance of the tube @ f [Ohms]
%   Ldc <= 'DC' internal partial self inductance of the tube [H]
%   Lac <= AC internal partial self inductance of the tube [H]
%James Lawson 2014
%Based off:
%'Numerical calculations of internal impedance of solid and tubular
'cylindrical conductors under large parameters' W. Mingli and F. Yu

if (t > a)
    fprintf(1, 'TUBE WALL IMPOSSIBLY THICK!');
end;

omega = 2*pi*f;
q = a/t; %Internal radius of tube
m = sqrt(omega*u/rho);
s = q/a;
Rdc = rho/(pi*(a^2*q^2)); %Unit length DC resistance of pipe/conductor

%Unit length DC inductance of pipe/solid conductor
if q == 0 %Solid conductor
    Ldc = u/(8*pi);
else %Pipe conductor
```

```

    %Calculate non skin effect inductance
    Ldc = (u/(2*pi))*((q^4/(a^2 q^2)^2)*(log(a/q)) (3*q^2 a^2)/(4*(a^2 q^2)));
end;

mr = m*a;
mq = m*q;

if (mr < 8) || (mq < 8)
    %Calculate in the traditional method and display warning
    fprintf(1, 'Internal radius of tube small compared to external');
    fprintf(1, '\nFor point: %d', q);
    fprintf(1, '\nmr: %d', mr);
    fprintf(1, '\nmq: %d\n', mq);
    if q == 0 %solid conductor
        Rac = Rdc*(mr/2)*(ber(0,mr)*bei_d(0,mr) bei(0,mr)*ber_d(0,mr))...
            /(ber_d(0,mr)^2+bei_d(0,mr)^2);
        Lac = Ldc*(4/mr)*(ber(0,mr)*ber_d(0,mr)+bei(0,mr)*bei_d(0,mr))...
            /(ber_d(0,mr)^2+bei_d(0,mr)^2);
    else %tubular conductor
        E = 1*(ber_d(0,mq)*ker_d(0,mq)+bei_d(0,mq)*kei_d(0,mq))...
            /(ker_d(0,mq)^2+kei_d(0,mq)^2);
        F = 1*(ker_d(0,mq)*bei_d(0,mq) kei_d(0,mq)*ber_d(0,mq))...
            /(ker_d(0,mq)^2+kei_d(0,mq)^2);
        G = E*ker(0,mr) F*kei(0,mr);
        H = F*ker(0,mr)+E*kei(0,mr);
        I = E*ker_d(0,mr) F*kei_d(0,mr);
        J = F*ker_d(0,mr)+E*kei_d(0,mr);
        K = G+ber(0,mr);
        L = H+bei(0,mr);
        M = I+ber_d(0,mr);
        N = J+bei_d(0,mr);
        Rac = Rdc*mr*(a^2 q^2)*(K*N M*L)/(2*a^2*(M^2+N^2));

        O = 1*(ber_d(0,mq)+li*bei_d(0,mq))/(ker_d(0,mq)+li*kei_d(0,mq));
        Z = Rdc*li*mr*(a^2 q^2)/(2*a^2);
        Z = Z*(ber(0,mr)+li*bei(0,mr)+O*(ker(0,mr)+li*kei(0,mr)));
        Z = Z/(ber_d(0, mr)+li*bei_d(0,mr)+O*(ker_d(0,mr)+li*kei(0,mr)));
        Lac = imag(Z)/omega;
    end;
else
    %Use numerical aproximation
    A = exp(sqrt(2)*(1+li)*(mr mq) theta(mr)+theta(mr)+theta(mq) theta(mq));
    if q == 0 %Solid conductor
        Rac = Rdc*real(li*mr/(2*phi(mr)));
        Lac = Ldc*real(4/(mr*phi(mr)));
    else %Tubular conductor
        Rac = Rdc*real(li*mr*(1 s^2)/2*(1+A*phi(mq)/phi(mq))...
            /(phi(mr) A*phi(mr)/phi(mq)*phi(mr)));
        Lac = Ldc*real((4*(1 s^2)^2)/(mr*(s^4*(34*log(s) 4*s^2+1))...
            *(1+A*phi(mq)/phi(mq))/(phi(mr) A*phi(mq)/phi(mq)*phi(mr)));
    end;
end;

Rdc = 1*Rdc; %Take into account length
Rac = 1*Rac;
Lac = 1*Lac;
Ldc = 1*Ldc;
end

```

```

function [ber] = ber(v, x)
    %Computes Ber(x) the v'th order kelvin function of the first kind
    %real component
    ber = real(besselj(v, x*exp(3*pi*1i/4)));
end

function [ber_d] = ber_d(v,x)
    %ber_d Compute Ber'(x)
    ber_d = real(exp(3*pi*1i/4)*(besselj(v 1, x*exp(3*pi*1i/4))));
end

function [bei] = bei(v, x)
    %Computes Bei(x) the v'th order kelvin function imaginary component
    bei = ( 1i/2)*(besselj(v, x*exp(3*1i*pi/4) ) besselj(v, x*exp( 3*1i*pi/4)));
end

function [bei_d] = bei_d(v,x)
    %bei_d Compute Bei'(x)
    bei_d = imag(exp(3*pi*1i/4)*(besselj(v 1, x*exp(3*pi*1i/4))));
end

function [ker] = ker(v, x)
    %Computes Kei(x) the v'th order modified kelvin function
    %of the 2nd kind real component
    ker = real(besselk(v, x*exp(pi*1i/4)));
end

function [ker_d] = ker_d(v,x)
    %ker_d Compute Ker'(x)
    ker_d = real( exp(pi*1i/4)*(besselk(v 1, x*exp(pi*1i/4))));
end

function [kei] = kei(v, x)
    %Computes Kei(x) the v'th order modified kelvin function
    %of the 2nd kind imaginary component
    kei = imag(besselk(v, x*exp(pi*1i/4)));
end

function [kei_d] = kei_d(v,x)
    %kei_d Compute Kei'(x)
    kei_d = imag( exp(pi*1i/4)*(besselk(v 1, x*exp(pi*1i/4))));
end

function [y] = theta(x)
    %theta is part of the numerical aproximation of the besel functions
    y = (0.0000000 1i*0.3926991)...
        +(0.0110486 1i*0.0110485)*(8/x) ...
        +(0.0000000 1i*0.0009765)*(8/x)^2 ...
        +( 0.0000906 1i*0.0000901)*(8/x)^3 ...
        +( 0.0000252+1i*0.0000000)*(8/x)^4 ...
        +( 0.0000034+1i*0.0000051)*(8/x)^5 ...
        +(0.0000006+1i*0.0000019)*(8/x)^6;

```

```

end

function [y] = phi(x)
%theta is part of the numerical aproximation of the besel functions
y = (0.7071068+1i*0.7071068)...
    +( 0.0625001 1i*0.0000001)*(8/x) ...
    +( 0.0013813+1i*0.0013811)*(8/x)^2 ...
    +(0.0000005+1i*0.0002452)*(8/x)^3 ...
    +(0.0000346+1i*0.0000338)*(8/x)^4 ...
    +(0.0000117 1i*0.0000024)*(8/x)^5 ...
    +(0.0000016 1i*0.0000032)*(8/x)^6;
end

```

## Appendix E

# MATLAB code for magnetic field calculation

This MATLAB code calculates the vector magnetic field contribution of a filament carrying a current.

```
function [B, unit_dir] = Bwire_vect(I, Wire_s, Wire_e, P)
%Finds the vector magnetic feild of a point in space due to a finite length
%of wire
%Wire is a filiment (no thickness) therefore off axis results may be
%dubious for wires with actual thickness
%James Lawson 2013
%Projects problem into 2d plane to find field magnitude and then uses
%projection to get unit direction vector of feild in 3D space
%I = current flowing in wire (start to end)
%Wire_s = wire start point (x,y,z)
%Wire_e = wire end point (x,y,z)
%P = point to find feild at (x,y,z)

u0 = 4e7*pi;

%Find vector of wire (u+(lambda)(v)) u = start
v_w = (Wire_e - Wire_s)/norm(Wire_e - Wire_s); %Direction vector of wire

%Find direction vector from P to infinite projection of the wire
%Direction vector from point to wire closest point if wire is infinite
%projection from start in direction towards the end
dir_p_w_fs = ((Wire_s - P) - ((Wire_s - P)*v_w'*v_w)*v_w);
%Direction vector from point to wire closest point if wire is infinite
%projection from end in direction towards the start
dir_p_w_fe = ((Wire_e - P) - ((Wire_e - P)*v_w'*v_w)*v_w);
R1 = sqrt(sum(dir_p_w_fs.^2)); %Distance from infinite projection of wire (from start)
R2 = sqrt(sum(dir_p_w_fe.^2)); %Distance from infinite projection of wire (from end)
%The furthest distance is the correct distance from the wire infinite
%projection as start/end lie on this projection and if closer the direction vector
%is pointing at one of these rather than the infinite projection of the wire and
%therefore isn't giving perpendicular distance
if R1 < R2
    R = R2;
    dir_p_w = dir_p_w_fe;
else
    dir_p_w = dir_p_w_fs;
```

```

    R = R1;
end;

% d_s and d_e are the offsets in the plane parallel with the wire
w_e_offset = Wire_e - dir_p_w;
w_s_offset = Wire_s - dir_p_w;
d_e = sqrt(sum((w_e_offset - P).^2)); % In plane distance from ends of wire
d_s = sqrt(sum((w_s_offset - P).^2));

% Calculate signs for offsets
lw = sqrt((Wire_s(1) - Wire_e(1))^2 + (Wire_s(2) - Wire_e(2))^2 + (Wire_s(3) - Wire_e(3))^2);
% From 'top' to 'bottom'
if ((d_s - lw) >= 0) && (d_s > d_e)
    d_e = d_e;
elseif ((d_e - lw) >= 0) && (d_e > d_s)
    d_s = d_s;
end;
d_s = d_s;

phi1 = atan(d_e/R);
phi2 = atan(d_s/R);
B = u0*I*(sin(phi1) - sin(phi2))/(4*pi*R); % Magnetic field magnitude

if isnan(B)
    B = 0;
end;

% now generate unit vector of field direction aXB
unit_dir = cross(dir_p_w, w_e_offset - w_s_offset);
unit_dir = unit_dir/norm(unit_dir);

end

```



## Appendix F

# MATLAB code for processing of impedance measurements

This MATLAB code processes an .s1p file extracted from an impedance measurement of a coil and fits it to a constant  $L$ ,  $C$  and variable  $R$  coil model.

```
%Attempts to remove capacitance from s parameter data of a coil
%can be used to process S11 data from CST MWS
%will give L, R(f) and C
%James Lawson 2015

%Constants
delta_c = 1e12;
Z0 = 50;

%Open s parameter data
s_params = read(rfdata.data);
z_params = s2z(s_params.S.Parameters,s_params.Z0);
z_params = z_params;

imagZ = imag(squeeze(z_params));
omega = 2*pi*s_params.Freq;

c_rem = delta_c; %Perform first estimate
run = 1;
pres = 0.01e12; %Presision to find capacitance to
while (run == 1)
    rZ = 1./(1./imagZ+omega*c_rem); %remove capacitor
    rZn = rZ./omega; %normalise
    f = fit(omega,rZn, 'poly1'); %compute gradient of linear best fit to imaginary impedance
    grad0 = f.p1;

    if grad0 > 0
        c_rem = c_rem+delta_c;
    else
        c_rem = c_rem - delta_c;
    end;

    rZ = 1./(1./imagZ+omega*c_rem); %remove capacitor
    rZn = rZ./omega; %normalise
    f = fit(omega,rZn, 'poly1'); %compute gradient of linear best fit to imaginary impedance
```

```

grad1 = f.p1;

if ((grad0 > 0 && grad1 < 0) || (grad0 < 0 && grad1 > 0))
    delta_c = delta_c/2;
end;

if delta_c < pres
    run = 0;
end;
end;

%Plot out fit data
figure(1)
plot(f,omega,rZn);
title('Line of best fit');

%Plot out R
R = real(1./(1./(squeeze(z_params))+1i*omega.*c_rem));
figure(2)
plot(s_params.Freq, R);
xlabel('Frequency [Hz]');
ylabel('R [\Omega]');
title('Extracted loss resistance');

%Print out L and C
L = f.p2;
C = c_rem;
display(L);
display(C);

%Plot out Q
Q = omega.*L./R;
figure(3)
plot(s_params.Freq, Q);
xlabel('Frequency [Hz]');
ylabel('Q');
title('Extracted Q');

%Output .slp of resistance data for Z0
%S11_R = (R - Z0)./(R+Z0);
%expand = ones(1,1,length(S11_R));
%for loop=1:length(S11_R)
%    expand(1,1,loop) = S11_R(loop);
%end;
%rfwrite(expand, s_params.Freq, 'resistance-coil.slp')

```